Spin and out-of-equilibrium transport in mesoscopic superconductors

Marko Kuzmanović

université
PARIS-SACLAY

Spin and out-of-equilibrium transport in mesoscopic superconductors

Thèse de doctorat de l'Université Paris-Saclay

École doctorale n° 564, physique de l'Ile-de-France (PIF)
Spécialité de doctorat: Physique
Unité de recherche: Université Paris-Saclay, CNRS, Laboratoire de Physique des Solides, 91405, Orsay, France
Référent: Faculté des sciences

Thèse présentée et soutenue à Orsay, le 29 janvier 2020, par

Marko KUZMANOVIĆ

Composition du jury:

Hervé COURTOIS Professeur des Universités, Université Grenoble Alpes	Président
Elke SCHEER Professeure, University of Konstanz, Germany	Rapportrice & examinatrice
Mark BLAMIRE Professeur, University of Cambridge, United Kingdom	Rapporteur & examinateur
Hélène BOUCHIAT Directrice de recherche, Laboratoire de Physique des Solides, CNRS - Université Paris-Saclay	Examinatrice
Wolfgang BELZIG Professeur, University of Konstanz, Germany	Examinateur
Marco APRILI Directeur de recherche, Laboratoire de Physique des Solides, CNRS - Université Paris-Saclay	Directeur
Charis QUAY Huei Li Maîtresse de conférences, Laboratoire de Physique des Solides, Université Paris-Saclay	Co-encadrante

Thèse de doctorat

NNT: 2020UPASS029

Contents

List of Figures

Acknowledgments

This document titled "Spin and out-of-equilibrium transport in mesoscopic superconductors" (my proposal for the title "Donald Duck explores superconductivity", a sequel to "Donald in Mathmagic Land" was promptly rejected by my supervisors, for reasons unknown to me), covers two of the several experiments that I worked on during my PhD. It's written in a rather utilitarian and non-verbose way (after all, a common exchange between my father and myself goes something like "So, how was the trip?" to which my answer would be just "Nice.", without feeling a need to provide a followup). I invite all readers to contact me without hesitation if further clarifications are needed.

During this period I have experienced many emotional highs and lows, as well as stress responses of both my body and mind previously unknown to me. In spite of this I would describe my PhD as an *positive* experience overall. The positives far outweigh the negatives: the days, weeks or even months of frustration while trying to fix the setup or fabricate a working sample were all offset by the excitement that one feels once the experiment finally works, when the puzzle presented by the data is cracked, while reading a good paper or a book, when engaged in an interesting discussion. All of these were there to remind me of the reasons for which I decided to pursue an academic career.

It would be easy to focus on the immediate past and by doing so to omit many people whose contributions should be acknowledged. In some respects the influences and support provided to me at a young age are more important than the recent ones, as they are the ones which led me to this path. After more than 20 years in the education system there are many people that I am grateful to: my teachers Ružica and Roža who recognized my interest in natural sciences; Sonja, Anika, Milan, Nataša, Ivan and Duško who devoted a lot of their time to feed my curiosity.

I would like to thank Branimir for the vital role that he played in my time spent at "Petnica Science Center", as well as Aleksandra, Vladan, Jelena and later on Nemanja and Ivan, where I got my first glimpse at what doing research is really like.

My university professors Mihajlo Vanević and Zoran Radović taught me a lot, and not only about physics: many of their offhand remarks about science and doing research I understood only much later on. I'm also thankful to them for recommending me as an intern to Marco Aprili, way back in 2014, which led me to where I am today.

Many thanks to Julien Basset for the work that he did on the experiment presented in the second part of the thesis.

I owe a great deal of gratitude to my supervisors Charis Quay and Marco Aprili. Without the energy and effort that they put into our work, the time and patience they devoted to my never ending stream of questions, none of what I did would have been possible. During the past three years they provided me with endless support and guidance, both professional and personal. I was always treated as a human being first and as an equal, for which I am

extremely grateful.

I would also like to thank the members of my defense committee: Hervé Courtois, Hélène Bouchiat, Wolfgang Belzig, and especially Elke Scheer and Mark Blamire, for the helpful comments and suggestions that made this thesis better.

Of course, none of this would have been possible without the support of friends and family. Kamila, Gianluca, Freek, Mathieu and Alexis made my life in the lab, and outside of it, much better than it otherwise would have been. Thanks to Luka, Ognjen, Lazar, Nikola, Stefan, Dušan, Vladimir and Stefan for the soundtrack to my life for the past three years, as well as the endless banter. Thanks to Daniel and Aleksandar for all the technical help, and alongside with Dušan and Ognjen for the many late-night games that we played.

Tijana and Jelena played hugely important roles in my life, and not only in past few years. Tijana thank you for making me laugh and cry, for making me feel better and safe in ways only you know how, especially during the toughest parts of my life. Jelena thanks for *always* being there for me, for all of the talks lasting until the wee hours, and for being the best flatmate I ever had.

Lastly I would like to thank members of my family for making me the person that I am today, for their love and care: my uncle Zoran, who encouraged me to play with his electronics and tools (even when it caused him physical harm: "That's a big hammer, you are going to get hurt!", "No I won't, you can hold the nail and I'll drive it in." You can guess what happened next.) which, in retrospect, is what sparked my interest in science; my grandmother Jermina for always believing in me, supporting me in my choices and encouraging me to pursue an academic career; my grandmother Ljubica for all of the carefree afternoons that I spent with her during my childhood and my teens; my father Dušan for all of the silly games that we played when I was a child and more recently, together with Milena, all of the affection and emotional support that I received; and my mother Ljiljana for showing me that math and programming can be fun, and above all the unconditional love and support!

Introduction

The key feature of superconductivity is a gap, Δ, in the excitation spectrum. Within the BCS theory of superconductivity, the amplitude of this gap is directly related not only to the strength of the pairing mechanism but also to the presence of excitations (quasiparticles) and their energy distribution. This is formally given by the self-consistent gap equation. While a stronger coupling constant can enhance the gap, excitations can only reduce it. Nevertheless it was recognized early on that engineering an out-of-equilibrium distribution function for the quasiparticles can lead to interesting unstable ground-states [1] or even to increase the critical temperature [2].

Quasiparticles can be excited thermally, by absorbing of radiation, and injection of non-superconducting electrons from a counter-electrode. When the perturbation is chargeless, which is the case for radiation or a finite temperature, only energy is transferred to the superconductor. Because of the intrinsic electron-hole symmetry of a BCS superconductor this results in a equal number of electron-like and hole like excitations. If instead a charged particle is injected into the superconductor the balance between electron and hole like excitation is broken, while charge neutrality is preserved by removing Cooper pairs from the condensate [3].

These two types of excitations correspond to different modes of the distribution function, called the energy and the charge mode. Formally they are classified based on the symmetry of the (nonequilibrium component) of the distribution function with respect to the Fermi level. These modes are also called longitudinal (f_L) and transverse (f_T), because they enter with a $\pi/2$ phase shift in the self-consistent gap equation [4].

The actual distribution function in the superconductor depends on quasiparticle excitation, relaxation and recombination rates. The different mechanisms at work set a hierarchy of the time-scales involved in relaxing f back to equilibrium. The key property of out-equilibrium superconductivity is that quasiparticle recombination occurs through the emission of low energy phonons [5], where the excess energy is carried away by the phonon. As the density of states of phonons at energies of the order the superconducting gap ($\approx$ 1meV) is low, and because the electron-phonon coupling is weak in BCS superconductors, the recombination time becomes the longest timescale, going up to 1ms [6]. As quasiparticles interact on a shorter timescale, set by the electron-electron interaction, in macroscopic samples, whose dimensions are larger than both the recombination and relaxation lengths, the distribution function is well described by a Fermi-Dirac distribution with an effective temperature higher than the bath one. Thus the energy mode excitations are the longest-lived ones, and are responsible for most observed nonequilibrium effects in superconductors. All other excitation modes relax at shorter time-scales, the details of (elastic) relaxation mechanisms are discussed in chapter 1 of this thesis.

Because quasiparticles are long-lived, superconductors can be used as efficient detectors of

radiation [7]. On the other hand quasiparticle poisoning limits quantum coherence through (finite frequency) dissipation [8]. Therefore, there is a renewed interest in out-of-equilibrium superconductivity in the context of both cryogenic detection and superconducting qubits. In superconducting circuits the central issue is the ability to drive quasiparticles away from the sensitive quantum device or alternatively in detectors to bring them closer to the sensor itself. Since the superfluid electrically shorts the sample, quasiparticles can not be driven by an electric field. Strategies based on quasiparticle trapping have been explored [9], where the idea is to confine the excitations to a part of the sample which is not superconducting. Once they have relaxed to an energy below the gap, quasiparticles can not leave this part of the sample, as the density of states is zero below $E = \Delta$ in a BCS superconductor.

Developing a detailed theoretical framework to describe energy and charge transport is not an easy task, as the kinetic equations for quasiparticle diffusion include (energy non-local) inelastic processes, which can locally change the number of quasiparticle and their distribution, and the order parameter. For instance, a low energy phonon, resulting from the recombination of two quasiparticles, can be reabsorbed elsewhere in the superconductor, breaking a Cooper pair in the process [10].

The situation is simpler when the size of the device becomes smaller than both the quasiparticle relaxation and recombination lengths. In absence of interactions, the distribution function is basically set by the boundary conditions. For instance for a wire connected to two reservoirs the (energy mode) distribution function at each point of the wire is a linear combination of the reservoir distribution functions. This is well described theoretically within the Keldysh-Usadel formalism [11, 12, 13], by neglecting the self-energy terms related to inelastic interactions.

The topic of this work is quasiparticle transport in this limit of negligible or weak quasiparticle interaction. Two specific questions, addressed in parts I and II of the thesis respectively, are:

- Can the spin degeneracy of the distribution function modes be lifted?
- Can the out-of-equilibrium distribution function have a dynamical feedback on the spectral properties of a superconductor?

The results presented in this thesis (hopefully) bring new insights into spin-dependent thermoelectric effects in mesoscopic superconductors and on the opportunities for coherent spin transport in these systems, as well as point to new routes for unconventional out-of-equilibrium states generated by both spin injection and microwave pumping.

Due to the nature od the theory used to describe these experiments simple analytical expressions which could be used to model the measurements are seldom available. Thus out of necessity, as well as personal curiosity, the theoretical calculations and modeling were performed by myself, with the goal of explaining the experimental data. Following this a decision was made to present both the literature review and the theoretical results specific to this work in the same style. It was brought to my attention by the referees that this made distinguishing the two difficult. To mitigate this comments at the beginning of chapters/sections briefly describing their contents were introduced.

Part I

Spin physics in out-of-equilibrium superconductors

Introduction

For a long time, work on out-of-equilibrium superconductivity concentrated mainly on spinless excitations [4]. Based on symmetry, the out-of-equilibrium quasiparticle (QP) distribution function $f(E)$ can be decomposed into energy $f_L(E) = f(-E) - f(E)$ and charge $f_T(E) = 1 - f(E) - f(-E)$ modes [4, 14]. The simplest $f(E)$ which excites these modes are, respectively, an effective temperature T^*_{QP} and a QP chemical potential $\mu_{QP} \neq 0$ (measured from the Fermi energy). The study of charge and energy transport in superconductors has led to applications in cryogenic detection of radiation and thermometry [15].

The energy mode can be excited by charge-neutral perturbations such as electromagnetic radiation whose frequency is larger than the superconducting energy gap Δ: the absorption of such radiation breaks pairs and creates quasiparticles [16]. The charge mode, on the other hand, can be excited by injecting charged carriers (i.e. electrons or holes) through a tunnel barrier into a superconductor, where they become quasiparticles [17]. As quasiparticles are not instantaneously converted into Cooper pairs, their chemical potential is shifted up or down with respect to that of Cooper pairs. This has been measured as a voltage drop between the superconductor and a normal electrode in contact with the superconductor via a tunnel barrier [18, 19]. If electrons or holes are injected at energy $|E| > \Delta$, both charge and energy modes are excited. The relaxation time for the energy mode is the inelastic (electron-phonon) scattering time [15] while the charge mode relaxes over the charge relaxation length [19, 20, 21, 22, 23].

In a theoretical paper published in 1976, A. Aronov introduced the concept of spin injection into superconductors [24]. The main idea of his paper was to use spin injection to produce an internal magnetic field in order to perform an NMR experiment in the superconducting state (the Meissner effect prevents external magnetic fields from penetrating into the volume of superconductors).

The possibility of different energy distribution functions for spin up and down electrons (or QPs) was then raised for both normal metals and superconductors. In superconductors [25, 26, 13, 11, 12, 27], the decomposition of the quasiparticle distribution function $f(E)$ above can be generalized to the spinful case by the addition of spin $f_{T3}(E) = f_{T\uparrow}(E) - f_{T\downarrow}(E)$ and spin energy $f_{L3}(E) = f_{L\uparrow}(E) - f_{L\downarrow}(E)$ modes [11, 12, 13]. These new modes exist only if spin up and down QPs have different distribution functions, i.e. $f_\uparrow(E) \neq f_\downarrow(E)$. For instance, a spin-dependent temperature (chemical potential) will give finite f_{L3} (f_{T3}) - see figure 1. By construction, f_L and f_{L3} are odd in energy, while f_T and f_{T3} are even in energy.

To generate $f_\uparrow(E) \neq f_\downarrow(E)$, it is necessary to preferentially generate excitations of one spin species.

In a pioneering experiment, Johnson et al. [28] showed that spin injection from a ferromagnetic electrode into a normal metal is possible by applying a voltage bias across the interface between the two. The out-of-equilibrium magnetization created in the normal metal

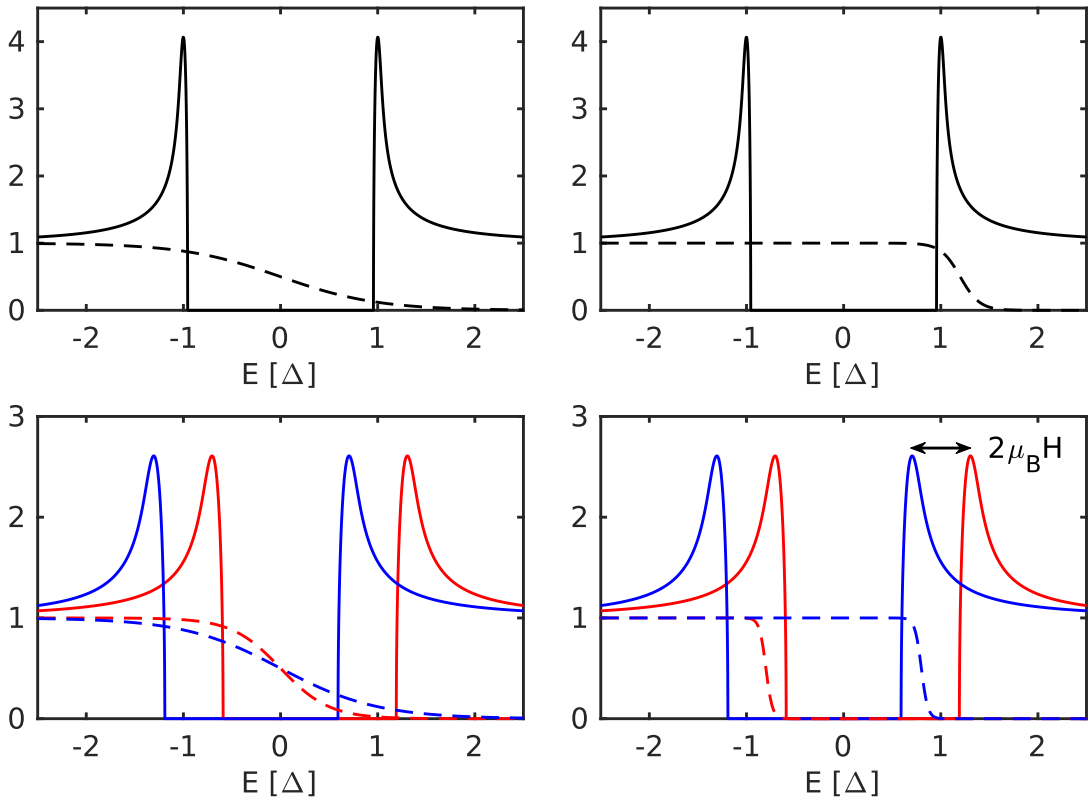

Figure 1: A depiction of the different distribution function modes: top left shows an effective temperature T^* ($H = 0$), which is a specific realization of the energy mode f_L, top right an effective chemical potential μ (with a finite temperature, $H = 0$) which is the simplest distribution function that excites the charge mode f_T. The bottom left and bottom right panels show a spin-dependent temperature and chemical potential, corresponding to the simplest realizations of the spin-energy f_{L3} and spin f_{T3} modes ($H > 0$).

is detected electrically, by measuring the voltage between it and a second ferromagnetic electrode [29]. This *nonlocal* signal is directly proportional to the shift in the chemical potential, μ_s, of spin up (down) electrons due to spin accumulation [30, 31], in which spin up and down chemical potentials shift by the same amount, but in opposite directions. The spin relaxation length measured in high purity light metals (which have low spin-orbit coupling) can reach 100μm, and the spin relaxation time is ≈ 50ns [28].

Subsequently, evidence for different effective temperatures for spin up and down electron was observed in the nonlinear contribution to the magnetoresistance of metallic nanopillar spin valves [32]. Indeed, a spin-dependent effective temperature is the simplest manifestation of the spin energy mode, in which the two spin species carry different energy currents.

In thin superconducting films, it is possible to preferentially excite QPs of one spin with current injection from a normal (rather than ferromagnetic) electrode, by applying an in-plane magnetic field H. This raises (lowers) the energy of spin up (down) QPs by $E_Z = \frac{g}{2}\mu_B H = \mu_B H$ and splits the DOS so that only spin down excitations are allowed in the energy range $\Delta - E_Z < |E| < \Delta + E_Z$. H also couples to the orbital degree of freedom, inducing screening supercurrents and a rounding of the QP coherence peaks [33, 34, 35]. In our experiments, $E_Z > \alpha$, the orbital depairing energy, up to the H_c, the critical field of the

superconductor. Thus, when we inject an electrical tunnel current from a normal metal into the superconductor, the DOS acts as an almost perfect spin filter for $\Delta - E_Z < |eV_{inj}| < \Delta + E_Z$, even if the barrier transmission is spin-independent.

Spin injection into superconductors using this method was shown to result in a finite, long-ranged spin accumulation, arising either from f_L or f_{T3} [36, 37, 38]. Subsequent measurements of the spin-flip time, the spin-orbit scattering time and the spin imbalance lifetime indicate that the spin accumulation beyond the spin-flip length λ_{sf} is almost entirely due to f_L, as it relaxes over λ_{rec} while f_{T3} relaxes over λ_{SF} [39, 40].

Among excitation techniques besides those mentioned above, we note in particular charge and spin currents generated by the magnetic losses of the precessing magnetization of a ferromagnet also called *spin pumping* [41, 42, 43, 44, 45, 46, 47]. In the case of a ferromagnetic insulator in contact with a superconductor, a pure spin current with no charge should be injected [48]. As this spin pumping technique injects spins at low energies, in contrast to spin-polarized current injection, it should in principle also result in little or no excitation of the charge mode. Nevertheless, while spin pumping into metals has been demonstrated experimentally, this technique has not been applied to superconductors.

In this part, the focus is on the f_{L3} or the spin energy mode by performing spin-sensitive spectroscopy on low-energy out-of-equilibrium quasiparticles generated by current injection from a normal metal. Within the spin-flip and electron-electron interaction lengths of the injection point, our measurements reveal quasiparticle distribution functions which are truly out-of-equilibrium, i.e. non-Fermi-Dirac. At a finite Zeeman field, we observe a charge imbalance indicating the presence of the spin energy mode. Our results agree well with quasiclassical Green's function calculations.

Chapter 1

Theory

The many-body approach to BCS superconductivity is to construct the equations of motion for the Green's function $\check{g}$, supplemented by the equations of motion for the anomalous part, which describes the superconducting correlations [49, 50, 51, 52, 53].

In a disordered superconductor, in which the mean free path is shorter than the superconducting coherence length, one can integrate over momentum space of the Eilenberger equation [54] and obtain the Usadel equation [55], which describes the system in terms of a position and energy dependent diffusion equation.

The out-of-equilibrium state of the system can be described within the Keldysh formalism, in which the Green's function (GF) can be written down as

$$\check{g} = \begin{pmatrix} \hat{g}^R & \hat{g}^K \\ 0 & \hat{g}^A \end{pmatrix} \tag{1.1}$$

where $\hat{g}^{R/A}$ is the retarded/advanced GF (related by $\hat{g}^A = -\tau_3 \hat{g}^R \tau_3$), and $\hat{g}^K$ the Keldysh component which takes into account the (out-of-equilibrium) distribution function.

For the case of a superconductor in a spin-splitting field the Usadel equation for the GF $\check{g}$ reads:

$$D\nabla \cdot (\check{g}\nabla\check{g}) + [iE\tau_3 - i\boldsymbol{h}\cdot\boldsymbol{\sigma}\tau_3 - \check{\Delta} - \check{\Sigma}, \check{g}] = 0 \tag{1.2}$$

where D is the normal state diffusion coefficient, E the energy, $\boldsymbol{h}$ the external magnetic field, σ_i and τ_i the Pauli matrices in the spin and Nambu (electron-hole) subspaces respectively [1], $\check{\Delta}$ a matrix related to the (complex) order parameter, and $\check{\Sigma}$ the self energy term.

In addition to the Usadel equation 1.2, one also needs to consider the so-called normalizing condition $\check{g}^2 = \check{I}$, where $\check{I}$ is the unit matrix in the Nambu-spin space.

This chapter provides a detailed overview of the theory of spin-dependent transport phenomena in Zeeman-split superconductors introduced in [56], and described in more detail in [11, 12], with a focus on the spin-energy mode, first introduced in [13], and its experimental signatures. The scope of the discussion is restricted to the aspects relevant to the experiment.

Anticipating the experimental conditions, in particular the use of Al as the superconductor, figures presented in this chapter show energy in units of μeV rather than Δ.

[1] Formally speaking $\hat{\sigma}_i = \hat{I} \oplus \sigma_i$ and $\hat{\tau}_i = \sigma_i \oplus \hat{I}$ where σ_i is the regular definition of the Pauli matrices. For example $\tau_2 = \begin{pmatrix} 0 & 0 & -i & 0 \\ 0 & 0 & 0 & -i \\ i & 0 & 0 & 0 \\ 0 & i & 0 & 0 \end{pmatrix}$, and $\sigma_3 = \begin{pmatrix} 1 & 0 & 0 & 0 \\ 0 & -1 & 0 & 0 \\ 0 & 0 & 1 & 0 \\ 0 & 0 & 0 & -1 \end{pmatrix}$. For the σ matrices in the Usadel equation the direct product with the unity matrix is in the Nambu space is implied.

1.1 Spectral equations

In the case of a uniform superconductor ($\hat{\Delta} = const$), in the R subspace (the "$\hat{g}^R$" block of equation 1.2) the gradient term vanishes from the Usadel equation and one is left with:

$$[iE\tau_3 - i\boldsymbol{h}\cdot\boldsymbol{\sigma}\tau_3 - \hat{\Delta} - \hat{\Sigma}, \hat{g}^R] = 0 \tag{1.3}$$

In the absence of gradients one can choose a gauge in which Δ is a real number, so that $\hat{\Delta}$ becomes $\hat{\Delta} = \Delta\tau_1$. In the following the self-energy contribution $\hat{\Sigma}$ describes the effects of spin relaxation through spin-flip and spin-orbit mechanisms, as well the effects of orbital depairing. Within the first Born approximation the self-energy contributions are:

$$\begin{aligned} \check{\Sigma}_{SF} &= \frac{\boldsymbol{\sigma}\cdot\tau_3\check{g}\tau_3\boldsymbol{\sigma}}{8\tau_{SF}}, \\ \check{\Sigma}_{SO} &= \frac{\boldsymbol{\sigma}\cdot\check{g}\boldsymbol{\sigma}}{8\tau_{SO}}, \\ \check{\Sigma}_{ORB} &= \frac{\tau_3\check{g}\tau_3}{6\tau_{ORB}} \end{aligned} \tag{1.4}$$

In the principle the self-energy should also contain terms describing the electron-electron and electron-phonon interactions. However these terms would be non-local in energy and would increase the complexity of the problem significantly.

If the out-of-equilibrium state is probed within a time shorter than the effective electron-electron interaction time, the effects of the pseudo-thermalization (i.e. redistribution of the quasiparticles towards a Fermi-Dirac-like distribution through particle collisions) will be small, and thus this term can be dropped. Likewise, if there is a faster relaxation mechanism than the quasiparticle recombination, which in this case is an absorbing boundary condition at the (geometrical) end of the system, the effects of the electron-phonon interaction can also be neglected. As a model without these contributions successfully captures the main physical effects observed in the experiment, which is shown in chapter 3.1, the omission of these terms is justified.

The normalization condition in the R subspace gives $(\hat{g}^R)^2 = 1$, which allows for a parametrization in the form $\hat{g}^R = \sum_{j=0}^{3}\left(g^R_{j,1}\tau_1 + g^R_{j,3}\tau_3\right)\sigma_j$. The components proportional to τ_1 are related to the anomalous part of the GF, and the ones proportional to τ_3 are related to the regular part. Similarly the components proportional to σ_0 describe singlet correlations, while the ones proportional to $\sigma_{i=\{1,2,3\}}$ describe triplet correlations in x, y and z directions, respectively. For a BCS superconductor, at zero field, we have $g^R_{0,3} = \frac{E}{\sqrt{E^2-\Delta^2}}$ and $g^R_{0,1} = \frac{i\Delta}{\sqrt{E^2-\Delta^2}}$, while the other ones are equal to zero. If the external magnetic field is applied along the z direction only the σ_0 and σ_3 terms need to be kept.

With the $\hat{\Delta}$ and the $\hat{\Sigma}$ as defined in eq. 1.4 the Usadel equation reduces to a system of nonlinear coupled algebraic equations, in terms of four complex numbers: $g_{0,1}$, $g_{3,1}$, $g_{0,3}$ and $g_{3,3}$. A numerical solution, obtained using a variant of the Powell method [57], of the Usadel equation presented in terms of the components of $\hat{g}^R$, calculated for the following parameters: $H = 1\text{T}$, $\Delta = 235\mu\text{eV}$, $H = 1\text{T}$, $\tau^{-1}_{ORB} = 6.5\mu\text{eV}$, $\tau^{-1}_{SO} = 13\mu\text{eV}$, $\tau^{-1}_{SF} = 0$ (these are the same values as for the rest of the theoretical figures in this document, unless otherwise stated), is shown in figure 1.1.

The spin-averaged density of states $N_+ = \frac{N_\uparrow + N_\downarrow}{2}$ is directly given by $N_+ = Re(g_{0,3})$, while the DOS spin-difference $N_- = \frac{N_\uparrow - N_\downarrow}{2}$ is given by $N_- = Re(g_{3,3})$ (see figure 1.1).

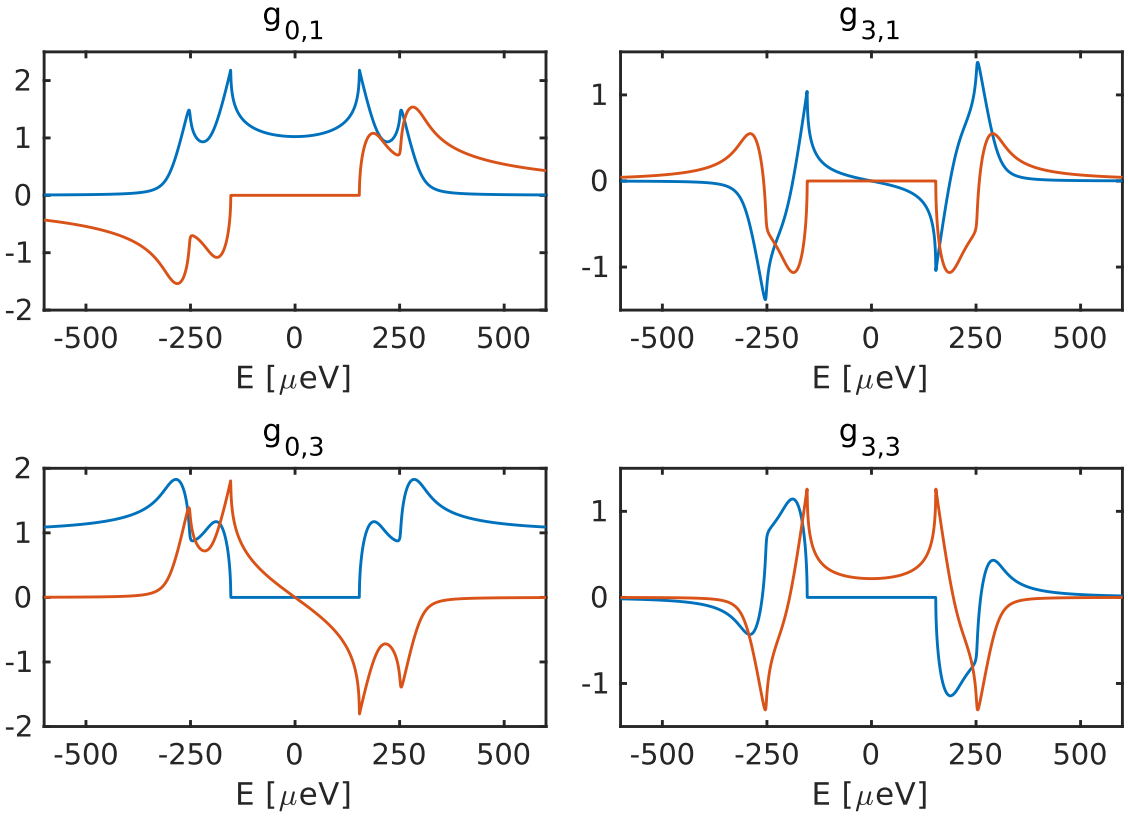

Figure 1.1: A numerical solution of the Usadel equation shown in terms of the real (blue lines) and imaginary (red lines) parts of $g_{0,1}$, $g_{3,1}$, $g_{0,3}$ and $g_{3,3}$.

1.2 Kinetic equations

After solving the spectral equations, and obtaining $\hat{g}^R$, we can now turn our attention to the kinetic part of the problem, which determines the out-of-equilibrium distribution function.

By utilizing the normalization condition, $\check{g}^2 = 1$, the Keldysh component can be rewritten as $\hat{g}^K = \hat{g}^R\hat{f} - \hat{f}\hat{g}^A$, where $\hat{f}$ is the generalized distribution function $\hat{f} = f_L + f_T\tau_3 + \sum_{i=1}^{3}(f_{Ti}\sigma_i + f_{Li}\sigma_i\tau_3)$. Following the same reasoning as before, if the external magnetic field is applied along the z direction, the distribution function can be reduced to:

$$\hat{f} = f_L + f_T\tau_3 + f_{T3}\sigma_3 + f_{L3}\sigma_3\tau_3 \tag{1.5}$$

In equilibrium only the f_L component is nonzero with $f_L^{eq} = \tanh(\frac{E}{2k_BT})$, where T is the temperature of the phonon bath. The particle distribution function can be obtained as $f^p(E) = (1 - f_L(E))/2$. The superconductor is considered out-of-equilibrium if the distribution function is different from f_L^{eq} (i.e. an effective temperature or chemical potential), while it is considered do be *truly* out-of-equilibrium if the distribution function is not a Fermi-Dirac one with an effective temperature and/or a chemical potential.

The spin-dependent particle distribution function can be recovered from eq. 1.5 as $f^p_{\downarrow/\uparrow} = \big(1 - f_L - f_T \mp (f_{L3} + f_{T3})\big)/2$.

If we allow the distribution function to be position dependent $\hat{f} = \hat{f}(x)$, and substitute this into the Usadel equation (eq. 1.2), the gradient term will be nonzero. In the Keldysh

subspace the equation then reads $\nabla\tilde{J} - \tilde{S} = 0$, which is in fact a continuity equation for the current $\tilde{J} = D\hat{g}^R\nabla\hat{g}^K$ with sink terms given by $\tilde{S} = [\check{g}, iE\tau_3 - i\boldsymbol{h}\cdot\boldsymbol{\sigma}\tau_3 - \check{\Delta} - \check{\Sigma}]^K$.

To compute physical observables, one needs to multiply $\tilde{J}$ by an appropriate matrix and take the trace:

$$\tilde{j}_{a,b} = \frac{1}{8}\mathrm{Tr}\left[\tau_a\sigma_b\tilde{J}\right]$$

The energy current density is given by $j_e = \tilde{j}_{0,0}$ (even in the electron-hole as well as the spin subspaces), the charge current density by $j_c = \tilde{j}_{3,0}$ (odd in the e-h subspace but even in the spin subspace), the spin current density by $j_s = \tilde{j}_{0,3}$ (e-h even, spin odd), and finally the spin-energy current is given by $j_{se} = \tilde{j}_{3,3}$ (odd in both subspaces). The total current is obtained by integrating these current densities with respect to energy: $J_e = \int_{-\infty}^{\infty} dE E j_e(E)$, $J_c = e\int_{-\infty}^{\infty} dE j_c(E)$, $J_s = \int_{-\infty}^{\infty} dE j_s(E)$, $J_{se} = \int_{-\infty}^{\infty} dE E j_{se}(E)$.

If we go back to the energy resolved quantities and utilize the previously laid out parametrization for $\hat{g}^R$ and $\hat{f}^K$ we can obtain[2] a simple system of equations for the currents:

$$\begin{aligned} j_e &= D_L\nabla f_L + D_{T3}\nabla f_{T3}, \\ j_s &= D_L\nabla f_{T3} + D_{T3}\nabla f_L, \\ j_c &= D_T\nabla f_T + D_{L3}\nabla f_{L3}, \\ j_{se} &= D_T\nabla f_{L3} + D_{L3}\nabla f_T \end{aligned} \tag{1.6}$$

In the equation 1.6, $D_{L,T,L3,T3}$ are the energy dependent diffusion coefficients given by the equation 1.7 and shown in figure 1.2.

$$\begin{aligned} D_L &= \frac{D}{2}\left(1 + |g_{0,3}|^2 + |g_{3,3}|^2 - |g_{0,1}|^2 - |g_{3,1}|^2\right), \\ D_{T3} &= \frac{D}{2}\left(g_{3,3}g^*_{0,3} + g_{0,3}g^*_{3,3} - g_{3,1}g^*_{0,1} - g_{0,1}g^*_{3,1}\right), \\ D_T &= \frac{D}{2}\left(1 + |g_{0,3}|^2 + |g_{3,3}|^2 + |g_{0,1}|^2 + |g_{3,1}|^2\right), \\ D_{L3} &= \frac{D}{2}\left(g_{3,3}g^*_{0,3} + g_{0,3}g^*_{3,3} + g_{3,1}g^*_{0,1} + g_{0,1}g^*_{3,1}\right) \end{aligned} \tag{1.7}$$

For each of these currents the sink terms can be computed in exactly the same way:

$$\tilde{s}_{a,b} = \frac{1}{8}\mathrm{Tr}\left[\tau_a\sigma_b\tilde{S}\right]$$

The continuity equation can then be restated as:

$$\begin{aligned} \nabla j_e &= 0, \\ \nabla j_s &= S_{T3}f_{T3}, \\ \nabla j_c &= R_T f_T + R_{L3}f_{L3}, \\ \nabla j_{se} &= (R_T + S_{L3})f_{L3} + R_{L3}f_T \end{aligned} \tag{1.8}$$

[2] As en example the energy current $j_e = \frac{1}{8}Tr\left[\tilde{J}\right]$ is found to be $j_e = \frac{D}{2}\left(1 + |g_{0,3}|^2 + |g_{3,3}|^2 - |g_{0,1}|^2 - |g_{3,1}|^2\right)\nabla f_L + \frac{D}{2}\left(g_{3,3}g^*_{0,3} + g_{0,3}g^*_{3,3} - g_{3,1}g^*_{0,1} - g_{0,1}g^*_{3,1}\right)\nabla f_{T3}$. The prefactor in front of ∇f_L is identified as D_L and the one in front of ∇f_{T3} as D_{T3}. The same quantities will appear in the expression for the spin current j_s. Likewise in the j_c-j_{se} subspace.

The relaxation rates R_T and R_{L3} correspond to Andreev-like charge relaxation processes, while the S_{T3} and S_{L3} correspond to spin relaxation processes. One can verify, by taking the appropriate traces and separating out the terms proportional to each of the distribution function modes, that they are as follows:

$$\begin{aligned} R_T &= 2\Delta Re(g_{0,1}), \\ R_{L3} &= 2\Delta Re(g_{3,1}), \\ S_{L3} &= R_S\big[Re(g_{0,3})^2 - Re(g_{3,3})^2 + \beta\big(Re(g_{3,1})^2 - Re(g_{0,1})^2\big)\big], \\ S_{T3} &= R_S\big[Re(g_{0,3})^2 - Re(g_{3,3})^2 - \beta\big(Im(g_{3,1})^2 - Im(g_{0,1})^2\big)\big] \end{aligned} \tag{1.9}$$

where $R_S = R_{SO} + R_{SF} = \frac{1}{\tau_{SO}} + \frac{1}{\tau_{SF}}$ and $\beta = \dfrac{R_{SF} - R_{S0}}{R_S}$. Figure 1.2 also shows the relaxation rates, calculated for the same parameters as figure 1.1.

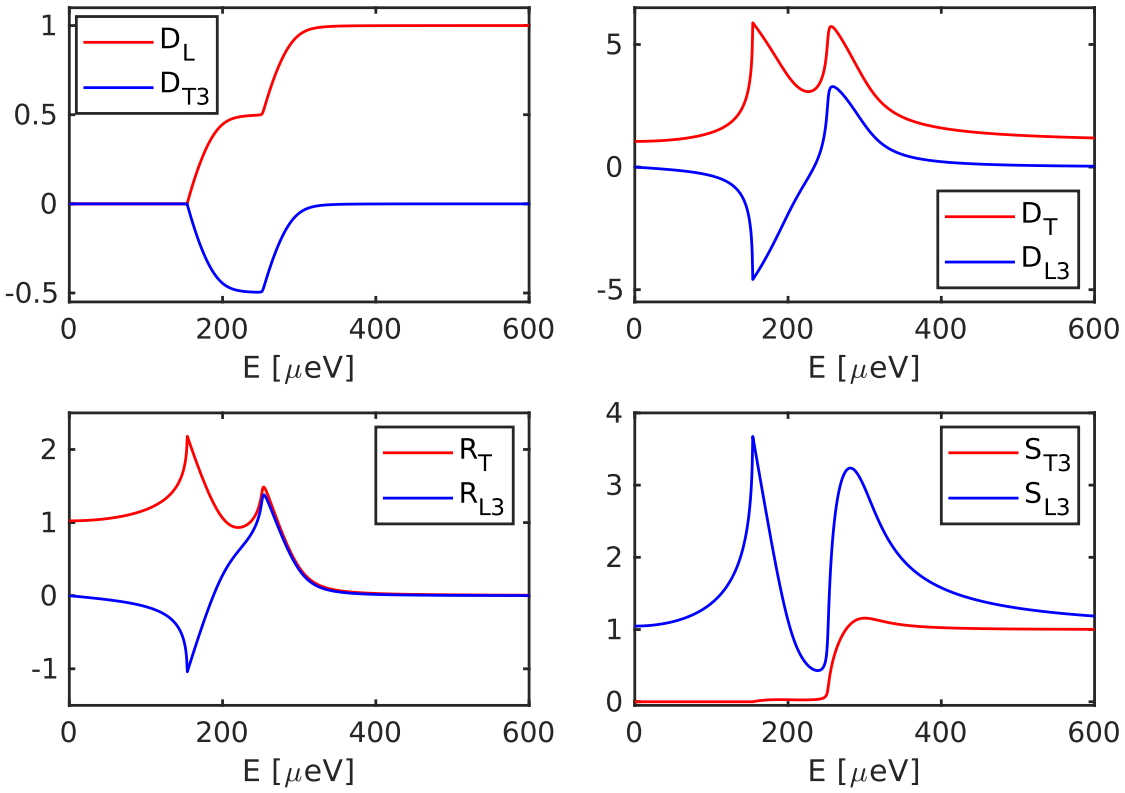

Figure 1.2: Top: the normalized ($D = 1$) energy dependent diffusion coefficients D_L and D_{T3} (left) as well as D_T and D_{L3} (right). Bottom: the charge (R_T and R_{L3}) and spin (S_{L3} and S_{T3}) relaxation rates, normalized to $2\Delta = 1$ and $R_S = 1$;

At $H = 0$ all of the $g_{3,i}$ components vanish and D_{T3} and D_{L3} do so, too. The expressions for the currents 1.6 are reduced to:

$$\begin{aligned} j_e &= D_L \nabla f_L, \\ j_s &= D_L \nabla f_{T3}, \\ j_c &= D_T \nabla f_T, \\ j_{se} &= D_T \nabla f_{L3} \end{aligned} \tag{1.10}$$

The transport of the spin dependent modes f_{T3} and f_{L3} is then decoupled and the transport equations 1.10 recover the result from [13] (without the supercurrent contribution), giving a more direct interpretation of the spin-energy current as the spin resolved energy current.

1.3 Transport eigenmodes

The transport problem for the four out-of-equilibrium modes can be separated into two independent subspaces: the first two equations from each of the systems 1.6-1.9 are expressed only in terms of the f_L and f_{T3} modes, while the remaining two are dependent only on f_T and f_{L3}. In the following two subsections the transport equations in these two subspaces will be addressed separately.

1.3.1 The f_L and f_{T3} modes

The $f_L - f_{T3}$ subspace of equation 1.6 can be rewritten as

$$\begin{pmatrix} j_e \\ j_s \end{pmatrix} = \begin{pmatrix} D_L & D_{T3} \\ D_{T3} & D_L \end{pmatrix} \nabla \begin{pmatrix} f_L \\ f_{T3} \end{pmatrix} \tag{1.11}$$

while the same subspace of equation 1.9 reads

$$\nabla \begin{pmatrix} j_e \\ j_s \end{pmatrix} = \begin{pmatrix} 0 \\ S_{T3} f_{T3} \end{pmatrix} \tag{1.12}$$

Substituting the first one into the second yields

$$\begin{pmatrix} D_L & D_{T3} \\ D_{T3} & D_L \end{pmatrix} \nabla^2 \begin{pmatrix} f_L \\ f_{T3} \end{pmatrix} = \begin{pmatrix} 0 \\ S_{T3} f_{T3} \end{pmatrix} \tag{1.13}$$

With the ansatz $\begin{pmatrix} f_L \\ f_{T3} \end{pmatrix} = e^{kx}\mathbf{v}$, we have

$$\begin{pmatrix} k^2 D_L & k^2 D_{T3} \\ k^2 D_{T3} & k^2 D_L - S_{T3} \end{pmatrix} \mathbf{v} = 0 \tag{1.14}$$

which has a nontrivial solution only if the determinant of the matrix is zero. Solving for k yields two solutions $k_1^2 = 0$ and $k_2^2 = \dfrac{D_L S_{T3}}{D_L^2 - D_{T3}^2}$, with the corresponding null-space vectors $\mathbf{v}_1 \propto \begin{pmatrix} 1 \\ 0 \end{pmatrix}$ and $\mathbf{v}_2 \propto \begin{pmatrix} -D_{T3} \\ D_L \end{pmatrix}$. The top panel of figure 1.3 shows the energy dependence of k_2.

The first solution corresponds to $\nabla^2 f_L = 0$ because of the absence of any inelastic relaxation mechanism in the model. The effective relaxation is taken into account through an absorbing boundary condition at the ends of the wire (where large, well thermalized, metallic reservoirs are located). Assuming that the quasiparticles are injected at $x = 0$ and the reservoir is located at $x = L$ the solution can be expressed as:

$$\begin{pmatrix} f_L \\ f_{T3} \end{pmatrix} = B_1 \mathbf{v}_1 (L - x) + B_2 \mathbf{v}_2 e^{-k_2 x} + B_2^+ \mathbf{v}_2 e^{+k_2 x} + \begin{pmatrix} f_L^{eq} \\ 0 \end{pmatrix}$$

Once again, invoking the boundary condition $\begin{pmatrix} f_L \\ f_{T3} \end{pmatrix}_{x=L} = \begin{pmatrix} f_L^{eq} \\ 0 \end{pmatrix}$, where $f_L^{eq} = \tanh(\frac{E}{2k_BT})$, one finds $B_2^+ = -B_2 e^{-2k_2 L}$. Finally the full form of the solution is found to be:

$$\begin{pmatrix} f_L \\ f_{T3} \end{pmatrix} = B_1 \begin{pmatrix} L-x \\ 0 \end{pmatrix} + B_2 \mathbf{v}_2 \left(e^{-k_2 x} - e^{+k_2(x-2L)} \right) + \begin{pmatrix} f_L^{eq} \\ 0 \end{pmatrix} \tag{1.15}$$

The energy dependent coefficients B_1 and B_2 are to be determined from the boundary condition at the point of quasiparticle injection. This is discussed in detail in section 1.3.3.

At vanishing magnetic field the transport eigenmodes in the f_L-f_{T3} subspace decouple as well. The second mode describes just the decay of the spin mode, which then relaxes within the spin-flip length (S_{L3} is nonzero even at $H = 0$). The transport of the f_L mode is the same as in [58], only modified by the energy dependent diffusion D_L.

1.3.2 The f_T and f_{L3} modes

By following the same procedure as in the previous section one can obtain the transport eigenmodes in the $f_T - f_{L3}$ subspace. From equations 1.6 and 1.8 we have:

$$\begin{pmatrix} k^2 D_T - R_T & k^2 D_{L3} - R_{L3} \\ k^2 D_{L3} - R_{L3} & k^2 D_T - R_T - S_{L3} \end{pmatrix} \mathbf{v} = 0 \tag{1.16}$$

In the limit of vanishing spin relaxation ($S_{L3} = 0$) two modes can be obtained with $k_3 = \frac{R_{L3} - R_T}{D_{L3} - D_T}$, $\mathbf{v}_3 \propto \begin{pmatrix} -1 \\ 1 \end{pmatrix}$ and $k_4 = \frac{R_{L3} + R_T}{D_{L3} + D_T}$, $\mathbf{v}_4 \propto \begin{pmatrix} 1 \\ 1 \end{pmatrix}$.

Taking into account the boundary condition, the following solution can be obtained:

$$\begin{pmatrix} f_T \\ f_{L3} \end{pmatrix} = B_3 \mathbf{v}_3 \left(e^{-k_3 x} - e^{+k_3(x-2L)} \right) + B_4 \mathbf{v}_4 \left(e^{-k_4 x} - e^{+k_4(x-2L)} \right) \tag{1.17}$$

If the spin relaxation rate is finite, the form of the solution 1.17 remains the same, however, $\mathbf{v}_3$ and $\mathbf{v}_4$ become energy dependent, while the expressions for k_3 and k_4 become slightly more complicated. The bottom panel of figure 1.3 shows the relaxation rates for both modes based on the calculation including the spin-relaxation mechanism.

At energies close to Δ the transport of the f_T and f_{L3} modes is closely coupled (because $D_{L3} \neq 0$). However, at higher energies $D_{L3} \to 0$ so the modes become decoupled. We can also see this by investigating the components of the k_3 and k_4 modes in the basis of f_T and f_{L3}. The decomposition of $\mathbf{v}_3$ and $\mathbf{v}_4$ is shown in figure 1.4; indeed at higher energies the k_3 mode becomes the charge mode, while the k_4 becomes the spin-energy mode.

Unlike the previous two modes, f_T and f_{L3} are not completely decoupled at $H = 0$ as the relaxation (equation 1.9) mixes the two at all magnetic fields.

1.3.3 Injector boundary conditions

In the experiment that was performed, the injector junction is an NIS tunnel junction ($Cu/Al_2O_3/Al$). The current density through this junction is given by equation 1.18:

$$\begin{pmatrix} j_e \\ j_s \\ j_c \\ j_{se} \end{pmatrix} = \frac{1}{\tilde{R}} \begin{pmatrix} N_+ & N_- & 0 & 0 \\ N_- & N_+ & 0 & 0 \\ 0 & 0 & N_+ & N_- \\ 0 & 0 & N_- & N_+ \end{pmatrix} \begin{pmatrix} \tilde{f}_L \\ \tilde{f}_{T3} \\ \tilde{f}_T \\ \tilde{f}_{L3} \end{pmatrix} \tag{1.18}$$

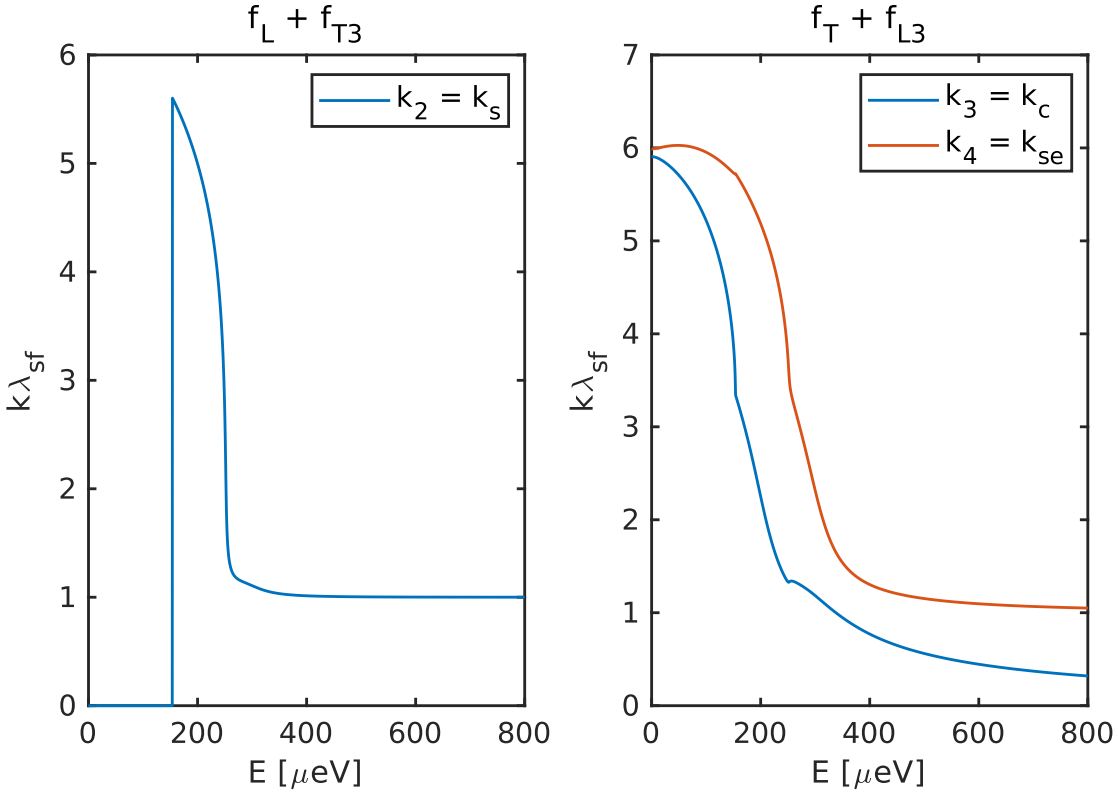

Figure 1.3: The relaxation rates of the exponentially decaying modes normalized by the spin-relaxation length $\lambda_{SF} = \sqrt{D\tau_{SO}}$ in the $f_L - f_{T3}$ (left) and $f_T - f_{L3}$ (right) subspaces. The labels are assigned to the traces based on the high energy behavior, as shown in figure 1.4.

where $\tilde{R}$ is the barrier resistance normalized by the ratio of the junction surface area and the cross section of the wire. $\tilde{f}_i = f_i - f_i^N$ is the difference between the distribution function in the superconductor and in the normal metal (indicated by the superscript N). The tunneling matrix is block-diagonal and again separates the problem into the $f_L - f_{T3}$ and $f_T - f_{L3}$ subspaces.

When the superconductor is Zeeman split $N_- \neq 0$, and even if the spin (f_{T3}) and spin-energy (f_{L3}) modes are not present, a finite spin and spin energy current will flow through the barrier: $j_s = \frac{N_-}{\tilde{r}}\tilde{f}_L$ and $j_{se} = \frac{N_-}{\tilde{r}}\tilde{f}_T$.

This current through the tunnel barrier must be component-wise equal to the current along the wire at $x = 0$; there are two components to this current the one which flows to the left $j_\leftarrow$ (and relaxes in the reservoir at $x = -L_L < 0$) and the one which flows to the right $j_\rightarrow$ (relaxes at $x = L_R > 0$). For the sake of simplicity only the case of a symmetric wire ($L_L = L_R = L$) will be discussed here, under which $|j_\leftarrow| = |j_\rightarrow|$ and allows one to consider only the right-moving current with an effective barrier resistance $\tilde{r} = 2\tilde{R}$.

In the $f_L - f_{T3}$ subspace, current conservation is given by (from equations 1.18 and 1.13):

$$\begin{pmatrix} D_L & D_{T3} \\ D_{T3} & D_L \end{pmatrix} \nabla \begin{pmatrix} f_L \\ f_{T3} \end{pmatrix}_{x=0} - \frac{1}{\tilde{r}} \begin{pmatrix} N_+ & N_- \\ N_- & N_+ \end{pmatrix} \begin{pmatrix} f_L \\ f_{T3} \end{pmatrix}_{x=0} = \frac{1}{\tilde{r}} \begin{pmatrix} N_+ & N_- \\ N_- & N_+ \end{pmatrix} \begin{pmatrix} f_L^N \\ f_{T3}^N \end{pmatrix} \tag{1.19}$$

When a voltage is applied to the normal metal the distribution function is shifted by the voltage $f(E, V) = f_0(E - V)$. Tunneling across the barrier will *imprint* this distribution

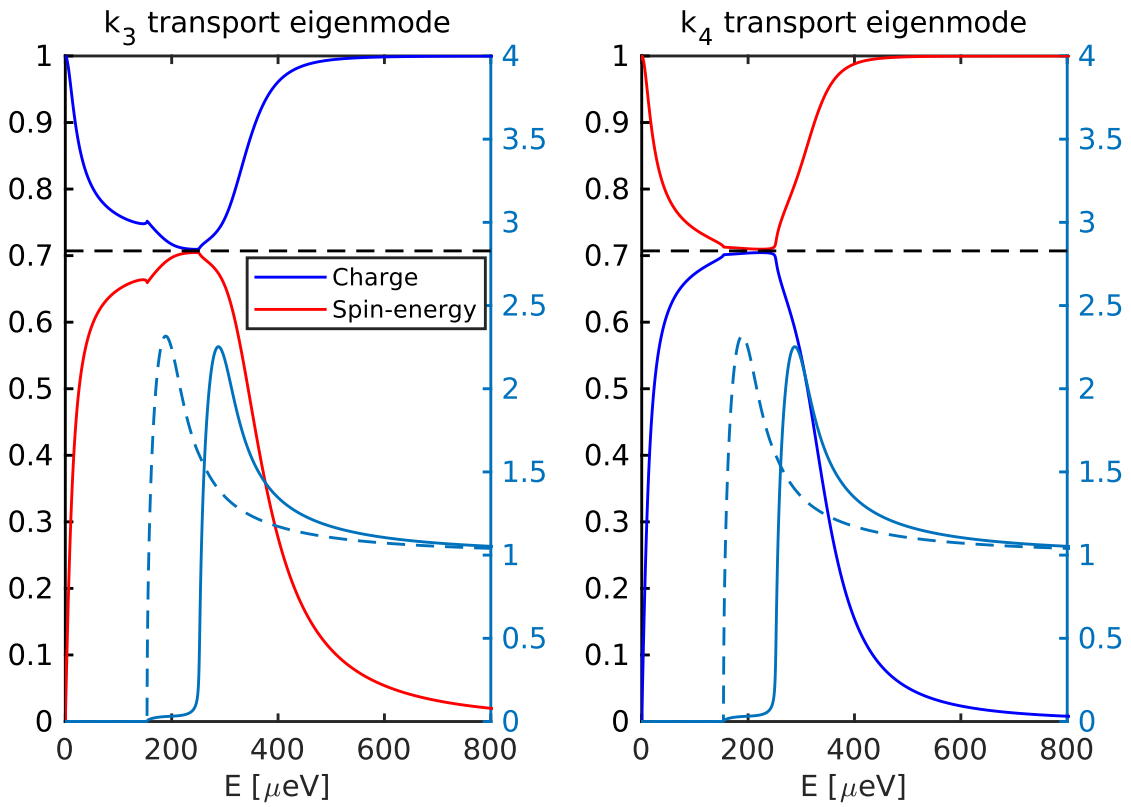

Figure 1.4: The decomposition of the k_3 (left) and k_4 (right) transport eigenmodes in terms of f_T (charge, blue line) and f_{L3} (spin-energy, red line). The dashed black line indicates an equal mixture of the f_T and f_{L3} modes. Note that below $E \approx 150\mu eV$ there are no quasiparticle states as indicated by the DOS (shown on the right scale).

into the superconductor, resulting in quasiparticles up to the energy $E \approx eV$, which can be parameterized by the four out-of-equilibrium modes. The normal metal will be driven out-of-equilibrium by this process, and kinetic equations should be solved for the nonequilibrium state.

Because of the large thickness of the injector electrode compared to the thickness of the Al wire, the distribution function is assumed to be the Fermi-Dirac one, offset by the applied voltage - for one tunneled electron the density of excitations in the Cu electrode is much smaller: the distribution function is modified by $\nu_N N_N \delta f_N = 1 = \nu_S N_S \delta f_S$ (ν is the volume and N the density of states at the Fermi level, the subscript N/S refers to the normal metal or the superconductor). As $\nu_N \gg \nu_S$ the superconductor is driven further out equilibrium, for a relatively small δf_S one can safely neglect the nonequilibrium state in the normal metal.

The right hand side of equation 1.19 depends solely on the distribution function of the injection electrode; when a finite voltage is applied in the L/T parametrization the distribution function is $f^N_{L/T} = \left(\tanh \frac{E-eV}{k_B T} \pm \tanh \frac{E-eV}{k_B T}\right)/2$.

By using the expression 1.15, the left hand side can be expressed in terms of B_1 and B_2. By solving the linear system of equations, and making all the necessary substitutions, at the

end one finds that the distribution function in the superconducting wire is given by:

$$\begin{aligned} f_L(E,x) &= \chi_L(E,x) f_L^N(E,V,T) + f_L^{eq}(E,T), \\ f_{T3}(E,x) &= \chi_{T3}(E,x) f_L^N(E,V,T), \\ f_T(E,x) &= \chi_T(E,x) f_T^N(E,V,T), \\ f_{L3}(E,x) &= \chi_{L3}(E,x) f_T^N(E,V,T) \end{aligned} \tag{1.20}$$

The χ coefficients of equation 1.20, calculated for the same parameters as in figure 1.1 and $x = 0$, are shown in figure 1.5.

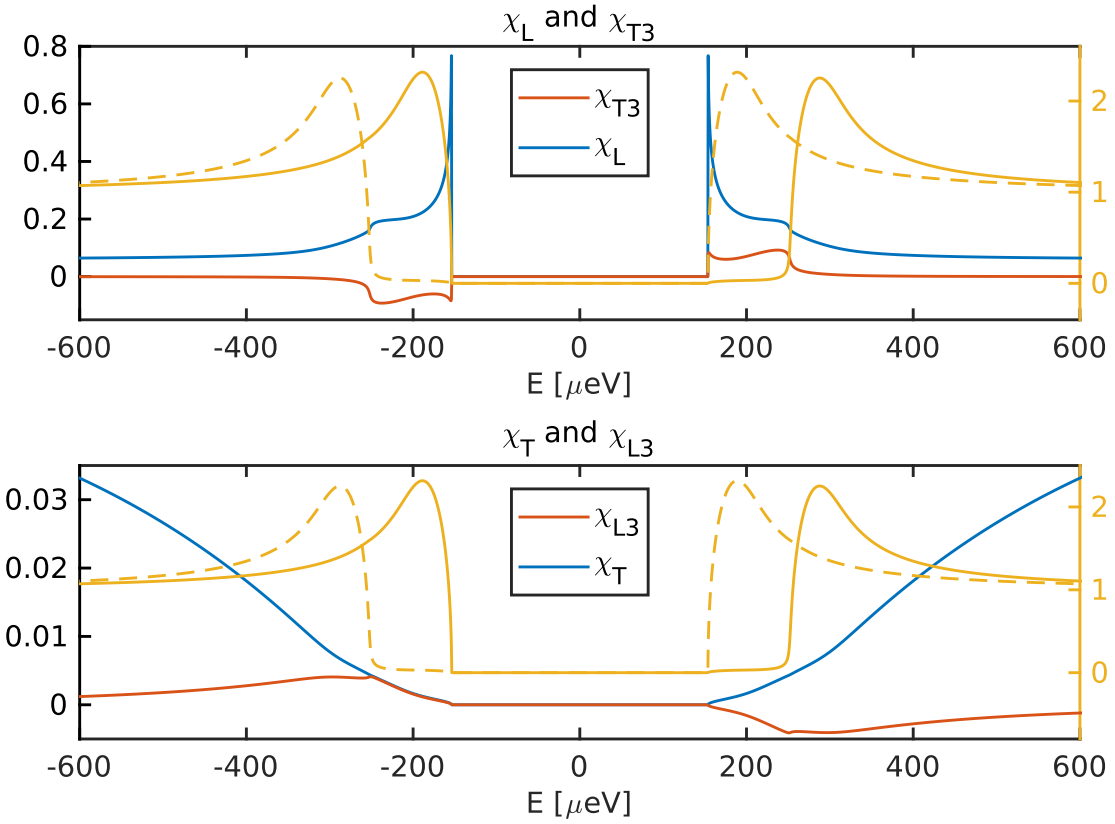

Figure 1.5: The χ coefficients from equation 1.20 calculated for the experimental parameters at $H = 1\text{T}$ and $x = 0$. The top panel shows χ_L and χ_{T3} while the bottom one shows χ_T and χ_{L3}; in both panels the DOS for both spins is shown on the right scale.

If $L_L \neq L_R$ the left and right moving currents are not the same, and a set of B parameters (eqs 1.15 and 1.17) determines both of them. However, by imposing the continuity of the distribution function at $x = 0$: $f_{\leftarrow}(x = 0) = f_{\rightarrow}(x = 0)$, the $B_{\leftarrow}$ can be expressed in terms of $B_{\rightarrow}$ and the problem is effectively reduced to the symmetric case.

In the experiment the corresponding values are $L_R \approx 6\mu$m, and $L_L \approx 4\mu$m. For the sake of simplicity, the calculations have been performed with $L_R = L_L = 5\mu$m.

1.4 Spin and charge accumulation

The currents introduced in section 1.2 have a corresponding charge (density), which is defined as

$$\tilde{q_{a,b}} = \frac{1}{8}\mathrm{Tr}\big[\tau_3\tau_a\sigma_b\hat{g}^K\big]$$

Compared to the definition of the currents there is an extra τ_3 matrix, coming from the structure of the time derivative term in the Gor'kov equation [49].

In terms of the components of the retarded Green's function and the generalized distribution function the accumulation of charge, spin, energy and spin-energy is respectively given by:

$$\begin{aligned}
\mu &= \int_{-\infty}^{\infty}\mathrm{Tr}\big[g(\hat{E},x)^K\big]dE = \int_{-\infty}^{\infty}\big[f_T\mathrm{Re}(g_{0,3}) + f_{L3}\mathrm{Re}(g_{3,3})\big]dE,\\
\mu_z &= \int_{-\infty}^{\infty}\mathrm{Tr}\big[\tau_3\sigma_3 g(\hat{E},x)^K\big]dE = \int_{-\infty}^{\infty}\big[f_{T3}\mathrm{Re}(g_{0,3}) + f_L\mathrm{Re}(g_{3,3})\big]dE,\\
\epsilon &= \int_{-\infty}^{\infty}\mathrm{Tr}\big[\tau_3 g(\hat{E},x)^K\big]EdE = \int_{-\infty}^{\infty}\big[f_L\mathrm{Re}(g_{0,3}) + f_{T3}\mathrm{Re}(g_{3,3})\big]EdE,\\
\epsilon_z &= \int_{-\infty}^{\infty}\mathrm{Tr}\big[\sigma_3 g(\hat{E},x)^K\big]EdE = \int_{-\infty}^{\infty}\big[f_{L3}\mathrm{Re}(g_{0,3}) + f_T\mathrm{Re}(g_{3,3})\big]EdE
\end{aligned} \tag{1.21}$$

The same result can be found using a more straight forward argument: in the particle (or electron-like) definition of the distribution function, and the semiconductor definition of the DOS, the density of spin up/down particles is given by $\rho_{\uparrow/\downarrow} = N_{\uparrow/\downarrow}(E)f^p_{\uparrow/\downarrow}(E)$, where $N_{\uparrow/\downarrow}$ is the density of states for each of the spins and f^p is the particle distribution function (i.e. in equilibrium the Fermi-Dirac distribution). The total (energy-independent) density of particles can be obtained by integrating this quantity $\rho^{tot}_{\uparrow/\downarrow} = \int_{-\infty}^{\infty} dE\rho_{\uparrow/\downarrow}(E)$. The total charge is then related to the number of particles present in the system $\rho^{tot} = \rho_\uparrow + \rho_\downarrow$. To obtain the charge imbalance one just needs to subtract the number of particles in equilibrium $\rho^{tot}_{eq} = \int_{-\infty}^{\infty} N_+(E)f_0(E,T)dE$ where f_0 is the Fermi-Dirac distribution. Likewise the total magnetization can be determined as the difference between the number of spin up and spin down quasiparticles. By using the expressions for the density of states $N_{\downarrow/\uparrow} = N_+ \pm N_-$ and the distribution function $f_{\uparrow/\downarrow} = (1 - f_L - f_T \pm (f_{L3} + f_{T3}))/2$ and by dropping the terms that yield zero under integration the same expressions for μ and μ_z are obtained.

Finally, to determine the out-of-equilibrium component of the charge and spin accumulation the equilibrium one must subtract the equilibrium one (i.e. to replace f_L with $f_L - f^{eq}_L$ in eq. 1.21):

$$\begin{aligned}
\mu_z &= \int_{-\infty}^{\infty} dE\big[\big(f_L(E) - f^{eq}_L(E)\big)N_- + f_{T3}N_+\big],\\
\mu &= \int_{-\infty}^{\infty} dE\big[f_T(E)N_+ + f_{L3}N_-\big]
\end{aligned} \tag{1.22}$$

The first equation, describing the spin accumulation, tells us that in the presence of a spin-splitting field the energy mode (f_L) results in a finite magnetization. In equilibrium and at nonzero temperatures this is the effect that results in a finite paramagnetic response of a superconductor [59]. The second equation describes the charge imbalance of the system: the first term describes the charge mode described by [18], while the second term describes the charge accumulation associated with the spin-energy mode.

Figure 1.6 shows the magnetic field dependence of the spin accumulation as well as the charge accumulation proportional to the f_T and f_{L3} modes versus the injection voltage (the field dependence of $\Delta(H)$ is as discussed in the section 1.5). The spin accumulation is dominantly due to the induced f_L mode and therefore grows with the magnetic field (as N_- becomes larger with increasing H), and again decays when $\Delta \to 0$ as the field approaches the critical one ($H_c \approx 2.6$T).

As discussed in [20, 21], the orbital depairing induced by the magnetic field facilitates the charge relaxation processes and therefore the f_T mode is suppressed by a finite magnetic field. However, as the charge imbalance due to the spin-energy mode μ_{L3} is a function of N_- it shows a qualitatively different behavior: although the charge relaxation increases at finite fields, so does the span of energies at which N_- is nonzero. These two contributions result in a charge imbalance which is maximal at $\Delta - \mu_B H < V_{inj} < \Delta - \mu_B H$ and doesn't monotonically decrease with the magnetic field, as can be seen in figure 1.6.

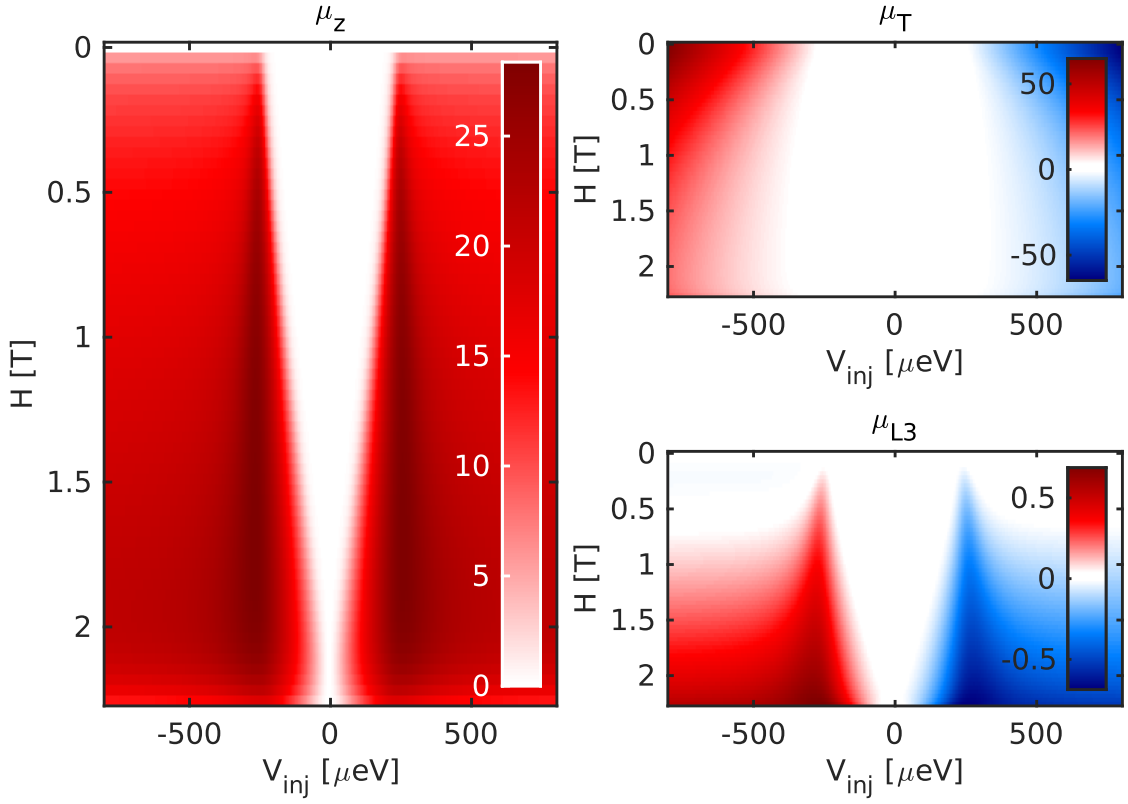

Figure 1.6: A color-plot showing the spin accumulation (left panel), the charge accumulation associated with the f_T (top right) and f_{L3} (bottom right) modes as a function of the applied magnetic field and the injection voltage. All quantities are plotted in arbitrary units.

1.5 The self-consistency relation

Within the Keldysh formalism the self-consistency for the pairing potential Δ is given by

$$\Delta = \frac{\lambda}{16i} \int_{-\omega_D}^{\omega_D} Tr\big[(\tau_1 - i\tau_2) g^K(E)\big] dE$$

where λ is the BCS pairing potential, ω_D is the Debye frequency, and the trace essentially "separates out" the anomalous part of the Keldysh component.

This expression can be expanded in terms of the distribution functions and the various components of the retarded GF:

$$\Delta = \frac{\lambda}{2}\int_{-\omega_D}^{\omega_D} dE\big[\mathrm{Im}(g_{0,1})f_L + \mathrm{Im}(g_{3,1})f_{T3} + i\big(\mathrm{Re}(g_{0,1})f_T + \mathrm{Re}(g_{3,1})f_{L3}\big)\big] \tag{1.23}$$

The first term is nonzero even at equilibrium (with $f_L = \tanh(\frac{E}{2k_BT})$), while the other three are nonzero only out-of-equilibrium. The last two terms are related to the charge imbalance (given by the f_T and f_{L3}) and add a nonzero imaginary component to the Δ.

While it is true that at equilibrium one can always choose a gauge such that Δ is strictly real, out-of-equilibrium this is not the case. As it was shown in section 1.2, the quasiparticle charge current is relaxed through Andreev processes, which means that the current is transferred from the quasiparticles to the condensate, which implies the existence of a finite phase gradient along the wire, which is precisely the meaning of the imaginary component of Δ in equation 1.23.

In order to solve the whole problem self-consistently one must:

- Solve the spectral equations at each position using the local $\Delta(x)$;
- Solve the transport problem in terms of all of the out-of-equilibrium modes (at each energy);
- Calculate the new $\Delta(x)$ using the self-consistency relation using the obtained modes at each x;
- Repeat the previous steps until convergence is reached.

While doing so one cannot rely on the previously laid out analytical results: the transport solution can no longer be obtained by diagonalizing the transport equations as the diffusion and relaxation terms are now position dependent, as Δ is a function of the position as well. Therefore the solution needs to be obtained numerically from start to finish, including at the boundary condition, which increases the complexity of the calculation drastically. We can, however, calculate the $\Delta(x, V_{inj})$ based on the analytical solution (without any gradients in Δ) to estimate the magnitude of the effect in our experimental situation. Figure 1.7 shows the absolute value, as well as the argument of Δ at $x = 0$ (where one can naively expect the largest deviation from the equilibrium values) - the maximum suppression turns out to be in the order of $\approx 10\%$, justifying the previous approach.

The self-consistency relation in equilibrium as function of the magnetic field will be further discussed in the section describing the sample properties (2 and 2.1).

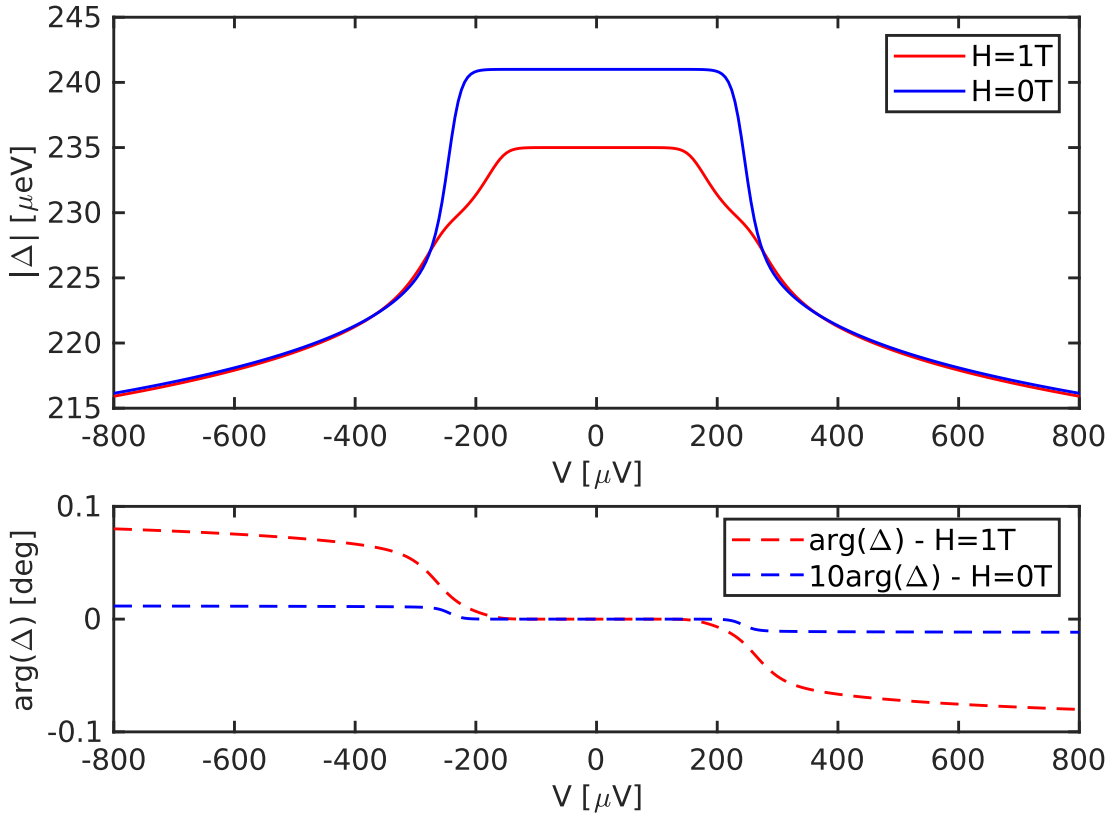

Figure 1.7: The self-consistent calculation of Δ at the injection sight ($x = 0$) as a function of the injection voltage at $H = 0$T (blue) and $H = 1$T (red). The top panel shows the absolute value of the complex Δ, while the bottom shows the argument. At $H = 0$ the argument is multiplied by a factor of 10 for clarity - this signifies that the supercurrent induced in the wire is lower at $H = 0$, as it should be for a slower charge relaxation.

1.6 Self-consistency within the relaxation time approximation

In this section a simplified version of the transport equations is presented and self-consistency for Δ is discussed. The aim is to construct a simple model in order to describe the zero field behavior shown in sections 2 and 3.2 on a *qualitative level*.

At $H = 0$ the complexity of the problem is greatly reduced as D_{T3}, N_- as well as other spin dependent quantities are equal to zero. Also, as quasiparticles are injected from a nonmagnetic electrode, the f_{T3} and f_{L3} modes will not be excited. A simplification that can be made is to completely disregard the presence of the charge mode, which is valid close to the gap edge, and especially at $H = 0$, as charge is efficiently relaxed there. Alternatively if the excitation junction is realized in the geometry proposed in [60], one can excite only the f_L mode.

Under these conditions the transport problem is greatly simplified as only the linearly decaying component of f_L will be nonzero: $f_L(x) = f_L \frac{L-x}{L}$. Most of the terms from the equation 1.19 vanish, and the gradient term can be simply replaced with f_L/L, where L is

the length of the wire. The equation can then be rewritten as:

$$\frac{N_+(E)}{\tilde{r}}\left[f_L^N(E) - f_L(E)\right] = \frac{f_L(E)}{\tau(E)} \tag{1.24}$$

where the effective "relaxation time" is given by $\tau(E) = \frac{L}{D_L(E)}$, and $\tilde{r}$ describes the barrier resistance as in section 1.3.3. As shown in [61] such a model will essentially "imprint" the (voltage biased) distribution function of the normal metal into the superconductor (see fig. 1.8). Quasiparticles are injected up to the energy of $E = eV_{inj}$, the height of the "step" is set by the ratio of $\frac{D_0\tilde{r}}{L}$ (D_0 is the normal state diffusion constant), while close to the gap edge due to the vanishing mobility of quasiparticles at the gap edge ($D_L \to 0$ as $E \to \Delta$) the distribution function will be peaked.

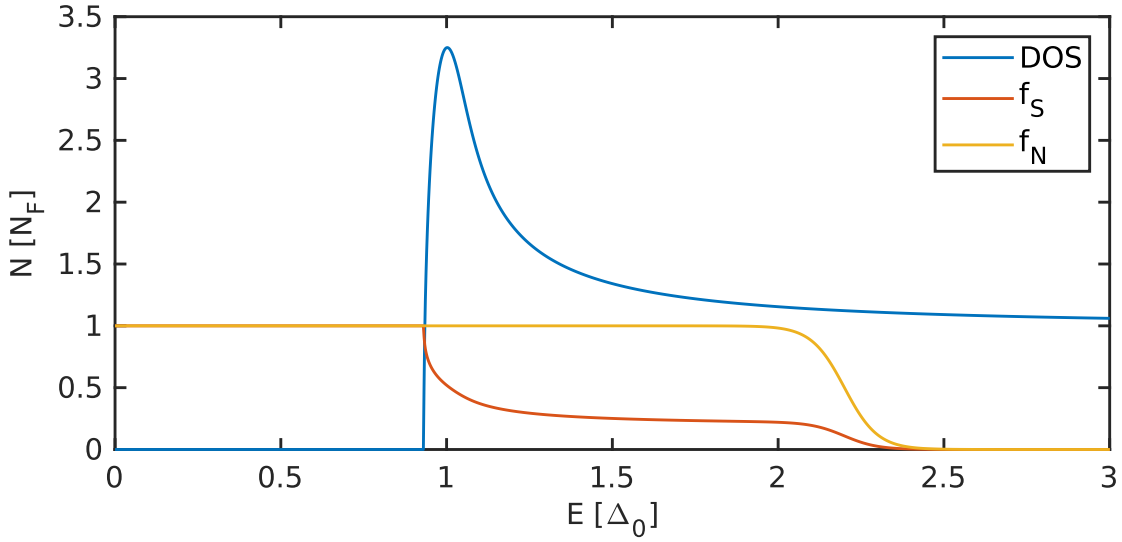

Figure 1.8: The DOS of the superconductor (blue), the distribution function in the normal metal (orange, $V_{inj} = 2.2\Delta_0$) and the induced out-of-equilibrium distribution function (red). The step height is set by the value of $\frac{D_0\tilde{r}}{L} = 0.2$, and the temperature of the normal is $T = 0.05\Delta_0$.

Under the same set of assumptions the self-consistency relation is reduced only to the first term of equation 1.23. Now for each injection voltage V_{inj} the self-consistent value of Δ can be computed (see figure 1.9), as well as the induced distribution function. Sufficiently below $eV_{inj} = \Delta_0$ there is no suppression of the order parameter: at $T = 0$ the gap suppression would start at $eV_{inj} = \Delta_0$ exactly, while at finite temperatures due to the thermal broadening of the distribution function it starts at $eV_{inj} + k_BT \approx \Delta_0$. When the injection voltage $V_{inj} \approx \Delta$, the order parameter can become bistable along with the existence of an unstable branch: if the gap is not substantially reduced from its equilibrium value only the exponential of the distribution function will inject quasiparticles, but there also exists a solution with a substantial number of excitations present. The size of the "S" shaped region is strongly dependent on the value of $\frac{D_0\tilde{r}}{L}$ and the temperature of the normal metal, and below a certain threshold value the unstable branch no longer exists. For clarity a set of parameters that highlights this behavior was used here, in practice this effect is significantly smaller - if observable at all.

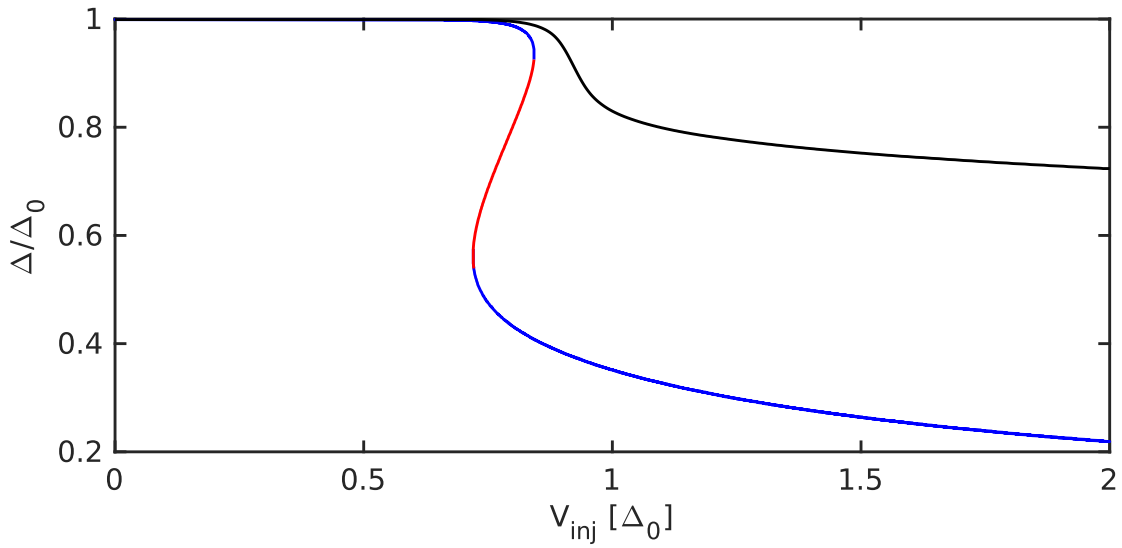

Figure 1.9: The suppression of the superconducting order parameter Δ as a function of the voltage applied to the normal metal injector. The black curve is calculated for $\frac{D_0\tilde{r}}{L} = 0.05$ and it is stable everywhere. The red-blue curve is calculated for $\frac{D_0\tilde{r}}{L} = 0.2$. It exhibits an S-shaped region of bistability, where the stable branches are given in blue, and the unstable one in red. The temperature of the normal metal is $T = 0.05\Delta_0$ which accounts for the suppression at $eV_inj \approx \Delta_0 - 3.5k_BT$.

Finally a comparison between the equilibrium and nonequilibrium self-consistency can be made. Close to equilibrium it can be shown that the suppression of the gap is given by the ratio of the number of quasiparticles and Cooper pairs [62, 63, 64], $\Delta = \Delta_0(1 - \frac{N_{QP}}{N_{CP}})$. Far from equilibrium this no longer holds and Δ is no longer a universal function of N_{QP}. Figure 1.10 shows a comparison between the nonequilibrium case, as described above, and an effective temperature. *As a consequence, to fully characterize an out-of-equilibrium state of a superconductor a detailed spectroscopic study is necessary, it is insufficient to probe the gap Δ of a superconductor, or even the number of quasiparticles.*

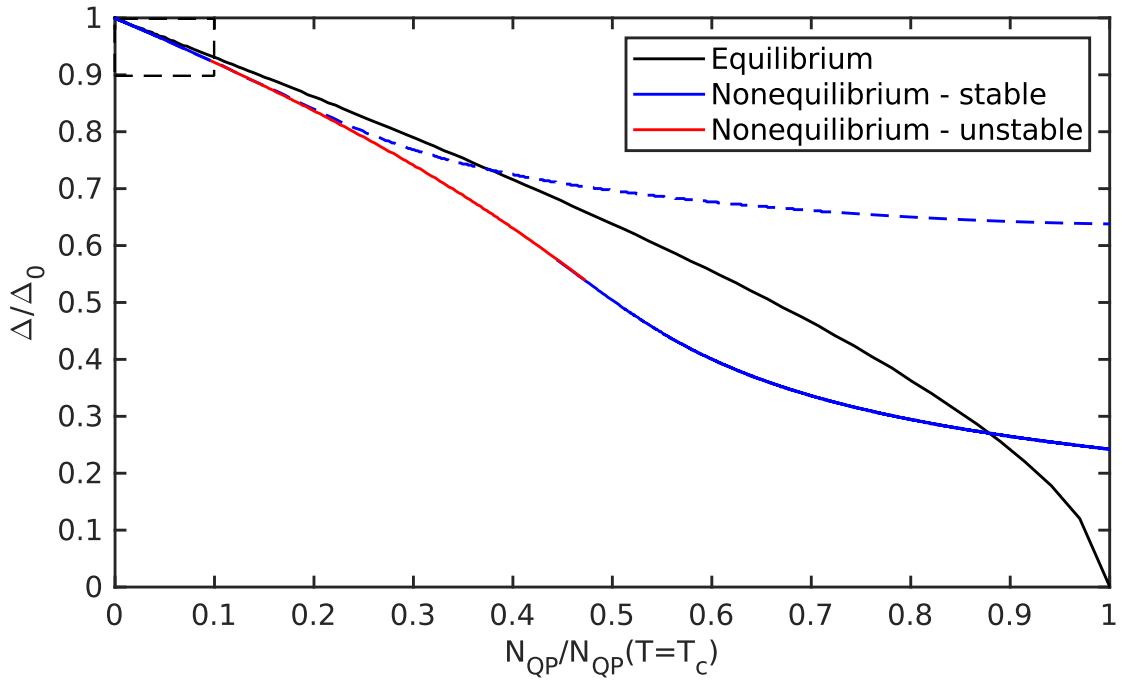

Figure 1.10: The dependence of Δ as a function of the number of excitations present in the system, for a thermal distribution function (black), and the two nonequilibrium solutions shown in 1.9 (the blue dashed curve corresponds to the black trace on the previous figure). The region bounded by the dashed rectangle corresponds to the range accessible in the experiment.

Chapter 2

Sample overview and properties

The sample shown in figure 2.1, consists of a $L = 10\mu$m long, $w = 200$nm wide superconducting Al wire. The total thickness of the wire, including the natively grown oxide layer on the top of the wire, is $d \approx 6$nm. The wire resistance at $T = 4$K is $R \approx 850\Omega$ resulting in a resistance per square of $R_\square \approx 17\Omega$ and the normal state diffusion coefficient of $D \approx 11\frac{\text{cm}^2}{\text{s}}$. The critical temperature of the wire is $T_c \approx 1.7$K (the increase of the critical temperature compared to the bulk value of ≈ 1.2K is related to the disorder induced by the small film thickness and is consistent with previous findings [65]), while the critical in plane magnetic field is $H_c \approx 2.7$T. On both ends the wire is terminated with large, well thermalized, metallic reservoirs.

On top of the wire there are several tunnel junctions (using the native oxide as the tunnel barrier):

- The injector junction J_{inj} (cyan in 2.1) - an NIS junction used for creating quasiparticle excitations in the wire by current injection. The normal metal N is Cu (100nm thick), the surface area of the junction is $S = 200\text{nm} \times 200\text{nm}$ and the normal state resistance is $R = 13\text{k}\Omega$.

- The detector junctions $J_{\{1,2,3\}}$ (red in 2.1) - SIS$'$ junctions, where the counter electrode S$'$ is an $d_{\text{Al}} \approx 8$nm thick layer of Al with a mono-layer of Pt ($d_{\text{Pt}} = 1$Å nominally) on top. The purpose and the effects of the Pt layer are described in detail in section 2.3. The surface area of these junctions is $S = 50\text{nm} \times 200\text{nm}$, while their normal state resistances, as well as their distances from the injector junction are:

  - J_1: $R = 31.2\text{k}\Omega$, $L_1 = 250$nm
  - J_2: $R = 38.3\text{k}\Omega$, $L_2 = 1.89\mu$m
  - J_3: $R = 29.5\text{k}\Omega$, $L_2 = 3.53\mu$m

More details, the motivation for the used materials, parameters and geometry, as well as more information on the measurement setup are given in appendix A.

The basic idea of the experiment is the following: quasiparticles are injected into the wire by applying a current through J_{inj}. As the diffusion time to the reservoirs $\tau_{dif} = \frac{L_{res}^2}{D} \approx 20$ns is much shorter than the quasiparticle-quasiparticle recombination time $\tau_{rec} \approx 400$ns [5] the quasiparticles relax only by diffusing to the end of the wire and thermalizing with the phonon bath there. An externally applied magnetic field will cause pair-breaking effects, and for an

in-plane field the pair breaking energy is determined to be $\alpha \approx 6.5\frac{\mu eV}{T^2}$ (see figures 2.2 and 2.4). Consequently, all the way up to the critical field $\alpha H_c^2 < \mu_B H$, which implies that the DOS of the superconductor will be Zeeman split, and allows us to create spin-polarized excitations by biasing the injector junction such that $\Delta - \mu_B H < V_{inj} < \Delta - \mu_B H$.

The out-of-equilibrium quasiparticles can then be probed by one of three spin-sensitive spectroscopic detectors, positioned at different distances away from the injection site. The spin relaxation mechanism in the wire is assumed to be through spin-orbit scattering and the effective relaxation time is estimated, based on [36], to $\tau_{SO} = 50$ps, giving a spin relaxation length of $L_{SO} \approx 240$nm, which is comparable to the distance between J_{inj} and J_1. Thus our device, due to the spin sensitivity of the detector, allows for the detection of a spin dependent distribution function at short distances from the injection site.

All of the measurements presented in this chapter were performed in a ^{3}He/^{4}He dilution refrigerator at $T = 90$mK.

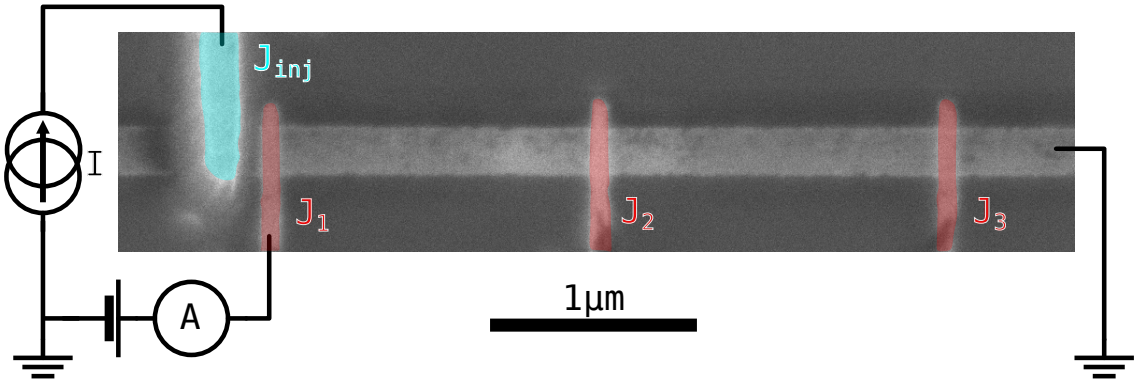

Figure 2.1: An SEM micrograph of the sample, with a simplified schematic of the principal measurement setup: J_{inj} (cyan) is current biased, and the $I(V)/G(V)$ curve of one of the detector junctions $J_{\{1,2,3\}}$ (red) is measured simultaneously.

The following sections will address the injection scheme (section 2.1) as well as the workings of the detectors in detail (sections 2.2 and 2.3).

2.1 The NIS injector

In a superconductor quasiparticles can be excited by current (or voltage) biasing an NIS junction, where the tunnel barrier allows for a finite voltage drop across the junction and thus quasiparticles with energies up to the voltage bias, $E \approx eV$, can be injected into the superconductor. Following [33] the tunneling current through such a junction is given by:

$$I(V) = \frac{1}{eR_{\mathrm{N}}} \int N(E)[f^p(E) - f_N^p(E - eV)]dE \tag{2.1}$$

while the differential conductance is:

$$G(V) = \frac{\partial I(V)}{\partial V} = \frac{1}{eR_{\mathrm{N}}} \int N(E) \frac{\partial f_N^p(E - eV)}{\partial V} dE \tag{2.2}$$

The quantity $\frac{\partial f_N^p(E - eV)}{\partial V}$ becomes the Dirac-delta function at $T = 0$, and at finite temperatures is a bell-like curve with a FWHM of $\approx 3.5k_BT$. Therefore the $G(V)$ curve of the

NIS junction depends only on the DOS of the superconductor and the effective temperature in the normal metal (and at a sufficiently low temperature the $G(V)$ approaches the DOS of the superconductor).

When a finite magnetic field is applied to a superconductor there are several observable effects [34]. The first of which is the orbital (Abrikosov-Gor'kov, AG) depairing, from the induced screening supercurrent, which results in a rounding of the DOS coherence peaks as well as a reduction of the spectroscopic gap below Δ. The strength of this effect is geometry dependent, and for a thin film superconductor with an in-plane field the depairing parameter is $\alpha = \frac{De^2d^2}{6\hbar}H^2$ [33, 66], where d is the sample thickness and D the normal state diffusion constant. The critical field, at zero temperature, due to the orbital depairing is set by $2\alpha(H) = \Delta(H = 0)$, and at low fields the $\Delta(H)$ curve is roughly linear: $\Delta(H) \approx \Delta_0 - 0.4\alpha(H)$. If the sample is thin, α is quadratically suppressed which leads to an increased H_c. The second effect is the Zeeman splitting of the DOS, a result of the coupling of the quasiparticle spin degree of freedom with the external field, which shifts the spin up/down quasiparticle DOS by $E_z = \pm\mu_B H$ (the Landé factor is $g = 2$) [67]. The Zeeman splitting can be observed only if the orbital smearing of the DOS is sufficiently small and if the (critical) field is larger than the temperature of the superconductor $\mu_B H > 3.5k_B T$. In the presence of the spin-orbit coupling, which is the relevant spin relaxation mechanism for this experiment, spin is only approximately a good quantum number, which leads to the spin-mixing of the DOS, as shown in figure 1.4 and [68] - the spin up DOS is nonzero even in the range $\Delta - \mu_B H < E < \Delta + \mu_B$. However, this contribution is not directly observable with an NIS junction with a spin-independent transmission.

Figure 2.2 shows the $G(V)$ of the injector at $H = 0$T and at $H = 1$T. Both of these traces show features beyond the simple equilibrium model. In particular, at $H = 0$T (fig. 2.2, the blue trace) the coherence peaks are sharper (higher and narrower) than what one should expect at $T = 90$mK.

This can be understood in terms of the out-of-equilibrium suppression of Δ: when a finite voltage is applied across the junction there is a nonzero current flowing through it which, due to the relatively low resistance of the junction $R(J_{inj}) = 13\text{k}\Omega$ and the thin superconducting wire, induces an out-of-equilibrium state in the wire. This leads to deviations from the simple BCS model, which can be taken into account by considering a voltage dependent gap $\Delta = \Delta(H, V_{inj})$. A calculation based on the model presented in section 1.6, can be used to illustrate this: figure 2.3 shows how the $\Delta(V_{inj})$ dependence can make the $I(V)/G(V)$ curve sharper than at equilibrium.

At $H = 1$T (fig. 2.2, the red trace), there are two observable peaks, corresponding to the spin down and spin up component of the DOS. The spin down peak, located at $V \approx 175\mu$V is slightly sharper than the model, while the main difference is in the spin up peak (located at $V \approx 290\mu$V) is significantly less pronounced than the equilibrium model predicts.

Figure 2.4 shows the $G(V)$ of the injection junction J_{inj} as a function of the magnetic field as a color-plot, as well as a numerical simulation of the same using the equilibrium $\Delta(H)$ dependence (based on 1.23) for comparison.

As a result of the nonequilibrium effects some of the sample properties, in particular the Abrikosov-Gor'kov depairing energy α, cannot be determined from a straightforward fit. The depairing rate was determined to be $\alpha_0 = 6.5\frac{\mu\text{eV}}{\text{T}^2}$ by using both the tunneling spectra of the injector junction as well as the detectors which also, albeit indirectly, probe the DOS without significant out-of-equilibrium effects. This value was also used for the theoretical calculation

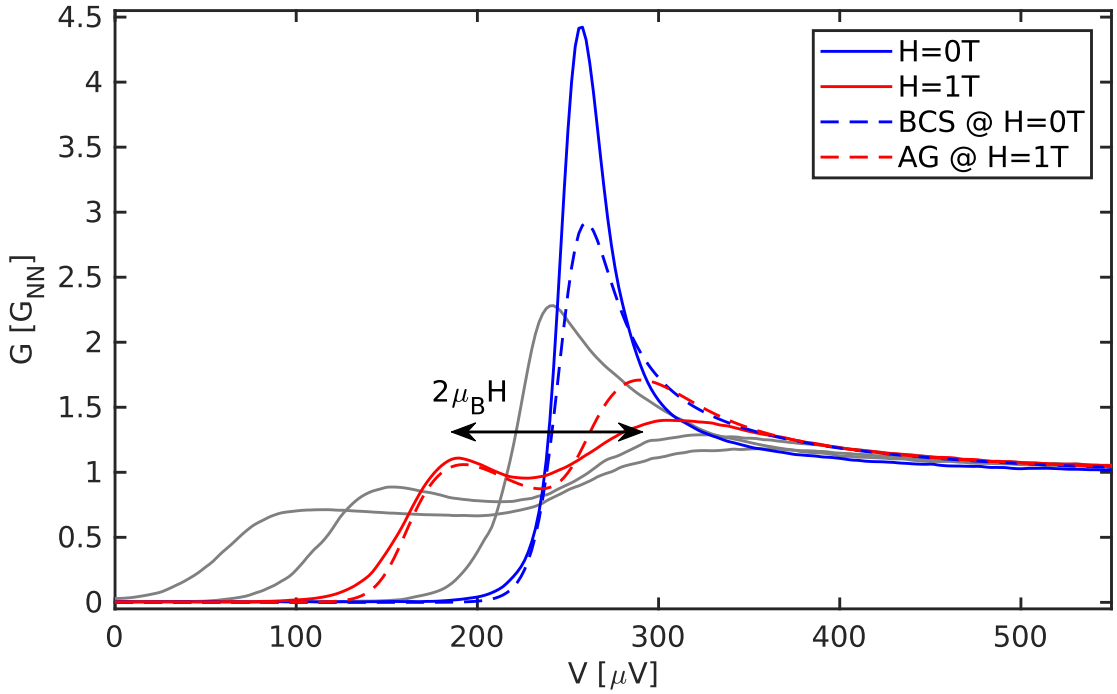

Figure 2.2: The experimental NIS $G(V)$ curves at $H = 0$T (blue) and at $H = 1$T (red). The gray traces are the measured $G(V)$ traces up to $H \approx 1.8$T in steps of $\Delta H \approx 0.4$T. The dashed blue and red traces are the simulated $G(V)$ curves for a BCS DOS at $T = 90$mK and an Abrikosov-Gor'kov DOS at $H = 1$T and $\alpha = 6.5\mu$eV and the same temperature.

shown in figure 2.4.

As the AG energy is lower than the Zeeman energy $\alpha(H) = \alpha_0 H^2 < \mu_B H$ all the way up to the critical field, at finite fields the DOS will be well Zeeman split, as shown in the same figure.

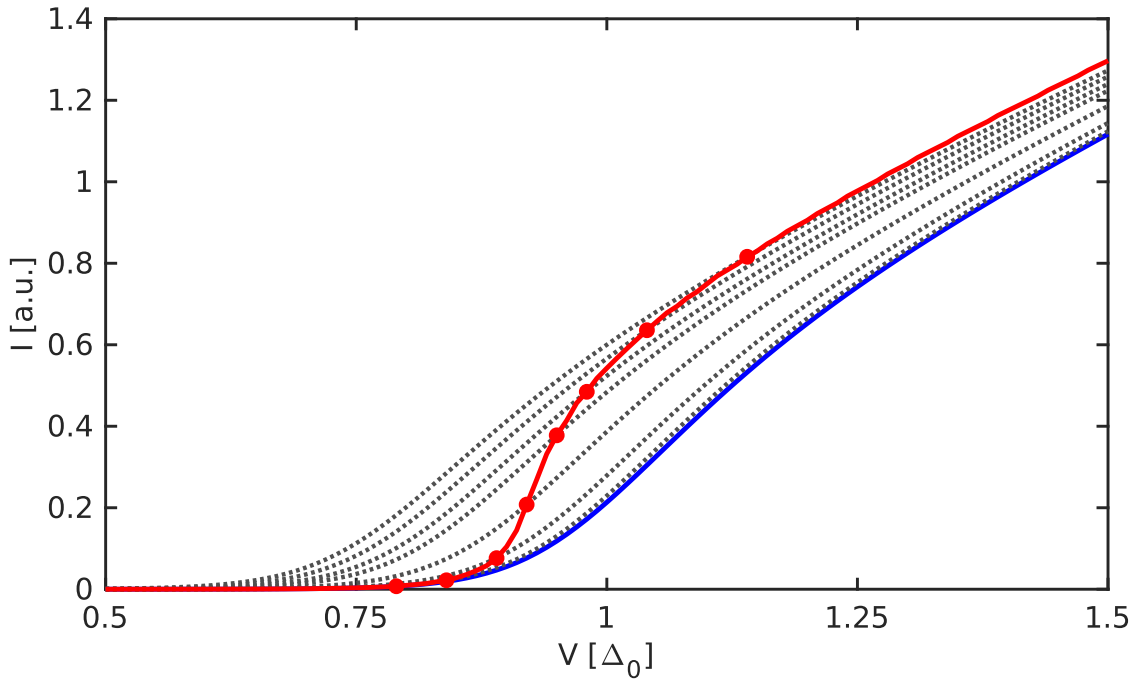

Figure 2.3: The simulated equilibrium $I(V)$ for $\Delta_0 = 1$ and $T = 0.05\Delta_0$ (the blue curve), as well as the nonequilibrium $I(V)$ with the $\Delta(V)$ dependence included (red trace), based on the model presented in section 1.6. The dotted gray traces show the equilibrium $I(V)$ curves for lower values of $\Delta = \Delta_i$, while the red dots represent the solutions of $\Delta(V_i) = \Delta_i$ - as the voltage is increased, the nonequilibrium trace shifts between different equilibrium $I(V, \Delta_i)$ traces leading to a sharper curve.

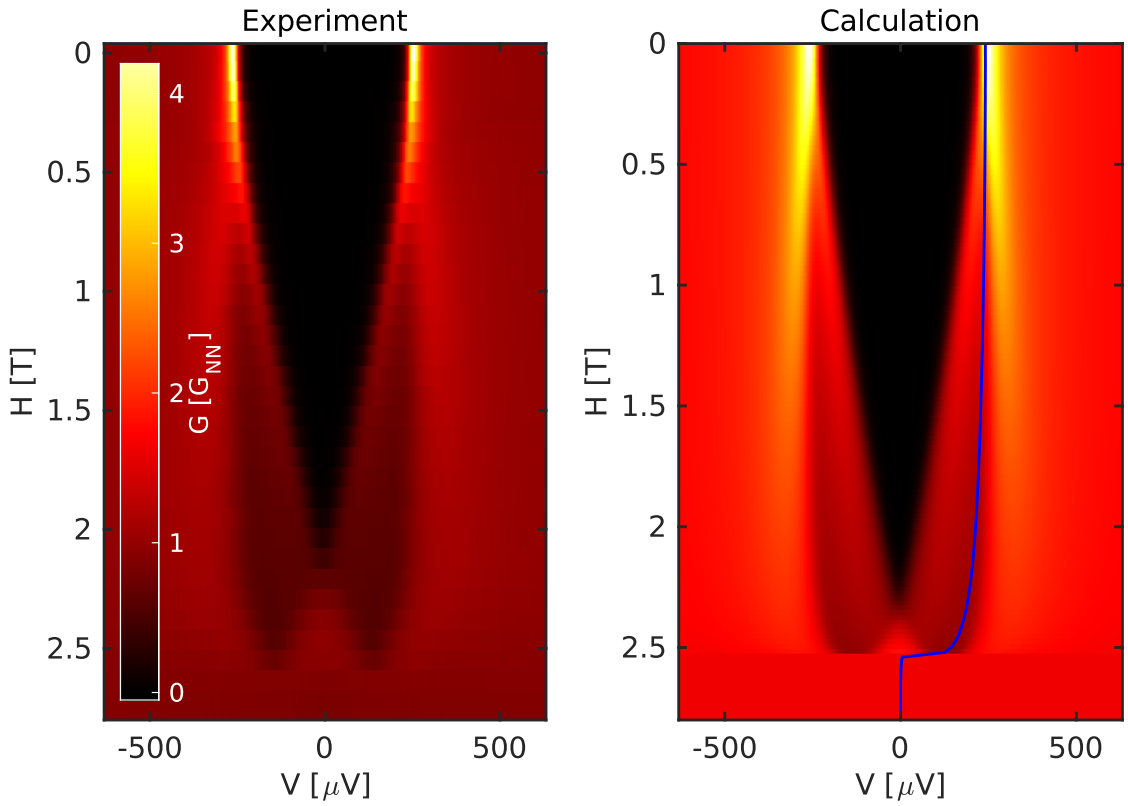

Figure 2.4: A color-map of the NIS $G(V)$ curves as a function of the magnetic field, from the experiment (left), and from the theory (right) using the **equilibrium** self-consistent $\Delta(H)$ (blue curve).

2.2 The SIS′ detector

The current across an SIS′ has two main contributions: the Josephson supercurrent and the quasiparticle tunneling current. In this chapter we will discuss how the tunneling current can be used as a spectroscopic probe of the out-of-equilibrium state in a superconductor, as well as how the supercurrent contribution can be suppressed.

2.2.1 The Josephson current

The Josephson supercurrent through an extended SIS junction, at a finite magnetic field, is given by [69]:

$$I_s = \int_{\frac{-d}{2}}^{\frac{d}{2}} j_s(x,H)\sin(\varphi_0 + kx)dx \tag{2.3}$$

where d is the junction width, and $j_s(x,H)$ describes both the current density profile along the axis orthogonal to the applied magnetic field as well as the field dependence of $\Delta(H)$. The wavenumber $k = 2\pi H(2\lambda + d_{barrier})/\Phi_0$ (λ is the field penetration depth and $\Phi_0 = 2\times10^{-15}$Wb the magnetic flux quantum), describes the total magnetic field flux trapped in the junction.

If the barrier is uniform, that is $j_c = const$, the following result is obtained: $I_s(\varphi) = \frac{j_s \sin(d\frac{k}{2})}{k/2}\sin(\varphi)$. Then the critical current is always obtained at $\varphi = \frac{\pi}{2}$ and it follows the usual Fraunhofer pattern - it is equal to zero when the trapped flux is equal to one flux quantum.

If, on the other hand, the barrier is not spatially uniform and $j_s(x)$ has an odd component ($x = 0$ is the center of the junction), the supercurrent can be expressed as $I_s(\varphi) = A\sin(\varphi) + B\cos(\varphi)$, where the field dependence is hidden in $A(H)$ and $B(H)$. The critical current then becomes $I_c = \sqrt{A(H)^2 + B(H)^2}$. Because these two coefficients are not simultaneously equal to zero the critical current cannot be fully suppressed by an application of the magnetic field. However the minimum of I_c is still obtained close to the field at which there is one flux quantum in the junction.

Experimentally the critical current can be accessed directly by measuring the $V(I)$ or by measuring the differential conductance $G(V) = \dfrac{\partial I}{\partial V}$ at $V = 0$. Additionally, there can be an excess supercurrent contribution at a finite voltage V, if the Josephson frequency matches a resonant frequency in the device $2eV = hf$, which for the device in question happens at $V \approx 256\mu$V ($f \approx 124$GHz) - see the inset of figure 2.5.

Figure 2.5 shows the normalized differential conductance at zero voltage bias of detector J_1. As expected from the geometry ($d_{junction} \approx 200$nm, $2\lambda + d_{barrier} \approx 10$nm) the Josephson critical current is minimal around $H = 1$T, and by measuring at (or close to) this magnetic field allows us to probe only the quasiparticle current contribution (as described in the section 2.2.2). The curve does not exactly follow the shape of a (smeared out) cardinal sine function, which is primarily because of the $\Delta(H)$ and $\Delta_D(H)$ (detector) dependencies which are not taken into account.

The residual Josephson contribution to the $G(V)$ curve at $H = 1$T, can be modeled as a Gaussian peak and subtracted from the trace, as is shown in figure 2.10.

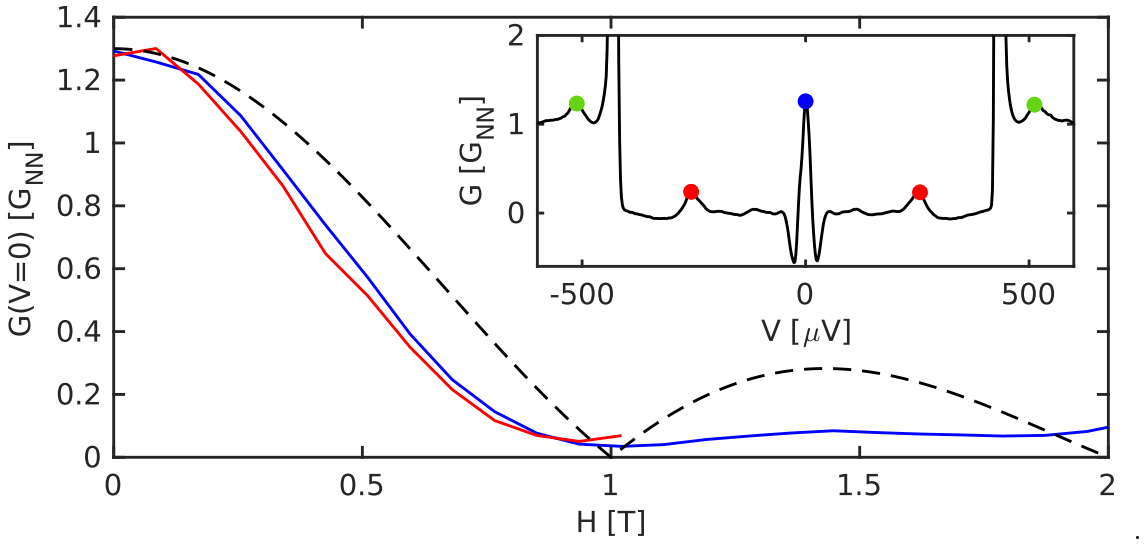

Figure 2.5: The measured magnetic field dependence of the zero bias Josephson peak ($G(V = 0)$ - blue curve) as well as the first Josephson resonance ($5.5G(V \approx 256\mu\text{V})$ - red curve) for the detector J_1. The red trace stops at $H = 1\text{T}$ as slightly above this field the spectral gap closes below the threshold $\Delta + \Delta_D = 256\mu\text{eV}$. The black dashed curve shows the Fraunhofer pattern normalized by the I_c at $H = 0$. The inset shows the $G(V)$ curve at zero magnetic field with the Josephson peak, as well as the first two resonances labeled (red and green dots).

2.2.2 The quasiparticle tunneling current

The tunneling current through an SIS′ junction is (see [33]):

$$I(V) = \frac{1}{eR_{\text{N}}} \int_{-\infty}^{\infty} N_D(E + eV) N(E) [f^p(E) - f_D^p(E + eV)] dE \tag{2.4}$$

where R_N is the junction resistance, N and N_D are the DOS functions for the probed superconductor and the detector electrode, respectively, while f^p and f_D^p are the distribution functions in the particle picture.

By applying a voltage $eV = \Delta + \Delta_D$ to the detector junction the (electron side) gap edge of the detector is brought down to the gap edge of the superconductor at $E = -\Delta$. As the density of states of the detector is $N_D(E > 2\Delta_D) \approx 1$ and the distribution function $f_D^p(E > 2\Delta_D) = 0$, the electron side of the superconductor is probed by a flat DOS with no excitations present. The tunneling on the hole side is blocked by the spectral gap of the detector down to $E = \Delta - 2\Delta_D$. Therefore the total current will be directly proportional to the number of electron-like excitations in the probed superconductor. Likewise, if a negative voltage of the same magnitude is applied the number of hole-like excitations is measured by the tunneling current.

Measuring the $G(V)$ curves can provide spectroscopic information about the quasiparticle population. If the detector is at equilibrium and at a sufficiently low temperature it will host a vanishingly small number of quasiparticles and, therefore, the term in the $G(V) = \dfrac{\partial I}{\partial V}$ proportional to $N_D(E + eV)\dfrac{\partial f_D^p(E + eV)}{\partial V} \ll 1$ can be neglected ($\frac{\partial f^p}{\partial E}$ is nonzero only in a

window of $3.5k_BT \ll \Delta$). The other, nonzero, term is

$$G(V) = \frac{1}{eR_{\mathrm{N}}} \int_{-\infty}^{\infty} N(E)[f^p(E) - f_D^p(E+eV)] \frac{\partial N_D(E+eV)}{\partial V} dE$$

At sub-gap voltages ($eV \leq \Delta + \Delta_D$) and in the relevant energy range ($|E| > \Delta$, where $N(E) > 0$), f^p can be replaced with $f^p(E, T = 0)$ (i.e. no quasiparticles are present in the detector which could contribute to the tunneling process), and so the term in the square brackets becomes $\delta f(E) = f^p(E) - f_D^p(E+eV) = f^p(E) - f^p(E, T = 0)$, which just accounts for the (out-of-equilibrium) excitations in the superconductor. Finally the relevant expression for the differential conductance becomes:

$$G(V) = \frac{1}{eR_{\mathrm{N}}} \int_{-\infty}^{\infty} \frac{\partial N_D(E+eV)}{\partial V} N(E)\delta f(E) dE \tag{2.5}$$

The derivative $\frac{\partial N_D(E+eV)}{\partial V}$ is very sharply peaked at $E \approx \Delta_D$, and from this it is clear that the $G(eV = E - \Delta_D) \propto N(E)\delta f(E)$ probes the number of excitations at energy E. This property allows for the use of an SIS junction as a spectroscopic detector of out-of-equilibrium quasiparticles.

A graphical representation showing all of this is given in figure 2.6, showing the DOS of the probed superconductor, an equilibrium distribution function, an out-of-equilibrium distribution function (only the f_L mode is nonzero), the DOS of the detector as well as its derivative. Figure 2.7 shows the corresponding $I(V)$ and $G(V)$ curves, along with a comparison with $N(E)f(E)$.

By integrating the previous expression for the $G(V)$ one again finds that the $I(V)$ measures the number total number of quasiparticles.

The whole discussion holds true in the spin-split case, the only difference is that the different spin channels have to be considered separately and their contributions should be then added, as the spin is conserved by tunneling.

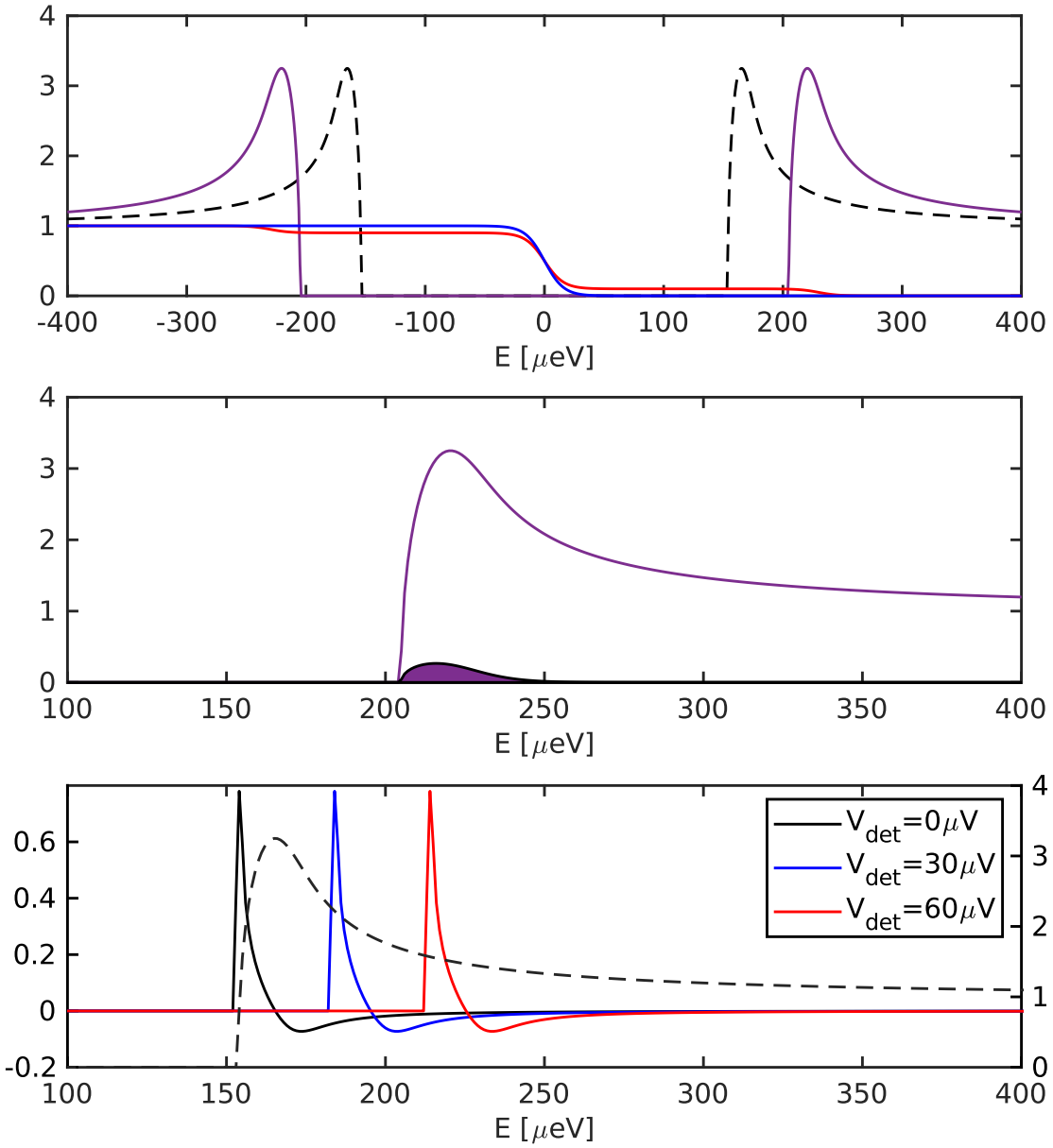

Figure 2.6: Top: the calculated superconductor DOS $N(E)$ (purple), the detector DOS $N_D(E)$ (black dashed), the equilibrium Fermi-Dirac distribution function (blue) and a nonequilibrium one (red, only $f_L \neq 0$). Middle: The density of states as above and the nonequilibrium quasiparticle density $N(E)f_{noneq}(E)$. Bottom: The simulated DOS of the detector (black dashed, right scale), as well as its derivative at $V_{det} = 0\mu$V (black), $V_{det} = 30\mu$V (blue) and $V_{det} = 60\mu$V (red). The two distribution functions shown in the top panel are also used used for the traces in figure 2.7.

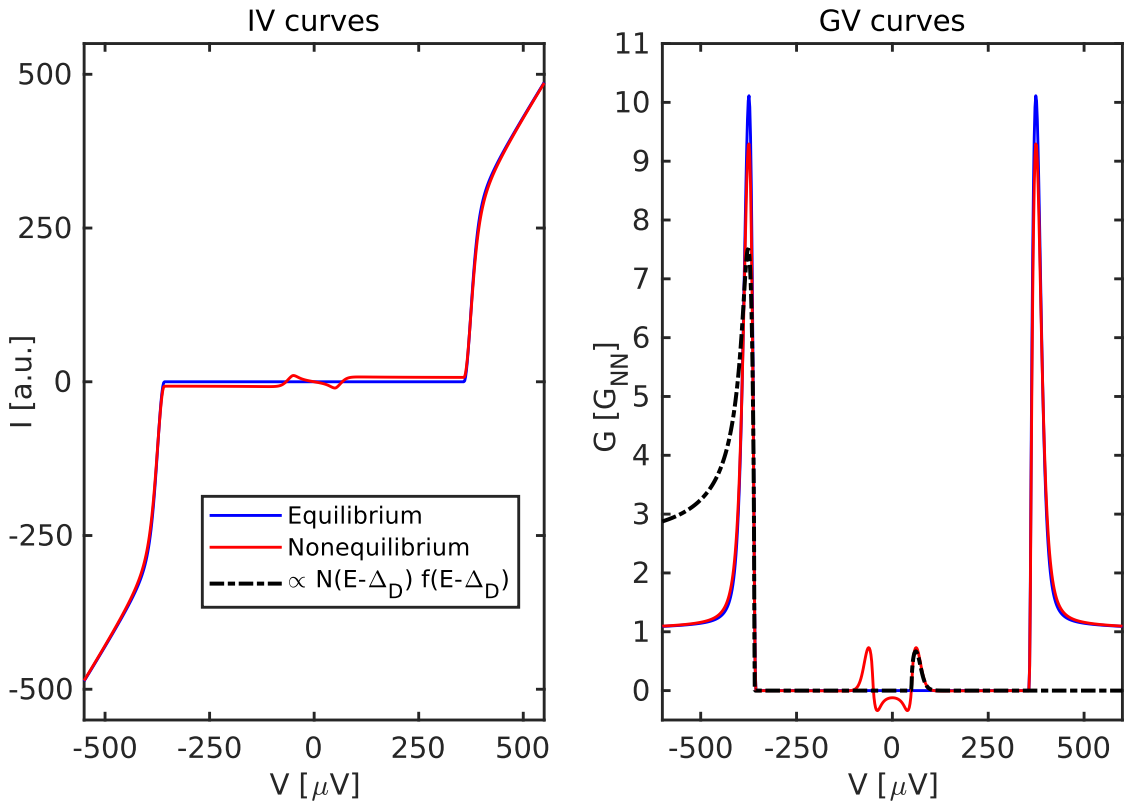

Figure 2.7: Left: the calculated $I(V)$ curve for the equilibrium and non-equilibrium distribution functions shown in figure 2.6. Right: the corresponding $G(V)$ curves and a comparison with $N(E)f(E)$.

2.3 The spin sensitive SIS′ detector

Contrary to an NIS junction, as shown in [68], the $I(V)/G(V)$ traces of an SIS junction will not show the Zeeman splitting under a finite magnetic field. This is because both superconductors become Zeeman split, and as the tunneling process needs to be considered separately for the spin up and spin down, this just amounts to having the *same* shift in the chemical potential/Fermi energy $\pm\mu_B H$ on both sides of the junction. However, if the detector side of the junction is not spin split (i.e. $N_\uparrow \approx N_\downarrow$), which is the case of the spin-mixing induced by spin-orbit interaction in the superconductor [68], it leads to an observable Zeeman splitting in the $G(V)$ curve. The top panel of figure 2.8 shows the difference between the DOS of a superconductor with a negligible spin-orbit interaction ($R_{SO} \ll \Delta$, blue traces) and with a large spin-orbit interaction ($R_{SO} \gg \Delta$, red traces) at $H = 1\mathrm{T}$. The bottom panel of the same figure shows the normalized differential conductance of an SIS junction made out of two superconductors with low SO interactions (blue) and an SIS′ where the one has a low and the other a high spin-orbit interaction.

A detector made out of a non-Zeeman-split superconductor can be used as a spin sensitive detector: following the discussion in section 2.2.2 the spin down quasiparticles will be detected at a detector voltage of $V_\downarrow = \Delta - \mu_B H - \Delta_D$, while the spin up ones will be detected at $V_\uparrow = \Delta + \mu_B H - \Delta_D$.

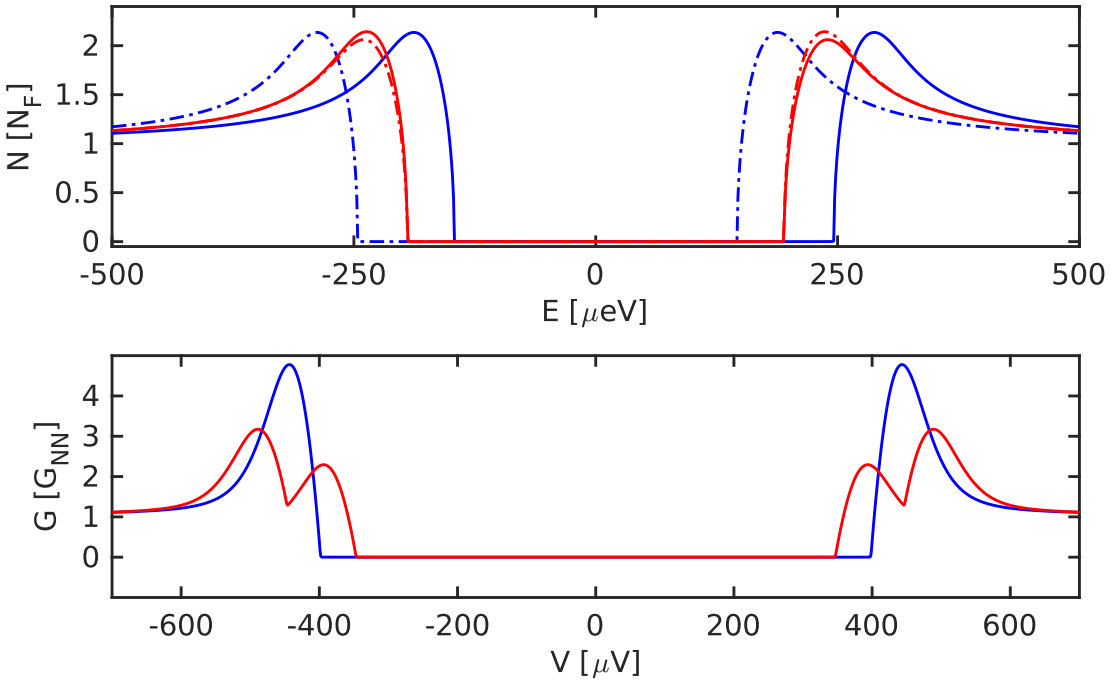

Figure 2.8: Top: The simulated spin down (dashed) and spin up (solid) DOS of a superconductor with $R_{SO} \ll \Delta$ (blue), and the same for $R_{SO} \gg \Delta$ (red). Bottom: If the simulated $G(V)$ curves of two SIS junctions - one couples two Zeeman split superconductors (blue), and the other one couples a Zeeman split superconductor with a non-split one (red).

Experimentally such a detector can be realized covering the Al detector electrode, with a mono-layer of Pt [70]. Because of the high atomic number of Pt it induces a strong spin-orbit effect in the detector and suppresses the Zeeman splitting. To verify this effect a separate

set of samples, fabricated in roughly the same geometry as the final device, were made with high resistance NIS junctions ($R \approx 250\text{k}\Omega$) to probe the equilibrium DOS. Figure 2.9 shows the magnetic field dependence of the DOS, with and without the Pt doping, verifying that the doped sample is not Zeeman split. Although such a measurement is not a reliable way to determine the strength of the SO interaction precisely, the key point is that there is a *single* gap edge, which allows the junction to be a spin sensitive spectroscopic detector. The $G(V)$ curve of the SIS′ at a finite magnetic field, showing the Zeeman splitting, is shown in figure 2.10. For reference the same figure includes a trace from a previous sample at the same field, where the detector electrode was Al only and is therefore Zeeman split, and the $G(V)$ traces do not show two separate coherence peaks. The difference in the amplitude of the peaks is due to a lower orbital depairing.

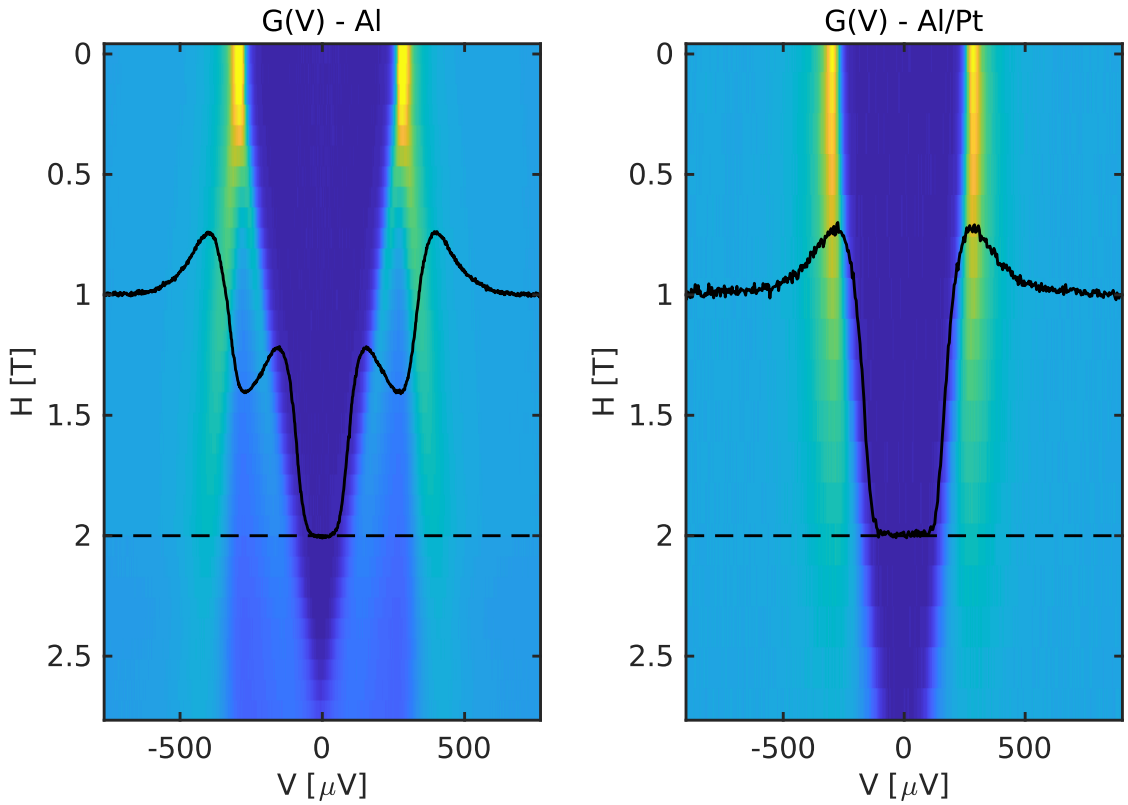

Figure 2.9: The tunneling differential conductance $G(V)$ color-map as a function of the magnetic field for an Al sample (left), and an Al/Pt sample. The black lines are the $G(V)$ traces at $H = 2\text{T}$. All data was taken at $T = 90\text{mK}$.

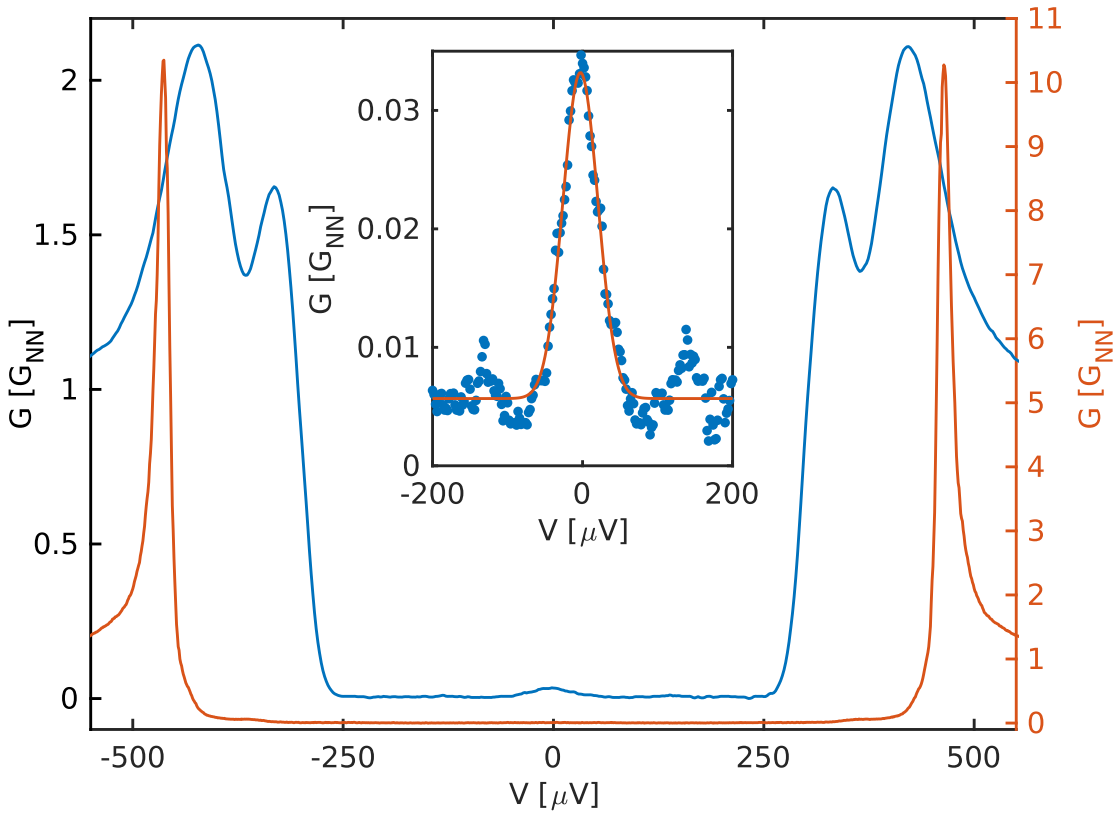

Figure 2.10: The $G(V)$ curve of J_1 at $H = 1\text{T}$ which shows the "splitting" of the coherence peaks at $|eV_{det}| = |\Delta \pm \mu_B H + \Delta_D|$, which is explained in detail in the section 2.3. The small Josephson contribution, close to $V = 0$, can be modeled as a Gaussian peak and subtracted from the data, as shown in the inset. The red trace (shown on the right scale) is from a previous device with a Zeeman-split detector, also at $H = 1\text{T}$.

Chapter 3

Nonspectroscopic measurements

As discussed in detail in section 2.2 the SIS′ junction can be used to measure the number of quasiparticles up to the energy $E = \Delta + \Delta_D$ by measuring the quasiparticle tunneling current at $I(V = \Delta + \Delta_D)$. Through self-consistency the quasiparticle population results in a reduction of Δ, and this can also be measured using the same detector as the threshold voltage at which the current abruptly rises. Figure 3.1 shows the $I(V)$ curves of J_1 at equilibrium and at $I_{inj} = 120$nA: an excess subgap current $I_{QP} \approx 2$nA can be observed together with a reduction in the gap.

These two properties will now be used to probe the out-of-equilibrium state, induced by current injection, as a function of space and magnetic field.

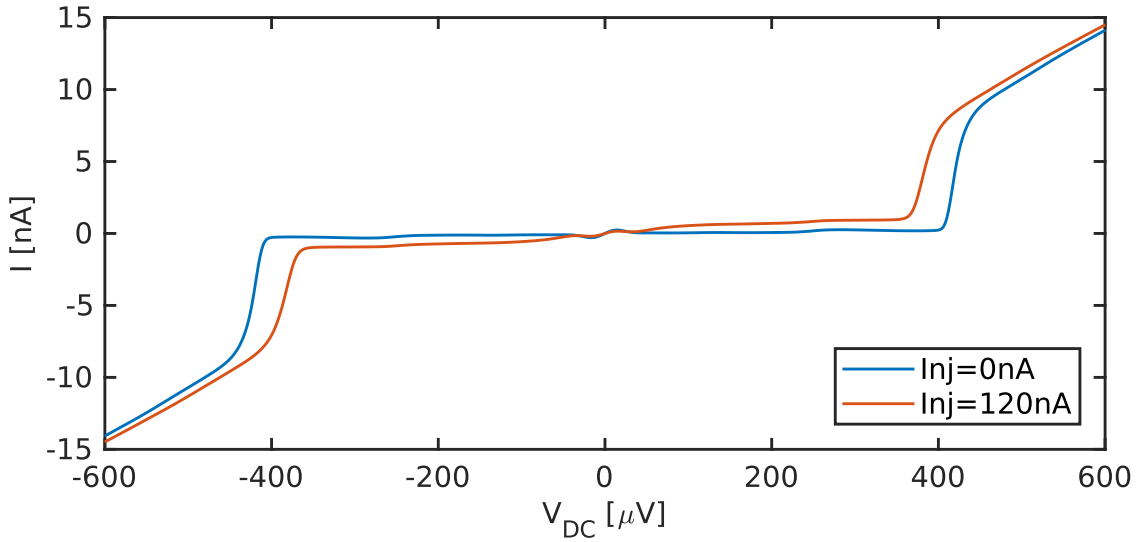

Figure 3.1: The experimental $I(V)$ curves of J_1 at equilibrium (blue) and at $I_{inj} = 120$nA (red). The nonequilibrium curve shows an excess subgap current as well as a reduction in $eV = \Delta + \Delta_D$.

3.1 Spatially resolved number of QPs at high injection

In this chapter the validity of the claim that the quasiparticles relax solely by the thermalization at the ends of the wire is verified. First a theoretical argument is given and than

the relevant measurements are presented.

A slight generalization of equations 1.13 and 1.16 reads:

$$D^*(E)\nabla^2 f(E) = I_{coll}(f, E) \tag{3.1}$$

where the $D^*(E)$ is the energy dependent diffusion matrix, $f(E)$ a vector describing the different distribution modes, and $I_{coll}(E)$ takes into account all of the different relaxation and scattering mechanisms.

The charge and spin relaxation processes, as well as an effective electron-electron interaction, conserve the number of quasiparticles. On the other hand the electron-phonon interaction will decrease the QP population through recombination. As a consequence at timescales shorter than the recombination time $\int_{\infty}^{\infty} I_{coll}(f, E)dE = 0$ vanishes for any distribution function f.

If most of the quasiparticles are injected at high energies (i.e. $E \gg \Delta$), where D^* is diagonal and proportional to D_0 (the normal state diffusion coefficient), one can simplify equation 3.1 by integrating over energy and disregarding the dependence at low energies, one gets:

$$D\nabla^2 f = 0 \tag{3.2}$$

To obtain a physical solution from the previous equation one must impose the proper boundary conditions, at the injector and at the ends of the wire.

As, at high energies, the number of quasiparticles is proportional only to f as the density of states is constant, according to the equation 3.2 one should expect a linear spatial dependence/decay of the number of quasiparticles.

As discussed in section 2.2.2, $I_D(eV_D = \Delta + \Delta_D)$ probes the total number of quasiparticles in the wire. A measurement of this quantity as a function of the injection current is shown in figure 3.2, where the data has been re-scaled by the junction resistance and normalized to a unit slope at high injection for J_1. The number of quasiparticles close to the injector (data from the detector J_1) has the following dependence on current: at low injection currents there is a rapid growth of the quasiparticle population, followed by a leveling off in the region $I_{inj} = 10 - 50$nA, after which there is again a linear dependence with a smaller slope than at low injection. The number of quasiparticles measured by J_2 and J_3 is smaller, in the beginning it has a concave shape and above $I_{inj} = 50$nA it also becomes linear. At high injection currents, when the energy dependence of the diffusion coefficient doesn't play such a big role anymore, as well as when the electron-electron time is finite (resulting in a pseudo-thermal distribution function), the number of quasiparticles is linear with the injection current. The same holds true for the other two detectors J_2 and J_3 (also in figure 3.2.

In this high injection regime the relation becomes $N_{QP} = k(x)I_{inj}$, where only the slope of the curve depends on the position. If we take the slope itself to be a measure of the number of quasiparticles present in the wire, and plot it versus the position of the detector, we find that it extrapolates to zero at the end of the wire (figure 3.3). Based on this we can safely argue that the quasiparticles relax to the equilibrium state by thermalization and recombination within the reservoirs at the end of the wire.

This model is only valid at high injection currents, and consequently high injection energies, when transport is linear and hence energy independent. The origin of the rapid increase

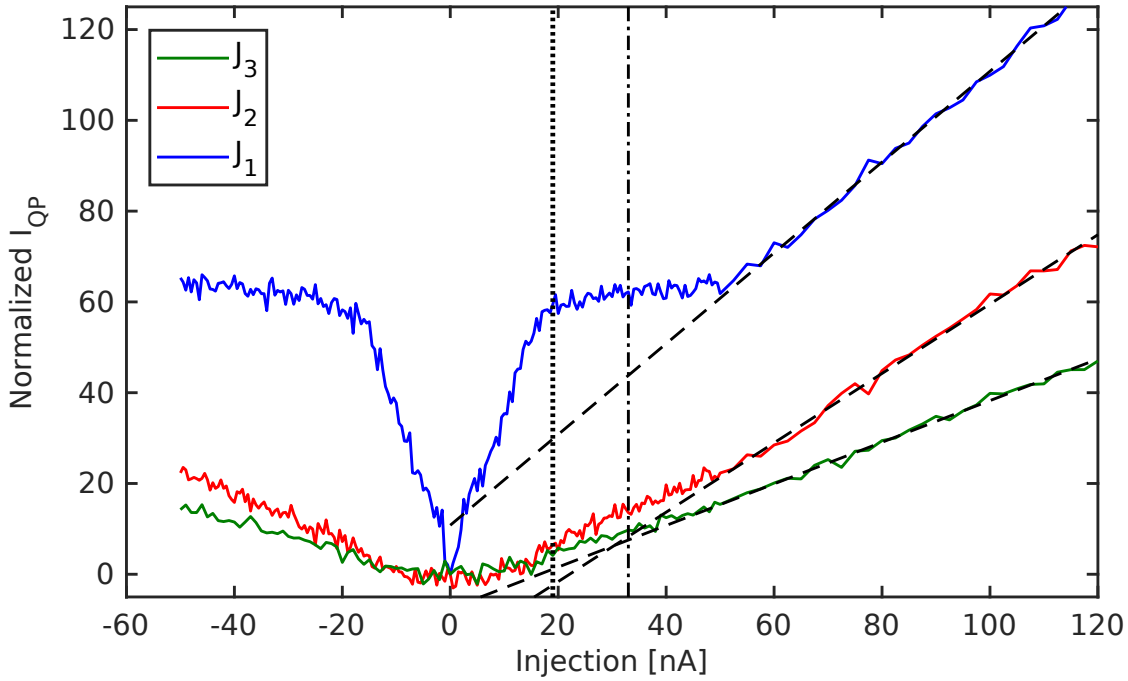

Figure 3.2: The number of quasiparticles measured by each of the detectors at $H = 0$. The data is normalized such that the linear, high injection, part of the J_1 trace have a unit slope. The black dashed lines are linear extrapolations to zero. The dotted vertical line indicates $eV_{inj} \approx 1.33\Delta_0$ and the dash-dot line indicates $eV_{inj} \approx 2\Delta_0$.

of the number of quasiparticles at low injection, as well as the following plateau, measured with J_1 will be discussed in detail in section 4.1.

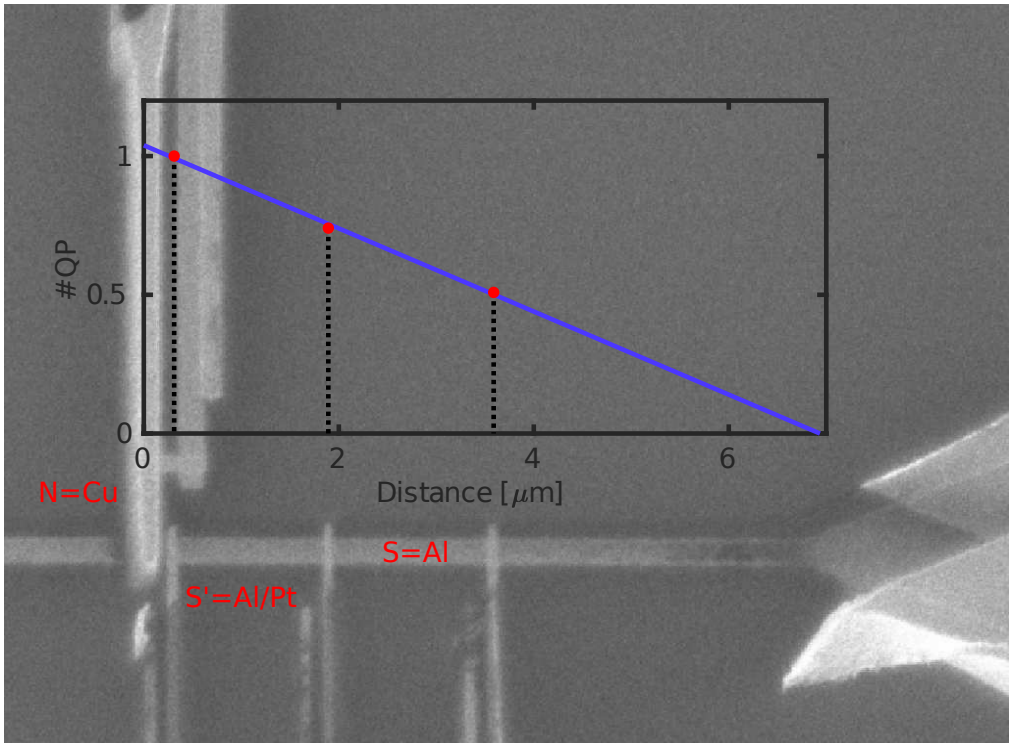

Figure 3.3: An SEM micrograph of the sample showing a wider view, as well as an inlay showing the linear decay of the number of quasiparticles as a function of space and its extrapolation to zero at the reservoir.

3.2 Spatially resolved gap suppression and self-consistency

The gap suppression $\delta\Delta(I_{inj}) = \Delta(I_{inj}) - \Delta_0$ was also measured as a function of the injection current for all three detectors (see figure 3.4). As predicted by the theory in section 1.6, the $\delta\Delta$ curve is reminiscent of the I_{QP} one (fig. 3.2). By plotting $\delta\Delta$ as a function of I_{QP}, and comparing it to 1.10, a difference between J_1 and the other two detectors can be observed (see figure 3.5): the traces for J_2 and J_3 collapse onto one curve while the J_1 trace is distinct.

The theory presented in the chapter 1, predicts that the distribution function induced by quasiparticle injection is a step-like function which extends up to $E = eV_{inj}$. This result was obtained under the assumption of negligible electron-electron interaction, which is applicable at low quasiparticle densities and short timescales. The electron-electron lengthscale is in the order of $l_{ee} = \sqrt{D\tau} \approx 1\mu$m [71, 72]. At distances larger than this one, which is the case for J_2 and J_3, the distribution function rapidly approaches a pseudo-thermal one. As $L_1 < l_{ee}$ the distribution function is better described by a step-like distribution function rather than a thermal one. One can then interpret figure 3.5, in analogy with figure 1.10, as evidence that at short distances away from the injection the superconductor is truly out-of-equilibrium (i.e. the distribution function f cannot be described by an effective temperature T^*). Additional spectroscopic evidence for this is presented in chapter 4.

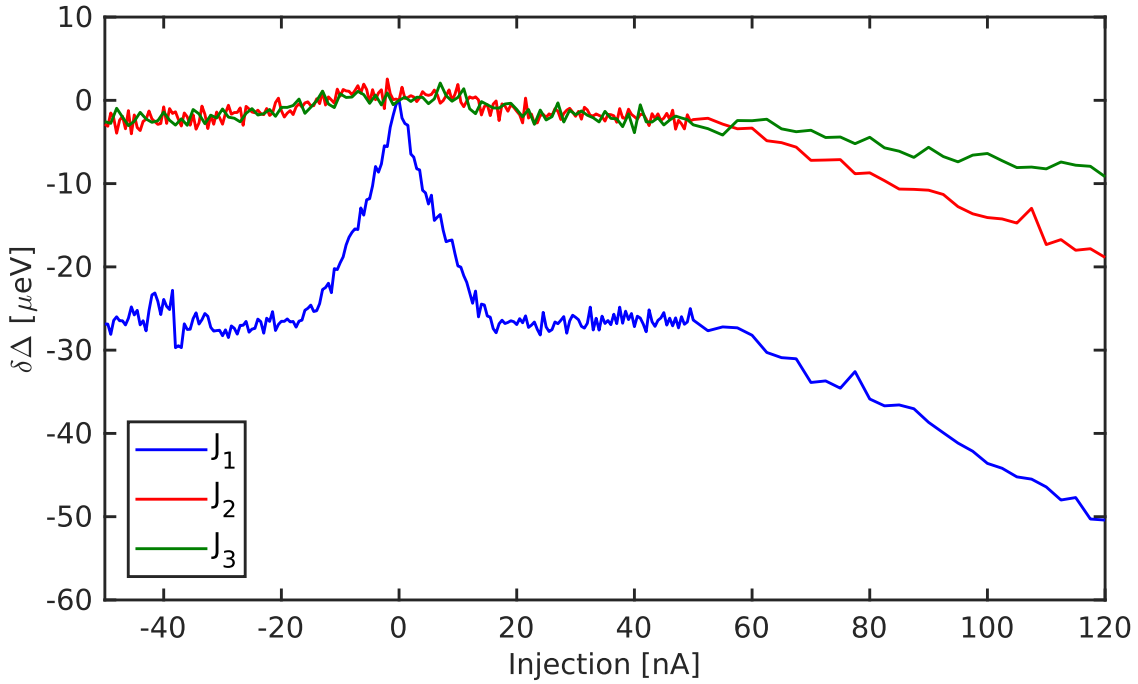

Figure 3.4: The gap suppression $\delta\Delta(I_{inj}) = \Delta(I_{inj}) - \Delta_0$ measured by each of the detectors at $H = 0$.

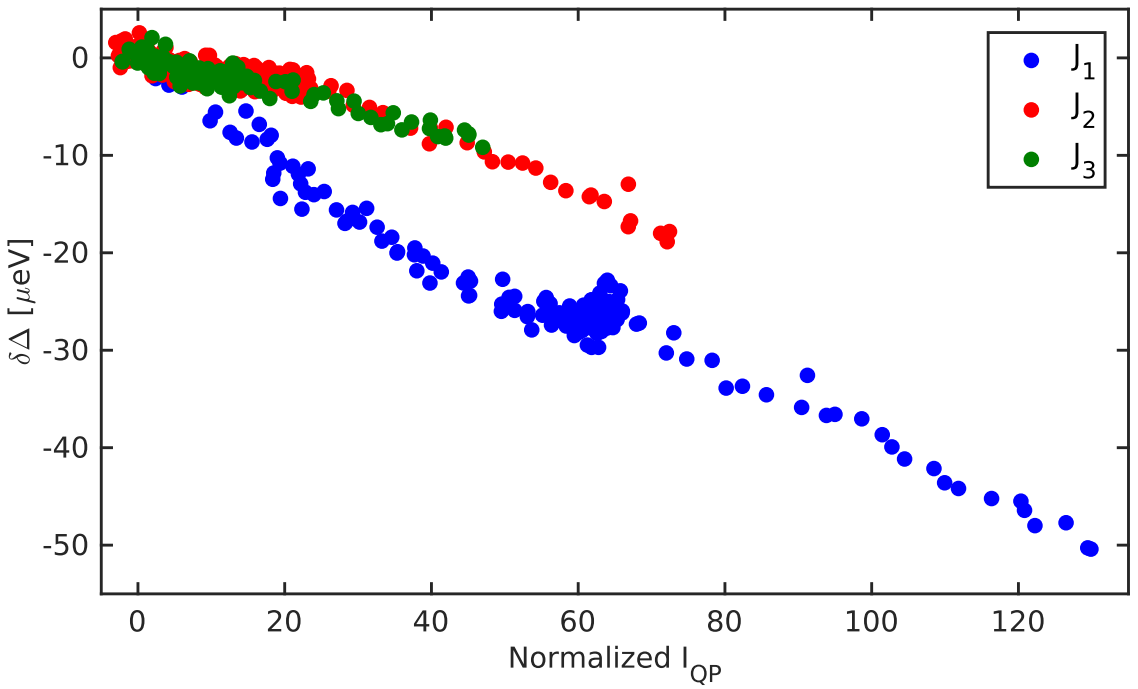

Figure 3.5: The gap suppression $\delta\Delta(I_{inj}) = \Delta(I_{inj}) - \Delta_0$ measured by each of the detectors at $H = 0$.

3.3 Field dependence of N_{QP} and Δ

The measurement of the gap Δ and the number of quasiparticles, up to the energy of $E = \Delta + \Delta_D$, can be carried out at finite magnetic fields as well. The results of these experiments are shown in figures 3.6 and 3.7, respectively.

In the limit of very low injection currents $I_{inj} < 10$nA, the same rapid increase of the number of quasiparticles, as well as the corresponding reduction of Δ is observed. However the initial slope as well as the value at which these quantities level off are field dependent. This can be understood in terms of the modified transport properties: as the magnetic field is increased the strength of the orbital depairing grows quadratically which results in the rounding of the DOS as well as the energy dependent diffusion constants (see figure 1.2). This increases the number of slow-moving quasiparticles close to the gap edge, and thus increases their effective lifetime. Additionally, as the DOS is Zeeman-split the number of available states at the spectroscopic gap edge $E \approx \Delta - \mu_B H$ is halved. Therefore a smaller number of quasiparticles can be injected in this range of injection currents and energies, which accounts for the lower "saturation threshold" seen in both figures.

At high injection currents $I_{inj} > 50$nA, when quasiparticles are injected at high energies where D_{T3}, D_{L3} and N_- are zero, the f_L mode is dominant and we recover the same linear behavior, with roughly the same slope, at all magnetic fields.

In between these two limiting cases the behavior at different fields is qualitatively different. At $H = 0$T there is an almost linear increase of N_{QP} / decrease of Δ. When the Zeeman splitting becomes larger than the temperature $2\mu_B H > 3.5 k_B T$, a slight reduction of the measured N_{QP} is observed. As discussed in section 2.2.2 at the detector voltage of $eV = \Delta + \Delta_D$ the measured current is directly proportional to the number of electron-like quasiparticles only if there are no quasiparticles below $E = -\Delta - 2\Delta_D$. Otherwise, the hole-like excitations can reduce the tunneling current. In practice this is a concern only at high fields where both Δ and Δ_D are sufficiently suppressed. While this might contribute to the reduction of the measured N_{QP}, the corresponding feature can be observed in the measurement of Δ which does not have such a sharp cut-off - see figure 3.7.

This behavior is not fully understood, it has been observed in several devices and only appears when the injector junction is relatively resistive $R_{inj} > 10$kΩ. It is unlikely that this is a result of quasiparticle-quasiparticle recombination processes as we believe that this process is much slower than the diffusion to the thermal reservoir at the end of the wire (as discussed in section 3.1). An argument can be made that this is due to the electron-electron interaction which relaxes the distribution function to a pseudo-thermal one. As the number of quasiparticles is increased, so is the rate for these scattering processes, but as this process conserves energy and is energy-nonlocal it is strongly dependent on the distribution function. If there are only (or predominantly) quasiparticles at the gap edge Δ, the scattering rate will be small as none of them can scatter to energies below the gap edge. In section 4.1 it will be argued that, at $H = 0$T, such a pseudo-thermal distribution function describes the nonequilibrium state measured far away from the injector, while close to the injector the distribution function a shape such as the one shown in figure 1.8. At high magnetic fields for the same injection current QPs are injected in a larger energy range, which should lead to an increase of the electron-electron scattering and thus a faster pseudo-thermalization. At the time of writing there is not enough data available to make a quantitative analysis of the effective electron-electron scattering rates. At the end of section 4.1 an experiment is

proposed which could address this question.

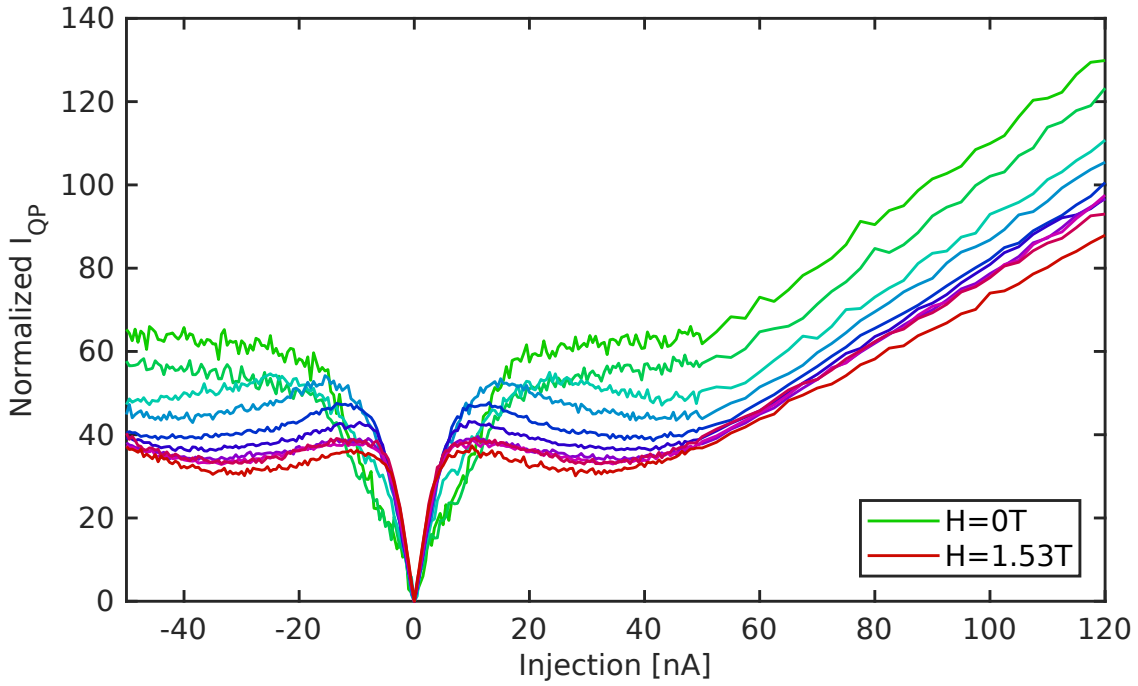

Figure 3.6: The number of quasiparticles measured at J_1 as a function of the applied magnetic field (10 equidistant steps from $H = 1.53$T to $H = 0$T) and the injection current.

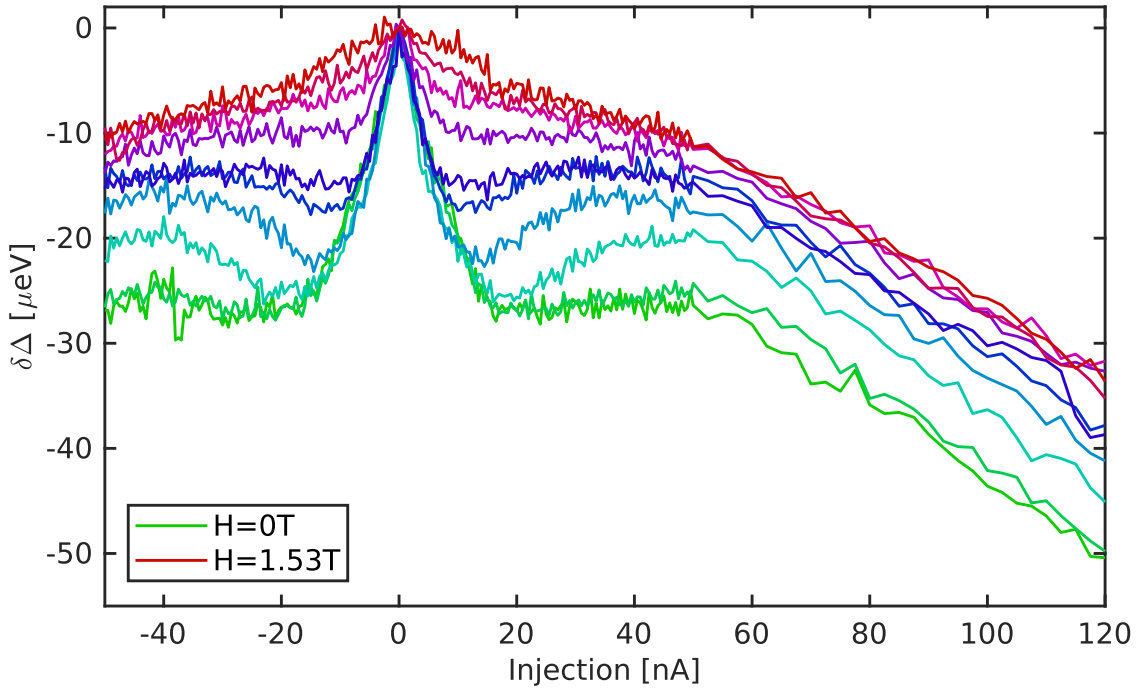

Figure 3.7: The gap suppression $\delta\Delta(I_{inj}) = \Delta(I_{inj}) - \Delta_0$ measured at J_1 as a function of the applied magnetic field (10 equidistant steps from $H = 1.53$T to $H = 0$T) and the injection current.

Chapter 4

Spectroscopic measurements

In this chapter the results of the spectroscopic study of the out-of-equilibrium state, induced by current injection through an NIS junction, will be presented. The first section, 4.1, will show the results of the zero field experiments which demonstrate that close to the injector junction the distribution function cannot be described by an effective temperature T^* or an effective chemical potential μ^*, or a combination of the two, and is thus truly out-of-equilibrium. At the same time the results from the further detectors show a distribution function which is better described by an effective temperature because $L_{J_2,J_3} > \sqrt{D\tau_{e-e}}$. The second section, 4.2, will show that at finite magnetic fields the distribution function becomes spin dependent. Evidence for the presence of the spin-energy mode f_{L3} will be presented through the observation of the energy-localized charge imbalance. At the end, in section 4.3, a comparison of this charge imbalance with the previously observed charge mode f_T is given.

4.1 Spectroscopy of injected quasiparticles at $H = 0\mathrm{T}$

As shown in section 2.2.2 the SIS detector can be used as a spectroscopic probe: in the sub-gap region ($eV < \Delta + \Delta_D$) the differential conductance signal $G(eV = E - \Delta_D)$ is proportional to the number of quasiparticles at $N_{QP}(E) = N_+(E)f(E)$. By measuring the $G(V)$ spectrum as a function of current injection one can then obtain spectroscopic information about the out-of-equilibrium state.

At zero magnetic field the Josephson coupling between the detector and the superconductor is non-negligible which results in a finite conductance even at equilibrium, as shown by figure 2.5. Aside from the zero bias peak and the strongest resonances which are marked in said figure, there is also a series of smaller ones resulting in a nontrivial background. As the signal associated with the out-of-equilibrium state is also rather small, carrying out a deconvolution procedure to obtain the raw distribution function is challenging. Because of this the discussion will be focused mainly on the number of quasiparticles at the gap edge Δ.

Figure 4.1 shows the $G(V)$ curve of the closest detector J_1 as a function of the current through the injector junction. At finite injection currents a peak becomes visible at $V \approx 70\mu\mathrm{V}$, which corresponds to $eV = \Delta - \Delta_D$. It shows up as soon as the injection voltage V_{inj} reaches the spectroscopic gap of the superconductor (the red trace in fig. 4.1), and steadily grows as the injection voltage / current is increased up to $eV_{inj} \approx 2\Delta$ (the purple, blue and green traces in fig. 4.1), without changing its width (FWHM $\approx 16\mu\mathrm{V}$). This implies that the quasiparticles are well localized in energy fairly close to $E = \Delta$. Only when the injection

voltage goes above $V_{inj} > 4\Delta$ a substantial number of quasiparticles does show up at higher energies (see the dashed black trace in fig. 4.1). This can be understood in terms of the distribution functions calculated based on the theory from chapter 1, in particular the shape of the distribution function shown in figure 1.8, where most of the quasiparticles are found near the gap edge due to the peaks in the distribution function as well as the DOS. These quasiparticles are accumulated there because of the vanishingly small mobility at the gap edge (see figure 1.2), and thus a large lifetime set by the diffusion.

To explain a QP peak of $\approx 0.35 G_{NN}$ at $eV_{det} = \Delta - \Delta_D \approx 70\mu$eV, with Δ and Δ_D as in the experiment, requires an effective temperature $T^* \approx 1.1$K (the detector is assumed to be in equilibrium) - see the dotted blue trace in figure 4.1. Additionally due to the long exponential tail of the Fermi-Dirac distribution function, such a model cannot reproduce the relatively sharp cutoff in energy/voltage at which the quasiparticles are detected.

The large accumulation of quasiparticles at the gap edge also suppresses Δ efficiently, as the anomalous part of the Green's function is peaked at the gap edge, resulting in the reduction observed in figure 3.4.

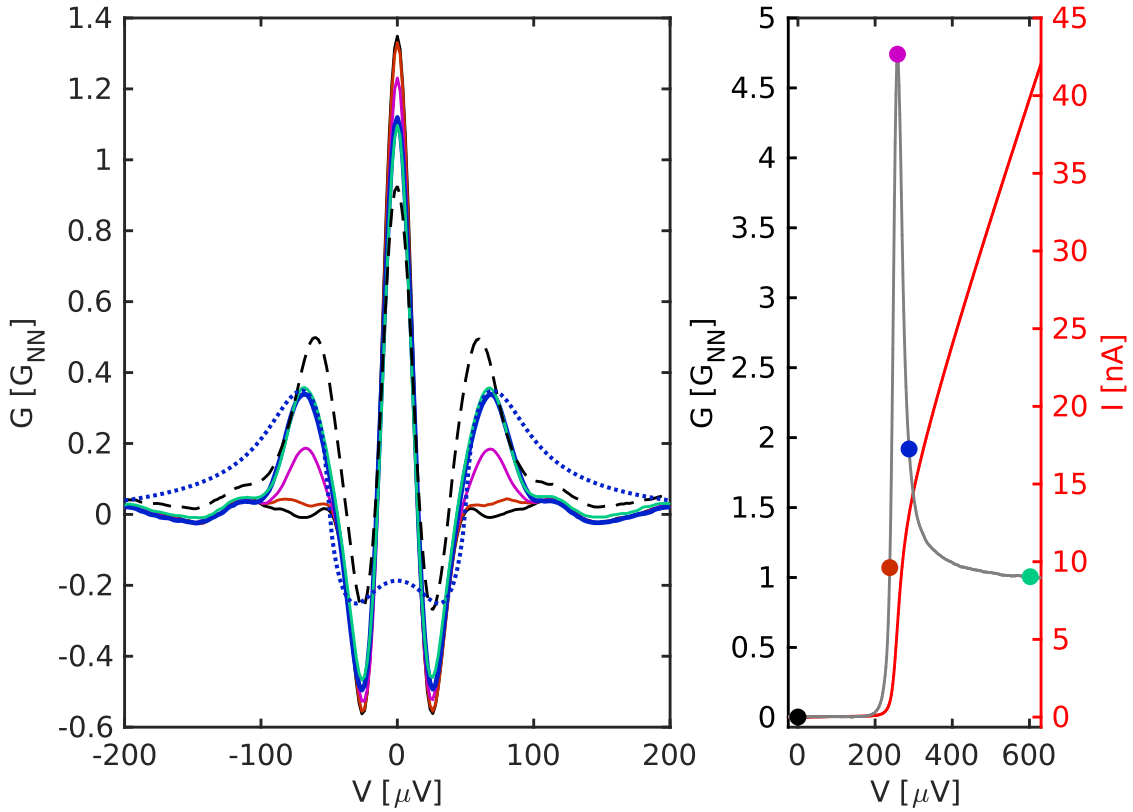

Figure 4.1: Left: the measured sub-gap $G(V)$ curve of detector J_1 as a function of the injection current ($H = 0$T). The full black trace is the equilibrium one ($I_{inj} = 0$nA), while the other ones are at finite currents. Right: the corresponding $G(V)$ curve (left scale) and the $I(V)$ curve (right scale) of the NIS injector junction. On top of the $G(V)$ curve there are several markers which correspond to the different detector traces shown in the left panel (the traces are color-coded). The dashed black curve shown in the left panel corresponds to $I_{inj} = 120$nA. The dotted blue curve is an effective temperature fit of the solid blue trace with $T^* = 1.1$K.

At higher energies only a comparatively small step, whose height is set by the normal state diffusion and the length of the wire, is found, which together with the flat DOS corresponds to a much smaller QP density. This step extends up to $E = V_{inj}$, and can be detected as a contribution in the $G(V)$ curve at $eV_{det} = eV_{inj} - \Delta_D$. This implies that the $I(V)$ curve of the injector is imprinted into the $G(V)$ curve of the detector as a threshold for the detection of nonequilibrium quasiparticles. To highlight this, figure 4.2 shows a 3D map of the detector conductance $G(V)$ in the sub-gap region, superimposed with the injector $I(V)$ curve offset by the detector gap. An increase of the detection signal at V_{det} can be observed as soon as the injection voltage exceeds $eV_{det} = eV_{inj} - \Delta_D$, demonstrating unequivocally that the system is driven truly out-of-equilibrium by quasiparticle injection (i.e. the distribution function is not a thermal one).

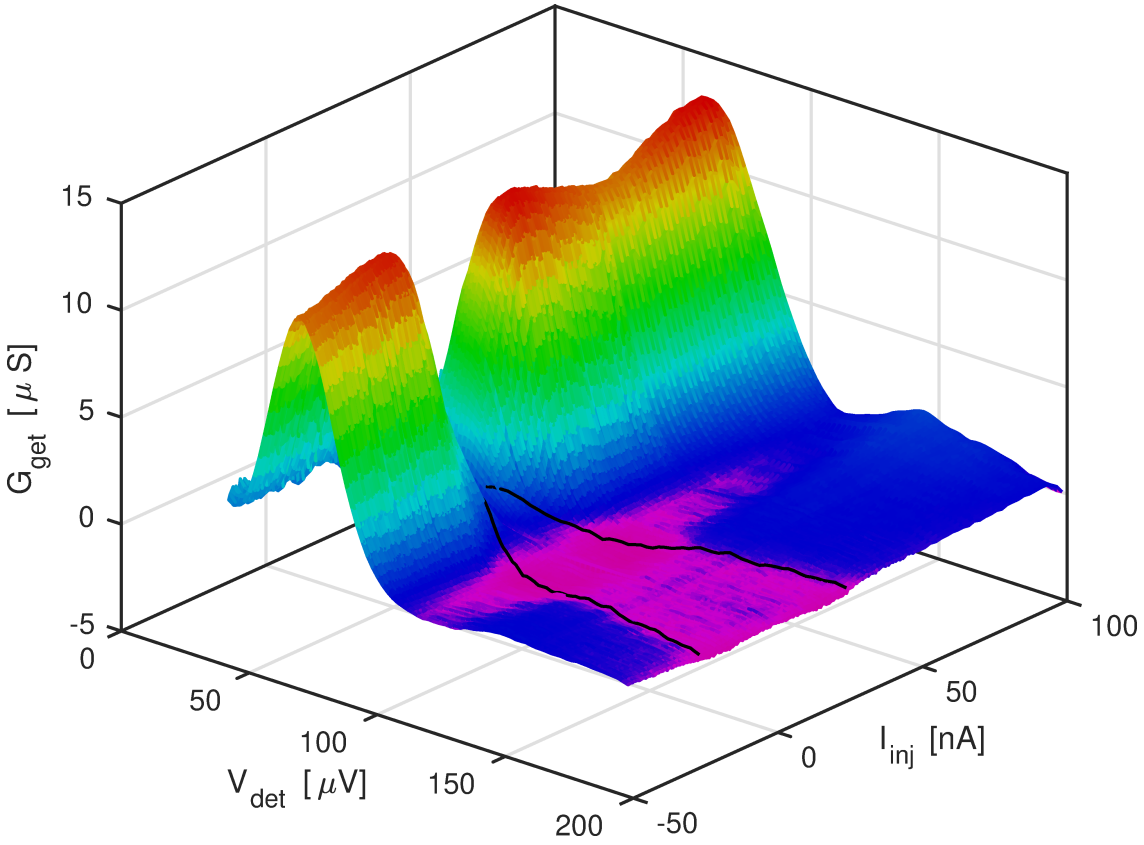

Figure 4.2: The detector $G(V)$ (at $H = 0$T) curve close to $eV_{det} = |\Delta - \Delta_D|$ as a function of the injection current. The zero injection curve has been subtracted from the trace to remove the Josephson background. The black curve shown on top is the $I(V$ curve of the injector junction. The equilibrium $G(V)$ trace was subtracted to remove the Josephson background and the color scale was chosen to highlight the step at $eV_{det} = eV_{inj} - \Delta_D$.

This is in contrast with the behavior observed at the other two detectors J_2 and J_3 shown in figure 4.3. At these distances the peak at $eV = \Delta - \Delta_D$ is still present but is much less prominent, and at all injection currents which show an increased number of QPs the out-of-equilibrium population cannot be confined to a finite energy/voltage range. This is more in line with a pseudo-thermal distribution function with a long (exponentially decaying) tail, in which a cut-off energy is not well defined.

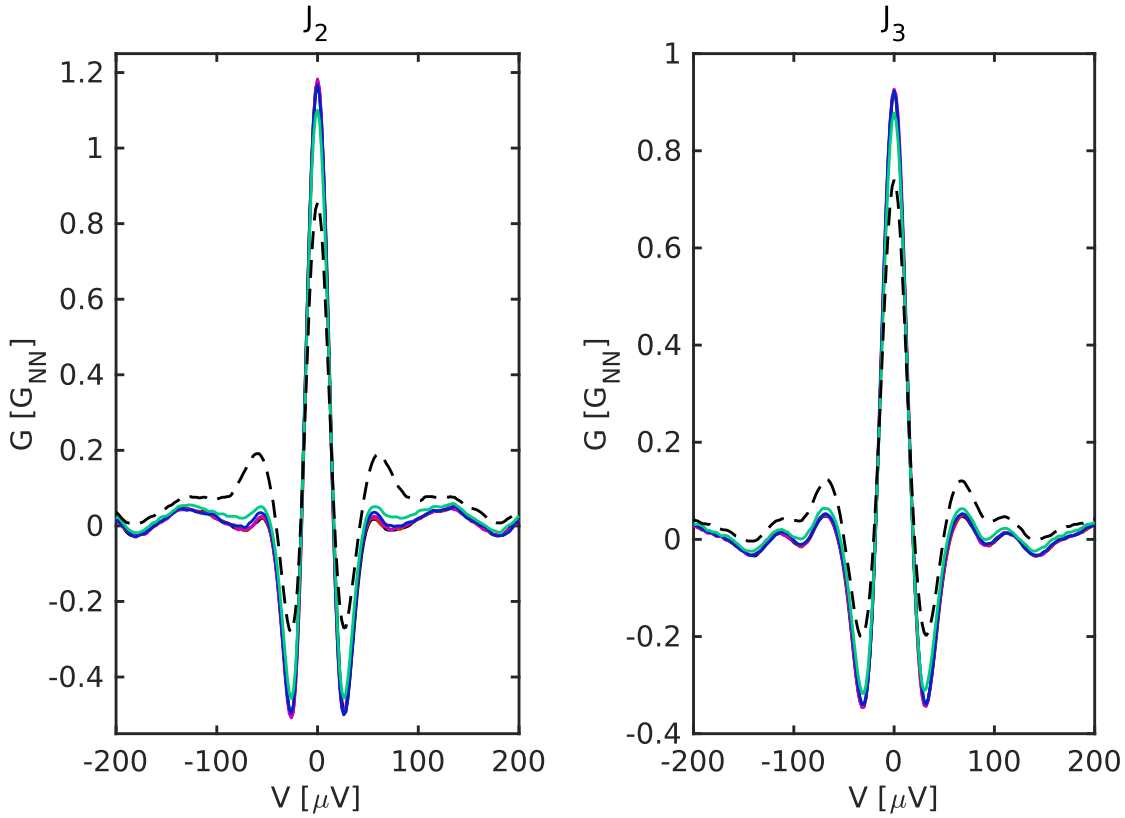

Figure 4.3: The sub-gap $G(V)$ curve of detector J_2 (left) and detector J_3 (right) as a function of the injection current ($H = 0$T). The traces are color coded and correspond to the same injection currents as in figure 4.1.

To show this in a clearer way the following analysis can be conducted: the out-of-equilibrium contribution to the peak at $eV = \Delta - \Delta_D$ can be integrated in a width corresponding to its FWHM, which measures only the quasiparticles close to the gap edge. This can then be compared to the total number of quasiparticles, and the ratio and/or difference between the two determines whether the excitations are localized in energy or not. This is shown in figure 4.4 for all three detectors. The two traces from J_1 are identical up to $I_{inj} \approx 20$nA, which corresponds to $V_{inj} \approx 1.4\Delta_0$, and separate after that. Even at the highest injection shown in the figure more than 75% of the quasiparticles remain in the vicinity of the gap edge. The J_2 and J_3 traces, on the other hand, show a large number of quasiparticles at higher energies, roughly 50% of the total. Again this can be understood in terms of a pseudo-thermal distribution function with a long tail.

The out-of-equilibrium distribution function can be calculated based on the formalism presented in section 1, including both the f_L and the f_T modes. Following this, a simulation of the SIS conductance traces can be calculated using the standard tunneling approach. A comparison of the $G(V)$ peak height at $eV = \Delta - \Delta_D$ between the experiment and the calculation is shown in figure 4.5. For the closest detector J_1 the theory and the experiment show excellent agreement for low injection currents ($I_{inj} < 10$nA). The theory predicts a saturation of the trace, because no interactions are included in the model, and thus the number of quasiparticles at low energies is not dependent on the number of quasiparticles injected at higher energies. The discrepancy between the two traces above $I_{inj} > 50$nA,

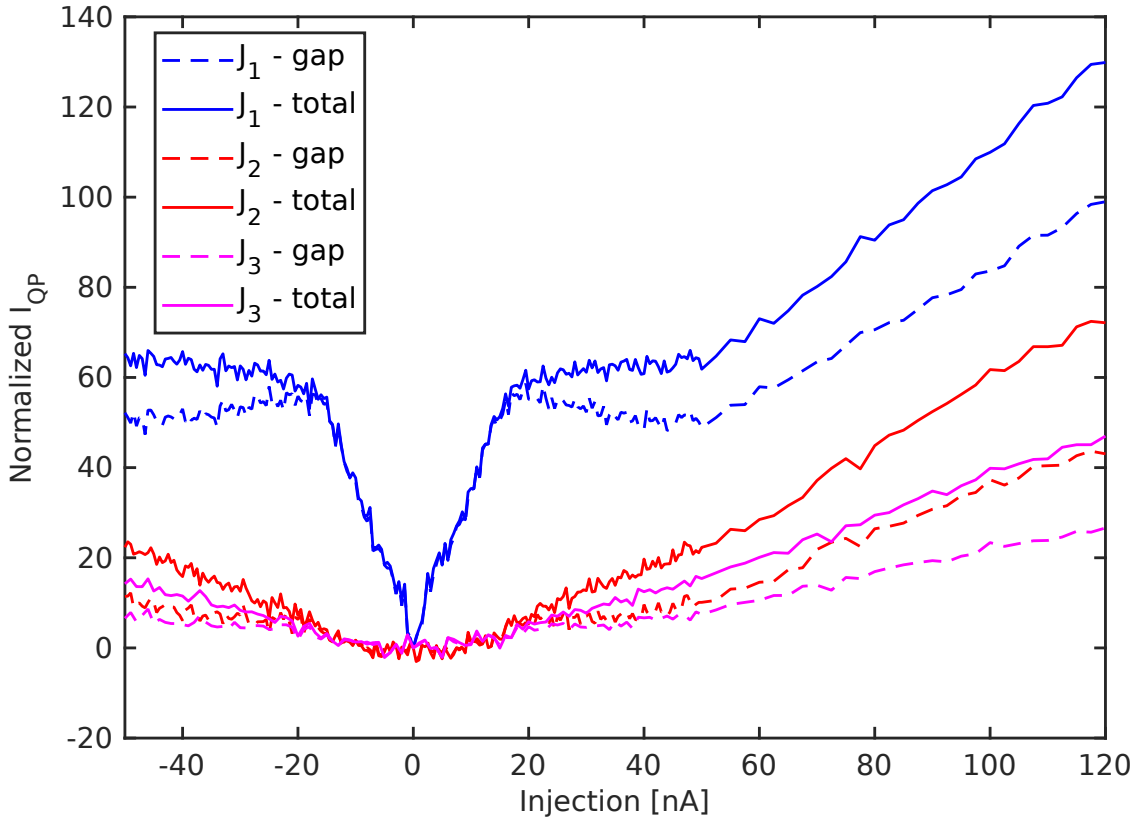

Figure 4.4: The total number of quasiparticles measured with the detectors (full traces) and the number of quasiparticles close to superconducting gap Δ ($40\mu\text{V} < V < 100\mu\text{V}$, dashed traces) for all three detectors as a function of the injection current. The traces are normalized such that the linear high injection part of the J_1 trace has a slope of unity.

i.e. the increase of the experimental signal, can then be interpreted as an effect of pseudo-thermalization at high quasiparticle densities, as the electron-electron interaction rate is no longer negligible to the injection and relaxation rates: the effect of the electron-electron interaction is to drive the distribution function towards a thermal one, giving rise to an exponential tail and reducing the number of quasiparticles at the gap edge. The slight decrease of the experimental signal in the range $10\text{nA} < I_{inj} < 50\text{nA}$ could, in principle, be a result of the non-locality in energy of the detection scheme: as shown in figure 2.6 the $\partial N_D(E)/\partial V$ is strongly peaked at the spectroscopic gap edge, but above the coherence peak it also has a small negative part. When quasiparticles are injected in this region of energies the observed signal should be reduced. This is, however, difficult to reproduce as it is strongly dependent on the spectral properties of the detector, a small pair breaking contribution or finite lifetime could in principle successfully model the effect.

The two other traces, from J_2 and J_3 do not match the theoretical prediction. In the non-interacting model without quasiparticle recombination the spatial evolution of the distribution function is roughly equivalent to a rescaling by a factor of $1 - \frac{x}{L}$ where x is the position of the detector and L the distance to the thermal reservoir. This preserves the large peak in the distribution function at $E = \Delta$, which is clearly not present in the experimental data. It is important to note that this behavior is not dependent on the values of the parameters used for the calculation, as the linear decay of the f_L mode is a general feature of the

model.

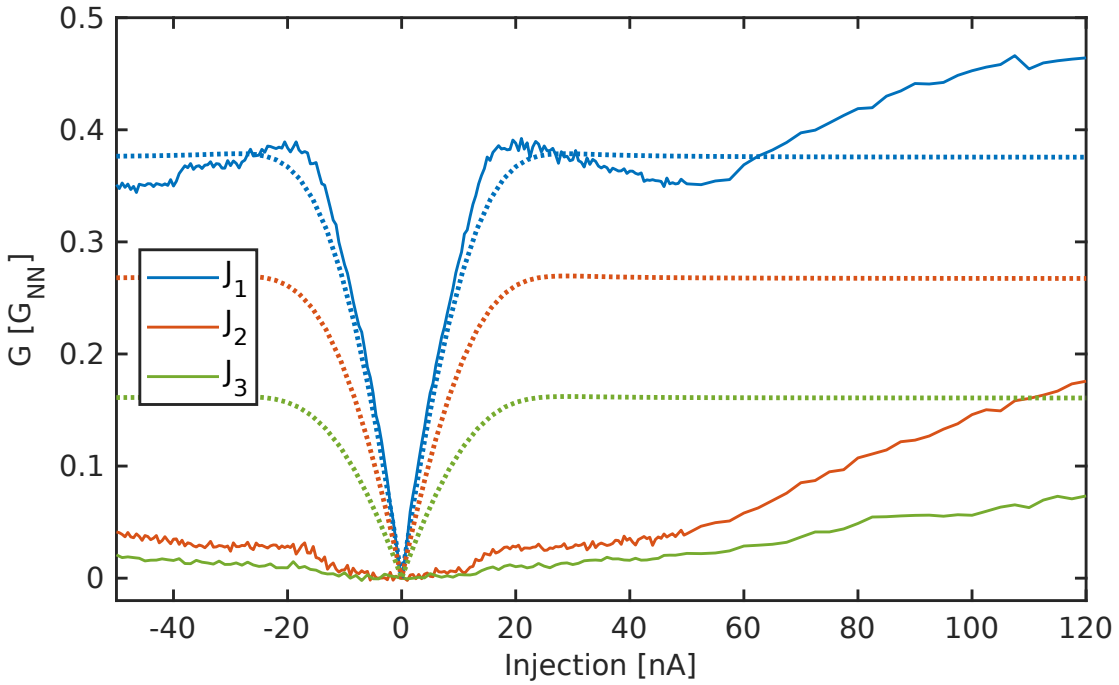

Figure 4.5: The peak in the $G(V)$ curves at $eV = \Delta - \Delta_D$ from the experiment (full lines) as well as the theoretical ones (dashed lines) as a function of the injection current for all three detectors.

All of the above leads to a conclusion that close to the injection junction the superconductor is is truly out-of-equilibrium (i.e. it cannot be described by an effective temperature), and the distribution function is sharply peaked close to the spectroscopic gap. At larger distances, however, the diffusion time approaches the electron-electron time and the distribution functions reach a pseudo-thermal state.

As the interaction mediated finite quasiparticle lifetime induces a Dynes(-like) density of states [73, 74], the measurement of the (energy-resolved) QP lifetime can be performed in an experiment similar to this one, but with a normal-metal detector. As the phonon temperature of the (rest of the) system is not modified by current injection into the superconductor a second high resistance junction can be used to probe the DOS and thus determine the scattering rates through deconvolution.

4.2 Spectroscopy of injected quasiparticles at $H = 1\mathrm{T}$

The same set of measurements as presented in the previous section can be performed at nonzero magnetic fields. The fundamental difference is that at finite fields the distribution functions for the two spin species will not necessarily be the same: when the injector is biased such that $\Delta - \mu_B H < V_{inj} < \Delta + \mu_B H$ the DOS of the superconductor behaves as an almost perfect spin filter and quasiparticles of one spin species are preferentially injected/excited. On top of this, as the detector electrode is not spin split (due to the Pt monolayer on top) one should expect to see two peaks in the detector $G(V)$, the first at $eV = \Delta - \mu_B H - \Delta_D$ and the other one at $eV = \Delta + \mu_B H - \Delta_D$ which probe the two spin states separately, allowing

for a spin sensitive spectroscopic study without the need for a spin polarized barrier. Figure 4.6 shows the $G(V)$ curve of the detector for $I_{inj} = 5$nA, which corresponds to the maximum spin polarized current at higher fields, as well as $I_{inj} = 40$nA (dashed traces), as a function of the applied magnetic field. For clarity the traces are offset such that $eV_{det} = \Delta - \Delta_D$ is at $V_{det} = 0$. At the higher of the two currents, when both spin up and spin down electrons are injected, two peaks are visible, separated by $2\mu_B H$ as indicated by the vertical black lines.

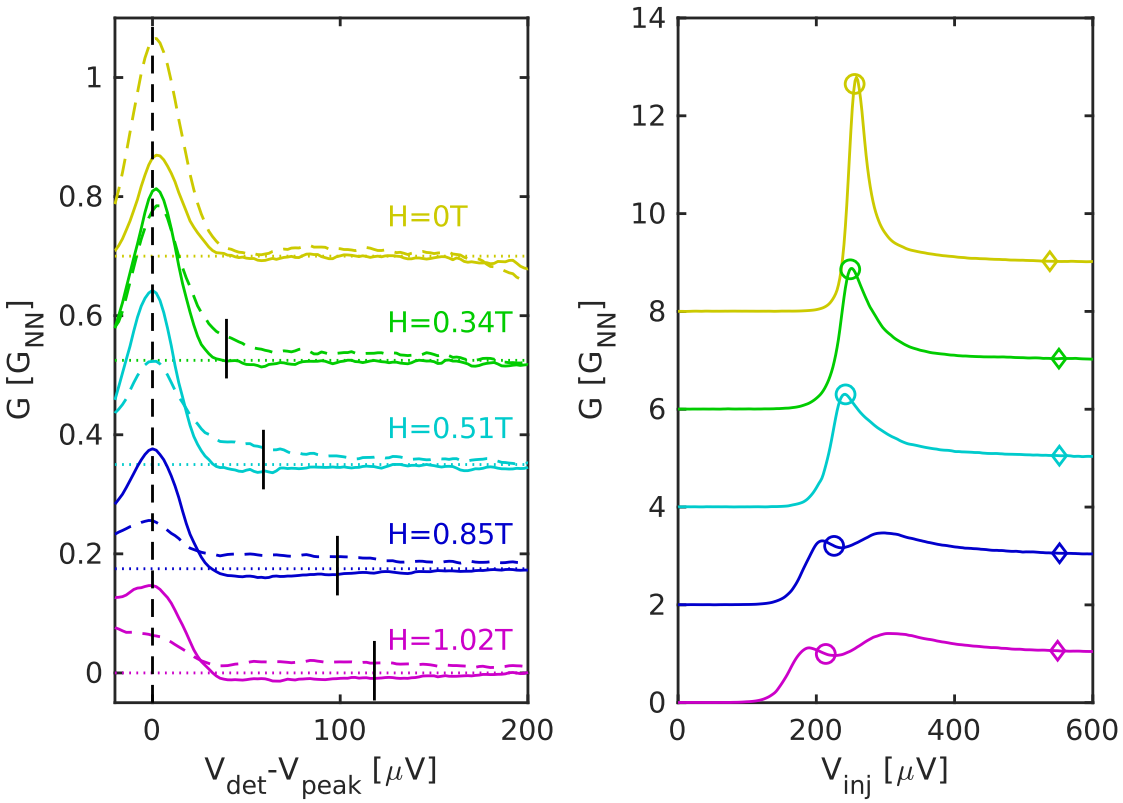

Figure 4.6: The detector $G(V)$ at $I_{inj} = 40$nA (dashed) and $I_{inj} = 5$nA (solid) for different fields, showing the detection of both spin down and spin up quasiparticles. The traces are offset such that the (dominant) spin down peak is at $V_{det} = 0$ and the $G(V)$ at $I_{inj} = 0$ is subtracted. The right panel shows the injector $G(V)$ curves at the same field as on the left. The circle and the diamond show the injection voltage at which $I_{inj}(V_{inj}) = 5$nA and $I_{inj}(V_{inj}) = 40$nA, respectively.

The rest of the measurements presented in this section are performed at a magnetic field of $H = 1$T as this field minimizes the Josephson contribution to the $G(V)$ curve (see figure 2.5).

Figure 4.7 shows the sub-gap $G(V)$ curves of J_1 as a function of the injection current in the same manner as at $H = 0$T (analogous to figure 4.1). When the injector voltage is in the range $\Delta - \mu_B H < V_{inj} < \Delta + \mu_B H$ only spin down quasiparticles are injected (blue and green traces in fig. 4.7), and the dominant out-of-equilibrium contribution shows up as two peaks at $V \approx \pm 40\mu$V which correspond to spin down electron-like and hole-like excitations in the superconductor. The Josephson component, observed as the zero-bias peak, is also enhanced compared to the equilibrium trace (black trace in fig. 4.7). As the voltage across the NIS injection junction goes from zero to above the spectroscopic gap the

effective junction resistance changes by a factor of ≈ 250 (goes from $R_{inj}(V=0) \approx 3.25\text{M}\Omega$ to $R_{inj}(\Delta - \mu_B H) \approx 13\text{k}\Omega$). This changes the electromagnetic environment seen by the SIS detector junction drastically and can lead to an increase of the Josephson current [33]. When the detector is biased to a higher voltage/current, electrons of the other spin can also tunnel into the superconductor (red and purple traces in fig. 4.7), and quasiparticles of the other spin are detected as a $G(V)$ peak at $V \approx 150\mu\text{V}$ (the separation between the two is $\approx 2\mu_B H$). These results, as at $H = 0\text{T}$, show that quasiparticles injected at low energies do not scatter to higher energies close to the injector. The other feature which can be observed when spin down quasiparticles are preferentially injected into the superconductor is that an odd component in the $G(V)$ appears: the peak at positive voltages is slightly higher than the one at negative detection voltages. The odd parity of the signal, coupled to the fact that the sign of the asymmetry is reversed when a negative bias current is applied, implies that a finite charge imbalance is induced in the superconducting wire.

The classification of the different modes, presented in chapter 1, shows that a charge imbalance can be associated with either the f_T or the f_{L3} mode. The charge imbalance related to the f_{L3} mode mode is confined to the region of energies where $N_- \neq 0$, that is close to the gap edge of spin down quasiparticles, relaxes within the spin-flip length, and is not monotonically suppressed by the magnetic field (for the details see section 1.4). On the other hand, f_T is dominant at high energies and is monotonically suppressed by the magnetic field due to the pair breaking of the orbital currents. These differences allow one to determine the origin of the charge imbalance.

The same measurements as shown in figure 4.7 can be performed for the other two detectors, which are shown in figure 4.8. Unfortunately, due to slightly different values of the detector gap Δ_D the spin down peaks are not individually observable, but are merged with the Josephson zero-bias peak. Nevertheless, it is clear that there is no odd component in these traces. As the distance between these detectors and the injection junction is larger than $L_{SO} \approx 240\text{nm}$, this is consistent with the f_{L3} mode as the origin of the charge imbalance observed with J_1.

To verify this claim the other two discriminative properties of the f_{L3} need to be utilized - the confinement of the signal in the range $\Delta - \mu_B H < \Delta < \Delta + \mu_B H$ and the characteristic field dependence. To this end a very high resolution measurement of the sub-gap $G(V)$ was performed as a function of the injection current using the closest detector J_1. For *visual clarity* the Josephson contribution was subtracted from the traces in the following way: the $G(V)$ trace can be modeled as a sum of 5 Gaussian peaks, one at $V = 0$ representing the Josephson component, while the others are located at $\pm\tilde{V}$ and $\pm(\tilde{V} + 2\mu_B H)$ representing the spin down and spin up electron-like quasiparticles (with the plus sign) and the spin down and spin up hole like quasiparticles (with the minus sign). Using $\tilde{V}$, the heights and widths of these peaks as fitting parameters, the data can be reproduced (see figure 4.9), and the Josephson contribution can be subtracted.

The result of this procedure is reported in figure 4.10, which shows the same features as figure 4.7: when spin down electrons are injected only spin down quasiparticles are detected (as peaks at $eV = \Delta - \mu_B H - \Delta_D$), and at higher injections quasiparticles of both spins are present. As at $H = 0\text{T}$, the colormap shows a dark blue "wing shaped" basin below $I_{inj} \approx 25\text{nA}$, which is an imprint of the injector $V(I)$ curve offset by the detector gap $V_{threshold} = V_{inj}(I_{inj}) - \Delta_D/e$ (the black dashed trace). This again verifies that the distribution function is truly out-of-equilibrium and that it has the step-like shape (with a peak at the

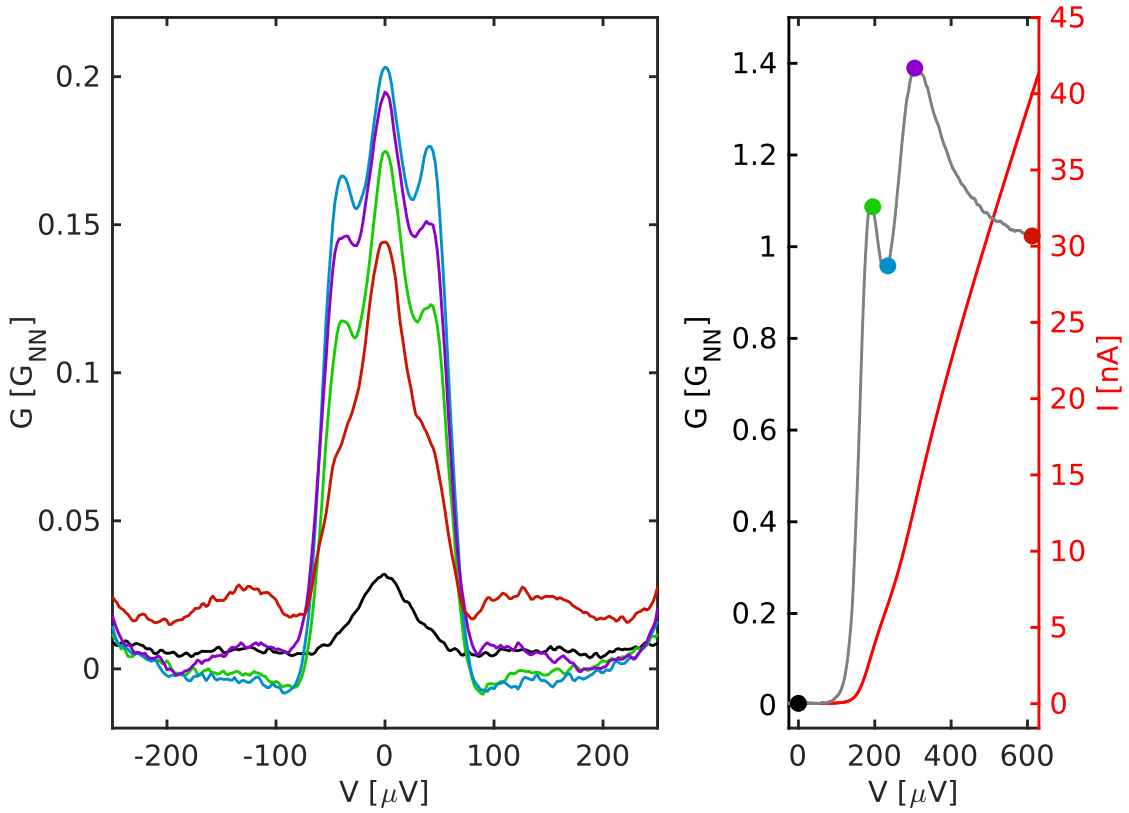

Figure 4.7: Left: the sub-gap $G(V)$ curve of detector J_1 as a function of the injection current ($H = 1$T). The full black trace is the equilibrium one ($I_{inj} = 0$nA), while the other ones are at finite currents. Right: the corresponding $G(V)$ curve (left scale) and the $I(V)$ curve (right scale) of the NIS injector junction. On top of the $G(V)$ curve there are several markers which correspond to the different detector traces shown in the left panel (the traces are color-coded).

gap edge) up to eV_{inj}. The panel on the right of this figure shows the line cuts made along the dashed lines at $eV = \Delta - \mu_B H - \Delta_D$. These two traces, or rather the difference thereof, show the evolution of the odd component of the $G(V)$ curve, which attains a maximum at the maximal 100% spin polarized injection current.

Using the theory presented in chapter 1, the full out-of-equilibrium distribution function, including all four modes, can be calculated. With a precise estimation of the detector parameters one can calculate the $G(V)$ theoretical curve, which is presented in the same way (e.g. as a colormap including the line cuts) in figure 4.11. At low injection currents, where the electron-electron interaction is negligible the theory reproduces the experimental data well. At higher injections the theory predicts the same prominence for the spin down and spin up peaks, which is not the case in the experiment because of the quasiparticle interaction. Unlike at $H = 0$T, where one looses all features above the coherence peak, at finite fields one can also probe the coherence peak, as well as the associated quasiparticles, at $E = \Delta + \mu_B H$, which could in principle be used to gauge the strength of the electron-electron interaction. However, as both the DOS and the distribution function are probed simultaneously, this is a nontrivial problem. The falloff in the line cuts is present in both the theory and the experiment and is a result of the nonlocality in energy of the detection scheme, as a consequence of the high pair breaking induced broadening of the detector DOS. As a result of the same

effect, the odd component of the $G(eV = \Delta - \mu_B H - \Delta_D)$ is suppressed at higher injection currents.

To verify that the charge imbalance is localized in the energy range $\Delta - \mu_B H < V_{inj} < \Delta + \mu_B H$, the odd component of the $G(V)$ colorplot is shown in the left panel of figure 4.12. As expected for the f_{L3}, mode the charge imbalance is indeed localized in the region where $N_- \neq 0$, and is dominantly observable at the voltage corresponding to the spectroscopic gap edge $\Delta - \mu_B H$. The right panel shows the odd component of the line cuts at the quasiparticle peak. The odd component is absent at zero magnetic field which is consistent with the charge imbalance associated with the f_{L3} mode, and shows up only when $2\mu_B H > 3.5 k_B T$, that is when spin-polarized quasiparticles can be excited by injecting a current through an NIS junction.

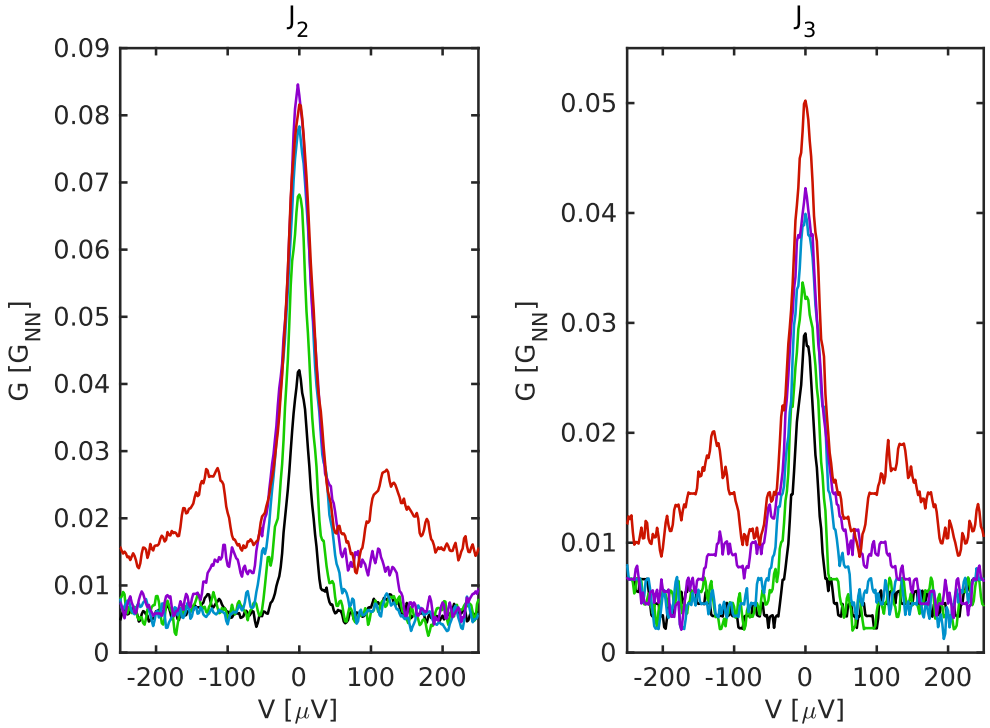

Figure 4.8: The sub-gap $G(V)$ curve of detector J_2 (left) and detector J_3 (right) as a function of the injection current ($H = 1$T). The traces are color coded and correspond to the same injection currents as in 4.7.

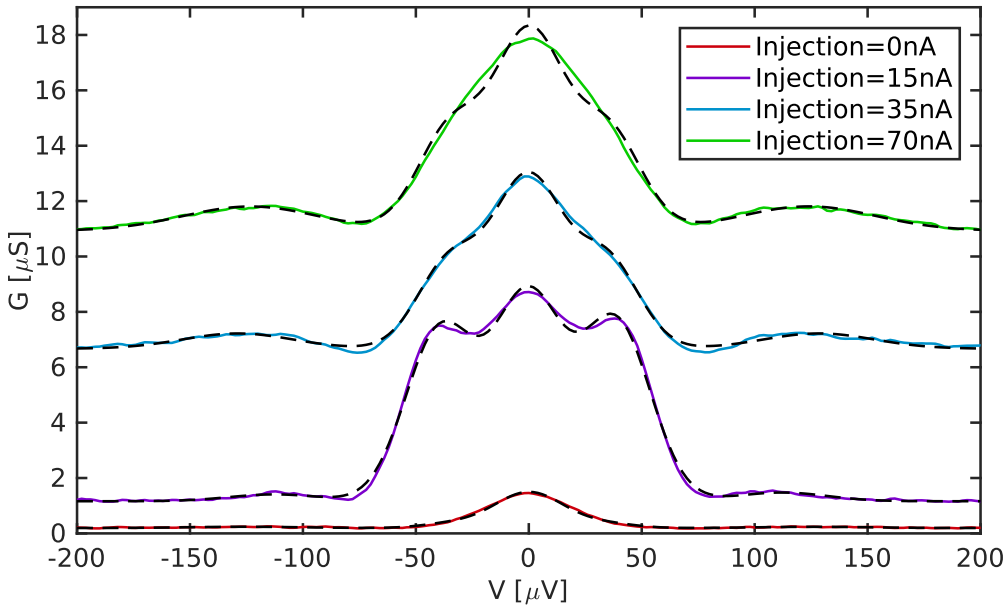

Figure 4.9: The sub-gap $G(V)$ of the J_1 detector at several injection currents ($H = 1$T) (full lines), as well as the sum of Gaussian peaks used to model the data for the subtraction of the Josephson contribution.

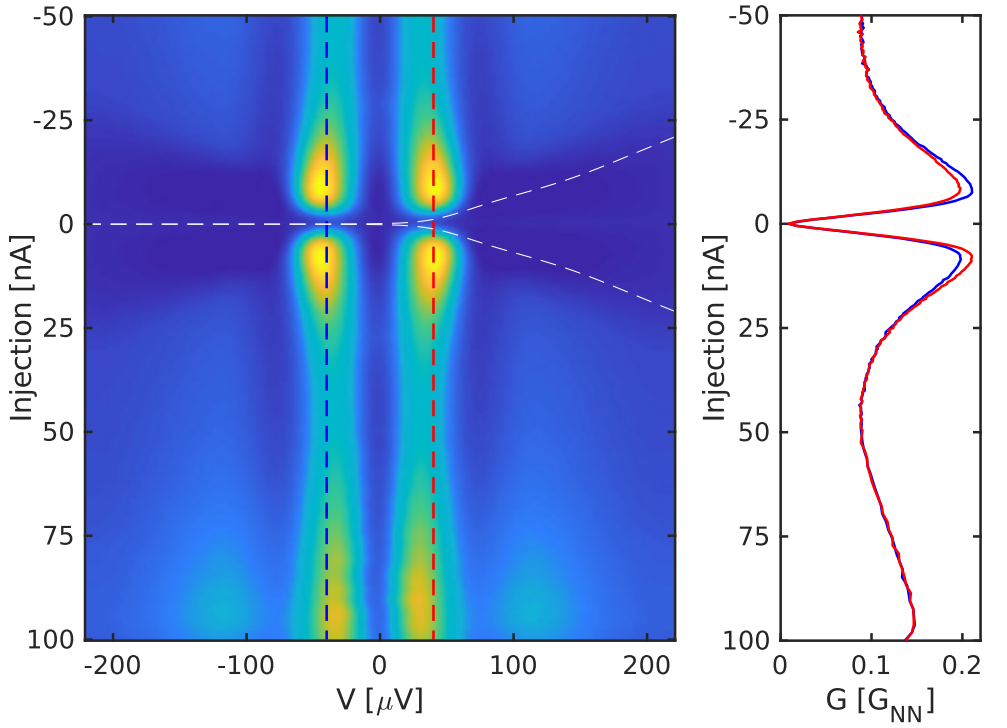

Figure 4.10: Left: the experimental $G(V)$ curves of the closest detector J_1 as a function of the injection current presented as a colormap. The dashed white lines are the NIS $\pm I(V - \delta_D/e)$ traces. Right: the line cuts at $eV = \Delta - \mu_B H - \Delta_D$ as a function of the injection current, taken along the dashed lines (the traces are color coded).

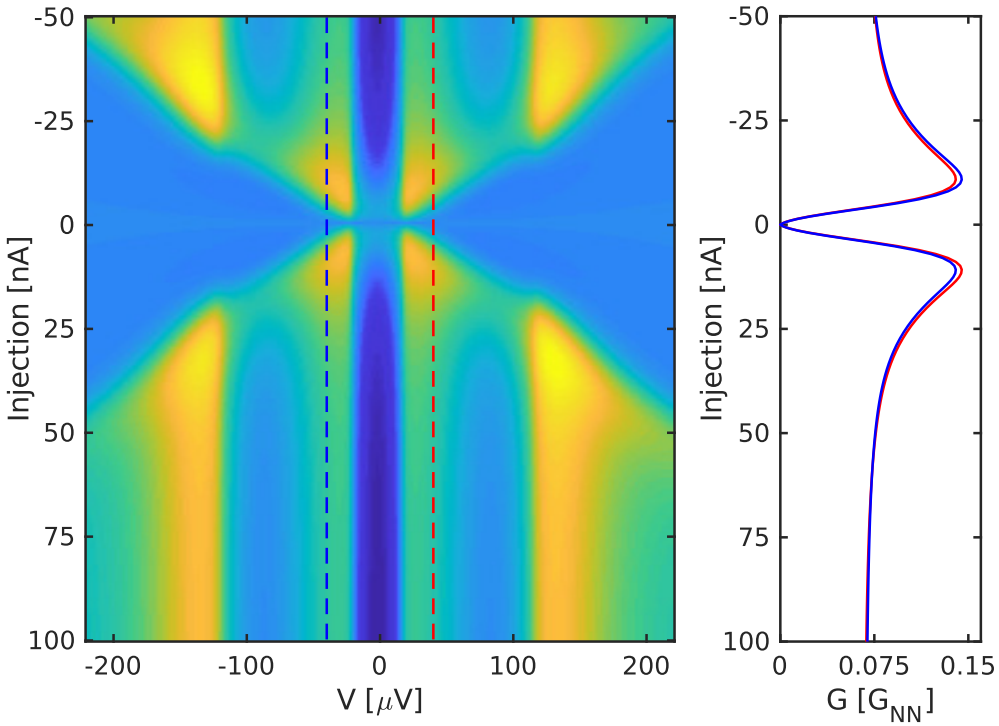

Figure 4.11: Left: the theoretical calculation of the $G(V)$ curves at a distance from the injector corresponding to the closest detector J_1 as a function of the injection current presented as a colormap. Right: the line cuts at $eV = \Delta - \mu_B H - \Delta_D$ as a function of the injection current, taken along the dashed lines (the traces are color coded).

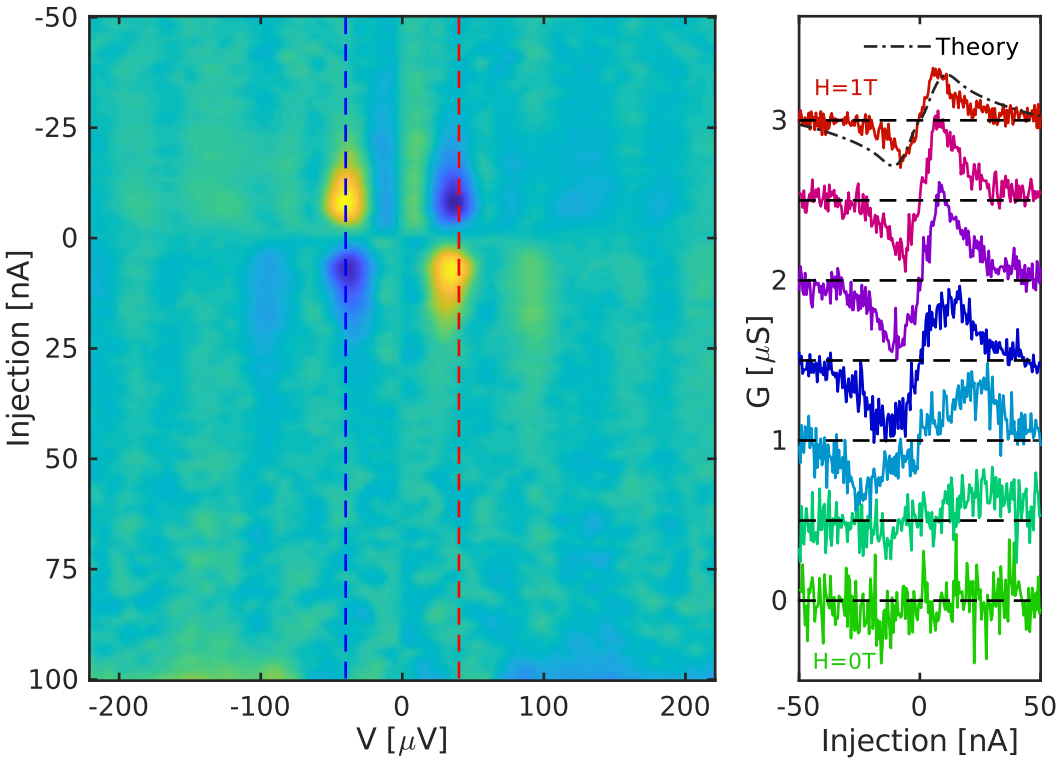

Figure 4.12: Left: the odd component of the colormap shown in figure 4.10. Right: the odd component of the $G(V)$ curves at $eV = \Delta - \mu_B H - \Delta_D$ as a function of the injection current, for several equidistantly spaced magnetic fields from $H = 0$T to $H = 1$T. The dot-dashed black line is the odd component of the theoretical curve shown in figure 4.11. The traces are offset vertically for clarity.

4.3 Differentiating between the f_T and the f_{L3} modes

As both of these modes contribute to the charge imbalance in a superconductor, one cannot distinguish between them by just measuring the voltage across a nearby normal metal probe, as was done previously [36]. The distinction between the two can, however, be made by performing a spectroscopic measurement: as shown in section 1.4 the f_T mode is dominantly present at low magnetic fields and at high injection energies, while the spin-energy mode f_{L3} is localized within $\Delta - \mu_B H < E < \Delta + \mu_B H$ and becomes more visible with increasing field, but dies off close to H_c.

To verify that the odd signal shown in the main text is indeed due to the spin-energy, the following analysis was performed. The left panel of figure 4.13 shows the $G(V)$ of detector J_1 at $H = 0$T for $I_{inj} = \pm 120$nA (the figure is presented in a similar fashion as in 4.6, offset such that the QP peak is at zero and the equilibrium trace is subtracted). Above the QP peak there is a difference between the traces, which changes sign with the sign of the injection current and detection voltage (only the positive part of the trace is shown here for clarity), indicating the presence of a charge imbalance induced by the f_T mode ($f_{L3} = 0$ at $H = 0$ in our experiment). The odd component of the trace can be integrated over the regions marked in the figure (the negative peak at $\approx 200\mu$V is related to the Josephson current and is therefore omitted), and the result is shown on the right panel of figure 4.13. The same panel also shows the results of a similar procedure done for $H = 1$T (integrated in the region $90\mu\text{V} \leq V_{det} \leq 210\mu\text{V}$ - see figure 4.7 for reference), which shows no asymmetry, signifying that the contribution of the f_T mode at $H = 1$T is negligible.

Together with section 4.2, the results presented here show that the charge imbalance observed at finite fields and close to the gap edge of the superconductor is associated with the presence of the f_{L3} mode excited by quasiparticle injection into a Zeeman split superconductor through an NIS junction.

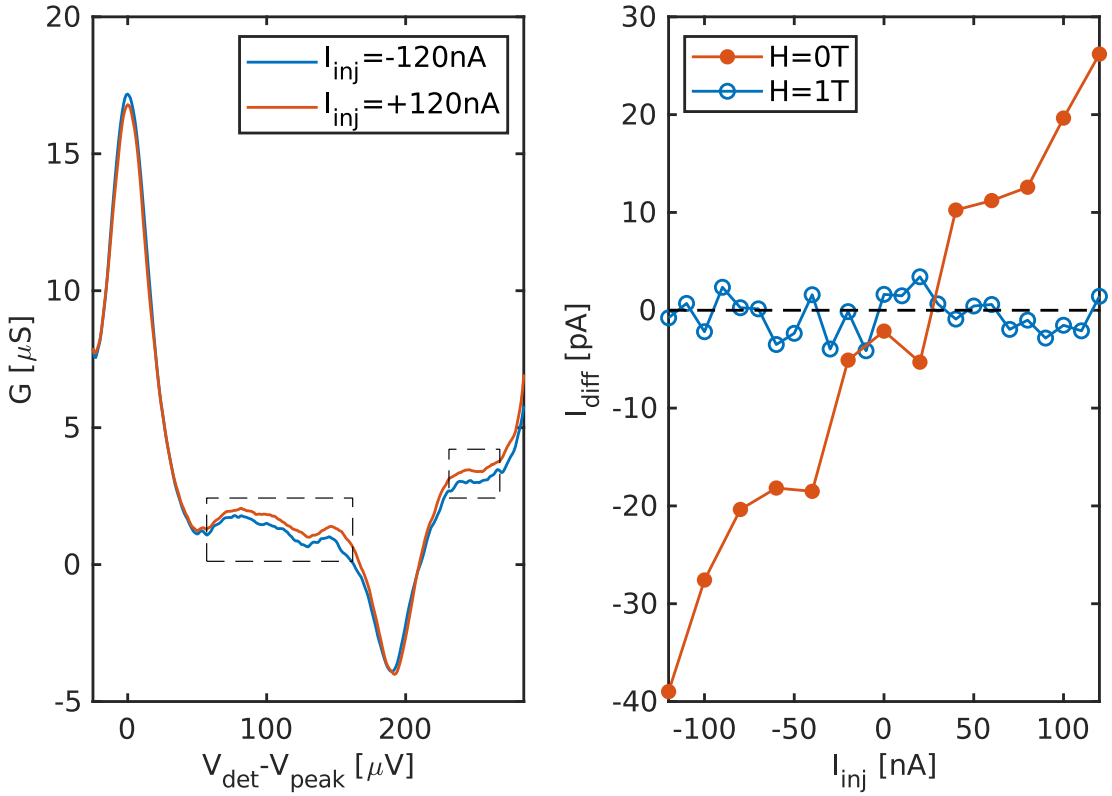

Figure 4.13: Left: A set of $G(V)$ curves from the detector J_1 at $H = 0$T, for $I_{inj} = 120$nA (red) and $I_{inj} = -120$nA (blue), which show a charge imbalance signal at high energies ($E \gg \Delta$). Right the integrated charge imbalance at high energies, for $H = 0$T (red) and $H = 1$T (blue), showing the suppression of the f_T mode by the applied magnetic field.

4.4 Data from similar devices

Spin-split detector: Figure 4.14 shows the data obtained from a previous generation of devices in which both the superconducting wire and the detector electrode were made out of Al and are both Zeeman split. The device has nominally the same geometry as the one presented in chapter 2. The data shown here was measured using the closest detector at $T = 70$mK and at $H = 1.2$T. The left panel shows the sub-gap portion of the detector $I(V)$ curve measured at $I_{inj} = 25$nA (blue trace). To highlight the odd component alongside it the flipped trace $-I(-V)$ is shown in red. As before the odd component only shows up close to $eV_{det} = \Delta - \Delta_D$. The right panel shows the (numerically obtained) odd component of the $I(V)$ curve as a function of the injection current - the odd component is maximal when only quasiparticles of a single spin are injected. Similar features were also seen in datasets obtained from other devices. Because of the lack of spin-sensitivity in these samples new devices were fabricated to spectroscopically verify that the odd component originates from the f_{L3} mode.

Spin-sensitive detector with in-gap states: Figure 4.15 shows data from a device with a spin sensitive detector (measured at $T = 90$mK and $H = 1$T). In this device instead of a Pt capping layer on top of the detector electrode, the detector was fabricated as a Al/Pt/Al sandwich. This resulted in some in-gap states leading to a nontrivial $G(V)$ curve at

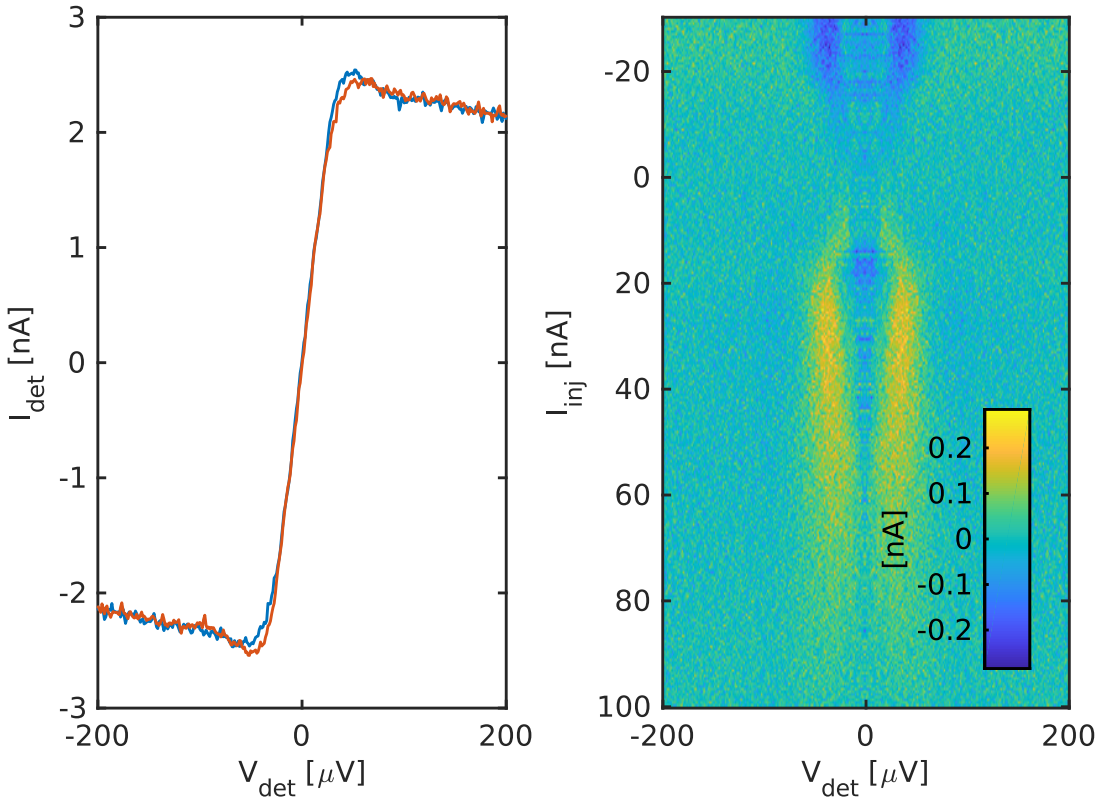

Figure 4.14: Left: an $I(V)$ curve (blue) and $-I(-V)$ (red, numerically obtained) from a spin-insensitive detector at $H = 1.4$T, $T = 70$mK and $I_{inj} = 25$nA showing an odd component localized close to the superconducting gap Δ. Right: the (numerically obtained) odd component at the same field and temperature as a function of the injection current.

equilibrium (black trace). Nevertheless, upon applying a finite current to the injector junction ($I_{inj} = \pm 9$nA red/blue trace respectively) QP's were observable at $eV_{det} = \Delta \mp \mu_B H - \Delta_D$, as well as an odd component related to a charge imbalance.

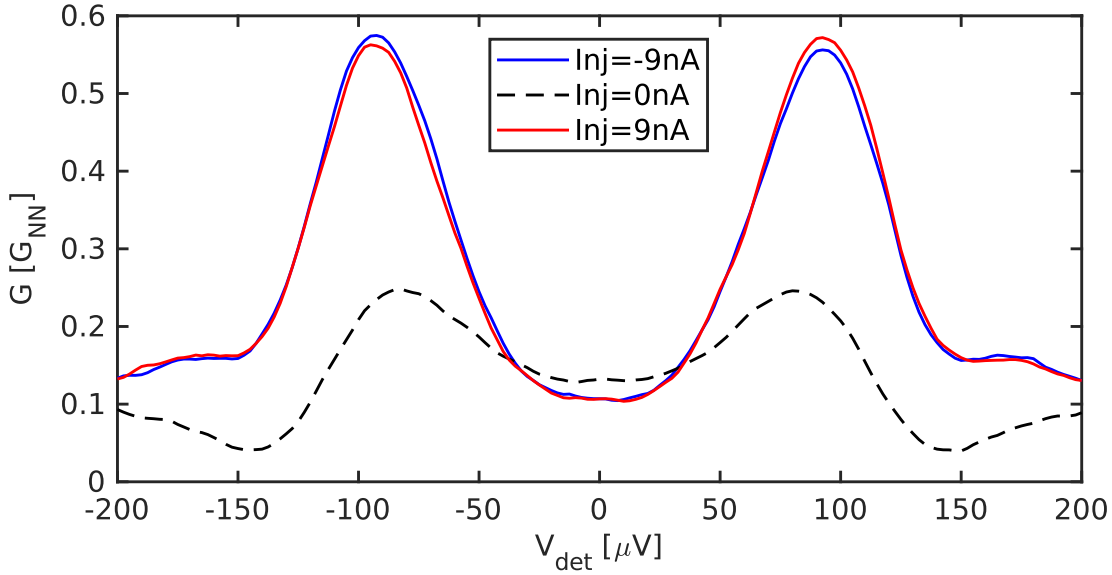

Figure 4.15: The $G(V)$ curves of the closest detector at equilibrium (black trace), $I_{inj} = 9$nA (red trace) and $I_{inj} = -9$nA (blue trace), showing the QP peak as well as an odd component. The data was taken at $T = 90$mK and $H = 1$T using an older sample.

Part II

Nonadiabatic dynamics in strongly driven diffusive Josephson junctions

Introduction

Josephson junctions are widely used in quantum electronics as nondissipative nonlinear devices. When two superconductors are coupled through a thin insulating layer, the dynamics of the junction are set by the reservoir dynamics, as the tunneling time is in the order of a few fs [75]. Furthermore because of the large energy gap in the insulator ($\approx$ 2eV) the barrier always remains in equilibrium.

The situation is different when the weak link is formed by a disordered (diffusive) normal-metal wire. Because of the finite density of states at the Fermi level and the diffusive transport in the wire two timescales appear [76]: the coupling between the two superconducting reservoirs is set by the diffusion time in the wire $\tau_D = \frac{L^2}{D}$, while the other timescale is the energy relaxation time τ_r at which the system returns back to thermal equilibrium. Therefore the dynamics of Josephson junctions in which the weak link is a normal metal (i.e. a Superconductor-Normal-Superconductor junction or SNS for short) is not related to the one found in the reservoirs but instead to diffusion and relaxation of the electrons in the normal metal (N).

As Cooper pair tunneling is not the transport mechanism in SNS junctions an alternative mechanism gives rise to a finite supercurrent: an electron in N, with an energy equal to or smaller than the gap of the superconductor, cannot traverse the N/S interface as there are no available states at those energies. Instead it is reflected back as a hole and a Cooper pair is transferred into the superconductor, this process is called Andreev reflection. The back-scattered hole acquires an extra phase equal to the one of the macroscopic wave function in the superconductor. The hole follows the time-reversed trajectory of the electron [77] until it reaches the second N/S interface, at which it is converted back to an electron by removing a Cooper pair from the superconductor. The phase acquired during this whole process must be an integer multiple of 2π giving rise to bound states, also called Andreev bound states (ABS). Because of the diffusive transport in SNS junctions these states form a continuum. As a consequence of the finite normal metal wire length these bound states have a minimum energy in the order of the Thouless energy $E_T = \frac{\hbar}{\tau_D} = \frac{\hbar D}{L^2}$. The Josephson effect is then understood in terms of the supercurrent carried by the continuous ABS spectrum. This is strictly true only when the phases of the two superconducting reservoirs are equal. When the phase difference φ is not zero, the minimum excitation energy is modified as $\propto |\cos(\varphi/2)|$.

This physical picture can be formalized theoretically by using the quasi-classical Green's function approach, in particular through the Usadel formalism which describes disordered systems [14, 55]. The single particle excitation spectrum in the normal metal is found to be gapped, and in the long junction limit ($E_T \ll \Delta$) it is equal to $E_g(\varphi = 0) \approx 3.1 E_T$ and closes at $\varphi = \pi$. Likewise from the Usadel equation the spectral-supercurrent can be computed as a function of energy and the phase difference $j_s(E, \varphi)$. To obtain the supercurrent through the junction one needs to multiply j_s with the (odd component of the) distribution function

and integrate over energies [78]. This results in a direct possibility of manipulating the SNS junction properties through a non-equilibrium distribution function. As an example, the fact first pointed out by Yip [79] that the spectral supercurrent changes sign at high enough energy can be used to reverse the flow of supercurrent, by modifying the distribution function through the application of a voltage [80], and gives rise to the "π state".

As pointed out by Eliashberg [81] for homogeneous superconductors and recently generalized theoretically to SNS junctions [82], microwave radiation can also be used to drive the distribution function out-of-equilibrium, such that the low-energy states which carry the highest weight in the self-consistency relation and the spectral-supercurrent get depopulated. Therefore this leads to an enhancement of the order parameter (for bulk superconductors) and an increase in the critical current for SNS weak links. In the same spirit, microwave pumping has been used also to increase the critical temperature of conventional superconductors by changing the energy distribution of thermally excited quasiparticles [83].

Unlike in a homogeneous superconductor, in an SNS junction the induced mini-gap depends on the phase difference φ, which in turn results in supercurrent that becomes phase dependent not only through the equilibrium dependence of $j_s(\varphi)$ but also through the absorption and emission rates which depend on the density of states [82]. As a consequence the current phase relationship (CPR) acquires higher harmonics that are not present at equilibrium [82, 84].

In this section we show that this anharmonicity induced by microwave pumping is not only related to the out-of-equilibrium distribution function but also, and primarily, to a dip in the spectral current density at the energy corresponding to the frequency of the microwave drive $E = \pm\omega_{RF}/2$. This feature is a consequence of the microwave absorption induced quasiparticle transitions across the mini-gap and can be seen as a dynamical pair-breaking effect. Experimentally the harmonics of the current phase relation were accessed by measuring the AC Josephson radiation emitted by the SNS junction at $f_F \approx 6$GHz while being irradiated with a microwave drive with a frequency of the order of the mini-gap $\hbar\omega_{RF} \geq 2E_g(0)$ [85].

Chapter 5

Theory

This section covers several topics. Firstly it describes how a Josephson junction can be modeled electrically and how it responds to a current or a voltage bias, as well as a microwave drive in terms of the phase dynamics. Following this, the quasiclassical theory of the supercurrent in SNS junctions will be presented and the equilibrium transport properties will be calculated. At the end a novel out-of-equilibrium situation is discussed, from a microscopic point of view, in which both the spectral supercurrent and the distribution function are driven out-of-equilibrium, as a consequence of a microwave drive at a frequency greater than the minigap energy.

5.1 Electrical properties of an SNS junction in a circuit

5.1.1 The DC RSJ model

This section provides an overview of the well established Resistively Shunted Josephson (RSJ) junction model, describing the (macroscopic) electrical response of an SNS junction under current bias [17, 86]. The result of the microscopic theory (presented in chapter 5.2) is that an SNS junction can be characterized by the current phase relation (CPR) $I = I_s(\varphi)$ as well as the 2nd Josephson equation which relates the voltage across the junction with the time derivative of the phase difference $V(t) = \frac{\hbar}{2e}\dot{\varphi}(t)$ [87].

The $V = 0$ solution, or equivalently $\dot{\varphi} = 0$, corresponds to a supercurrent flowing through the junction. If the junction is biased with a current smaller than the critical one, φ will attain a value such that $I_{DC} = I_s(\varphi)$. For currents larger than the critical one a zero-voltage solution does not exist, and other transport channels need to be taken into account - the displacement current related to the charging and discharging of the junction capacitance and the dissipative current through the resistive channel. For an SNS junction the effective capacitance is usually negligible and only the resistive channel needs to be included [88, 86]. The total current is then:

$$I_{DC} = I_s(\varphi(t)) + \frac{V}{R_N} = I_s(\varphi(t)) + \frac{\hbar\dot{\varphi}}{2eR_N} \tag{5.1}$$

If the bias current (i.e. left hand side of 5.1) is time independent and the current phase

relation is $I_s(\varphi) = I_c \sin(\varphi)$, the RSJ equation can be integrated analytically to obtain:

$$\dot{\varphi}(t) = R_N \frac{I_{DC}^2 - I_c^2}{I_{DC} + I_c \cos \omega_{DC} t} \tag{5.2}$$

where $\omega_{DC} = \frac{2eR_n}{\hbar}\sqrt{I_{DC}^2 - I_c^2}$ is the Josephson frequency. A Fourier series expansion of this result gives the DC voltage as $V_{DC} = R_N\sqrt{I_{DC}^2 - I_c^2}$ and the harmonics of the Josephson emission as $V_{k\omega_{DC}} = \dfrac{2V_{DC}(I_c R_N)^k}{(I_{DC}R_N + V_{DC})^k}$ $(k \in \mathbb{N})$, which means that a pure DC current above the critical one generates both a DC and an RF voltage.

At finite temperatures, aside from a suppression of the critical current $I_c(T)$, one needs to consider the effects of thermal fluctuations, which originate from the Johnson noise of the normal wire resistance. These can be included in the model by adding a Langevin term $\delta I(t)$ to the current bias, which is assumed to have zero mean and to be white $< \delta I(t+\tau)\delta I(t) >= \frac{2k_B T}{R}\delta(\tau)$. The RSJ model then becomes a Fokker-Planck equation, which can be solved in terms of the probability distribution function for the phase $\sigma(\varphi, t)$ (see [86]). At the end the intensity of the fluctuations is described by $\gamma = \dfrac{\hbar I_c}{e k_B T}$. The same approach can be used even if the source of the fluctuations is not the Johnson noise of the normal state resistance but the noise of the biasing circuit, then γ (which can be determined by fitting the $V(I)$ curve) sets the effective noise temperature of the setup.

The $V(I)$ curves calculated with and without thermal fluctuations are shown in figure 5.1 - the main effect of thermal fluctuations is to wash out the sharp transition from the nondissipative to the dissipative regime seen in the RSJ solution.

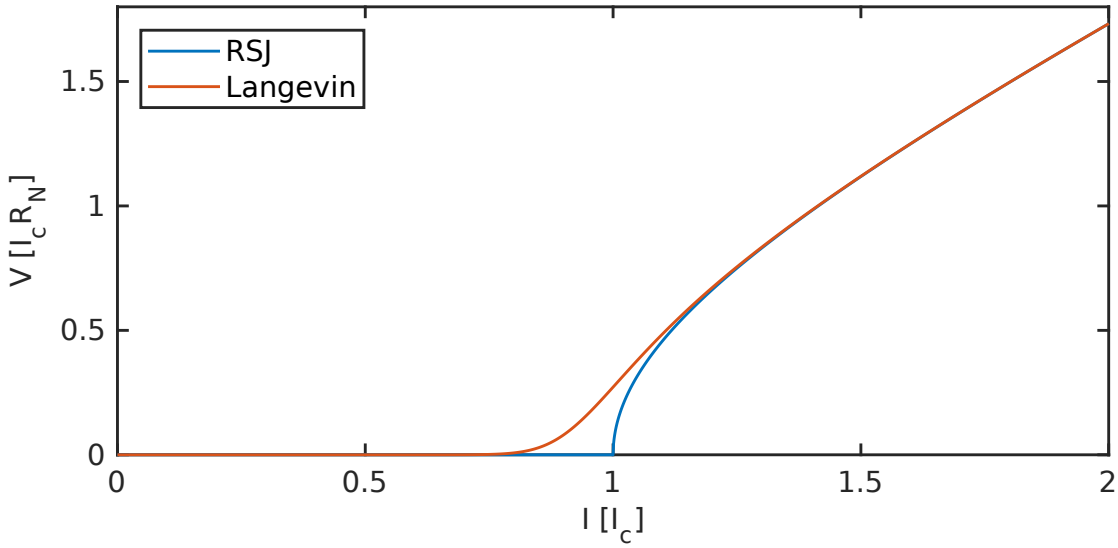

Figure 5.1: The $V(I)$ curve of a junction based on the RSJ model without fluctuations (blue) and with a Langevin term ($\gamma = \dfrac{\hbar I_c}{e k_B T} = 50$, red curve).

5.1.2 Shapiro steps and the AC RSJ model

This section covers a review the physics leading to the appearance of Shapiro steps under voltage bias, as well as generalization to the current bias case, developed with the goal of

modeling the experiment.

Irradiating a Josephson junction with microwaves leads to significant changes in the $V(I)$ curve - constant voltage steps appear at $V_{DC} = n\frac{\hbar\omega_{RF}}{2e}$, where ω_{RF} is the angular frequency of the microwave drive and n is an integer [89, 33]. The numerical value of $\frac{2e}{h} \approx 483\text{MHz}/\mu\text{V}$ means that one needs to apply radiation with a frequency above 1GHz to easily observe this effect experimentally.

If the junction is voltage biased by

$$V(t) = V_{DC} + V_{RF}\cos(\omega_{RF}t)$$

the phase difference will, according to the 2nd Josephson relation, evolve as

$$\varphi(t) = \varphi_0 + \omega_{DC}t + \frac{2eV_{RF}}{\hbar\omega_{RF}}\sin(\omega_{RF}t)$$

where $\omega_{DC} = \frac{2eV_{DC}}{\hbar}$ and φ_0 is a free parameter, the meaning of which will be discussed later. For simplicity we can assume that the current phase relation is given by $I(\varphi) = I_c\sin(\varphi)$, and by substituting the expression for $\varphi(t)$ one gets [33, 90]:

$$I(t) = I_c\sum_n(-1)^n J_n(\frac{2eV_{RF}}{\hbar\omega_{RF}})\sin\left(\varphi_0 + \omega_{DC}t - n\omega_{RF}t\right) \tag{5.3}$$

where J_n is the n-th Bessel function, and its parameter $s = \frac{2eV_{RF}}{\hbar\omega_{RF}}$ measures the effective power of the RF drive (the first two Bessel functions are shown in figure 5.3). The current will have a DC component only if $\omega_{DC} = n\omega_{RF}$, or alternatively $2eV_{DC} = n\hbar\omega_{RF}$ - the energy of a $2e$ Cooper pair traversing a voltage drop V_{DC} is converted into n photons of frequency ω_{RF}. The $n = 0$ term, proportional to $J_0(s)$, describes how the critical current is suppressed by microwave irradiation, while the higher order ones result in constant voltage steps. φ_0 is still a free parameter, and for a given $\omega_{DC} = n\omega_{RF}$, it determines the value of the DC current: when the Josephson radiation and the RF drive are in phase $\varphi_0 = 0$, and there will be no current. The extremal cases are when the two waves are dephased by $\varphi_0 = \pm\pi/2$ and the corresponding current is $I = \pm I_c J_n(s)$, giving the full width of the step as $2I_c|J_n(s)|$.

The generalization to the case of an arbitrary current phase relation, which has higher order terms in it, $I(\varphi) = \sum_k I_{c,k}\sin(k\varphi)$ is straightforward: the same expression for $\varphi(t)$ is substituted into the CPR and the result is evaluated termwise. For the k-th harmonic of the current phase relation the resonant condition is $k\omega_{DC} = n\omega_{RF}$ where n is the order of the conversion process. The corresponding current will scale as $J_n(ks)$, and the total current can be evaluated by summing over k.

In practice it is challenging to truly voltage bias devices with a low resistance, compared to the one of the electromagnetic environment, and thus they are often current biased. The resulting phase dynamics can be captured with the RSJ model by including a time dependent bias current on the left-hand side of the equation:

$$I_{DC} + I_{RF}\sin(\omega_{RF}t) = I_s(\varphi(t)) + \frac{\hbar\dot{\varphi}}{2eR} \tag{5.4}$$

This equation can be numerically solved for $\varphi(t)$ as a function of I_{DC}, I_{RF} and ω_{RF}. The $V(I)$ curve based on the numerical solution of the RSJ model, for several values of I_{RF}, can be seen in figure 5.2 - in the limit of vanishing I_{RF} the square root solution is recovered, while

at higher values the critical current is suppressed and a step at $V_{DC} = \frac{n\hbar\omega_{RF}}{2e}$ becomes visible. A measure of the strength of the microwave drive, analogous to the one defined for a voltage biased junction, can be defined as $s = \frac{2eI_{RF}R_N}{\hbar\omega_{RF}}$. The dependence of the critical current as well as the full width of the 1st Shapiro step on s is shown in figure 5.3, which reproduces the Bessel dependence (up to the noise and finite resolution of the numerical calculation).

A colorplot of the differential resistance of $R = \frac{dV}{dI}$ versus s and I_{DC} is shown in figure 5.4, showing the higher order Shapiro steps.

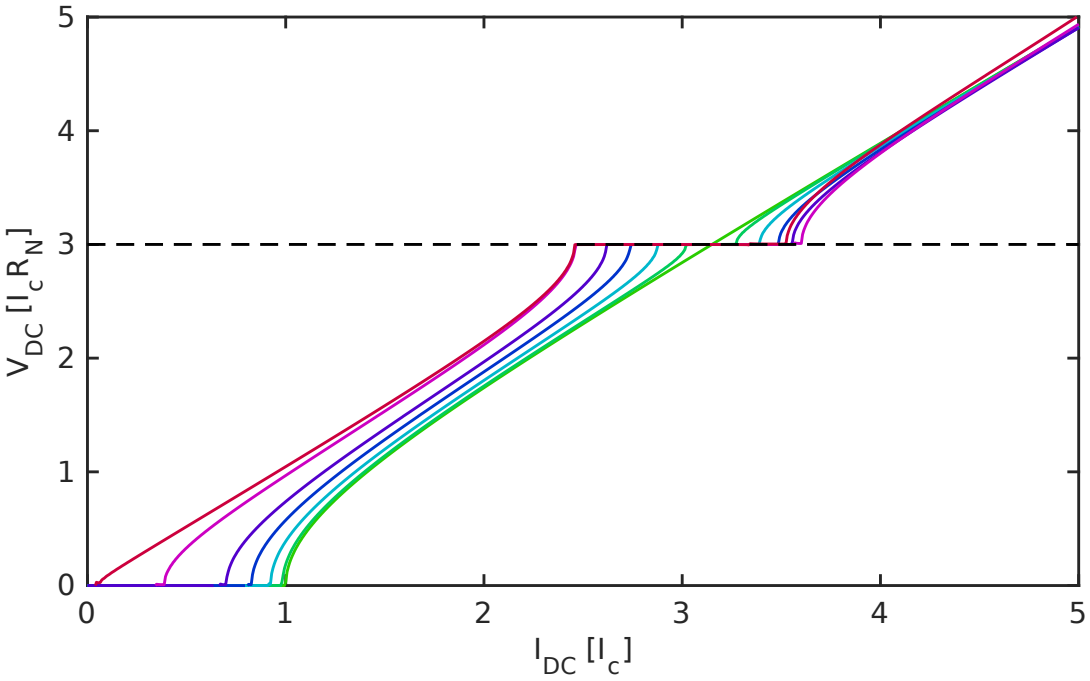

Figure 5.2: The $V(I)$ curve computed using the RSJ model. The frequency of the drive is $\omega_{RF} = 3\frac{2eI_cR_N}{\hbar}$, resulting in a Shapiro step at $V_{DC} = 3I_cR_N$. The traces correspond to different values of the microwave drive: the green curve corresponds to $s = 0$, the purple one corresponds to $s = 1.84$ which maximizes the width of the Shapiro step and the red one is close to $s = 2.4$ which suppresses the critical current fully. The higher order steps are also reproduced, but are not shown as they appear at higher voltages.

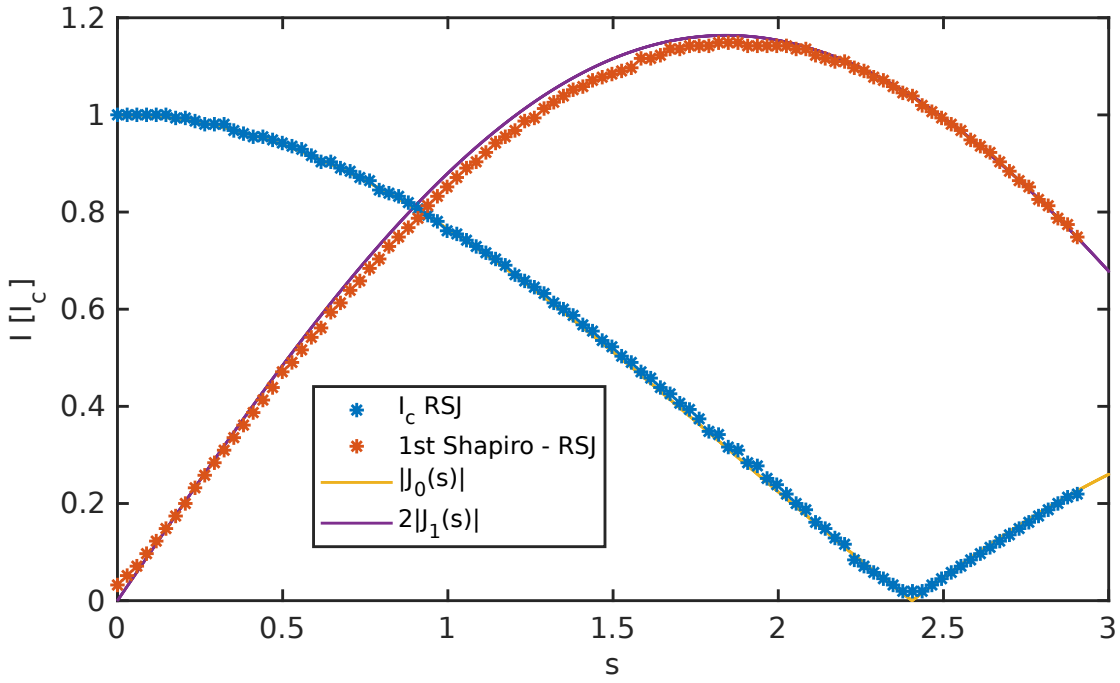

Figure 5.3: The calculated power dependence of the critical current (blue dots) and the full width of the 1st Shapiro step (red dots) from the RSJ model ($\omega_{RF} = 3\frac{2eI_cR_N}{\hbar}$) versus the power of the microwave drive s, as well as the absolute value of the first two Bessel functions.

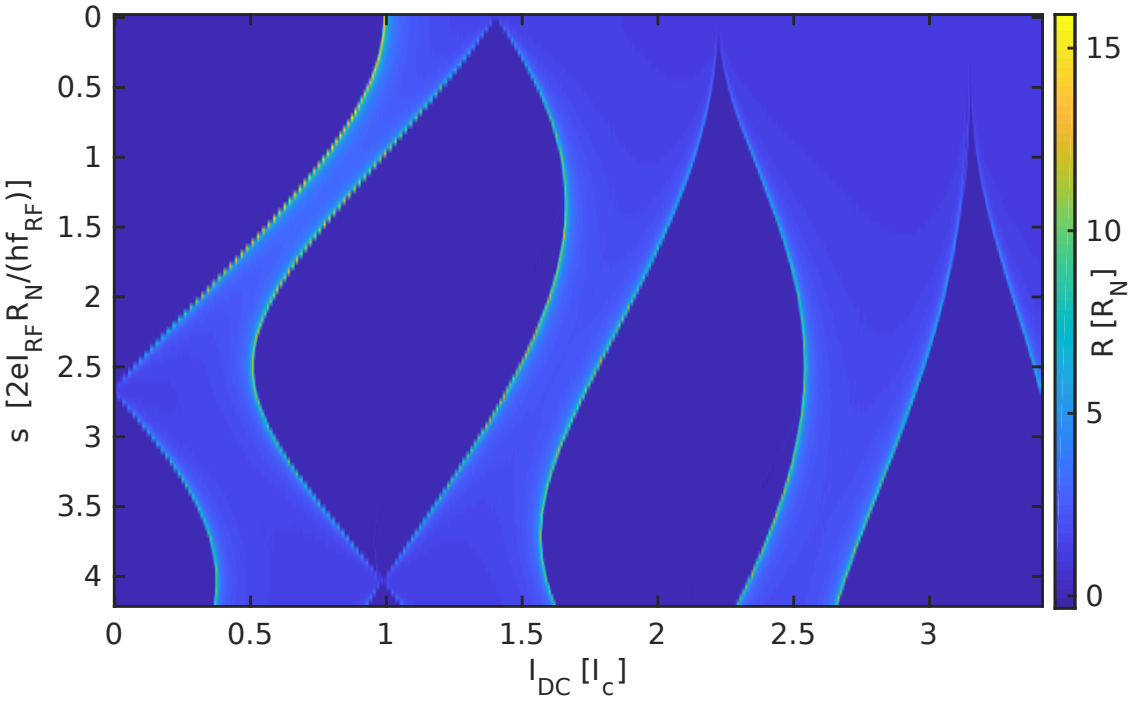

Figure 5.4: A colorplot of the differential resistance $R = \frac{\partial V}{\partial I}$, computed using the RSJ model for $\omega_{RF} = \frac{2eI_cR_N}{\hbar}$, as a function of microwave power s and the DC current bias I_{DC}. The dark blue regions are constant voltage steps (i.e. $R = 0$) corresponding to, from left to right, the critical current and the first three Shapiro steps. Due to the high junction nonlinearity at low bias currents, s slightly overestimates the applied microwave power.

In the current biased RSJ model the maximum width of the 1st Shapiro step is frequency dependent (see figure 5.5). The high frequency limit, $\hbar\omega_{RF} \gg 2eI_cR_N$ recovers the voltage biased result, while at low frequencies the effect is substantially suppressed (also see [91]). This is due to the nonlinearity of the junction at low bias currents, where the currents carried by the resistive and the superconducting channel are comparable and the $V(I)$ curve is highly nonlinear. At higher frequencies the Shapiro steps appear at sufficiently high DC bias currents where the junction is approximately linear and the behavior is adequately described by a voltage bias $V_{RF} = I_{RF}R_N$.

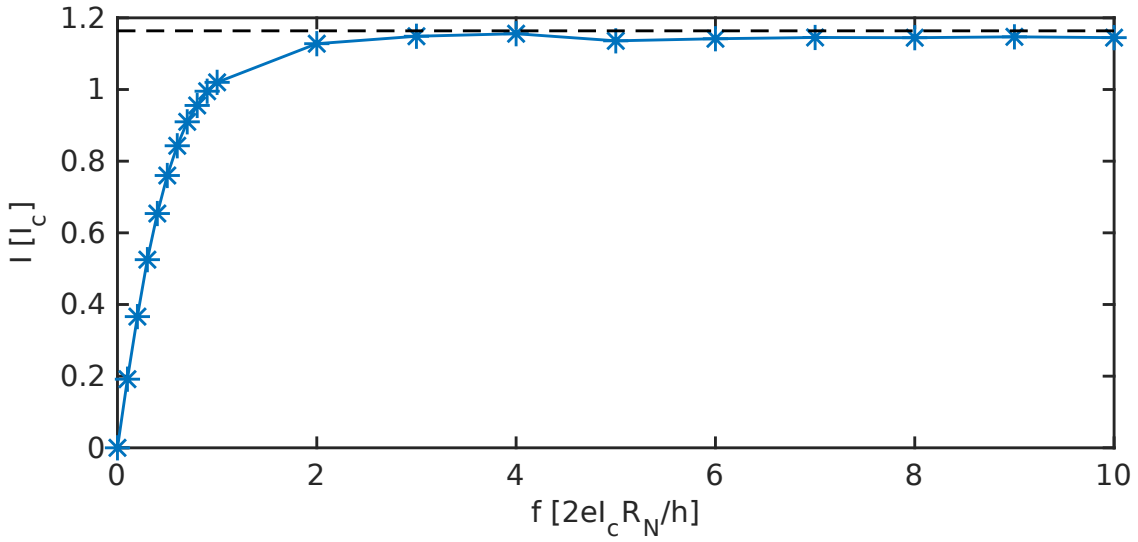

Figure 5.5: The maximum of the Shapiro step width, computed using the RSJ model, as a function of the frequency of the microwave drive. The value of $\approx 1.16I_c$ (dashed line) predicted for a voltage biased junction is attained only above $\omega_{RF} = \dfrac{2eI_cR_N}{\hbar}$.

5.1.3 Josephson microwave emission and the low-frequency adiabatic RSJ model

This section reviews the so-called Josephson emission briefly, as well as introduce a simple adiabatic model used for calculating the amplitude of the emitted radiation.

A nonzero DC voltage across the junction will drive the phase and will result in emission of radiation at the frequency $\omega_{DC} = \frac{2eV_{DC}}{\hbar}$ [92, 93], while the higher order harmonics of the current phase relation will radiate at $k\omega_{DC}$, where k is the harmonic order. The application of microwaves will induce additional dynamics at the frequency of the drive ω_{RF}. Through the non-linearity of the junction these two signals can be mixed, resulting in radiation at frequencies $|m\omega_{DC} - n\omega_{RF}|$ (where m and n are integers), which is the principle of operation for SNS mixers [94, 90]. For a voltage biased sample this can be directly seen from equation 5.3: when the frequencies ω_{DC} and ω_{RF} are unequal a current with the frequency $|\omega_{DC} - n\omega_{RF}|$ and the amplitude $I_cJ_n(s)$ will appear. For a current biased junction the simplest approach for describing the mixing is by looking at the power spectrum of $\dot{\varphi}(t)$ calculated based on the RSJ model (equation 5.4). A colorplot proportional to the spectral power of the emitted radiation, showing the direct Josephson emission as well as the various components

up and down converted by the RF drive is shown in figure 5.6. The relevant case for the experiment presented in chapter 6.3 is when the junction is driven by microwaves at very high frequencies and the low frequency Josephson radiation is measured to probe the junction. This brute force approach is then computationally relatively challenging: the time step of the numerical integration is set by $\max(\omega_{DC}, \omega_{RF})$, while to have a good resolution it is necessary to integrate over long times.

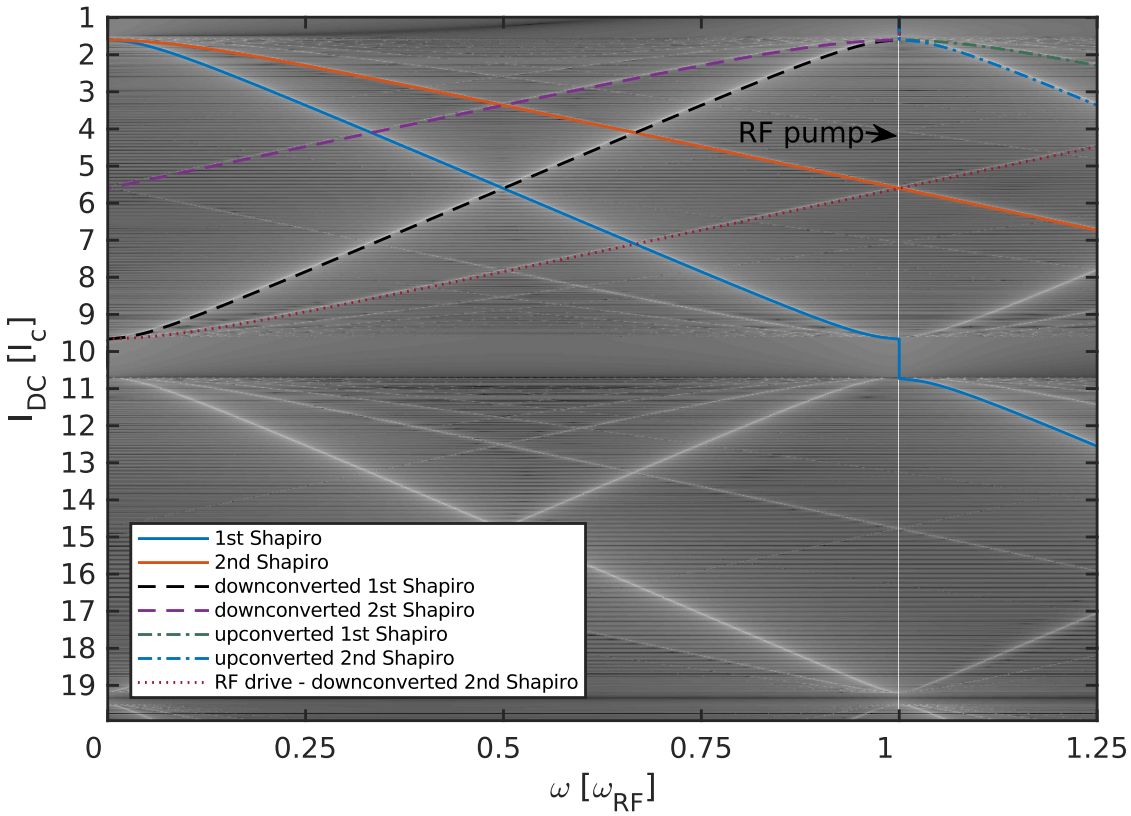

Figure 5.6: The power spectrum of the Josephson emission as a function of the radiation frequency and the applied I_{DC} current, calculated using the RSJ model for $s = 1.35$ and $\omega_{RF} \approx 10\frac{2eI_cR_N}{\hbar}$. The lines corresponding to direct emission (blue and red lines) are visible as well as many down converted (e.g. the dashed black and purple lines) and up converted ones (e.g. the dotted red line).

To mitigate this issue an alternative approach can be utilized. The phase dynamics can be separated into two components $\varphi(t) = \varphi_L(t) + \varphi_H(t)$, where $\varphi_L(t)/\varphi_H(t)$ are the low/high frequency components. Substituting this ansatz into equation 5.4, under the assumption that the high frequency component is dominantly carried by a resistive current, yields:

$$I_{DC} + I_{RF}\sin(\omega_{RF}t) = \tilde{I}(\varphi_L(t)) + \frac{\hbar\dot{\varphi_L}}{2eR} + \frac{\hbar\dot{\varphi_H}}{2eR} \tag{5.5}$$

Compared to eq. 5.4, the $I_c\sin(\varphi(t))$ term is replaced by $\tilde{I}(\varphi_L(t))$ which is the instantaneous low frequency current-phase relation, averaged over the period of the drive at ω_{RF}. If the junction has a sinusoidal current phase relation $I(\varphi) = I_c\sin(\varphi)$ the form of $\tilde{I}(\varphi)$ can be found from equation 5.3. Separating the low and the high frequency components of the phase gives the result $\tilde{I}(s, \varphi_L(t)) = J_0(s)I_c\sin(\varphi_L(t))$. If the current phase relation has higher order

harmonics, $\tilde{I}(s,\varphi)$ becomes, by analogy with the behavior of higher-order harmonics under voltage bias, $\tilde{I}(s,\varphi) = \sum_{n=1} I_{c,n} J_0(ns)\sin(n\varphi)$.

In general $\tilde{I}(\varphi)$ can be calculated from the microscopic theory, taking into account out-of-equilibrium effects and the high frequency phase dynamics. A theoretical framework for doing so is presented in section 5.3.

Matching the low and high frequency components on the left hand and right hand sides of equation 5.5 gives:

$$\begin{aligned} I_{DC} &= \tilde{I}(\varphi_L(t)) + \frac{\hbar\dot{\varphi_L}}{2eR}, \\ I_{RF}\sin(\omega_{RF}t) &= \frac{\hbar\dot{\varphi_H}}{2eR} \end{aligned} \tag{5.6}$$

The second of the two equations is solved by $\varphi_H(t) = -\frac{2eI_{RF}R_N}{\hbar\omega_{RF}}\cos(\omega_{RF}t)$, and the prefactor can be recognized as $s = \dfrac{2eI_{RF}R_N}{\hbar\omega_{RF}}$ introduced earlier. The solution of the first equation can be obtained by integration:

$$t(\varphi_L) = \frac{\hbar}{2eR}\int_0^{\varphi_L} d\phi' \left[I_{DC} - \tilde{I}(\phi')\right]^{-1} \tag{5.7}$$

The k-th harmonic of the emitted Josephson radiation (i.e. the power at $k\omega_{DC}$) can be obtained as:

$$\begin{aligned} V_k &= \frac{\omega_{DC}}{2\pi}\int_0^{2\pi/\omega_{DC}} dt e^{-ik\omega_{DC}t} V(t) \\ &= \frac{\hbar\omega_{DC}}{4e\pi}\int_0^{2\pi/\omega_{DC}} dt e^{-ik\omega_{DC}t}\dot{\varphi_L}(t) \\ &= \frac{V_{DC}}{2\pi}\int_0^{2\pi} d\varphi e^{-ik\frac{2\pi}{t(2\pi)}t(\phi)} \end{aligned} \tag{5.8}$$

Using this result the amplitude of the Josephson emission can be calculated for an arbitrary current phase relation.

Figure 5.7 and 5.8 show the power dependence of the Josephson emission, for a sinusoidal current phase relation and an anharmonic one respectively, as a function of the applied high-frequency microwave power. Anticipating the experimental design in which the emission is measured at a fixed frequency, the traces show the amplitude of the first two harmonics as a function of s for a fixed Josephson frequency, i.e. $V_{DC}(I_{DC}, s) = \frac{\hbar\omega_D}{2e} = const$ is solved for I_{DC} at each s where ω_D is the frequency at which the measurement is performed.

If ω_D is low this condition is met at a low bias current, close to the critical one and the resulting phase dynamics is highly nonlinear. This nonlinearity can produce a finite power at twice the frequency, where one should normally expect to see the emission from the second order process, even if the current phase relation is sinusoidal - see figure 5.7. At a sufficiently high frequency the emission spectrum approaches the linear response solution - no power is emitted at higher frequencies and the 1st harmonic attains the Bessel power dependence.

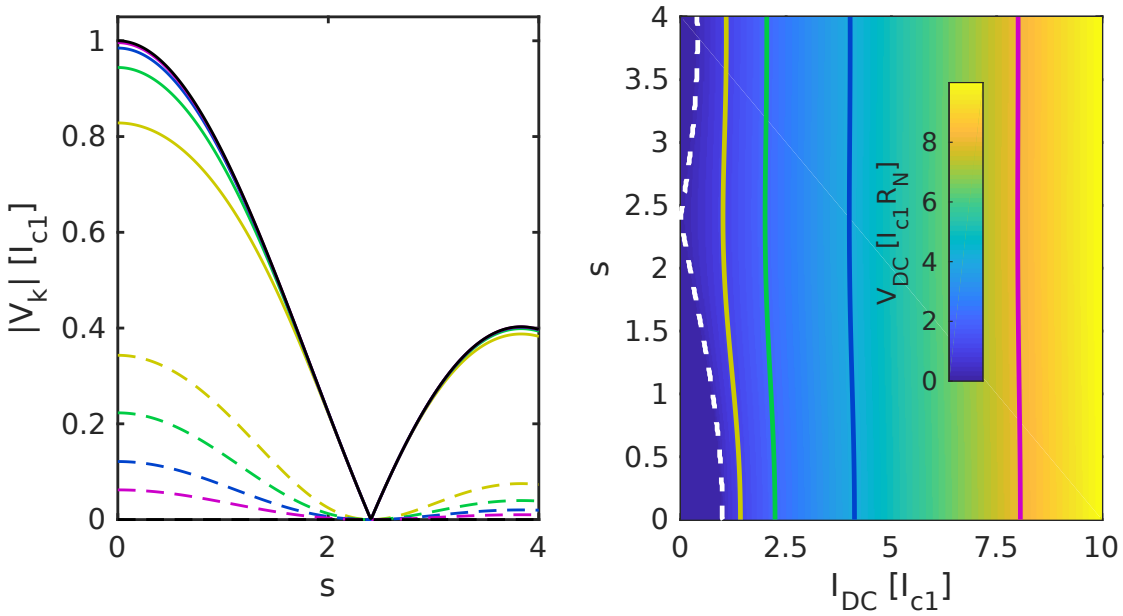

Figure 5.7: The Josephson emission calculated using the adiabatic RSJ model for a sinusoidal current phase relation. The left panel shows the amplitude of the radiation emitted at $\omega = \omega_{DC}$ (full lines) and at $\omega = 2\omega_{DC}$ (dashed lines) as a function of applied microwave power. The traces correspond to the different values of $\omega = \{1, 2, 4, 8\}2eI_cR_N\hbar^{-1}$ (in order: yellow, green, blue and purple lines), while the black line is $J_0(s)$. The right panel shows the colorplot of the DC voltage across the junction as a function of the applied power and DC current, the colored lines correspond to solutions $2eV_{DC}(I_{DC}, s) = \hbar\omega$ shown on the left, and the white line indicates $I_c(s)$. If the detection frequency is high enough compared to $2eI_cR_N\hbar^{-1}$, the emission at $\omega = \omega_{DC}$ is a reliable measure of the critical current.

If the current phase relation is $I(\varphi) = I_{c,1}\sin(\varphi) + I_{c,2}\sin(2\varphi)$, the results are qualitatively the same: at low frequencies the nonlinearity mixes the radiation at ω_{DC} and $2\omega_{DC}$, while at higher frequencies the radiation at ω_{DC} ($2\omega_{DC}$) originates solely from the first (second) harmonic of the CPR and evolves as $J_0(s)$ ($J_0(2s)$) with the applied power.

It is important to note that at high powers the emission follows the Bessel function regardless of the measurement frequency. Thus by measuring the finite frequency spectrum of the emitted Josephson radiation one can noninvasively probe the adiabatic current phase relation of a Josephson junction.

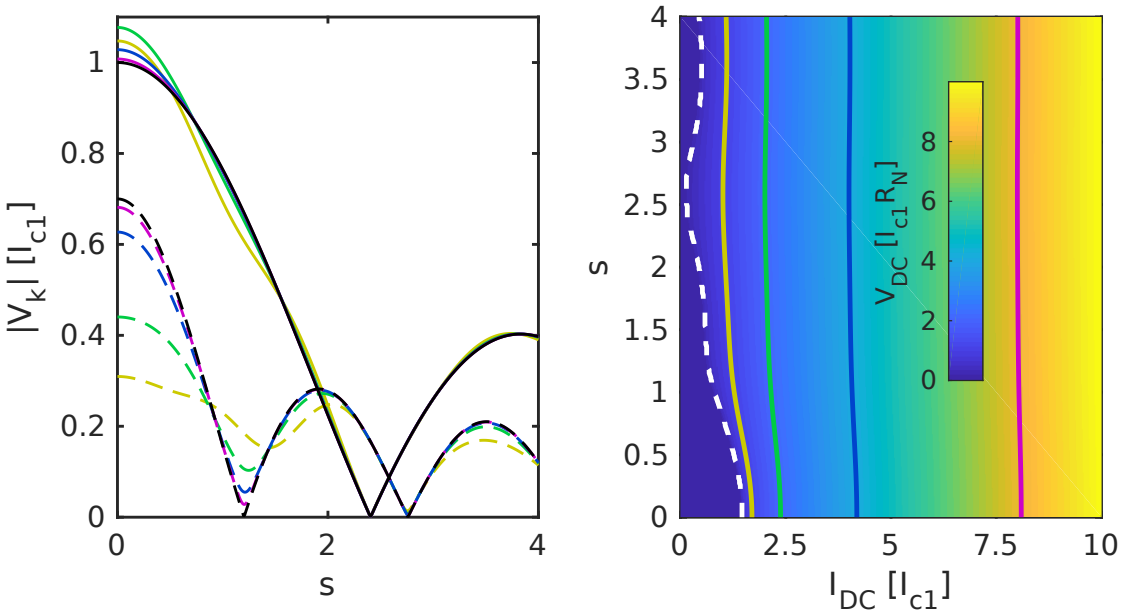

Figure 5.8: The Josephson emission calculated using the adiabatic RSJ model non-sinusoidal current phase relation $I(\varphi) = \sin(\varphi) + 0.7\sin(2\varphi)$. The left panel shows the amplitude of the radiation emitted at $\omega = \omega_{DC}$ (full lines) and at $\omega = 2\omega_{DC}$ (dashed lines) as a function of the applied microwave power. The traces correspond to the different values of $\omega = \{1, 2, 4, 8\}2eI_cR_N\hbar^{-1}$ (in order: yellow, green, blue and purple lines), while the black (dashed) lines are $J_0(s)$ ($J_0(2s)$). The right panel shows the colorplot of the DC voltage across the junction as a function of applied power and DC current, the colored lines correspond to solutions $2eV_{DC}(I_{DC}, s) = \hbar\omega$ shown on the left, and the white line indicates $I_c(s)$. If the detection frequency is high enough compared to $2eI_cR_N\hbar^{-1}$, or the applied microwave power is sufficiently high, the emission at $\omega = \omega_{DC}$ ($\omega = 2\omega_{DC}$) becomes a good probe of the amplitude of the first (second) harmonic of the CPR.

5.2 Equilibrium microscopic theory of SNS junctions

This section is provides a review of the physics, on a microscopic level, describing the properties of SNS junctions within the Usadel formalism.

The microscopic properties of an SNS junction can be described within the Keldysh-Usadel formalism presented in chapter 1 of part I. If the self energy contribution is neglected, at zero magnetic field the Usadel equation reads:

$$D\nabla \cdot (\check{g}\nabla\check{g}) + [iE\tau_3 - \check{\Delta}, \check{g}] = 0 \tag{5.9}$$

In the previous equation D is the normal state diffusion constant, $\check{g}$ is the Keldysh-Usadel Green's function (GF):

$$\check{g} = \begin{pmatrix} \hat{g}^R & \hat{g}^K \\ 0 & \hat{g}^A \end{pmatrix} \tag{5.10}$$

$\hat{g}^R$ is the retarded component of the Green's function, $\hat{g}^A$ the advanced one, and the Keldysh component of the Green's function is $\hat{g}^K = \hat{g}^R\hat{f} - \hat{f}\hat{g}^A$, and $\hat{f}$ is the distribution function

matrix, and $\hat{g}^A = -\tau_3 \hat{g}^R \tau_3$ (see chapter 1). The $\hat{\Delta}$ term in the previous equation describes the superconducting order parameter and is given by:

$$\check{\Delta} = \begin{pmatrix} \hat{\Delta} & 0 \\ 0 & \hat{\Delta} \end{pmatrix}, \hat{\Delta} = \begin{pmatrix} 0 & \Delta(x) \\ \Delta^*(x) & 0 \end{pmatrix} \tag{5.11}$$

The (local) value of $\Delta(x)$ is set by the self-consistency relation, while the phase gradients are directly related to a presence of a supercurrent.

A diffusive SNS junction can be modeled as a normal metal wire terminated with two large superconducting reservoirs. In the normal wire the intrinsic pairing potential is zero and therefore in this region $\Delta = 0$. However, the wire can be proximitized through the contact with the superconducting reservoir, and Cooper pairs can diffuse into it.

From the normalization condition $(\hat{g}^R)^2 = 1$ the retarded component of the Green's function can be parameterized as [78]:

$$\hat{g} = \begin{pmatrix} \cosh(\theta) & \sinh(\theta) e^{i\chi} \\ -\sinh(\theta) e^{-i\chi} & -\cosh(\theta) \end{pmatrix} \tag{5.12}$$

Here θ is the complex pairing angle and χ is the complex phase of the induced superconducting state. For a quasi one dimensional wire, pointing along the x axis, this parametrization reduces to $\theta = \theta(E, x)$ and $\chi = \chi(E, x)$. Substituting this into the Usadel equation (eq. 5.9), with a change of variables such that the length is measured in units of the wire length L and the energies are measured in units of the Thouless energy $E_T = \frac{\hbar D}{L^2}$, gives the equations of motion for the parameters θ and χ are:

$$\begin{aligned} \partial_x \theta = -2iE \sinh(\theta) + \frac{1}{2} (\partial_x \chi)^2 \sinh(2\theta), \\ j_s = \sinh^2(\theta) \partial_x \chi, \\ \partial_x j_s = 0 \end{aligned} \tag{5.13}$$

Unlike in chapter I, where only the homogeneous, spatially invariant, solution to the Green's function was of interest, in this case the spatial dependence is essential for describing the properties of the system.

The quantity j_s, introduced in the second line of 5.13, is the spectral supercurrent density. In equilibrium the supercurrent flowing along the wire is

$$I_s = \int_{-\infty}^{\infty} \mathrm{Im}(j_s) f_L(E) dE \tag{5.14}$$

where $f_L(E)$ is the odd component of the distribution function. In equilibrium $f_L(E) = \tanh(\frac{E}{2k_B T})$. The third equation in 5.13 simply states that the current is conserved along the wire.

The NS interfaces at the end of the wire impose boundary conditions for equation 5.13, which can be described by a scattering matrix for interfaces of arbitrary transparency [95]. For an ideal interface the boundary condition is just given by the continuity of the Green's function. If the volume of the normal wire is sufficiently small compared to the volume of the superconductors, one can assume that the order parameter is unmodified in the reservoirs. The θ in the reservoirs is then $\theta_{reservoir} = \mathrm{arctanh}(|\Delta|/E)$. As the absolute value of the phase

of the pairing potential is not observable, but only the phase difference, the phases of the two superconducting leads can be set to $\chi_L = -\varphi/2$ and $\chi_R = \varphi/2$, where φ is the total phase difference.

With Δ, E_T, or rather the ratio of the two, and φ as the parameters properties of an SNS junction can now be calculated. For a diffusive superconductor the coherence length is set by the diffusion constant $\xi = \sqrt{\frac{\hbar D}{\Delta}}$. The ratio Δ/E_T therefore classifies the junction based on its length compared to the coherence length.

A short junction $L < \xi$ corresponds to $\Delta/E_T < 1$, in which case the superconducting correlations "leak" into the wire and proximitize it completely, with the $\varphi = 0$ density of states similar to the one of the superconductor. In the limit of a long junction $L > \xi$ ($\Delta/E_T > 1$) the structure of the induced DOS, as well as the spectral supercurrent j_s, are set solely by the Thouless energy [96]. In the wire a position independent mini-gap is induced with the spectral gap equal to $E_g(\varphi = 0) \approx 3.1E_T$ [97]. Figure 5.9 shows the spatial dependence of the DOS for a long junction.

Junctions of intermediate length show properties of both: within $\approx \xi$ from the superconducting reservoirs a peak in the DOS at $E = \Delta$ appears while in the center of the wire the DOS is similar to the one of the long junction (see figure 5.10).

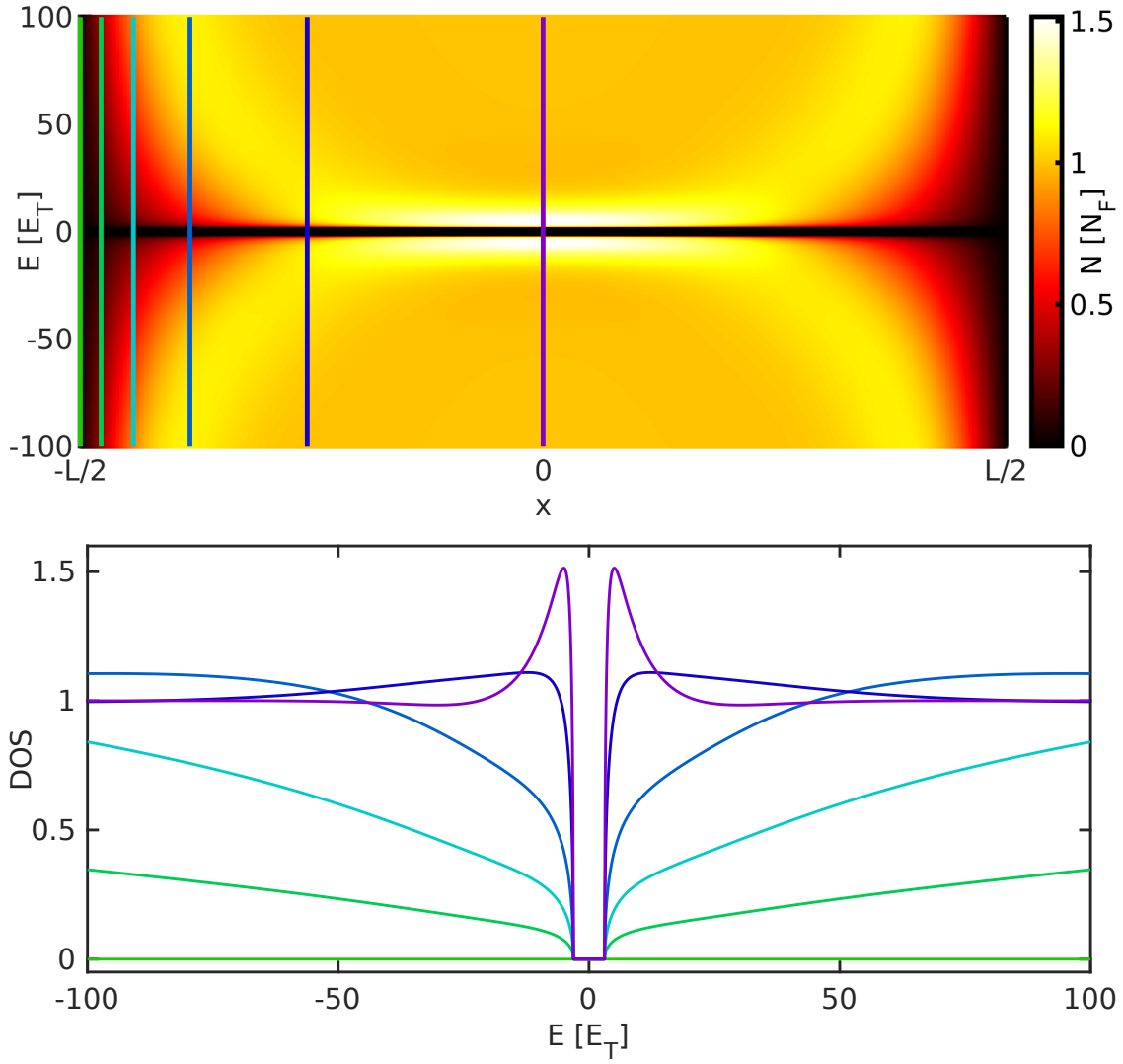

Figure 5.9: The top panel shows a colormap of the DOS in the long junction limit, as a function of the energy and position along the wire. Cuts along the colored lines are shown in the bottom panel. Close to the superconducting leads there are no states, while in the middle of the wire a spectral gap of $\approx 3.1E_T$ opens up. The calculation was performed for $\Delta/E_T = 1000$ and $\varphi = 0$.

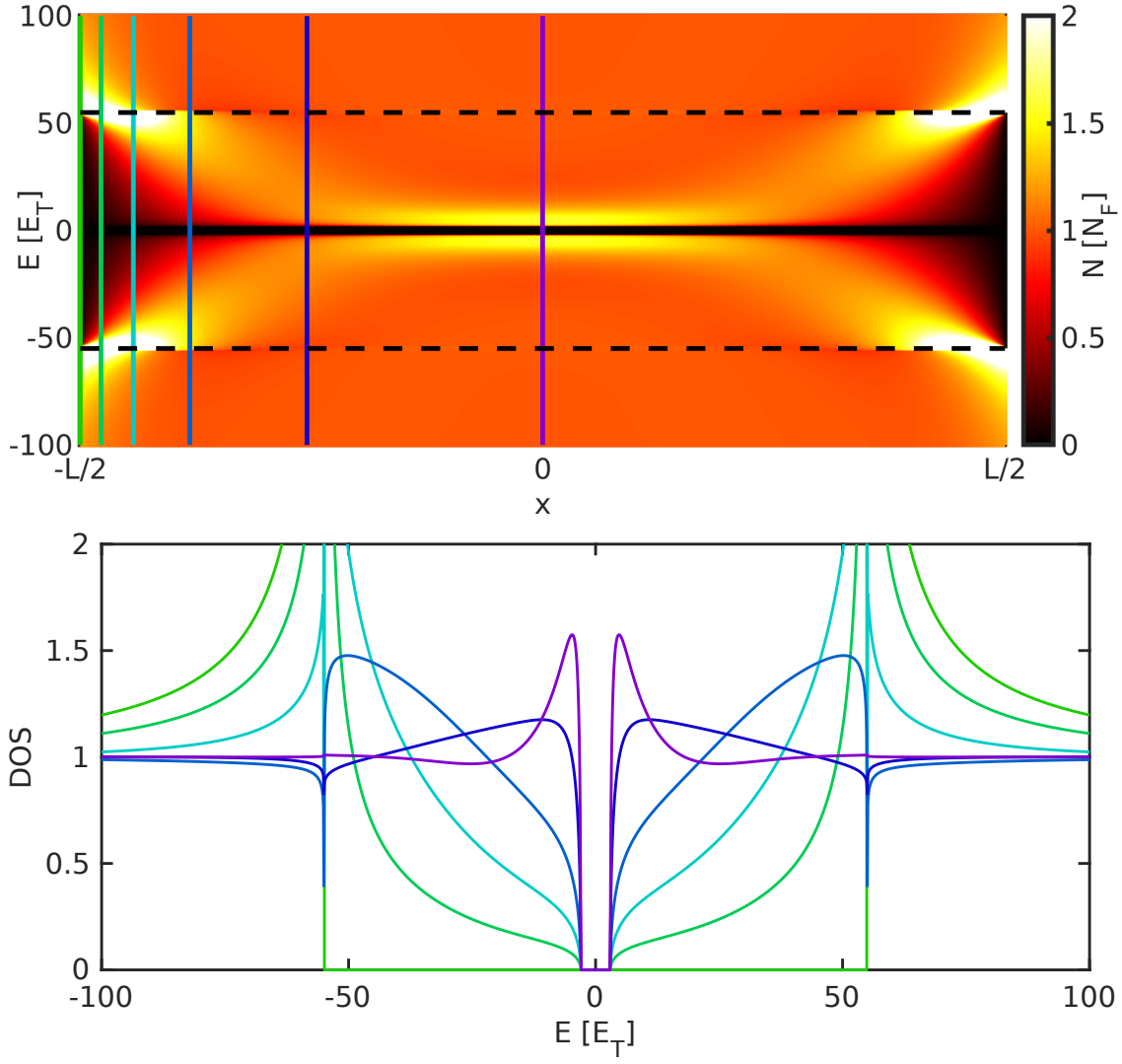

Figure 5.10: The top panel shows a colormap of the DOS of a junction of intermediate length, as a function of the energy and position along the wire (the black dashed line indicates $E = \Delta$). Line cuts along the colored lines are shown in the bottom panel. Close to the superconducting leads the DOS resembles that of a BCS superconductor, while in the middle of the wire a spectral gap of $\approx 3.1 E_T$ opens up. The calculation was performed for $\Delta/E_T = 55$, which is the value found in the experiment, and $\varphi = 0$.

At nonzero phase gradients the mini-gap in the proximitized wire is modulated roughly as $E_g(\varphi) \approx |\cos(\varphi/2)|3.1E_T$, and closes completely at $\varphi = \frac{\pi}{2}$ [97]. For intermediate and long SNS junctions at the center of the wire the DOS is not strongly dependent on the wire length - the phase dependence of the induced minigap is shown in figure 5.11.

By solving the set of equations 5.13 it can be seen that a nonzero φ induces a nonzero gradient of the complex phase χ and therefore a finite supercurrent will flow along the wire. Figure 5.12 shows the evolution of $\mathrm{Im}(j_s)$ as a function of the energy and the phase difference φ.

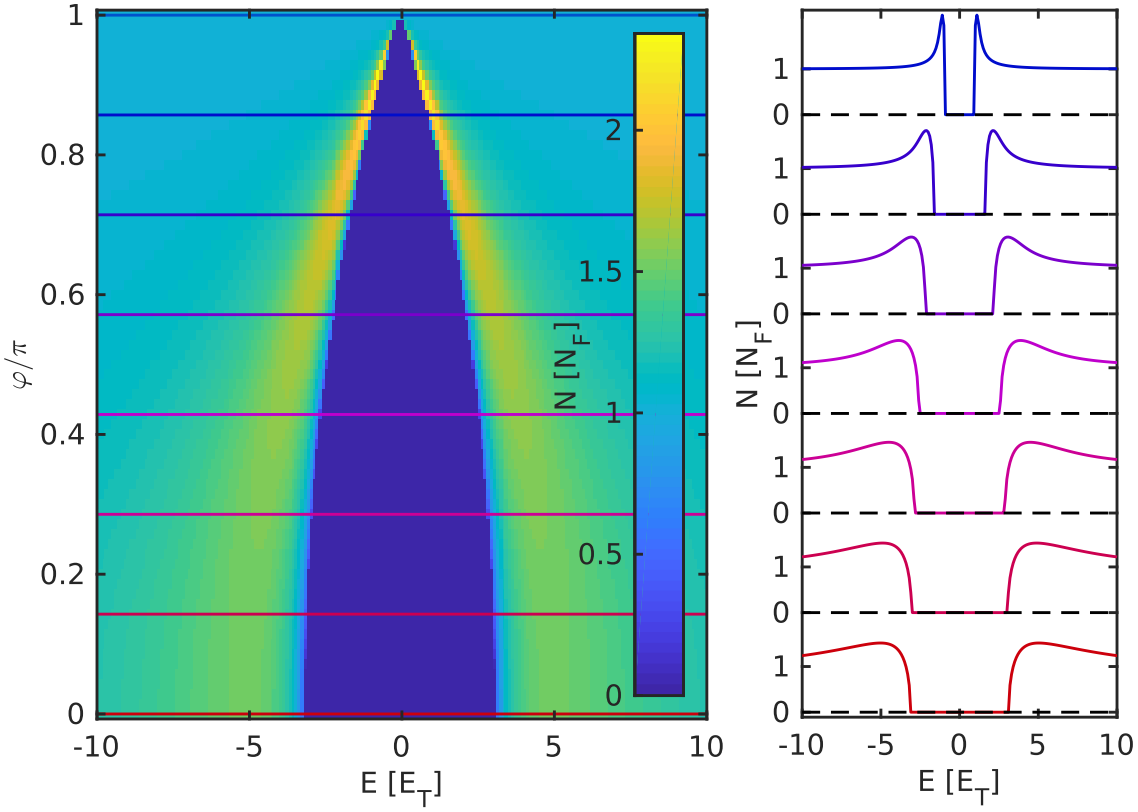

Figure 5.11: A colormap of the DOS of the proximitized wire as a function of the energy and the phase difference φ (left panel). The colored horizontal lines correspond to the different traces shown in the right panel. The calculation was performed for $\Delta/E_T = 1000$ at $x = 0$.

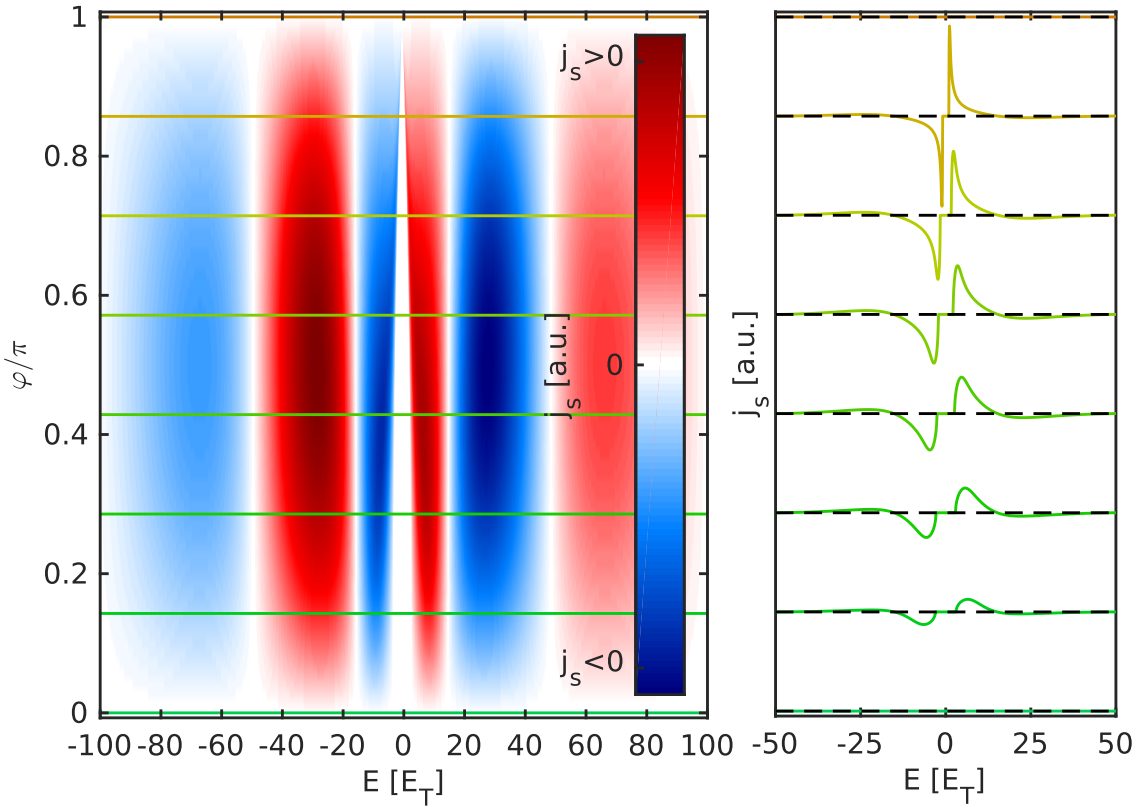

Figure 5.12: Left: a colormap of the imaginary part of the spectral supercurrent j_s as a function of energy and the phase difference φ. The contrast is enhanced to highlight the quasi-periodic changes in the sign of j_s as a function of energy. The horizontal colored lines correspond to the slices shown in the right panel, where the rapid decay of $|j_s|$ as a function of energy can be seen. The calculation was performed for $\Delta/E_T = 1000$ at $x = 0$.

At *thermal* equilibrium to obtain the total current through the junction, $\mathrm{Im}(j_s)$ should be multiplied by $f_L = \tanh(\frac{E}{2T})$ (eq. 5.14) to account for the thermal activation of the current carrying states, and integrated over energy. Figure 5.13 shows the current-phase relation of a long junction at different temperatures. The high temperature traces, $k_BT > 5E_T$, show a sinusoidal current-phase relation, while at low temperatures the current-phase becomes anharmonic and the maximum shifts towards $\varphi = \pi$.

To understand this, $j_s(\varphi, E)$ can be Fourier transformed into $j_s(n, E)$ such that $j_s(\varphi, E) = \sum_{n=1} j_s(n, E)\sin(n\varphi)$ [78]. The energy dependence of the first five harmonics of $j_s(n, E)$ is shown in figure 5.14 - only the first harmonic has a contribution at energies larger than $\approx 10E_T$, and the higher order ones are well localized around $E = 0$ - see the left panel of figure 5.14. The total current through the junction is a sum of these terms, weighted by $f_L = \tanh\frac{E}{2T}$. Only when $3.5k_BT < E_g(\varphi) < 3.1E_T$, where $E_g(\varphi)$ is the phase dependent minigap (shown in fig. 5.9), will the higher order harmonics contribute to the current. The current phase relation $I(\varphi)$ can also be expanded as $I(\varphi) = \sum_{n=1}^{\infty} I_{c,n}\sin(n\varphi)$. The amplitudes of the first 5 harmonics as a function of temperature are shown in figure 5.14.

The critical current I_c (the maximum current that can flow through the junction without dissipation) can be found as $I_c = \max(I(\varphi))$, and the phase at which this current is maximized as $\varphi_c = \mathrm{argmax}(I_\varphi)$. The temperature dependence of both of these quantities is shown in

figure 5.15. The low temperature saturation of I_c, which can also be seen in the harmonics shown in fig. 5.14, is due to the fact that the maximum current is obtained at a phase difference smaller than π. Thus the DOS and the spectral supercurrent j_s are gapped at this critical phase φ_c, with a spectral gap of E_g^c. When $3.5k_BT < E_g^c$ the distribution function can effectively be replaced with a sign function; a further reduction in temperature does not result in a higher activation of the current carrying states and so the critical current saturates.

It is important to note that in equilibrium the sign of the n-th harmonic alternates as $(-1)^{(n+1)}$, which is visible directly in figure 5.14, as well as in figures 5.14 and 5.15 as a maximum of the current phase relation shifted towards $\varphi = \pi$ at low temperatures.

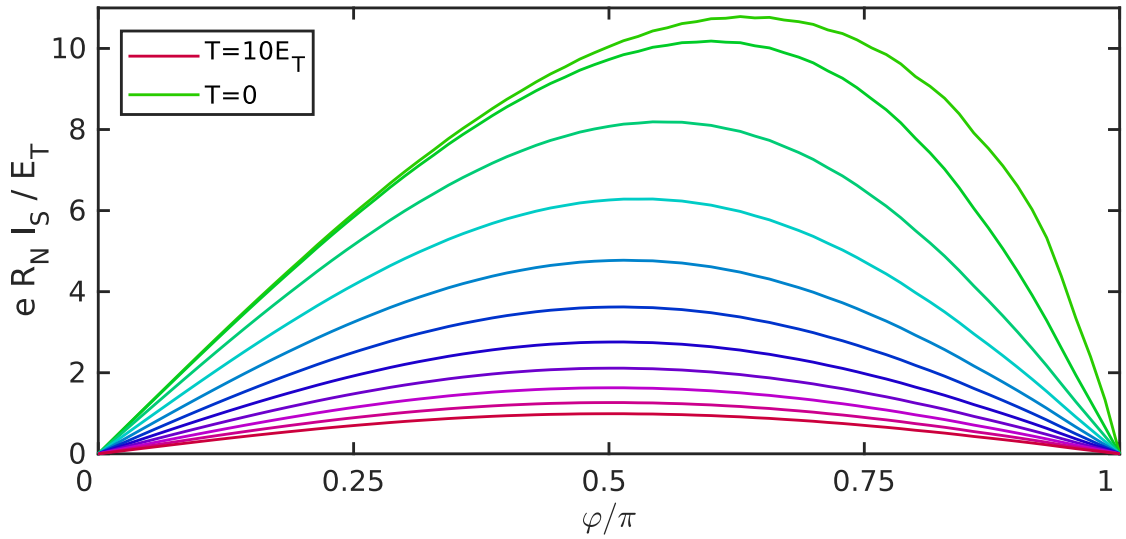

Figure 5.13: The current-phase relation of a long SNS junction ($\Delta/E_T = 1000$), as a function of temperature from $k_BT = 0$ to $k_BT = 10E_t$ in steps of $1E_T$.

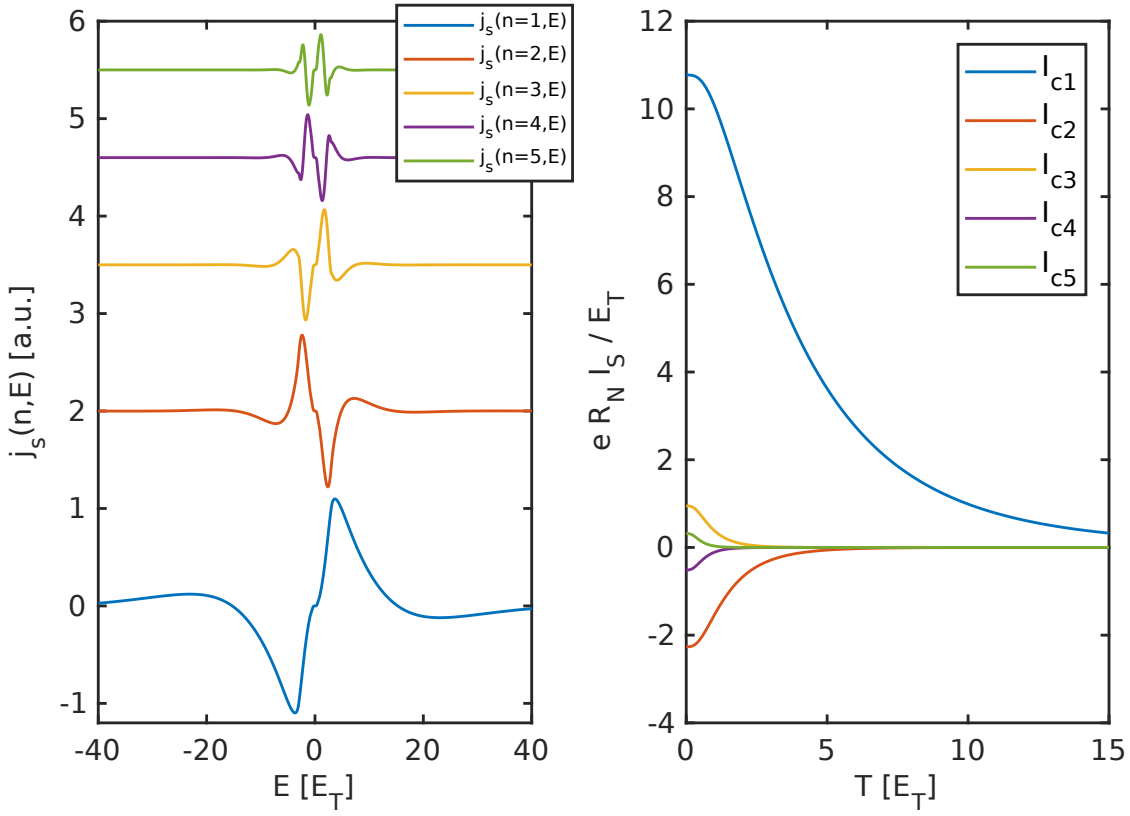

Figure 5.14: Left: the first five harmonics of the spectral supercurrent as a function of energy (the traces are offset for clarity), showing that the higher order contributions are well localized close to $E = 0$, and the alternating sign of the supercurrent with the order. Right: the amplitude of the first five harmonics of the CPR as a function of temperature: the higher order terms become significant close to $k_B T \approx E_T$. The calculation was performed for $\Delta/E_T = 1000$ at $x = 0$.

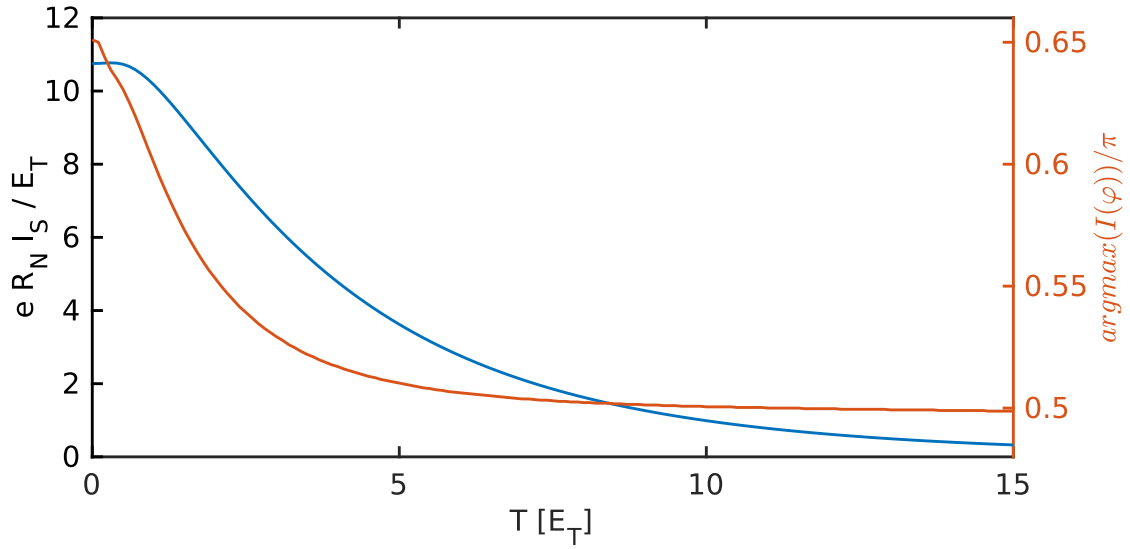

Figure 5.15: The critical current of a long SNS junction (blue, left scale) and the value of φ which maximizes the supercurrent as a function of temperature (red, right scale). The calculation was performed for $\Delta/E_T = 1000$ at $x = 0$.

5.3 Microwave assisted supercurrent is SNS junctions

This section will present an overview of the theoretical results obtained in [82] and how they can be utilized to model the experimental results presented in 6.3.

The paper investigates the effects of high intensity microwave radiation on supercurrents in long diffusive Josephson junctions theoretically, with the aim of explaining the drastic supercurrent enhancements observed in e.g. [76, 84].

As in equilibrium the diffusive SNS junction can be modeled within the quasiclassical Usadel formalism, while the out-of-equilibrium effects can be taken into account through the Keldysh approach (i.e. the equation describing the system is formally the same as 5.9).

In the real time GF approach the microwave field can be included through its vector potential $\vec{A}(t) = \vec{A}_0 \cos(\omega t)$, where ω is the microwave frequency and $\vec{A}_0$ points along the axis of the junction. The vector potential can be assumed to be position independent as the wavelength of the microwaves ($\approx$ 1cm) is much larger compared to the typical lengths of SNS junctions ($< 1\mu$m). A_0 sets the amplitude of the radiation and relates to the s factor, introduced in 5.1.2, as $s = 2eA_0L$. A consequence of this periodic drive is that the Green's function will be time dependent and can be expanded in terms of the harmonics at ω.

By Fourier transforming the Keldysh-Usadel equations to the energy representation the inclusion of the vector potential leads to a coupling between energies E and $E+n\hbar\omega$, resulting in a coupled system of differential equations, which reflect the modulation of the GF at ω.

As heat transport is blocked by the NS interface if the microwave frequency is smaller than the gap in the superconducting reservoirs it is sufficient to solve the Usadel equation only in the normal wire, with the BCS solution imposed as the boundary condition.

The inelastic energy relaxation is modeled within the relaxation time approximation, set by an effective relaxation rate Γ, the amplitude of which can be tuned to match the (temperature dependent) electron-phonon interaction strength. As usual, if Γ is too high the system will always be in equilibrium and if it is too low, the system will be driven out-of-equilibrium, to a state well described by an effective temperature. Thus it is vital to have the possibility of tuning the (effective) Γ in order to observe a nontrivial out-of-equilibrium state.

The kinetic equations, obtained from the Keldysh component, set the distribution function in the normal wire. If the relaxation time is sufficiently longer than the diffusion time the distribution function becomes spatially independent. The kinetic equations then reduce to a balance between the microwave collision integral and the electron-phonon mediated relaxation:

$$\Gamma\langle N\rangle\delta f = \eta^-(E_+)f_+(1-f_0) - \eta^+(E)f_0(1-f_+)\eta^+(E_-)f_-(1-f_0) - \eta^-(E)f_0(1-f_-) \quad (5.15)$$

where $\langle N\rangle$ is the spatially averaged DOS, f_0 is the equilibrium Fermi-Dirac distribution function and δf is the deviation of the distribution function from equilibrium $\delta f = f - f_0$. All quantities with the +/- subscript are evaluated at $E \pm \hbar\omega$. The η^+ and η^- terms are the microwave absorption and emission rates respectively and can be expressed in terms of the components of the (retarded) Green's function (see [82] for details).

In the limit of small microwave power $s < 1$ and low frequencies $\hbar\omega_{RF} < 2E_g(\varphi)$ one can neglect the changes in the spectral equations and solve just the kinetic ones. The absorption

and emission rates then become:

$$\eta^{+}(E) = \eta^{-}(E + \hbar\omega) = \langle NN_{+} + \frac{1}{4}\mathrm{Re}\big[(f^{R} + f^{R*})(f_{+}^{R} + f_{+}^{R*})\big]\rangle \tag{5.16}$$

which gives the Mattis-Bardeen result [98] ($\langle\rangle$ denotes the spatial average). The kinetic equation then recovers the Eliashberg result [81], in which the distribution function develops peaks above the spectral gap spaced by $\hbar\omega$. However, at frequencies $\hbar\omega > 2E_g(\varphi)$, where E_g is the phase dependent spectral gap, this simplification is no longer valid for all powers and the full form of η based on the GF's must be used. Panel b of figure 5.16 shows the absorption rate η_+ calculated using the full theory and the approximate one. The largest difference is at $E = -4E_T = -\omega_{RF}/2$, where the absorption peak is greatly enhanced compared to the Mattis-Bardeen prediction. It induces transitions across the minigap (interband transitions) which will be identified as the key ingredient necessary to explain the experimental results.

After solving the spectral and the kinetic equation, the supercurrent can be in the same way as in equation 5.14, but with the inclusion of the higher order AC harmonics in both the spectral supercurrent and the distribution function. To relate this to the experimentally accessible DC properties the time average needs to be taken. The "low frequency" current-phase relation computed in such a way takes into account the high frequency response of the junction to the applied microwave drive and in the limit of fast relaxation should reproduce the equilibrium Bessel dependence $J_0(s)$ of the critical current with the applied power.

Figure 5.16 shows some of the results presented in [82]: the absorption rate η^+, the nonequilibrium modifications of the distribution function δf and the modified current-phase relation. In contrast to what was found in equilibrium, the second harmonic induced by microwave irradiation (panel a of fig. 5.16) has the same sign as the first one and consequently the critical current is obtained below $\varphi = \frac{\pi}{2}$.

Due to the complexity of the problem, both conceptual and computational, the theoretical part of this work was done in collaboration with Pauli Virtanen and Tero Heikkilä. The numerical simulation and the numerous discussions were vital in understanding the observed effects.

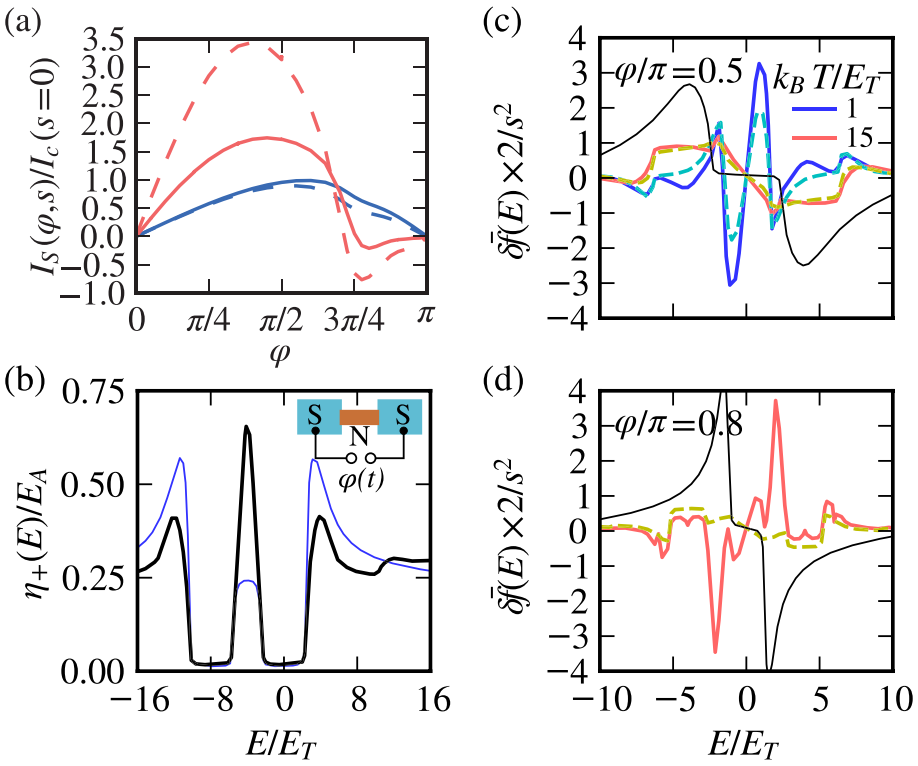

Figure 5.16: Figures adapted from [82]. (a) Current-phase relation normalized to equilibrium critical current at $k_BT/E_T = \{15, 1\}$ (blue and red, respectively) and $s = 0.25$ (solid) and 0.5 (dashed), for $\hbar\omega/E_T = 4$, $\Delta/E_T = 100$ and $\Gamma/E_T = 0.05$. (b) Absorption rate η^+ for a high frequency $\hbar\omega/E_T = 8$ and $\varphi = \pi/2$, $s = 0.25$. Thin line shows the approximation from eq. 5.16. Inset: Schematic representation of the SNS junction. (c) Correction $\delta f = f - f_0$ to the electron distribution function vs energy at two different temperatures for $\varphi = \pi/2$, $\hbar\omega/E_T = 4$, and $s = 0.25$. Solid lines correspond to the exact numerical results and the dashed lines to the approximation in eq. 5.16. The thin black line shows the spectral supercurrent $j_s(E)$ in the absence of microwaves. (d) The same as in (c) for $k_BT/E_T = 15$ and $\varphi = 0.8\pi$.

Chapter 6

Experiment

In this chapter the sample and the measurement technique is presented, followed by a set of measurements used to characterize the sample. The measurement of the direct Josephson emission as a function of microwave power and frequency are presented next, along with theoretical calculations, showing an increased anharmonicity of the CPR under microwave irradiation with a frequency larger than the minigap. The interband transitions induced by the drive are identified as the origin of this effect. At the end an experiment which probes the dynamics of the junction at timescales shorter than the diffusion time $\tau_D = \frac{\hbar}{E_T}$ is briefly discussed.

6.1 Sample fabrication and the experimental setup

The sample was fabricated on top of a Si/SiO_2 substrate, using e-beam lithography with a PMMA 495-A6/PMMA 950-A3 resist bi-layer. The junction is a $L = 400$nm long, $w = 150$nm wide and $d = 40$nm thick Ag wire, while the superconducting reservoirs are $d = 70$nm thick Nb pads - see figure 6.1. The metals were deposited by angle evaporation, where by evaporating at $\theta = 0°$ Ag was deposited everywhere, and the Nb layer was evaporated at $\theta = 45°$ such that the e-beam defined shadow-mask shields the normal wire from it. Because this technique results in a offset between the two layers it creates normal metal shadows next to the S reservoirs (but away from the wire), which act as quasiparticle traps [9] and aid in thermalization.

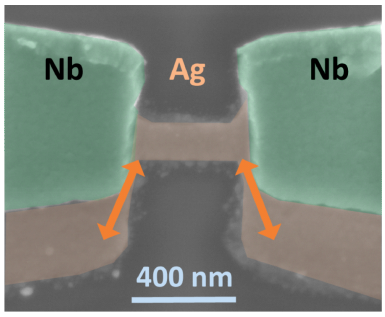

Figure 6.1: An SEM micrograph of the sample showing the Ag wire (brown), the Ag quasiparticle traps (also brown) and the Nb superconducting reservoirs.

The measurements were performed in either a dilution refrigerator or in a pumped ^{4}He

cryostat in the temperature range from $T = 250$mK to $T = 4.2$K.

Both ends of the sample were connected to bias tees to allow for biasing and measurement in the DC (low frequency: DC-100kHz) and the microwave (high frequency: $>$ 100kHz) domains separately. A schematic of the setup is shown in figure 6.2. In DC the sample was current biased and the $V(I)$ or $\frac{\partial V}{\partial I}$ curves were measured. The high frequency drive is realized by connecting one side of the sample to the output of an RF source (through the RF branch of the bias tee). To measure the Josephson emission the other side of the sample was connected to a band-pass filter and the signal was subsequently amplified (the cold amplifier was a "Caltech 1-12 LNA L002" with a gain of $\approx$ 40dB and a noise temperature of $T \approx 10$K, while the gain of the room temperature amplifier was 40dB). The sample was shielded from the wide band RF noise by attenuators on the source side (both room temperature and low temperature ones) and by a cold circulator on the probe side. The transmission of the band-pass filter is also shown in figure 6.2, with a center frequency $f_F \approx 6$GHz and a width of about $\delta f_F \approx 2$GHz. There are two distinct ways in which the Josephson radiation emitted by the sample can be observed. When the Josephson frequency is within the bandwidth of the filter $|n\omega_{DC} - \omega_F| \pm \delta\omega_F = \omega_F$ (as before ω_{DC} is the Josephson frequency set by V_{DC}, and n is an integer enumerating the different harmonics of the CPR) the power of the emitted radiation can be measured directly. Alternatively the nonlinearity of the junction itself can be used to mix with the pump, the Josephson radiation can be up or down converted resulting in a finite power at $\omega = |n\omega_{DC} - m\omega_{RF}|$ where m and n are integers. With this setup the up or down converted radiation will be measurable when $\omega \approx \omega_F$. The technical benefit of measuring in a finite frequency window is that the results are not influenced by the frequency dependence of the attenuation and amplification stages in the setup, which are difficult to control and calibrate for.

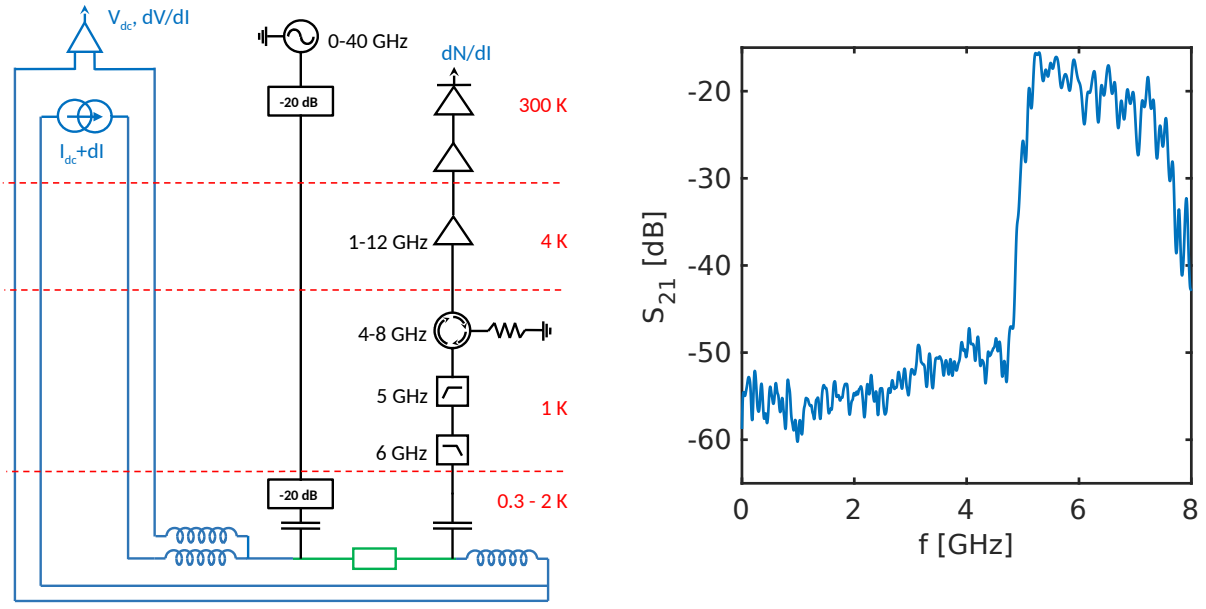

Figure 6.2: Left: the schematic of the experimental setup. Right: the transmission coefficient of the bandpass filter (shown on the left) used to measure the Josephson emission (the rightmost line in the schematic).

6.2 DC measurements and sample characterization

The properties of the sample can be determined by measuring the $V(I)$ or the $\frac{\partial V}{\partial I}$ curves. Figure 6.3 shows the $V(I)$ curve of the sample measured at $T = 1.6$K (to avoid thermal hysteresis), along with a fit which includes the Langevin noise, which gives the following values: $I_c = 5.24\mu$A, $R_N = 1.4\Omega$ and $\gamma = 22.6$. The square root $V(I)$ curve predicted by the RSJ model ($\gamma \to \infty$) is also shown in the same figure, for the same value of I_c, and is quite different than the measured one. The effective noise temperature for the extracted value of γ is $T_N \approx 11$K. This rules out the Johnson noise of the normal state resistance as the source of the fluctuations, they likely originate from the insufficient filtering and the broad band ($BW > 40$GHz) of the RF line which is used for the microwave drive and should be only weakly temperature dependent.

The most straightforward way of measuring the critical current, or the width of the Shapiro steps, is to define a threshold voltage V_{th} and to obtain the critical current as $I_{c,m} = argmax(V(I) < V_{th})$. Likewise the measurement of the differential resistance can be used in the same way yielding $I_{c,m} = \text{argmax}(R(I) < R_{th})$ where R_{th} is now the threshold resistance. These two methods, although slightly different, give consistent results. Similarly the width of the Shapiro steps can be measured as the range of I which satisfies $|V(I) - V_{sh}| < V_{th}$ where $V_{sh} = \frac{\hbar\omega_{RF}}{2e}$. These approaches are compatible with a counting experiment, in which I is ramped and the time during which the previously defined conditions are met is measured. The major benefit of this approach is that a high resolution measurement can be made with a high repetition rate, giving a statistically precise result. The drawback is that the low value of γ reduces the accuracy, as there isn't a cusp which clearly identifies the transition to the dissipative regime. The difference between the extracted value $I_{c,m}$ and the true value I_c is shown in figure 6.4. For the sake of simplicity the argument is made for the $R(I)$ measurements, but the conclusions are applicable to the other approach as well. The upper inset shows the $R(I)$ curve as well as its fit, corresponding to the $V(I)$ curve shown in figure 6.3. The black dashed line shows an example of a threshold resistance value that was typically used in the experiment. As the main focus of the latter results will be on the microwave power dependence of the critical current this is utilized for the demonstration, the colorplot show the differential resistance R as a function of the applied power s and the DC bias current I_{DC} under the assumption that $I_c(s)$ behaves as $I_c(s) = I_{c0}J_0(s)$, where J_0 is the zeroth order Bessel function. The red trace shows the $I_{c,m}$ obtained for a relatively low threshold value, which differs substantially from the ground truth (black curve). However, as the bottom inset shows the difference between the two is just a multiplicative factor. If one is only interested in the shape of this curve, as will be the case later, and not the absolute value, this approach gives adequate results.

To further characterize the junction the $I_c(T)$ was measured, which is shown in figure 6.5. $I_c(T)$ can be computed from the microscopic theory, or more directly by summing over the Matsubara frequencies as done in [99], and gives a functional form $I_cR_N = f(\Delta, E_T, T)$, where Δ is the pairing potential in the superconducting reservoirs, and E_T the Thouless energy. Based on the measurement of $T_c \approx 6.6$K (or equivalently $\Delta \approx 1$meV), it can be safely assumed that Δ will be roughly constant below $T = 2$K. The reduced value of the critical temperature, compared to the reference value of $T_c \approx 9.3$K [100], is due to the out-gassing of the PMMA resist during the evaporation of the Nb layer and the oxidation of the thin leads after lift-off. The value of E_T extracted by fitting the experimental data (black trace

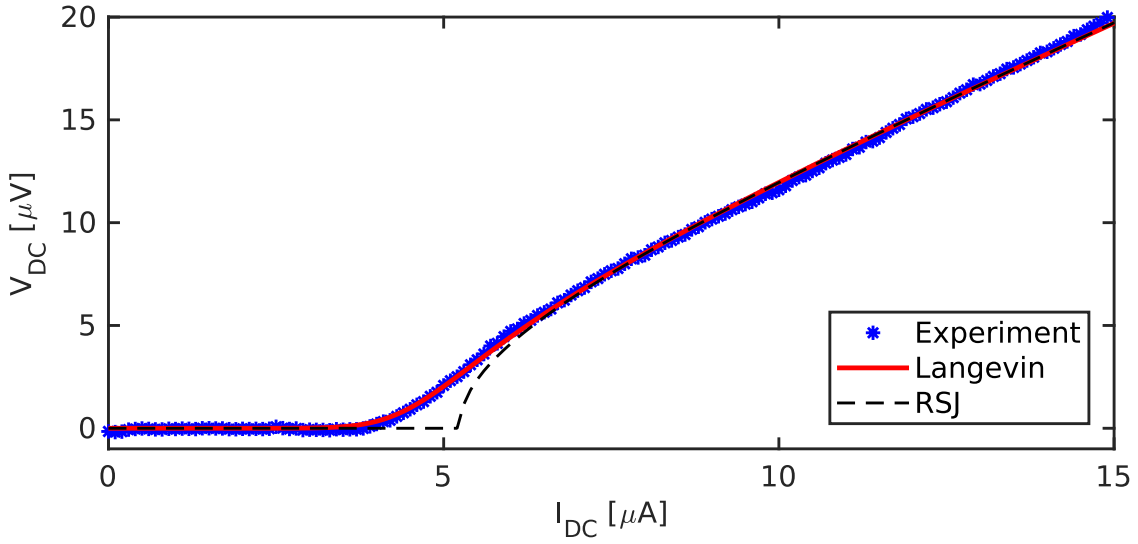

Figure 6.3: The $V(I)$ curve of the sample measured at $T = 1.6$K (blue dots), the Langevin fit with $\gamma = 22.6$ and $I_c = 5.25\mu$A (red line), and the RSJ square root curve with the same I_c.

on figure 6.5) is $E_T = 19\mu$eV. Two additional junctions were made in the same geometry but with wire lengths $L_2 = 250$nm and $L_3 = 150$nm, and their Thouless energies are found to be $E_{T3} = 25\mu$eV and $E_{T3} = 36\mu$eV, respectively. Overall the Thouless energy scales as $\propto L^{-2}$ with an effective length which is about ≈ 250nm larger than the geometrical one. The same effect was observed before, e.g. in [99], and can be attributed to the reduction of Δ close to the NS interface, either due to the inverse-proximity effect or the intrinsic reduction of the pairing potential as a consequence of the fabrication process.

When the current is ramped from $I_{DC} = 0$ upwards one measures the critical current as the transition to the dissipative state. However, when the current is ramped down the value at which the system transitions back to the non-dissipative state, the retrapping current I_r (also shown in figure 6.5), can be different from I_c. Above I_c the finite voltage leads to Joule heating which can raise the temperature substantially. The effective electron temperature T_{eff} is the result of a balance between the Joule heating and the electron-phonon mediated cooling, which leads to the following law $T_{eff}^5 = T^5 + P/K$ [101, 15], where T is the temperature of the phonon bath, P the dissipated power in the junction, and K the effective electron-phonon coupling. The value of $K = \Omega\Sigma$ where Σ is the electron-phonon scattering rate, and Ω the geometric volume of the normal wire (as heat transport is blocked by the NS interface at the end of the junction the volume and the value of Σ are set by the normal metal part only). At low temperatures a small value of P will lead to a significant increase of T_{eff} and I_c and I_r diverge, while the same P at higher temperatures will lead only to a minor increase in T_{eff} and the two coincide - see figure 6.5.

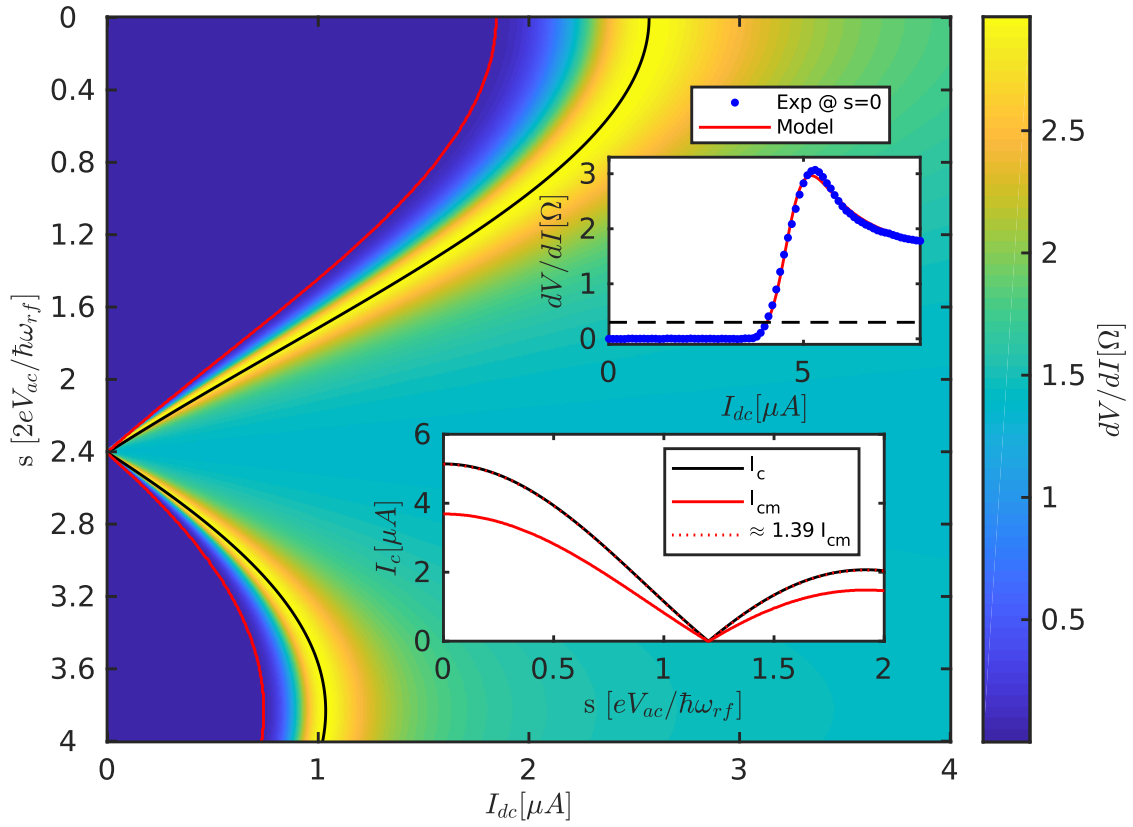

Figure 6.4: The simulated differential resistance of an SNS junction with a finite Langevin term $\gamma = 22.6$ as a function of the DC bias current and the applied microwave power s assuming that $I_c(s) = J_0(s)I_c^0$. Top inset: the differential resistance of the sample measured at $T = 1.6$K and $s = 0$ (blue dots) along with the Langevin fit (red line). The black dashed line corresponds to a threshold resistance used to experimentally determine the critical current. Bottom inset: a comparison between the simulated critical current measurement $I_{c,m}$ (based on the threshold voltage of the top inset and the model of the main panel) and the ground truth $I_cJ_0(s)$, which can be recovered from the measured value by rescaling the data with an appropriate coefficient.

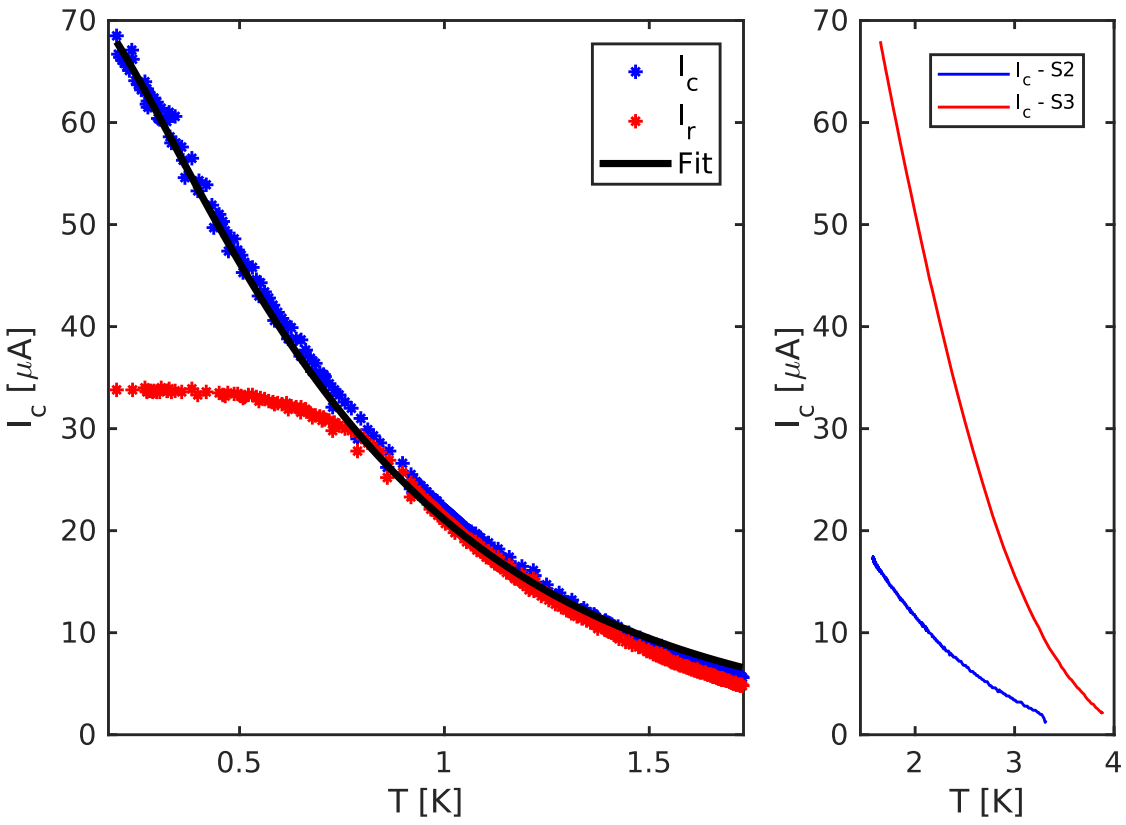

Figure 6.5: Left: The critical (blue dots) and the retrapping (red dots) current of the longest sample as a function of temperature, as well as a fit with $E_T = 19\mu$eV (black line). Right: The critical currents of the shorter two samples as a function of temperature.

The value of K can be extracted from $I_r(T)$ by fitting the temperature and frequency dependence of the Shapiro steps. Both were performed and led to the same results. Here the second option is presented as it allows to verify the energy dependence of the electron-phonon cooling. Figure 6.6 shows the evolution of the $R(I)$ with the applied microwave power. At low powers the $R = 0$ state is found only below I_c (bottom trace), and as the power is increased several dips in the $R(I)$ curve appear, which correspond to different constant voltage steps in the $V(I)$ curve. The dominant one is located at $2eV = \hbar\omega$, which is the 1st Shapiro originating from the $I_{c,1}\sin(\varphi)$ component of the current phase relation. Other steps, which may not be perfectly flat (i.e. $\frac{\partial V}{\partial I} > 0$) also appear at $2(2eV) = \hbar\omega$ (the 2nd harmonic of the CPR), $3(2eV) = \hbar\omega$ and $3(2eV) = 2\hbar\omega$ (the 1st and 2nd Shapiro steps coming from the 3rd harmonic of the CPR) and lastly at $4(2eV) = \hbar\omega$ (the fourth harmonic of the CPR), see the annotation in figure 6.6. As the data was taken at $T = 1.6\text{K} \gg \frac{E_T}{k_B}$ the current-phase relation should have been almost purely sinusoidal, and only the step at $2eV = \hbar\omega$ should be present. The origin of these higher order harmonics is still debated and will be discussed later on (see also [99, 102]).

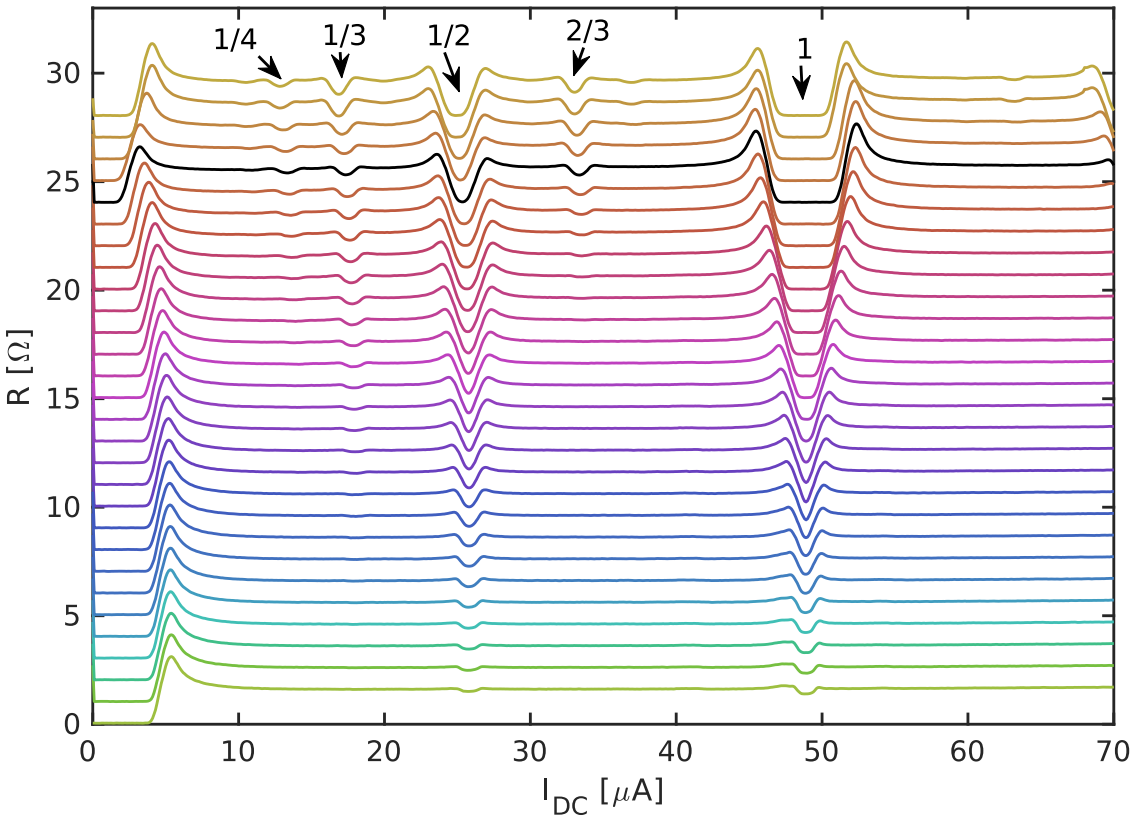

Figure 6.6: The differential resistance of the sample as a function of I_{DC} and the microwave power (at the source) starting from $P = -10$dBm to $P = 17$dBm in 1dBm steps. The black trace is the one which maximizes the width of the 1st Shapiro step. The steps are labeled in the following way: n/k denotes the n-th Shapiro step of the $k-th$ CPR harmonic; in equilibrium the full width of the step is given by $2I_{c,k}J_n(ks)$. $n/k = 1/1$ is abbreviated as 1. The data was taken at $T = 1.6$K and the irradiation frequency was $f = 35.18$GHz.

With the goal of determining K only the first harmonic of the current phase relation is considered, in particular the frequency dependence of the maximum width of the 1st Shapiro.

As the resistance of the sample $R_N \approx 1.4\Omega$ is much smaller than the characteristic impedance of the RF lines (50Ω), it is appropriate to assume that the sample is current biased by the microwaves. As was shown in section 5.1.2, at low irradiation frequencies the nonlinearity of the junction close to the critical current reduces the width of the Shapiro steps, only when it is larger than $f = 2eI_cR_Nh^{-1}$ the full width of the 1st Shapiro step becomes $2I_cJ_1(s_1 = 1.84)$ ($s = 1.84$ maximizes J_1) - see figure 5.5.

Figure 6.7 shows the maximum width of the 1st Shapiro step as a function of f_{RF} at $T = 1.38$K. Unlike the RSJ prediction at high frequencies the step width decreases. This is attributed to overheating as elaborated below. The power dissipated at the junction is the sum of the DC and RF powers $P = P_{DC} + P_{RF}$, where $P_{DC} = \frac{V_{DC}^2}{R_N} = \frac{\hbar^2\omega_{RF}^2}{4e^2R_N}$ and $P_{RF} = \frac{V_{RF}^2}{2R_N} = \frac{s_1^2\hbar^2\omega_{RF}^2}{8e^2R_N}$. The dissipated power increases the effective electron temperature which in turn reduces I_c.

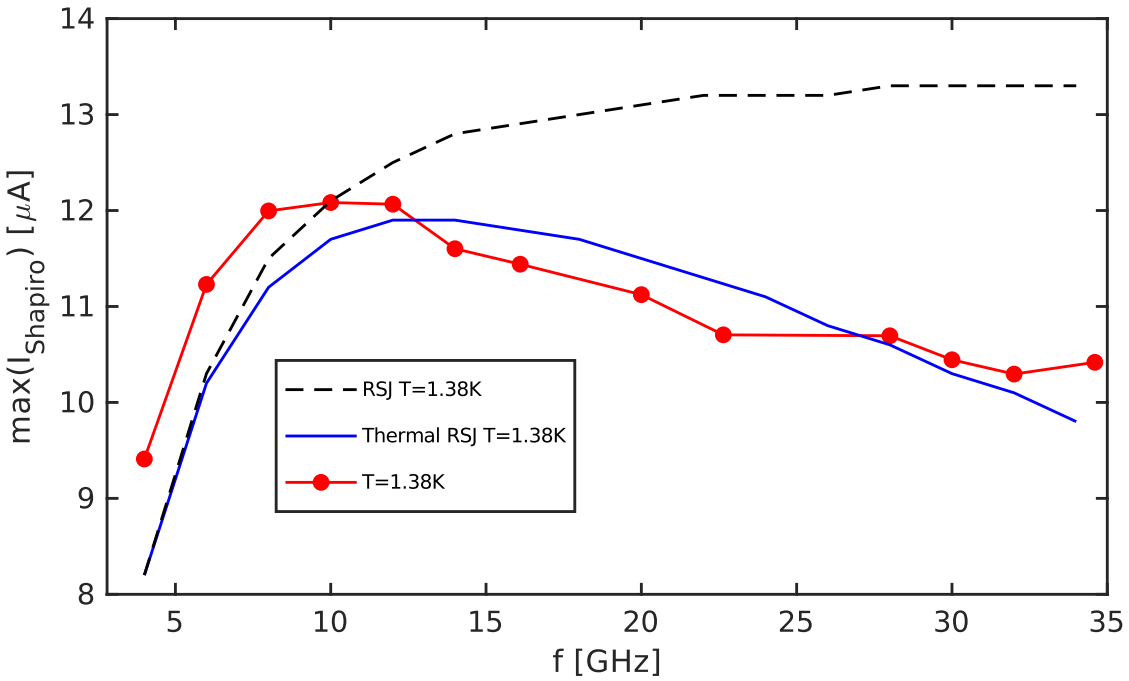

Figure 6.7: The measured maximum width of the 1st Shapiro step as a function of the drive frequency at $T = 1.38$K (the power was chosen such that the step width is maximized). Compared to the RSJ result (dashed trace) there is a reduction of the step width due to overheating, which can be modeled with $I_c(T^*)$ (blue trace).

Focusing only on frequencies larger than $f = 2eI_cR_Nh^{-1}$ enables a direct probe of K, where the Shapiro width should be $2J_1(s_1)I_c(T_{eff}) \approx 1.16I_c(T_{eff})$. From the previously found $I_c(T)$ dependence the data can be modeled as $I_{shapiro} = \alpha I_c(T_{eff} = \sqrt[5]{P_{tot}(\omega_{RF})/K + T^5})$, where α and K are fitting parameters and T the phonon temperature. Figure 6.8 shows the temperature dependence of the maximum Shapiro step width for several RF frequencies (colored lines), the fits based on this model (dashed lines), and the extracted parameters in the inset graph. The simple model is able to reproduce the data well, which confirms the electron-phonon interaction as the cooling mechanism. The small frequency dependence of the parameters is not understood. At high frequencies, where most of the emission measurements

were taken the parameters are approximately constant. The value obtained for α is consistent with the expected value $\max(2|J_1(s)|) = 1.164$.

K is the product of the electron-phonon scattering rate (for Ag the electron-phonon scattering rate is $\Sigma \approx 3\frac{\mathrm{nW}}{\mu\mathrm{m}^3\mathrm{K}^5}$ [103]) and the volume of the sample. To reproduce the value of $K \approx 2.8\frac{\mathrm{nW}}{\mathrm{K}^5}$, found at high frequencies, results in an effective volume about 300 times larger than the geometrical one. As there is no reason for Σ to be greatly enhanced this is understood to be the effect of the normal metal quasiparticle traps, which are the result of the angle evaporation (see fig. 6.1). Using the extracted values of K, the electron-overheating can be included in the RSJ model as $I_c(T_{eff})$, where T_{eff} is found by iteratively computing the dissipated power and solving the RSJ model at the obtained I_c until convergence. Figure 6.7 also shows the RSJ model with and without overheating computed for the base temperature of $T = 1.38$K.

In summary, at $T = 1.6$K the electron-overheating due to the dissipated power is limited for voltages below $V_{DC} = 100\mu$V, or equivalently frequencies below ≈ 48GHz; the estimated reduction of the I_c is at most 5%. Thus by performing measurements at this temperature enables one to explore novel nonequilibrium effects, beyond the well understood thermal ones.

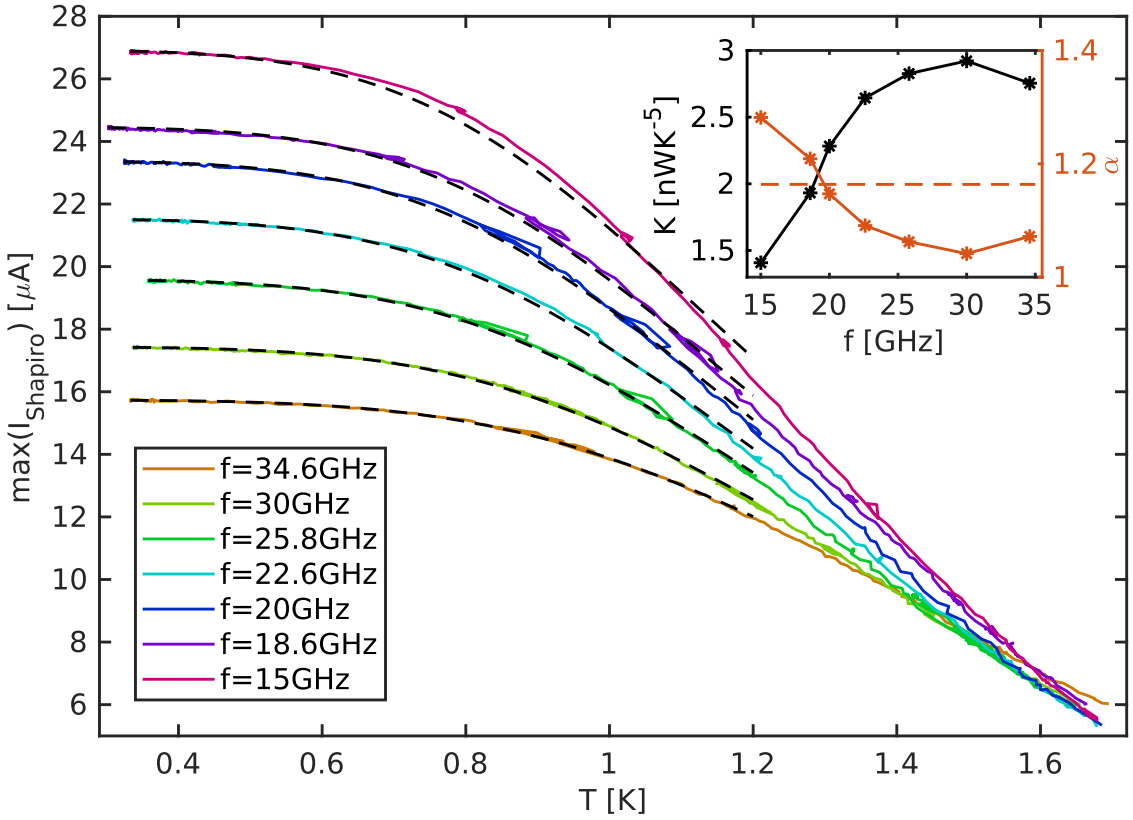

Figure 6.8: The measured temperature dependence of the maximum Shapiro step width for several frequencies (all above $2eI_cR_N\hbar^{-1}$) as a function of temperature. Due to the electron overheating the steps saturate to a frequency dependent value at low temperature. A thermal model (black dashed traces), allows for the extraction of the effective electron-phonon coupling (shown in the inset).

6.3 Direct measurements of the Josephson emission

When the DC voltage across the Josephson junction is equal to $2eV_{DC} = \hbar\omega_F$ the power measured by the detector is proportional to $N \propto I_{c,1}^2$. Likewise $n2eV_{DC} = \hbar\omega_F$ probes $I_{c,n}^2$ with the same proportionality factor. Figure 6.9 shows the microwave detector power as a function of the voltage across the junction (see the measurement circuit 6.2), which exhibits two separated peaks A and B, centered at $V_A \approx 6\mu$V and $V_B \approx 12\mu$V. The data can be reproduced perfectly if the spectrum of the Josephson radiation is modeled by two Gaussian distributions centered at ω_{DC} and $2\omega_{DC}$, and by convolving it with the profile of the filter (figure 6.2).

The amplitudes and widths of the Gaussians are fitting parameters, the best fit is obtained for $\frac{A_B}{A_A} = 25$, $\sigma_A = 5\mu$V and $\sigma_B = 1.1\mu$V. One should expect that $\sigma_A > \sigma_B$ as their widths are set by $n2e\delta V = \hbar\delta\omega$. The voltage noise δV is set by $R_N(I)\delta I$, where $R_N(I)$ is the differential resistance and δI the noise of the current biasing circuit. Although the value of $\frac{\sigma_B}{\sigma_A}$ predicted in this way is slightly lower than the observed one, the order of magnitude of the smearing is consistent with thermal noise in a bandwidth of ≈ 40GHz.

The origin of the peak at $4eV = \hbar\omega_F$ can, in principle, have two contributions. The first is the intrinsic presence of the 2nd harmonic in the CPR and the second one is due to the nonlinearity of the junction at low bias currents as shown in figures 5.7 and 5.8. The observation of the Shapiro step at twice the frequency even at low RF power, shown in 6.6, suggests that the second harmonic is in fact present in the CPR, but the ratio of these two contributions cannot be gauged from this measurement. Higher order harmonics, which should as well be present based on the Shapiro steps - see figure 6.6, are vanishingly small and could not be observed in direct emission..

In the following the Josephson emission will be used as a probe of the harmonic content of the CPR to investigate how it is modified by microwave irradiation of variable power and frequency. The amplitude of the detected emission power versus the applied power and I_{DC} is shown in figure 6.10 for two frequencies $f = 20.72$GHz and $f = 35.17$GHz. Two peaks corresponding to the first two harmonics, labeled A and B, are visible but their amplitudes are strongly modified by the RF field. They do not appear at the same I_{DC} due to the changing critical current as a function of the applied power (see figure 6.11).

Assuming that the peak A originates only from the 2nd harmonic, the CPR can be reconstructed as $I^r(\varphi) \propto \sqrt{B}\sin(\varphi) + \sqrt{A}\sin(2\varphi)$, and the critical current can be found as $I_c^r = \max(I^r(\varphi))$. Then the value measured in DC I_c^m, as described in the section 6.2, can be compared to the reconstructed one, with the proportionality factor as a free parameter the comparison is shown in figure 6.11. The main finding of these measurements is that if the irradiation frequency is higher than the $2E_g(\varphi_0)$ the critical current will be nonzero, and even comparable to the one at $s = 0$. This cannot be explained with an adiabatic current phase relation in the form $I(\varphi, s) = I_{c,1}J_0(s)\sin(\varphi) + I_{c,2}J_0(2s)\sin(2\varphi)$ with a constant $I_{c,1}$ and $I_{c,2}$. The reasonable agreement between the emission-reconstructed critical current and the DC one implies that the junction nonlinearity results in a negligible contribution to peak A and that the detected power is a reliable probe of harmonic-resolved critical current. Moreover, as the value obtained at a finite voltage and the one obtained in DC coincide, the effect of the $V_{DC} > 0$ is limited to driving the phase at the corresponding frequency without further modifying the harmonic content of the CPR. This finding has two important consequences: firstly the Josephson emission can be used as a good probe of the low frequency current phase

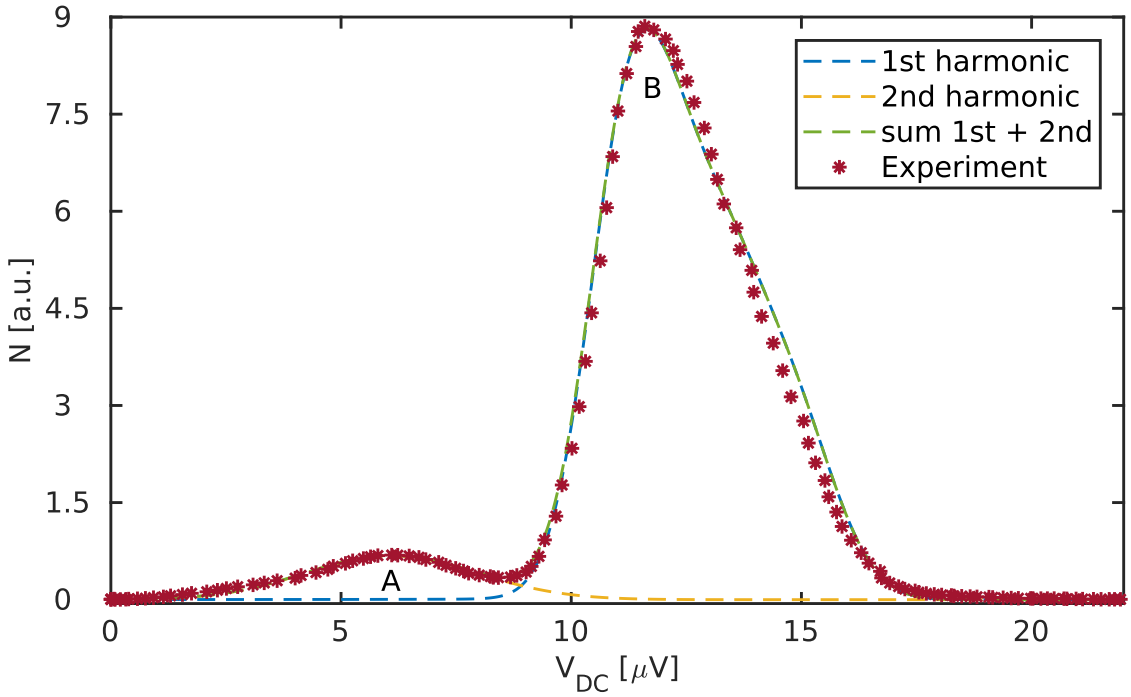

Figure 6.9: The amplitude of the Josephson emission power (in arbitrary units) as detected by the setup as a function of the voltage across the sample. Two peaks, A and B, are visible, centered at $\approx 6\mu$V and $\approx 12\mu$V, respectively. This is consistent with the emission originating from the 2nd and 1st harmonic of the CPR through a filter with a center frequency of $\approx$ 6GHz. The measurement was performed at $T = 1.6$K and no applied RF power.

relation and secondly the nonequilibrium theory (sec. 5.3) developed for $V_{DC} = 0$ can be utilized to describe the system.

Figure 6.12 shows the amplitudes of peaks A and B as a function of the applied power (upper two panels). In adiabatic equilibrium the effect of the microwave drive is to modulate the $I_{c,n}$ as $J_n(s)$, which is also shown in the same figure. At low powers the measurements can be explained by the Bessel function, but at higher ones, and especially if the frequency is high (right panel), there is a striking increase of the second harmonic, pointing to a nonequilibrium effect.

The nonequilibrium theory presented in section 5.3 is now used to calculate the time-averaged adiabatic current phase relation. Using the parameter values extracted from the experiment gives the bottom two panels of figure 6.12. The Eliashberg approximation (i.e. replacing the absorption rate by the one given by equation 5.16) predicts that the 1st harmonic behaves qualitatively as $J_0(s)$, but severely underestimates the amplitude of the 2nd harmonic. Taking the AC harmonics of the Green's function in the expression for η gives a correct amplitude of the 2nd harmonic at higher powers, which implies that the AC component of the spectral supercurrent plays an important role. At $s = 0$ the theory reduces to the equilibrium one and the amplitude of the 2nd harmonic vanishes for $k_BT/E_T > 5$ (see figure 5.14). To explain the power dependence of the 2nd harmonic amplitude qualitatively a term can be added by hand as $I_{c,2} = I^0_{c,2}J_0(2s) + I^{th}_{c,2}(s)$, where $I^{th}_{c,2}$ is the calculated value and $I^0_{c,2}$ accounts for the second harmonic at $s = 0$, which yields a satisfying result in the full range of s. It's possible to consider the effects of the junction nonlinearity as well, which

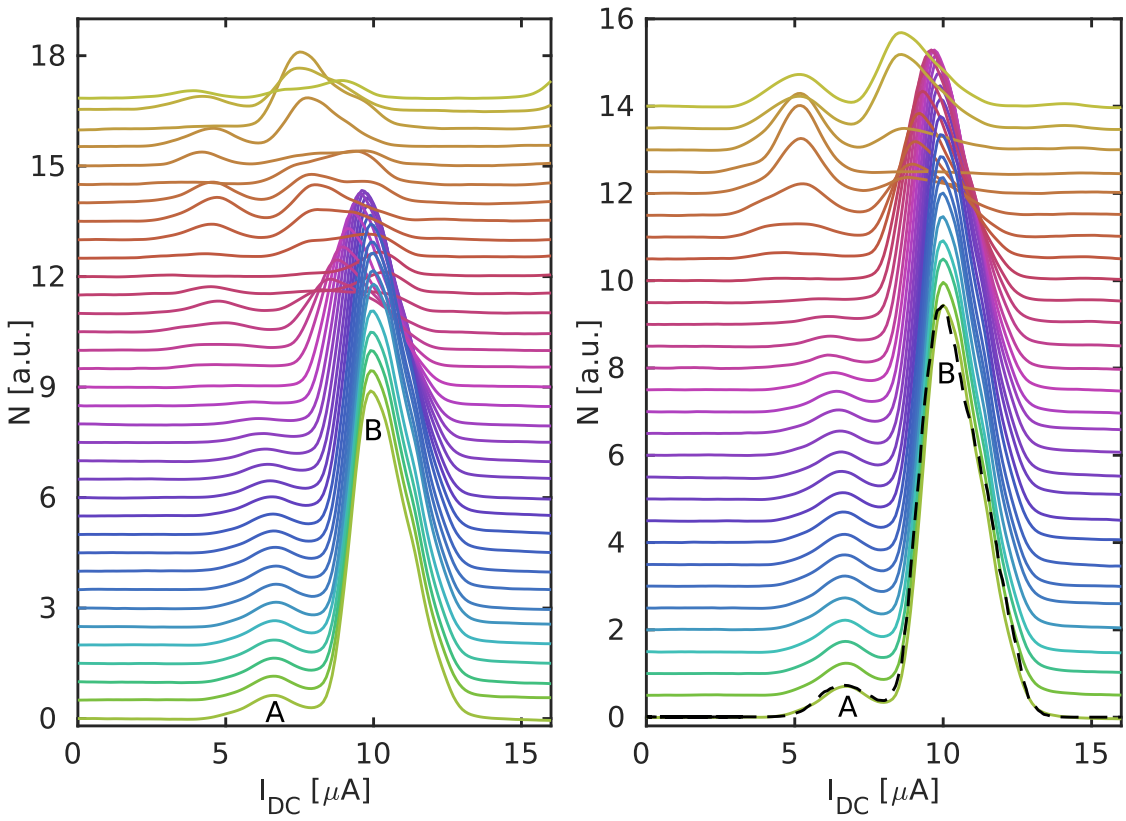

Figure 6.10: The Josephson emission as a function of I_{DC} for $f = 20.72$GHz (left, from $P = -20$dBm to $P = 14$dBm) and $f = 35.18$GHz (right, from $P = -10$dBm to $P = 17$dBm). As in figure 6.9 the same two peaks, A and B, are visible, corresponding to the emission of the 2nd and the 1st CPR harmonic.

will enhance the 2nd harmonic emission. This will not give a qualitatively good result as the 2nd harmonic emission will not vanish for any power (see figure 5.8), which is the case experimentally (around $s \approx 1.2$).

As discussed in section 5.3, microwave pumping can modify both the distribution function as well as the spectral characteristics of the junction. If the frequency of the microwaves is lower than $\hbar\omega_{RF} < 2E_g(\varphi)$ (intraband) transitions in the region above $E = E_g(\varphi)$ or below $E = -E_g(\varphi)$ (blue arrows in figure 6.13) are dominant and mostly the distribution function is modified with respect to the equilibrium value. Conversely, when the frequency is high enough to drive transitions across the gap (interband transmission) (green arrow in 6.13), which is possible if the frequency is higher than the phase dependent minigap $2E_g(\varphi = 0)$, both the spectral supercurrent density and the distribution functions are driven out-of-equilibrium. As the minigap vanishes when the phase approaches π this effect is, in principle, present at all irradiation frequencies, but will be small in our experiment below $\hbar\omega_{RF} < 2E_g(\varphi = 0)$ as the interband transitions can occur only a part of the time (i.e. lowering the frequency reduces the "duty cycle" of the interband pumping). The right panel of figure 6.13 shows the induced changes to the distribution function f as well as the nonequilibrium j_s compared to the equilibrium one. In total the supercurrent is suppressed close to $\varphi = \pi$ and for high enough values of s it even reverses sign (left panel of fig 6.14), leading to a significantly anharmonic current phase relation.

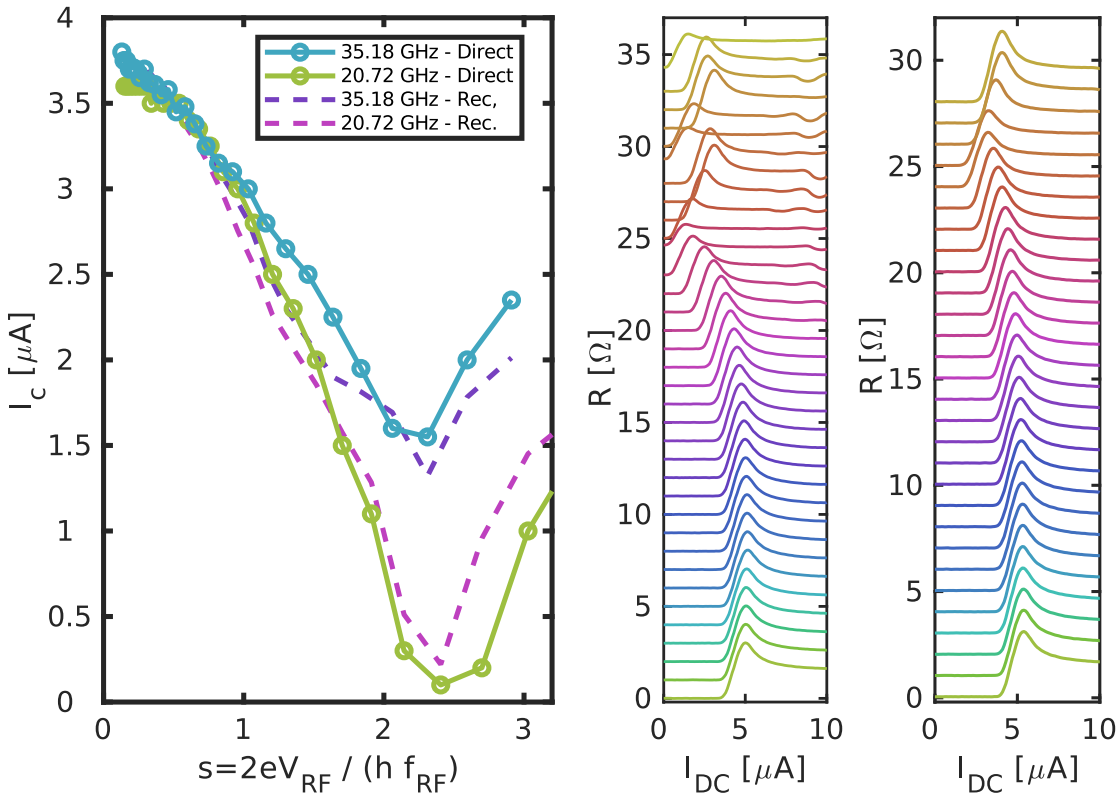

Figure 6.11: Left: the critical current measured in DC and reconstructed from the measured value of the first two CPR harmonics as a function of the applied microwave power s at $f = 20.72$GHz and $f = 35.18$GHz. Right and middle: differential resistance curves for the two frequencies (traces offset for clarity) - at $f = 20.72$GHz there is a value of s at which the critical current vanishes, while at $f = 35.18$GHz the critical current is substantially bigger than zero at all s. The data was taken at $T = 1.6$K and the power ranges are the same as in figure 6.10.

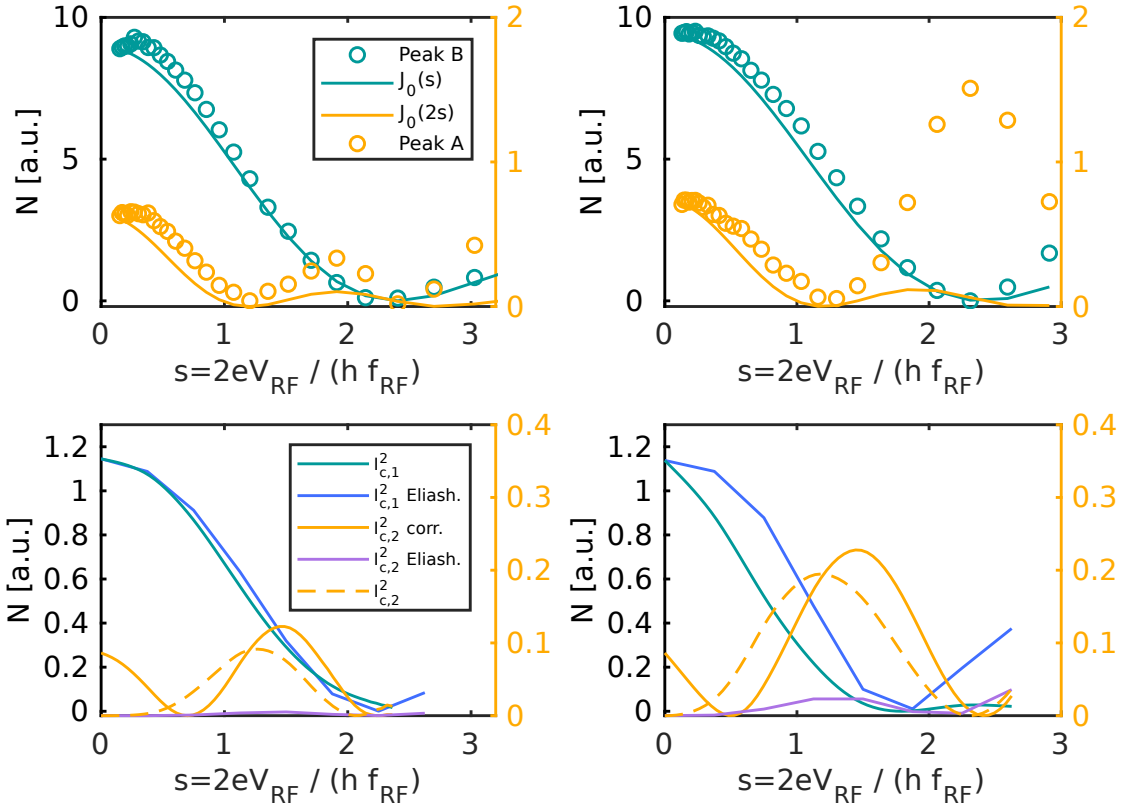

Figure 6.12: Top left: the observed amplitudes of peaks A and B as a function of microwave power at $T = 1.6$K and $f = 20.72$GHz. In all four panels the 2nd harmonic is shown on the right scale. The calibration of s was done such that the low power behavior of peak B follows $J_0(s)$. The second harmonic (peak A) roughly follows $J_0(2s)^2$. Top right: the same as top left but at $f = 35.18$GHz - at high powers the second harmonic (peak A) is significantly increased compared to $A(s = 0)J_0(2s)^2$. Bottom left (right): theoretical curves computed using the theory presented in chapter 5.3, with $\Gamma/E_T = 0.4$, $k_BT/E_T = 7$, $\Delta/E_T = 55$ and $\hbar\omega_{RF}/E_T = 3$ ($\hbar\omega_{RF}/E_T = 7$), respectively. Within the Eliashberg approximation the second harmonic is negligible at all powers. Using the full theory the amplitude of the second harmonic is qualitatively in agreement at high s but it fails to reproduce the component at $s = 0$ as $k_BT > E_T$. Using $I_{c,2} = I^0_{c,2}J_0(2s) + I^{th}_{c,2}(s)$, where $I^0_{c,2}(< 0)$ is a free parameter produces a good qualitative match at all values of s.

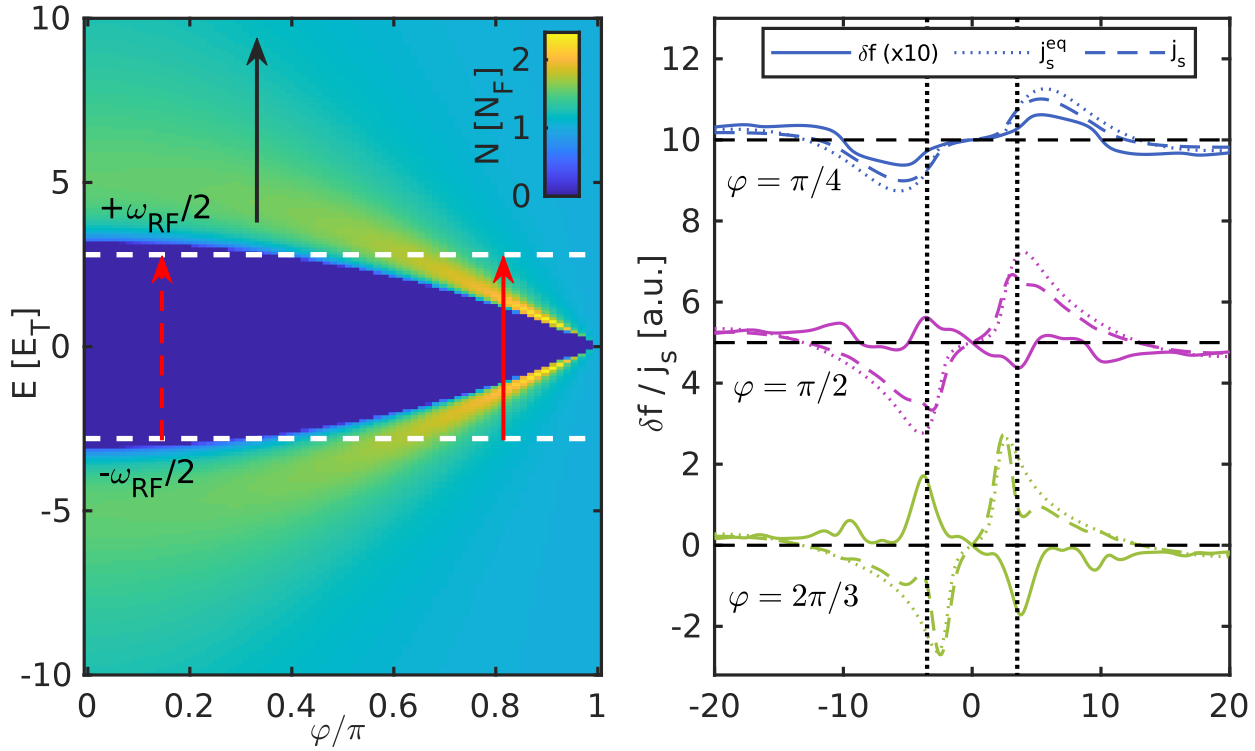

Figure 6.13: Left: a schematic of the microwave induced transitions, the white dashed lines indicate the microwave frequency, the black arrow shows the allowed intraband transition, while the (dashed) red arrows show the (dis)allowed interband transition, due to the phase dependent minigap. The induced changes to the spectral supercurrent and the distribution function, calculated using the microscopic theory, are shown on the right panel, where the dashed vertical lines indicate the microwave frequency. If the minigap is sufficiently low (i.e. if the phase is close to π) there are significant changes with respect to the equilibrium values, especially at $E = \pm\hbar\omega_{RF}/2$ as a consequence of the absorption peak shown in 5.16. The parameters used for the calculation are the same as in figure 6.12 with $\hbar\omega_{RF}/E_T = 7$.

In the formalism of chapter 5.3 both the distribution function f and the spectral supercurrent will be time dependent and can be expanded through the harmonics of the drive frequency ω_{RF}. The total time dependent current will be given by an equation analogous to 5.14. As we are only interested in the DC value of the current an average over $T = \frac{2\pi}{\omega_{RF}}$ needs to be taken, which will have contributions from the DC components of f^{DC} and j_s^{DC} as well as the products of f^n and j_s^n (where n enumerates the harmonics). This can now be used to investigate where does the observed anharmonicity originate from. By replacing f with the equilibrium one and using only the DC component of j_s (the higher ones average out to zero) results in a CPR different than the full calculation, neither the amplitude nor the anharmonicity are reproduced - see figure 6.14. Likewise, j_s can be replaced by the equilibrium value and only the DC component of f needs to be kept, doing so also leads to a significantly different trace. Finally, if only the DC components of the nonequilibrium f and j_s are kept the result is almost the same as the full calculation. In total this analysis implies that both the nonequilibrium form of f and j_s are needed to explain the observed effects.

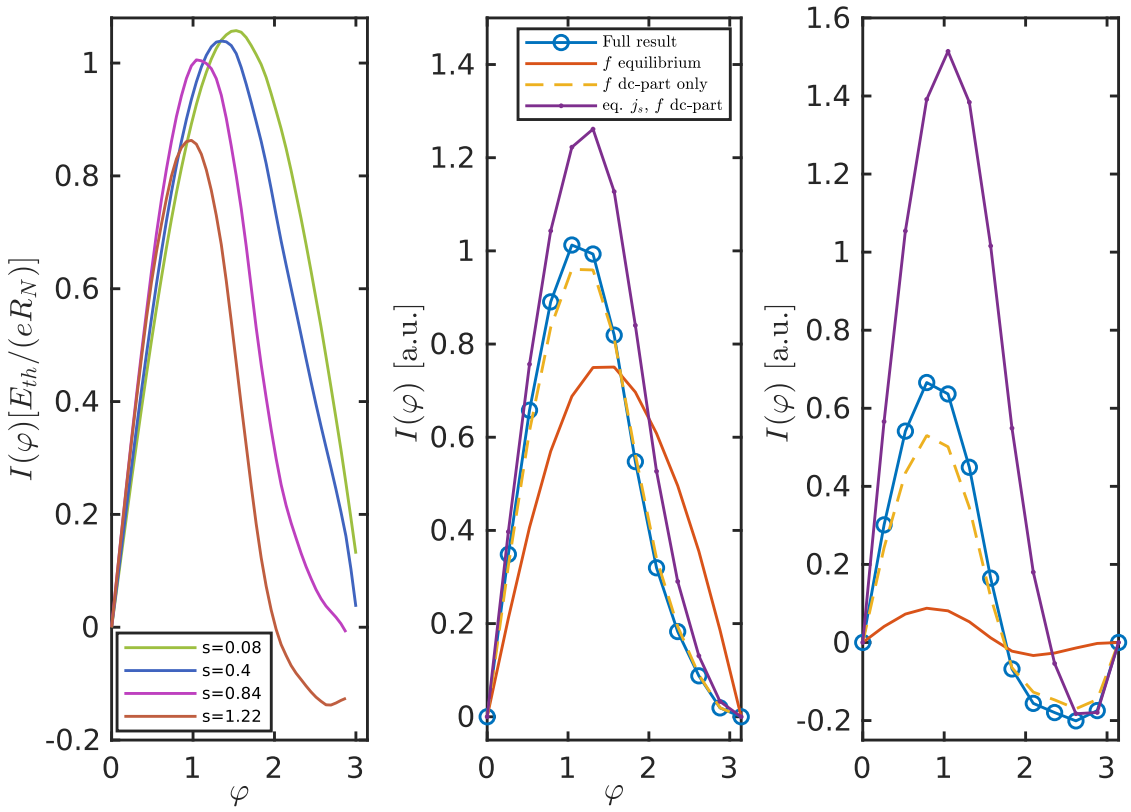

Figure 6.14: Left: the current phase relation computed using the nonequilibrium theory with $\Gamma/E_T = 0.4$, $k_BT/E_T = 7$, $\Delta/E_T = 55$ and $\hbar\omega_{RF}/E_T = 7$. Right and middle: the CPR computed using the full theoretical result, the equilibrium distribution function, the *DC* part of the distribution function, and the equilibrium spectral supercurrent at $s = 0.77$ and $s = 1.5$ respectively.

6.4 Downconverted Josephson radiation

In SNS junctions the timescale at which the two superconducting leads are coupled is set by the Thouless energy as $\tau = \frac{\hbar}{E_T}$. The previous section focused on the low frequency response of the junction to a microwave drive at high frequencies: the average phase difference φ is well defined and is either constant below the critical current or driven at a (comparatively low) frequency $\dot{\varphi} = \frac{2eV_{DC}}{\hbar}$ while the microwaves induce transitions between the quasiparticle states above, below or across the minigap. The regime which is explored here is when $\hbar\dot{\varphi}$ exceeds the Thouless energy, where one might naively expect a breakdown of the Josephson effect. Experimentally this can be explored by studying the high frequency Josephson emission up/down converted by the microwave drive. Figure 6.15 shows the detected power in an extended range of bias currents for several RF powers. In addition to the peaks A and B studied previously, one can identify peaks C and D (up and down converted Josephson emission of the 2nd harmonic around $4eV_{DC} = \hbar\omega_{RF}$), F and G (down and up converted Josephson emission of the 2nd harmonic around $2eV_{DC} = \hbar\omega_{RF}$) and lastly E and H (up and down converted Josephson emission of the 1st harmonic around $2eV_{DC} = \hbar\omega_{RF}$). The power dependence of these peaks, for a high frequency RF drive, is shown on the left panel of figure 6.16. At low to moderate powers the amplitudes of these peaks are almost unchanged with respect to their adiabatic expectations. At high powers the most notable change, aside from the one observed for peaks A and B discussed earlier, is the increase of the down converted signal H compared to the up converted counterpart E. In spite of the higher DC voltage, and therefore the effective heating, at which it is observed. As shown in the right panel of figure 6.16 the strength of this effect is greatly increased as the drive frequency is raised well above the Thouless energy. The theoretical model used to explain previous results is not applicable here as the high frequency phase dynamics play an important role. The observed effect cannot be explained by the up/down conversion efficiency within the RSJ model, which predicts an equal amplitude for the two peaks or even a reduced one for the down converted signal if the overheating is included.

At the time of writing a satisfactory explanation is not known and further investigation is needed.

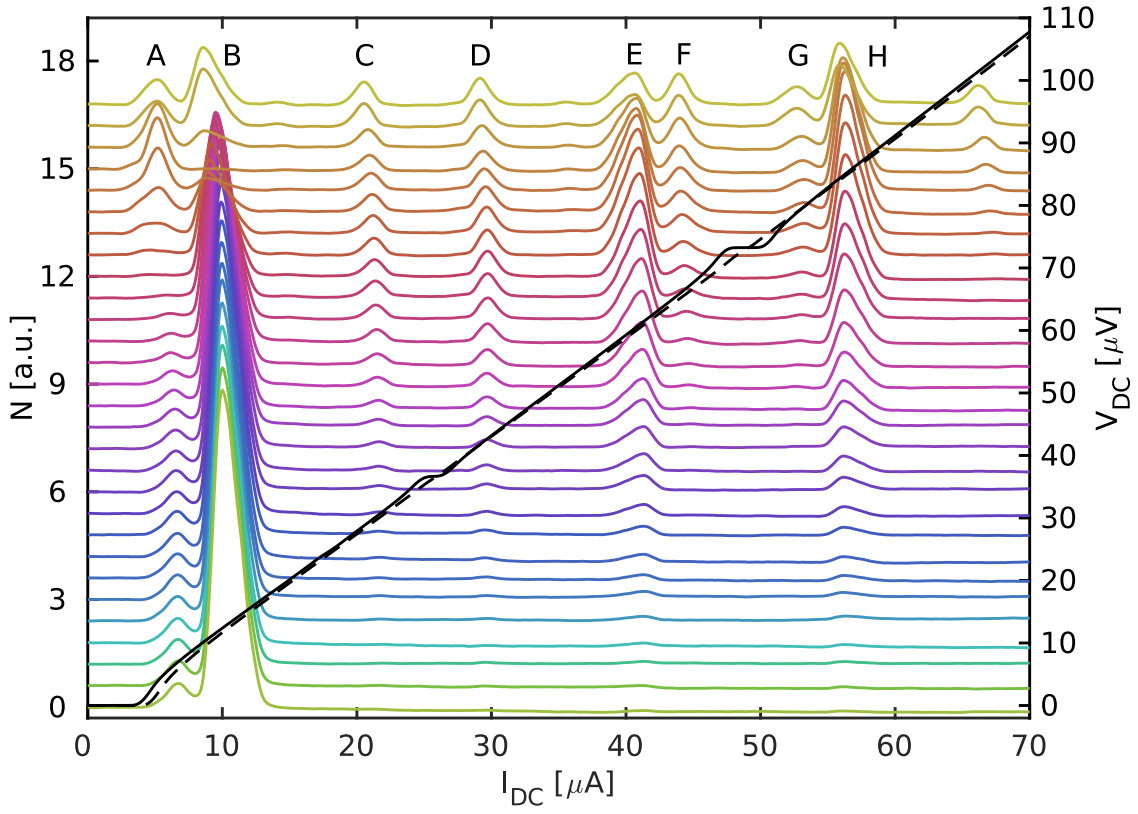

Figure 6.15: The Josephson emission measured directly (peaks A and B), or up/down converted (peaks C through H) by the microwave drive at $f_{RF} = 35.18$GHz. The bottom trace is taken at $P_{source} = -10$dBm and the top one at $P_{source} = 17$dBm. The $V(I)$ curves are shown on the right scale. The experiment was performed at $T = 1.6$K.

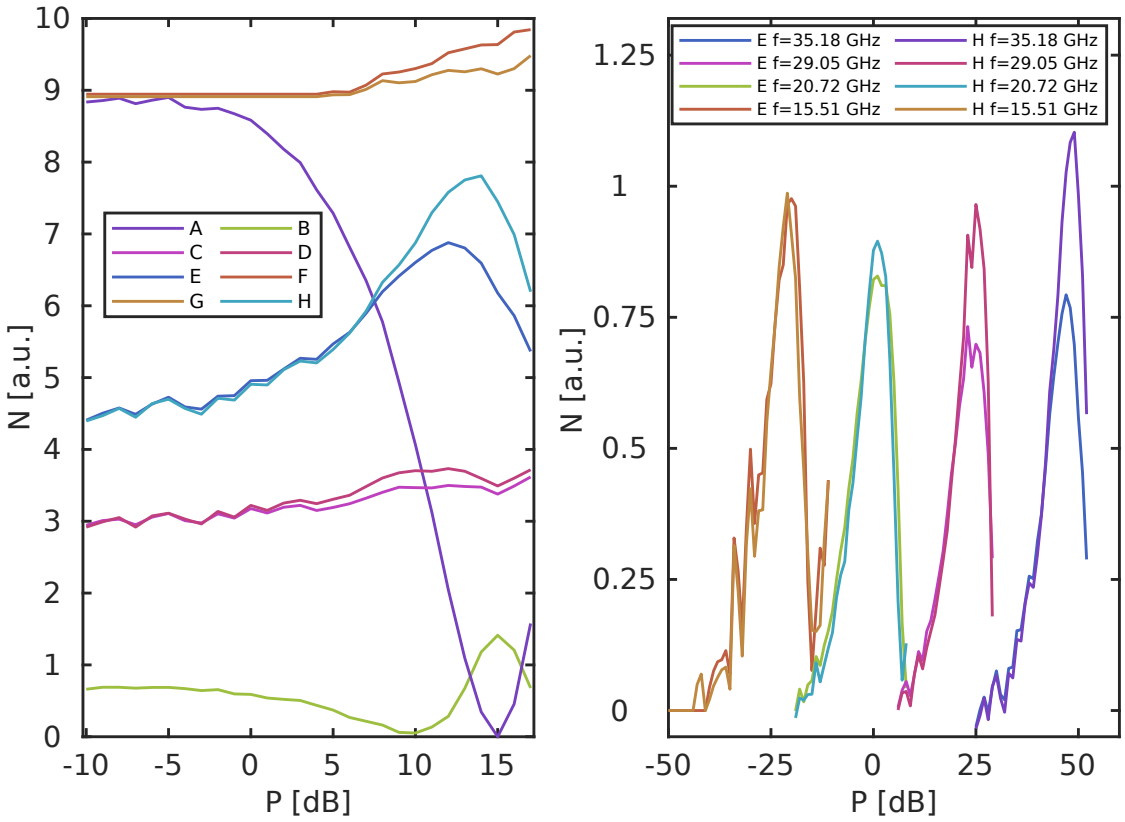

Figure 6.16: Left: the power dependence of the peaks A through H (shown in figure 6.15) at $f_{RF} = 35.18$GHz (the traces are offset vertically for clarity). Right the power dependence of peaks E and H at several frequencies; the enhancement of the down-converted peak H is observed only for higher frequencies. Both data-sets were measured at $T = 1.6K$.

Summary

This thesis covers a part of the work that I did during my PhD. It is split into two parts, each describing a separate experiment.

The first experiment investigates non-equilibrium modes and transport in a Zeeman split superconducting Al wire. Unlike the ground state of BCS superconductors, which can carry an electrical current without dissipation but not an energy or a spin current, the quasiparticle excitation spectrum is composed out of spin 1/2 Fermions and can acquire a finite magnetization. To adequately describe the out of equilibrium state of a Zeeman split superconductor one must expand on the energy (f_L - odd in energy) and charge modes (f_T - even in energy) through their spinful generalizations: the spin mode ($f_{T3} = \frac{f_{T\uparrow} - f_{T\downarrow}}{2}$) and the spin-energy mode ($f_{L3} = \frac{f_{L\uparrow} - f_{L\downarrow}}{2}$). To illustrate the physical meaning of these modes one can resort to the following: a finite quasiparticle (effective) temperature is associated with the energy mode f_L, while a nonzero QP chemical potential induces the charge mode f_T. Likewise, a spin-dependent QP temperature can be understood in terms of the spin-energy mode f_{L3}, and a spin-dependent chemical potential in terms of the spin mode f_{T3}. Due to the symmetry of the (Zeeman-split) excitation spectrum, as well as the symmetry of the non-equilibrium modes, the energy and spin modes result in a finite spin accumulation in the superconductor, while the charge and the spin-energy modes lead to a charge imbalance. The charge mode relaxes through Andreev-like processes, the energy mode relaxes through inelastic electron-phonon interactions (quasiparticle recombination), while the spin-energy and the spin mode decay through spin relaxation mechanisms (spin-orbit scattering or spin-flip events).

With the goal of probing these non-equilibrium modes several device were fabricated in the shape of a thin Al wire. By applying and in-plane field the excitation spectrum becomes Zeeman-split, and by injecting quasiparticles (from a normal-metal tunnel junction, by applying a voltage or a current bias) in the energy range $\Delta - \mu_B H < E < \Delta + \mu_B H$ (Δ is the gap of the superconductor) one can preferentially excite spin down quasiparticles. In order to probe the excited state several superconducting tunnel junction detectors were placed at different distances from the injector, the closest of which was within the spin-flip length. The measurements were performed in a dilution refrigerator with a base temperature of $T = 90$mK. The coherence peak od the detector electrode at Δ_D can be used as a spectroscopic probe of the non-equilibrium state: by measuring the differential conductance $G_{det}(V_{det})$ one probes the QP density at $E = \Delta_D + eV_{det}$. The detector electrodes were also made out of Al with a thin Pt capping layer, which induces a high spin-orbit interaction in the detector and acts as a spin-mixer. Thus the detector electrode is not spin-split and results in a spin-sensitive detector: the spin down/up quasiparticles are detected at different voltages/energies $eV_{det}^{\downarrow/\uparrow} = \Delta \mp \mu_B H - \Delta_D$.

The main results of the experiment can be broken down as follows:

- Observation of a nontrivial out-of-equilibrium state: By applying a voltage V_{inj} to the injector junction electrons with energies up to $E \approx eV_{inj}$ tunnel into the superconductor, imprinting the distribution function of the normal metal onto the superconductor. The resulting distribution function is not equivalent to an effective temperature or a chemical potential and the superconductor is considered to be *truly* out-of-equilibrium. Such a state is observed at low to moderate injection currents and close to the injection junction, both spectroscopically as a step-like cutoff in the detected quasiparticles coinciding with $E \approx eV_{inj}$, as well as through the measurements of the self-consistent gap as a function of the quasiparticle density $\Delta(N_{QP})$. At large injection currents or further away from the injector a thermal-like state is observed, as the electron-electron interaction redistributes the quasiparticles. This effect was observed at both zero and finite magnetic fields.

- Observation of a spin-dependent distribution function: At finite Zeeman fields a charge imbalance was observed when spin-polarized quasiparticles were injected $\Delta - \mu_B H < eV_{inj} < \Delta + \mu_B H$. By performing a spin-sensitive spectroscopic study it was found that the odd-in-energy component of the quasiparticle population was confined to $\Delta - \mu_B H < E < \Delta + \mu_B H$ suggesting that the spin and charge of the quasiparticles are coupled. By investigating the field dependence of said charge imbalance, comparing it to the charge mode observed at zero field and a comparison with a theoretical model, the spin-energy mode was identified as the origin of the signal. This is the first observation of a spin-dependent distribution function in a superconductor.

A direct follow-up to the experiment could be to improve the detection scheme and to perform a deconvolution to directly probe the distribution function, or to probe the electron-electron interaction rates while injecting quasiparticles. Additionally, using devices with similar geometry, one could look for the recently predicted spin-to-charge conversion [104] and voltage induced superconductivity at high fields [105].

The second experiment deals with high-frequency transport properties of Superconductor-Normal-Superconductor (SNS) Josephson junctions. In such devices the normal metal is proximitized by the superconductors leading to a state which can support a finite supercurrent. Microscopically this is realized through Andreev reflections of electrons at the NS interface, where the electrons pick up an extra phase equal to the one of the macroscopic wave-function in the superconductor. Requiring that the phase accumulated during one cycle is an integer multiple of 2π leads to a series of bound states (Andreev levels). In diffusive samples, such as the one studied in this experiment, the states form a continuum with a minimum energy $E_g \approx 3.1E_T$, set by the diffusion time through the wire $E_T = \frac{\hbar D}{L^2} = \frac{\hbar}{\tau_D}$. The supercurrent through the junction is given by the spectrum of these states as well as their occupation numbers. Overall the phase dependence of the supercurrent (current-phase relation or CPR) can be Fourier expanded as $I_s \sum_n I_{c,n} \sin(n\varphi)$, where $I_{c,n}$ is the (temperature dependent) current carried by the n-th harmonic, and φ the macroscopic phase difference between the superconducting leads.

The experiment presented here explores the high-frequency dynamics of SNS junctions, in particular the response of the system to a drive whose frequency exceeds the inverse diffusion time. The device under study is a mesoscopic SNS junction (S=Nb, N=Ag) of intermediate length ($\Delta_S = 55E_T$). The experiment was set up in such a way to enable DC biasing and measurements, as well as the application of RF radiation in a wide range of frequencies and

the detection of emitted radiation in a narrow band (centered at ω_D). If the junction is biased in DC such that a finite voltage V_{DC} appears, according to the 2nd Josephson relation, the phase difference will be driven at a frequency $\omega_J = \frac{2eV_{DC}}{\hbar}$. Then, finite RF power will be emitted by the junction (Josephson emission) at $n\omega_J$ with $P_n \propto I_{c,n}^2$. When $n\omega_J$ coincides with ω_D, the detection frequency, this radiation can be detected and acts as a noninvasive probe of the junction current-phase relation. The experiments were performed in in a range of temperatures from $T = 250$mK to $T = 4.2$K for sample characterization, while most of the experiments were performed at $T = 1.6$K, where the junction CPR is almost sinusoidal (in equilibrium).

Again the results can be broken down into two parts:

- Enhanced quasiparticle cooling: During the first part of the experiment the sample was characterized in detail. It was found, by measuring the temperature dependence of the critical and retrapping currents as well as the temperature and frequency dependence of the Shapiro step width, that the electron-phonon mediated cooling rate is several orders of magnitude larger than the expected value (inferred based on the geometry of the device and the e-ph interaction rate in Ag). The normal metal shadows adjacent to the junction, which are a consequence of the fabrication procedure, were found to behave as "quasiparticle traps" and are the source of this effect. Although this is a rather technical finding, this mechanism enabled the observation of a novel nonequilibrium state.

- Nonadiabatic dynamics of strongly driven junctions: When the junction is irradiated with radiation whose frequency is comparable to the mini-gap in N $\hbar\omega_{RF} \approx 2E_g$ it was found that the critical current no longer follows the equilibrium Bessel relation $I_c = I_{c,1}J_0(\frac{2eV_{RF}}{\hbar\omega_{RF}})$ (for harmonic junctions), in particular it never vanishes. This is in contrast with the data taken at lower frequencies where the Bessel function dependence is recovered. By measuring the harmonic content of the emitted radiation an increase of the second harmonic $I_{c,2}$, and especially so at high irradiation powers, was detected. It is not possible to explain these results in terms of microwave-assisted cooling (Eliashberg effect). Based on a microscopic theoretical model a novel out-of-equilibrium state was identified as the cause, in which both the distribution function as well as the spectrum of the current carrying states are modified by quasiparticle pumping across the mini-gap in the normal wire.

Additionally, when the phase difference is driven at a high frequency $2eV_{DC} \approx 2E_g$ and the junction is irradiated with high-frequency microwaves the power dependence of the emitted radiation shows nontrivial behavior which is not yet understood.

The spectroscopic approach developed here could be used for several other types of weak links: it could be used to study the microwave induced CPR modifications in atomic contacts [106, 107]. In nanowire junctions with Majorana bound states, the microwave affected CPR might reveal signatures about the topologically forbidden transitions [108, 109, 110].

Appendix A

Sample fabrication and experimental details

The sample was fabricated on top of a Si/SiO_2 chip, using standard e-beam lithography techniques. The electron-sensitive resist used was a tri-layer of MMA 850/MMA 850/PMMA 950-A3 (bottom to top) spin-coated on the chip at 4000RPM (spin duration was 60s). The two MMA layers were used due to their higher sensitivity to the (back-scattered) electron-beam which created an undercut at low exposures, while leaving the top PMMA layer intact. This created a suspended mask suitable for an angle evaporation. The CAD file used for the e-beam lithography is shown in figure A.1, with the leads extending far beyond the shown area. The main features were exposed with $400\frac{\mu C}{cm^2}$, while the undercuts were dosed with $60 - 160\frac{\mu C}{cm^2}$. The mask was developed in a $3:1$ MIBK:IPA solution at $T \approx 20°C$.Each fabrication attempt consisted of a 4x4 grid of devices on a 1cm x 1cm chip.

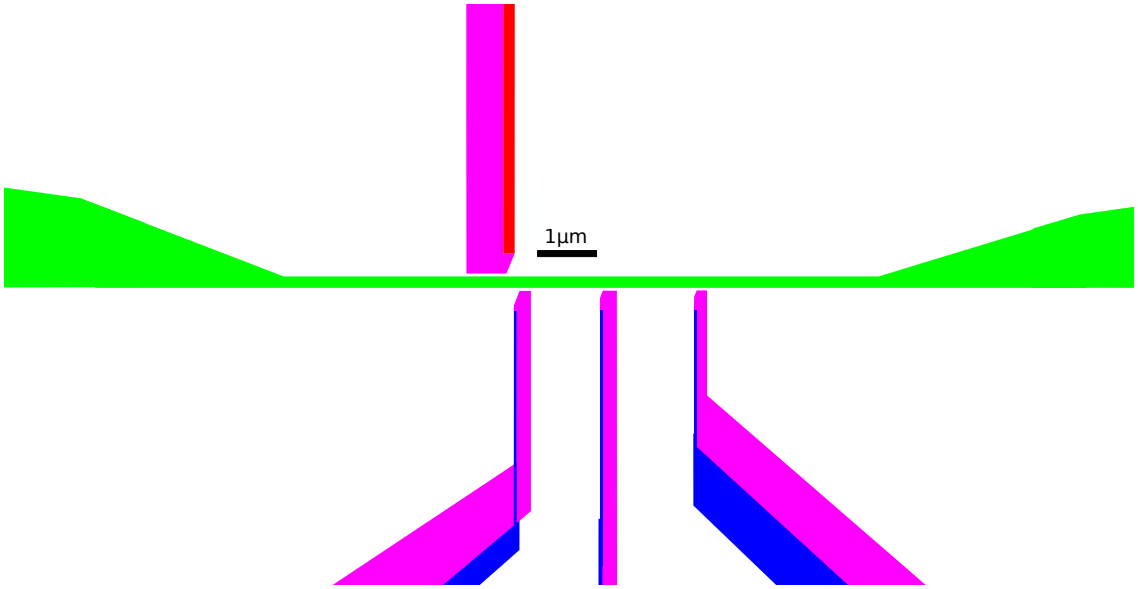

Figure A.1: E-beam defined evaporation mask: the superconducting Al wire is colored green, the injector electrode red and the detector electrodes are blue. Pink regions are lower-dosed undercuts.

The evaporation procedure was as follows:

- The Al wire (green in figure A.1) was evaporated from above (i.e. perpendicular to the plane of the drawing), with a thickness of $d = 6$nm.

- An oxide layer was grown using dynamic-pressure oxidation at $P \approx 1\text{e}-1$mBar of pure O_2 introduced in the chamber for $t = 10$min.

- The detector leads (blue in figure A.1) were evaporated at $\theta = -45°$ (out of plane rotation, measured perpendicular from the wire axis) and $\varphi = 27°$ (in-plane rotation). The material evaporated was Al and the thickness was $d = 8$nm

- A mono-layer ($d = 1 \pm 0.05$) of Pt was evaporated at the same angles, as a capping layer for the detector leads.

- The injector electrode (red in figure A.1) was evaporated at $\theta = 45°$ and $\varphi = 17°$. The material chosen was Cu and the thickness was $d = 100$nm.

Before any evaporation was performed, and after the oxidation, the chamber was pumped down below $P \approx 1\text{e} - 7$mBar, and a short flash of Nb was evaporated to lower the ^{2}O concentration even further. During the evaporation the pressure in the chamber did not exceed $P = 1\text{e} - 6$mBar. The thickness of the evaporated material was monitored using a quartz detector, the thickness quoted above is perpendicular to the plane of the chip, while the evaporated thickness at an angle was a factor $1/\sqrt{2}$ higher. Sometimes the Cu injector was covered with a thin Al layer for protection, but this did not make a difference provided that the sample was quickly (less than 12h) placed under vacuum.

The following was taken into consideration while choosing the sample geometry and parameters:

- The orbital depairing, from an in-plane magnetic field, increases as the square of the wire thickness, and so it is desirable to make it as thin as possible. However this would reduce the spin-relaxation, as the spin is preserved for about 1000 scattering events. As a balance between these two effects a thickness of $d = 6$nm was chosen.

- The oxide barrier transparency was chosen such that the injector resistance is in the order of 10kΩ, while at the same time this gives a detector resistance of about 30kΩ. A more transparent barrier would lead to non-equilibrium effects induced by the detectors, and a more resistive barrier would greatly reduce the number of QP's that can be injected near the gap edge. A two step fabrication procedure was attempted, which could greatly simplify the e-beam defined mask and decouple the injector and detector resistances, but it was unsuccessful as most of the detector junctions were open.

- While it would be beneficial to reduce the detector thickness as well, as they are evaporated after the Al wire making them too thin causes breaks at the wire edge. The thickness of $d = 8$nm provided a reasonable balance between a low orbital depairing rate and sample yield. Pt was used as a spin-mixer as it does not oxidize, and because previous publications demonstrated the effect.

- The injector was made as thick as possible to keep it as close to equilibrium as possible. Making it much thicker than $d = 100$nm would sometimes collapse the suspended mask and reduce the sample yield.

- Due to the thick injector the thin electrodes needed to be evaporated first. As a consequence the oxidation step needs to be tuned for the detector junctions. An additional degree of freedom can be introduced by first oxidizing the barrier heavily (i.e. $R_{det} \approx 200\text{k}\Omega$), and placing a thin layer of Pt below the injector junction to lower its resistance. Otherwise an additional oxidation step can be taken to increase the resistance of the injector junction.

- The injector J_{inj} and the closest detector J_1 need to be spaced within λ_{SF} of each other, while making sure that there is no electrical contact between them. The evaporation angles and the placement of the undercuts were chosen as a function of these limitations, and the requirement that the shadows (which can be seen in figure 3.3) from other evaporations do not touch the detector finger, at least not within 1μm from the junction.

A more detailed experimental set-up is shown in figure A.2. The sample was mounted in a enclosed Cu sample holder and cooled down to $T = 90\text{mK}$ in a ^{3}He/^{4}He dilution refrigerator. The magnetic field was applied using a superconducting vector magnet, along the axis of the wire. The out of plane component was less than 0.5%.

The main results were obtained by current biasing the injector junction (by applying a voltage to a room temperature 100MΩ resistor), while measuring the $I(V)$ and $G(V)$ curves of a detector junction simultaneously. One of the ends of the wire was connected to ground through a (room temperature) current amplifier with a gain of 1e7/1e8. A DC+AC voltage was applied to the detector junction; the DC component of the current was measured using a DMM and the AC one with a lock-in amplifier (typically $V_{AC} \leq 5\mu\text{Vrms}$ and $f_{AC} = 17 - 37\text{Hz}$). This way the injection current would create an offset in the measured current, but this setup resulted in less noise than placing the current amplifier in line with the detector excitation voltage.

The unused junctions, as well as the other end of the wire were connected to ground using resistances of 100MΩ or greater.

All of the lines leading to the sample were filtered by room temperature π filters ($BW = 1\text{MHz}$) and by a $C = 1.5\text{nF}$ capacitance to ground within the shielded sample holder.

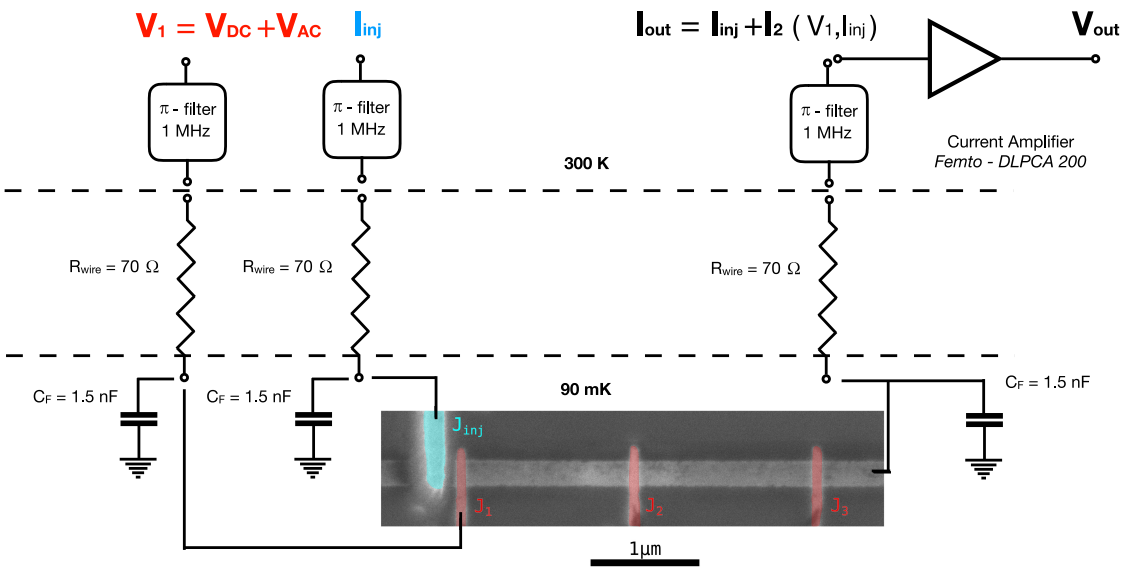

Figure A.2: A schematic of the experimental setup.

Appendix B

Long summary in English

This appendix provides a standalone summary of the thesis. For more details the reader is invited to consult the main text or the publications, which are reproduced in full in appendix D.

The key feature of superconductivity is a gap, Δ, in the excitation spectrum. Within the BCS theory of superconductivity, the amplitude of this gap is directly related not only to the strength of the pairing mechanism but also to the presence of excitations (quasiparticles) and their energy distribution. This is formally given by the self-consistent gap equation. While a stronger coupling constant can enhance the gap, excitations can only reduce it. Nevertheless it was recognized early on that engineering an out-of-equilibrium distribution function for the quasiparticles can lead to interesting unstable ground-states [1] or even to increase the critical temperature [2].

Quasiparticles can be excited thermally, by absorbing of radiation, and injection of non-superconducting electrons from a counter-electrode. When the perturbation is chargeless, which is the case for radiation or a finite temperature, only energy is transferred to the superconductor. Because of the intrinsic electron-hole symmetry of a BCS superconductor this results in a equal number of electron-like and hole like excitations. If instead a charged particle is injected into the superconductor the balance between electron and hole like excitation is broken, while charge neutrality is preserved by removing Cooper pairs from the condensate [3].

These two types of excitations correspond to different modes of the distribution function, called the energy and the charge mode. Formally they are classified based on the symmetry of the (nonequilibrium component) of the distribution function with respect to the Fermi level. These modes are also called longitudinal (f_L) and transverse (f_T), because they enter with a $\pi/2$ phase shift in the self-consistent gap equation [4].

The actual distribution function in the superconductor depends on quasiparticle excitation, relaxation and recombination rates. The different mechanisms at work set a hierarchy of the time-scales involved in relaxing f back to equilibrium. Thus the energy mode excitations are the longest-lived ones, and are responsible for most observed nonequilibrium effects in superconductors.

Developing a detailed theoretical framework to describe energy and charge transport is not an easy task, as the kinetic equations for quasiparticle diffusion include (energy non-local) inelastic processes, which can locally change the number of quasiparticle and their distribution, and the order parameter. For instance, a low energy phonon, resulting from

the recombination of two quasiparticles, can be reabsorbed elsewhere in the superconductor, breaking a Cooper pair in the process [10].

The situation is simpler when the size of the device becomes smaller than both the quasiparticle relaxation and recombination lengths. In absence of interactions, the distribution function is basically set by the boundary conditions. For instance for a wire connected to two reservoirs the (energy mode) distribution function at each point of the wire is a linear combination of the reservoir distribution functions. This is well described theoretically within the Keldysh-Usadel formalism [11, 12, 13], by neglecting the self-energy terms related to inelastic interactions.

The topic of this work is quasiparticle transport in this limit of negligible or weak quasiparticle interaction. Two specific questions, addressed in parts I and II of the thesis respectively, are:

- Can the spin degeneracy of the distribution function modes be lifted?
- Can the out-of-equilibrium distribution function have a dynamical feedback on the spectral properties of a superconductor?

Part I: Spin physics in out-of-equilibrium superconductors

For a long time, work on out-of-equilibrium superconductivity concentrated mainly on spinless excitations [4]. Based on symmetry, the out-of-equilibrium quasiparticle (QP) distribution function $f(E)$ can be decomposed into energy $f_L(E) = f(-E) - f(E)$ and charge $f_T(E) = 1 - f(E) - f(-E)$ modes [4, 14]. The simplest $f(E)$ which excites these modes are, respectively, an effective temperature T^*_{QP} and a QP chemical potential $\mu_{QP} \neq 0$ (measured from the Fermi energy). The energy mode contributes to a finite (non-equilibrium) energy stored in the QP excitations, while the charge mode leads to a finite charge imbalance [18].

The possibility of different energy distribution functions for spin up and down electrons (or QPs) was then raised for both normal metals and superconductors. In superconductors [25, 26, 13, 11, 12, 27, 56], the decomposition of the quasiparticle distribution function $f(E)$ above can be generalized to the spinful case by the addition of spin $f_{T3}(E) = (f_{T\uparrow}(E) - f_{T\downarrow}(E))/2$ and spin energy $f_{L3}(E) = (f_{L\uparrow}(E) - f_{L\downarrow}(E))/2$ modes [11, 12, 13, 56]. By construction, f_L and f_{L3} are odd in energy, while f_T and f_{T3} are even in energy. These new modes exist only if spin up and down QPs have different distribution functions, i.e. $f_\uparrow(E) \neq f_\downarrow(E)$. To illustrate the physical meaning of these modes one can resort to the following: a finite quasiparticle (effective) temperature is associated with the energy mode f_L, while a nonzero QP chemical potential induces the charge mode f_T, which is shown on the top two panels of figure B.1. To fully understand the physical meaning of the spin-dependent modes it is easiest to consider the case of a Zeeman-split superconductor, obtained by applying an external magnetic field H. This raises (lowers) the energy of spin up (down) QPs by $E_Z = \frac{g}{2}\mu_B H = \mu_B H$ and splits the DOS so that only spin down (magnetized) excitations are allowed in the energy range $\Delta - E_Z < |E| < \Delta + E_Z$. A spin-dependent QP temperature can be understood in terms of the spin-energy mode f_{L3}, and a spin-dependent chemical potential in terms of the spin mode f_{T3}, see the bottom two panels in figure B.1.

Due to the symmetry of the (Zeeman-split) excitation spectrum, as well as the symmetry of the non-equilibrium modes, the spin mode results in a finite spin accumulation in the

superconductor, and so does the energy mode provided that the superconductor is Zeeman-split. Likewise, the charge mode lead to a charge imbalance and so does the spin-energy mode at finite Zeeman fields. These statements are formally described by equation B.1:

$$\begin{aligned} \mu_z &= \int_{-\infty}^{\infty} dE\big[f_L(E)N_- + f_{T3}N_+\big], \\ \mu &= \int_{-\infty}^{\infty} dE\big[f_T(E)N_+ + f_{L3}N_-\big] \end{aligned} \tag{B.1}$$

where $N_\pm = \frac{N_\uparrow \pm N_\downarrow}{2}$ spin average / difference of the quasiparticle density of states, μ the charge imbalance and μ_z the spin imbalance.

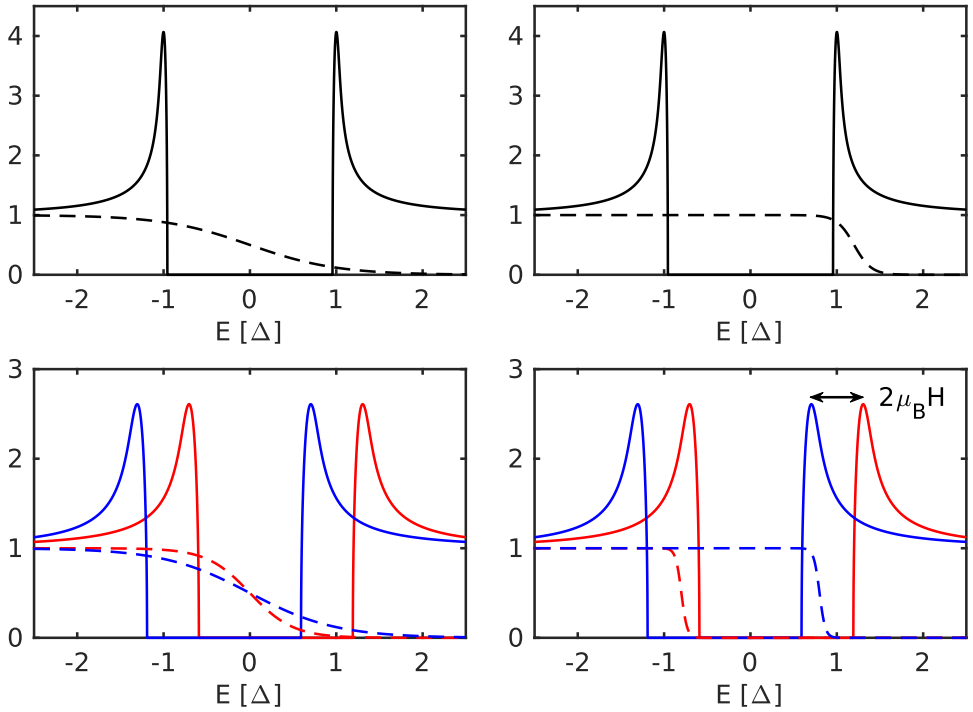

Figure B.1: A depiction of the different distribution function modes: top left shows an effective temperature T^* ($H = 0$), which is a specific realization of the energy mode f_L, top right an effective chemical potential μ (with a finite temperature, $H = 0$) which is the simplest distribution function that excites the charge mode f_T. The bottom left and bottom right panels show a spin-dependent temperature and chemical potential, corresponding to the simplest realizations of the spin-energy f_{L3} and spin f_{T3} modes ($H > 0$).

The energy mode can be excited by charge-neutral perturbations such as electromagnetic radiation whose frequency is larger than the superconducting energy gap Δ: the absorption of such radiation breaks pairs and creates quasiparticles [16]. The charge mode, on the other hand, can be excited by injecting charged carriers (i.e. electrons or holes) through a tunnel barrier into a superconductor, where they become quasiparticles [17]. As quasiparticles are not instantaneously converted into Cooper pairs, their chemical potential is shifted up or down with respect to that of Cooper pairs. This has been measured as a *nonlocal* voltage drop between the superconductor and a normal-metal tunnel electrode upon quasiparticle injection [18, 19]. If electrons or holes are injected at energy $|E| > \Delta$, both charge and

energy modes are excited. The relaxation time for the energy mode is the inelastic (electron-phonon) scattering time [15] while the charge mode relaxes over the charge relaxation length [19, 20, 21, 22, 23].

In a pioneering experiment, Johnson et al. [28] showed that spin injection from a ferromagnetic electrode into a normal metal is possible by applying a voltage bias across the interface between the two. The out-of-equilibrium magnetization created in the normal metal is detected electrically, by measuring the voltage between it and a second ferromagnetic electrode [29]. This *nonlocal* signal is directly proportional to the shift in the chemical potential, μ_s, of spin up (down) electrons due to spin accumulation [30, 31], in which spin up and down chemical potentials shift by the same amount, but in opposite directions. The spin relaxation length measured in high purity light metals (which have low spin-orbit coupling) can reach 100μm, and the spin relaxation time is ≈ 50ns [28].

In thin superconducting films, it is possible to inject spin and to preferentially excite QPs of one spin with current injection from a normal (rather than ferromagnetic) electrode: the orbital screening currents are suppressed quadratic ally with the sample thickness, allowing one to apply a large enough magnetic field to induce Zeeman-splitting in the sample. Then, spin can be injected into a superconductor by biasing the injector junction such that $\Delta - E_Z < |eV_{inj}| < \Delta + E_Z$. In this energy range, according to the previous discussion, only spin-down DOS is non-zero, leading to a finite spin accumulation in the superconductor.

Spin injection into superconductors using this method was shown to result in a finite, long-ranged spin accumulation, arising either from f_L or f_{T3} [36, 37, 38]. Subsequent measurements of the spin-flip time, the spin-orbit scattering time and the spin imbalance lifetime indicate that the spin accumulation beyond the spin-flip length λ_{sf} is almost entirely due to f_L, as it relaxes over λ_{rec} while f_{T3} relaxes over λ_{SF} [39, 40].

Around the same time evidence for different effective temperatures for spin up and down electron was observed in the nonlinear contribution to the magnetoresistance of metallic nanopillar spin valves [32]. Indeed, a spin-dependent effective temperature is the simplest manifestation of the spin energy mode, in which the two spin species carry different energy currents.

This work focuses on probing the out-of-equilibrium state generated by current injection from a normal metal, with a special focus on spin-energy mode f_{L3}.

In principle there are two possible approaches to achieve this: either to probe the spatial decay of charge and spin accumulations, as the four modes relax over different length-scales, or to perform spin-sensitive spectroscopy of the QP population. In this experiment we adopted the second approach.

To this end several device were fabricated in the shape of a thin diffusive Al wire and quasiparticles are injected from a normal-metal tunnel junction. In our experiments, $E_Z > \alpha$, the orbital depairing energy, up to the H_c, the critical field of the superconductor, allowing us to fully resolve the spin down and up coherence peaks in the excitation spectrum. Thus, when we inject an electrical tunnel current the DOS acts as an almost perfect spin filter for $\Delta - E_Z < |eV_{inj}| < \Delta + E_Z$, even if the barrier transmission is spin-independent, allowing us to inject spin and to induce $f_\uparrow(E) \neq f_\downarrow(E)$ simultaneously. In order to probe the excited state several superconducting tunnel junction detectors were placed at different distances from the injector. With the goal of observing a spin-dependent distribution in mind the closest detector was within the spin-flip length away from the injector, as the relaxation length of the spin-energy mode is in the order of λ_{SF}. In our experiment the spin relaxation length is

estimated to $\approx$ 240nm, while the minimum injector-detector distance is 250nm. The other detectors were placed a few μm away, giving us information about the spatial distribution of quasiparticles. As argued in detail in the main text of the thesis, the coherence peak of the detector electrode at Δ_D can be used as a spectroscopic probe of the non-equilibrium state: by measuring the differential conductance $G_{det}(V_{det})$ one probes the QP density at $E = \Delta_D + eV_{det}$, where Δ_D is the detector gap. The detector electrodes were made out of Al with a thin Pt capping layer, which induces a high spin-orbit interaction in the detector and acts as a spin-mixer. Thus the detector electrode is not spin-split and results in a spin-sensitive detector: the spin down/up quasiparticles are detected at different voltages/energies $eV_{det}^{\downarrow/\uparrow} = \Delta \mp \mu_B H - \Delta_D$. The measurements were performed in a dilution refrigerator with a base temperature of $T = 90$mK. All of the theoretical results were obtained using the framework developed in [56]. The corresponding manuscript can be found at [111], and is currently under review for publication. In this summary only the data obtained using the closest detector is shown, as the further ones show results consistent with the long-ranged effects observed in previous experiments [36, 37, 38].

The main results of the experiment can be broken down as follows:

- **Observation of a nontrivial out-of-equilibrium state**: By applying a voltage V_{inj} to the injector junction electrons with energies up to $E \approx eV_{inj}$ tunnel into the superconductor, imprinting the distribution function of the normal metal onto the superconductor. The resulting out-of-equilibrium state is a non-thermal one, characterized by a large number of quasiparticles at the gap edge, due to the sharp coherence peak and vanishing mobility of quasiparticles close to $E = \Delta$, and a step-like tail up to $E \approx eV_{inj}$. By performing quasiparticle spectroscopy in the limit of low to moderate injection currents at $H = 0$ using the closest detector precisely this is found, as shown in figure B.2. The previous statement is strictly true only if the quasiparticle-quasiparticle interaction rate is vanishingly small. Indeed at higher injection currents or further away from the injection junction a more smeared quasiparticle population is found and the step-like cutoff cannot be observed. The argument for the shape of the distribution function can be justified more rigorously within the Keldysh-Usadel formalism: The diffusion time of quasiparticles from the injector to the end of the wire, terminated with large metallic reservoirs ($\approx$ 20ns), is much shorter than the inelastic quasiparticle-quasiparticle recombination time ($\approx$ 400ns [5]), and the energy relaxation mechanism is identified as quasiparticle thermalization / trapping in the reservoirs. This claim was experimentally verified by probing the spatial decay of the out-of-equilibrium quasiparticles. Additionally if we focus on the low injection region the quasiparticle-quasiparticle interactions can also be neglected, thus removing all energy-non-local inelastic interactions from the model, greatly simplifying the problem. Thus the transport equations can be easily solved, indeed resulting in a step-like distribution function. A simulation of the detector spectrum, obtained based on this calculation, is also shown in figure B.2, which is in qualitative agreement with the experimental result. This effect was observed at both zero and finite magnetic fields (see the dark blue regions close to $I_{inj} = 0$ in the experimental panel of figure B.3) and indirectly through the measurements of the self-consistent gap as a function of the quasiparticle density $\Delta(N_{QP})$. These findings show that at short length-scales quasiparticle injection results in a non-thermal distribution function and the superconductor is considered to be *truly* out-of-equilibrium.

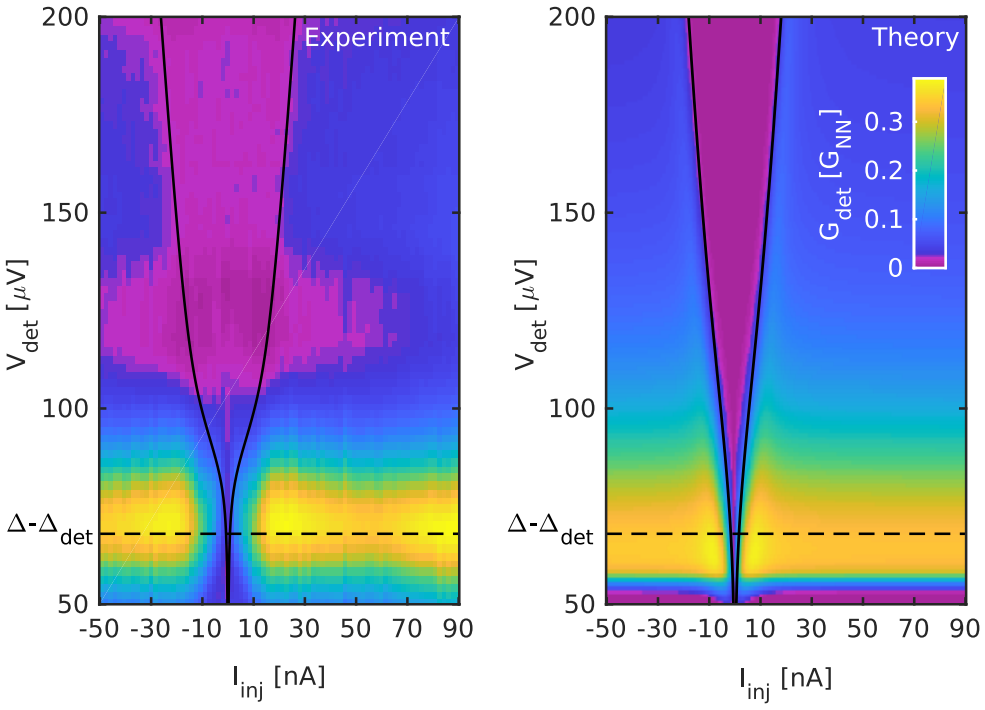

Figure B.2: Left: The $G(V_{det}) \propto N_{QP}(E = eV_{det} + \Delta_D)$ spectrum obtained using the closest detector at $H = 0$ as a function of the injection current. Two features can be identified: a large signal at $E = \Delta$ along the horizontal dashed line. Secondly, no quasiparticles are detected within the purple region, which is bound by the experimental $I_{inj}(V_{inj})$ curves of the injector (solid black lines), outside of which a finite QP density is detected. This implies that This implies that QPs are detected only at energies below $E = eV_{inj}(I_{inj})$. The unaccounted-for purple areas outside of the $I_{inj}(V_{inj})$ bounds are due to the nontrivial background subtraction, as detailed in the main text of the thesis. Right: A simulation of the detector spectrum based on the Keldysh-Usadel approach presented in the same fashion. The color-bar is common for the two panels.

- **Observation of a spin-dependent distribution function**: As discussed previously, at finite Zeeman fields injecting quasiparticles with energies $\Delta - \mu_B H < |E| < \Delta + \mu_B H$ should, in principle, lead to a spin-dependent distribution function. In our experiment the focus was on the spin-energy mode, which can be detected through it's charge imbalance signature. It can be seen from figure B.1, as well as from equation B.1, that the presence of the spin-energy mode creates an unequal number of "low energy" excitations - spin down electron-like and spin up hole-like quasiparticles (both of these excitations carry the same magnetization as spin-up hole removes a spin down electron). This charge imbalance is located at the spectroscopic gap edge, and is only there if $N_\downarrow \neq N_\uparrow$ i.e. if the superconductor is Zeeman split. These properties and signatures of the spin-energy mode were used to detect its presence experimentally. The spin sensitivity of our SIS′ detectors is achieved by using a non-split superconductor as the detector electrode. As before the detector $G(V)$ trace probes the quasiparticle number at $E = eV_{det} + \Delta_D$, while the quasiparticles close to the spin down/up coherence peaks are probed at $eV_{det}^{\downarrow/\uparrow} = \Delta \mp \mu_B H - \Delta_D$. Figure B.3 shows the spectrum of the closest detector at $H = 1$T as a function of the detection

voltage and the injection current, both theoretically (top) and experimentally (bottom). Both of them exhibit 4 distinctive peaks P_{1-4} corresponding to spin-down holes, spin-up holes, spin-down electrons and spin-up electrons respectively. Experimentally peaks P_1 and P_4 are smeared as injecting higher energy excitations necessitates injecting a higher current thus increasing QP density and reducing the QP-QP interaction time, leading to a smoothing of the distribution function. However, the low energy excitations, P_2 and P_3, are of main interest here. By plotting their heights as a function of the injection current (two panels to the right in figure B.3) an asymmetric component is found when quasiparticles are injected at $\Delta - \mu_B H < |eV_{inj}| < \Delta + \mu_B H$, implying a spin-dependent charge imbalance. To verify that this charge imbalance is localized within $\Delta - \mu_B H < |E| < \Delta + \mu_B H$ the odd component (with respect to the detection voltage) of the experimental trace is shown in figure B.4. The charge imbalance is indeed found only when a spin-polarized current is injected and close to the spectroscopic gap edge of the system.

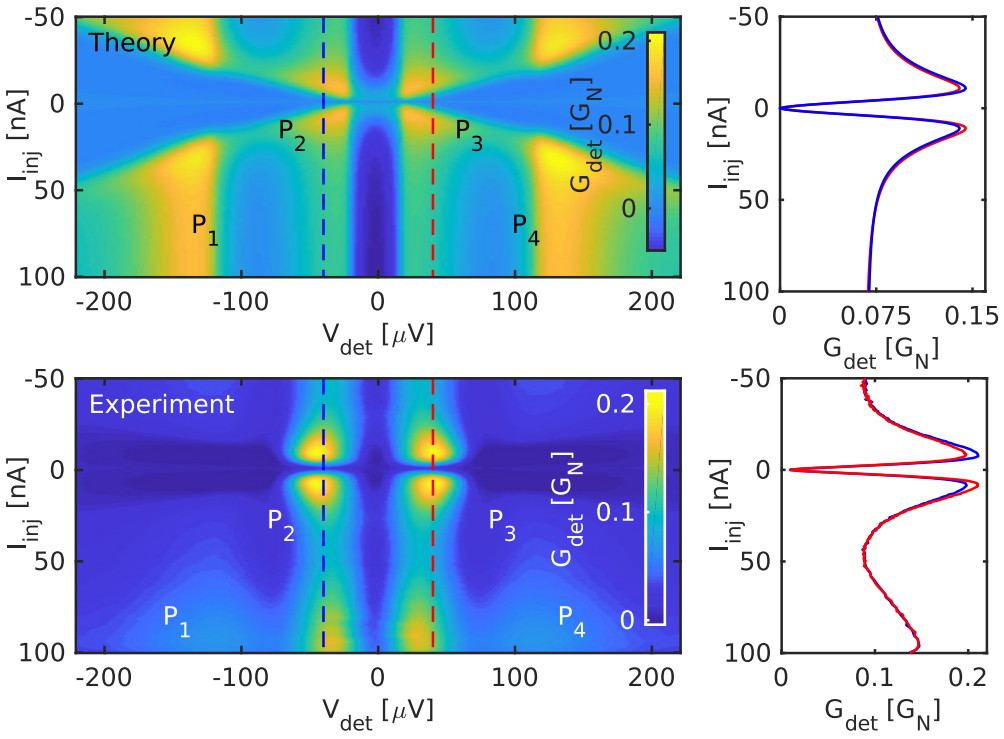

Figure B.3: Left: the theoretical (top) and experimental (bottom) $G_{det}(V_{det})$ curves of the closest detector as a function of the injection current presented as a colormap at $H = 1$T. Right: the corresponding line cuts at $eV = \Delta - \mu_B H - \Delta_D$ as a function of the injection current, taken along the dashed lines (the traces are color coded). The odd component in these traces implies the presence of a spin-dependent charge imbalance.

If this charge imbalance is related to the spin-energy mode it should vanish as $H \to 0$ (because $N_- \to 0$). The right panel of figure B.4 shows the evolution of the odd component at the gap edge as a function of the magnetic field, verifying that it indeed vanishes at $H = 0$. Based on this, along with additional checks to distinguish between the charge imbalance induced by the charge and spin-energy modes, we claim that the observed effects are attributed to the spin-energy mode induced by quasiparticle injection into a Zeeman-split superconductor. This is the first observation of a spin-dependent distribution function

in a superconductor.

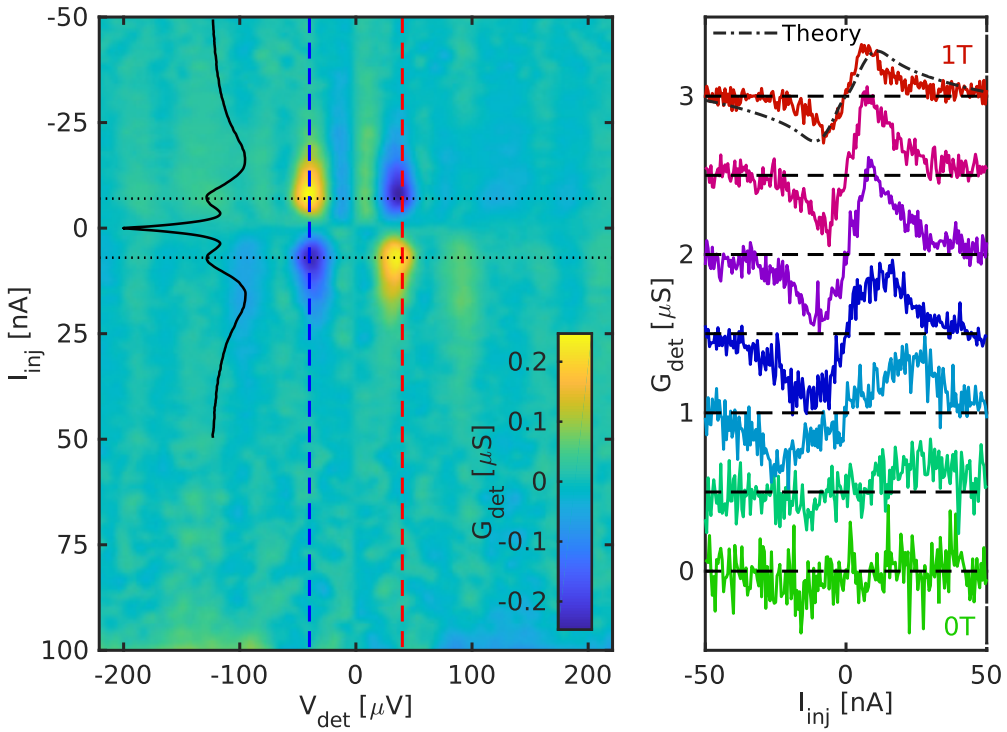

Figure B.4: Left: the odd component of the experimental colormap shown in figure B.3. Right: the odd component of the $G_{det}(V_{det})$ curves at $eV_{det} = \Delta - \mu_B H - \Delta_D$ as a function of the injection current, for several equidistantly spaced magnetic fields from $H = 0$T to $H = 1$T. The dot-dashed black line is the odd component of the theoretical curve shown in figure B.3. The traces are offset vertically for clarity.

A direct follow-up to the experiment could be to improve the detection scheme and to perform a deconvolution to directly probe the distribution function, or to probe the electron-electron interaction rates while injecting quasiparticles. Additionally, using devices with similar geometry, one could look for the recently predicted spin-to-charge conversion [104] and voltage induced superconductivity at high fields [105].

Part II: Dynamics of strongly driven SNS junctions

Josephson junctions are widely used in quantum electronics as nondissipative nonlinear devices. When two superconductors are coupled through a thin insulating layer, the dynamics of the junction are set by the reservoir dynamics, as the tunneling time is in the order of a few fs [75]. Furthermore because of the large energy gap in the insulator (≈ 2eV) the barrier always remains in equilibrium.

The situation is different when the weak link is formed by a disordered (diffusive) normal-metal wire. Because of the finite density of states at the Fermi level and the diffusive transport in the wire two timescales appear [76]: the coupling between the two superconducting reservoirs is set by the diffusion time in the wire $\tau_D = \frac{L^2}{D}$, while the other timescale is the energy relaxation time τ_r at which the system returns back to thermal equilibrium. Therefore the dynamics of Josephson junctions in which the weak link is a normal metal (i.e. a

Superconductor-Normal-Superconductor junction or SNS for short) is not related to the one found in the reservoirs but instead to diffusion and relaxation of the electrons in the normal metal (N).

As Cooper pair tunneling is not the transport mechanism in SNS junctions an alternative mechanism gives rise to a finite supercurrent: an electron in N, with an energy equal to or smaller than the gap of the superconductor, cannot traverse the N/S interface as there are no available states at those energies. Instead it is reflected back as a hole and a Cooper pair is transferred into the superconductor, this process is called Andreev reflection. The back-scattered hole acquires an extra phase equal to the one of the macroscopic wave function in the superconductor. The hole follows the time-reversed trajectory of the electron [77] until it reaches the second N/S interface, at which it is converted back to an electron by removing a Cooper pair from the superconductor. The phase acquired during this whole process must be an integer multiple of 2π giving rise to bound states, also called Andreev bound states (ABS). Because of the diffusive transport in SNS junctions these states form a continuum. As a consequence of the finite normal metal wire length these bound states have a minimum energy in the order of the Thouless energy $E_T = \frac{\hbar}{\tau_D} = \frac{\hbar D}{L^2}$. The Josephson effect is then understood in terms of the supercurrent carried by the continuous ABS spectrum. This is strictly true only when the phases of the two superconducting reservoirs are equal. When the phase difference φ is not zero, the minimum excitation energy is modified as $\propto |\cos(\varphi/2)|$.

This physical picture can be formalized theoretically by using the quasi-classical Green's function approach, in particular through the Usadel formalism which describes disordered systems [14, 55]. The single particle excitation spectrum in the normal metal is found to be gapped, and in the long junction limit ($E_T \ll \Delta$) it is equal to $E_g(\varphi = 0) \approx 3.1 E_T$ and closes at $\varphi = \pi$. Likewise from the Usadel equation the spectral-supercurrent can be computed as a function of energy and the phase difference $j_s(E, \varphi)$. To obtain the supercurrent through the junction one needs to multiply j_s with the (odd component of the) distribution function and integrate over energies [78]:

$$I_s = \int_{-\infty}^{\infty} \mathrm{Im}(j_s) f_L(E) dE \tag{B.2}$$

The phase dependence of the supercurrent (current-phase relation or CPR) can be Fourier expanded as $I_s = \sum_n I_{c,n} \sin(n\varphi)$, where $I_{c,n}$ is the (temperature) dependent current of the n-th harmonic and φ the macroscopic phase difference between the superconducting leads.

This results in a direct possibility of manipulating the SNS junction properties through a non-equilibrium distribution function. As an example, the fact first pointed out by Yip [79] that the spectral supercurrent changes sign at high enough energy can be used to reverse the flow of supercurrent, by modifying the distribution function through the application of a voltage [80], and gives rise to the "π state".

As pointed out by Eliashberg [81] for homogeneous superconductors and recently generalized theoretically to SNS junctions [82], microwave radiation can also be used to drive the distribution function out-of-equilibrium, such that the low-energy states which carry the highest weight in the self-consistency relation and the spectral-supercurrent get depopulated. Therefore this leads to an enhancement of the order parameter (for bulk superconductors) and an increase in the critical current for SNS weak links. In the same spirit, microwave pumping has been used also to increase the critical temperature of conventional superconductors by changing the energy distribution of thermally excited quasiparticles [83].

Unlike in a homogeneous superconductor, in an SNS junction the induced mini-gap depends on the phase difference φ, which in turn results in supercurrent that becomes phase dependent not only through the equilibrium dependence of $j_s(\varphi)$ but also through the absorption and emission rates which depend on the density of states [82]. Two different types of microwave induced transitions can be identified: intraband transmissions which redistribute quasiparticles within the hole or electron part of the spectrum, and interband transitions which promote electrons across the spectral gap, thus creating a pair of (electron- and hole-like) excitations. These interband transitions can be understood a dynamical "pair breaking" effect, which also change the spectral properties of the system - a dip/peak appears in the spectrum (and the spectral supercurrent) at $E = \pm\hbar\omega_{RF}/2$, which is shown in figure B.5. This will inherently change the current flowing through the weak link and as a consequence the current phase relationship acquires higher harmonics that are not present at equilibrium [82, 84].

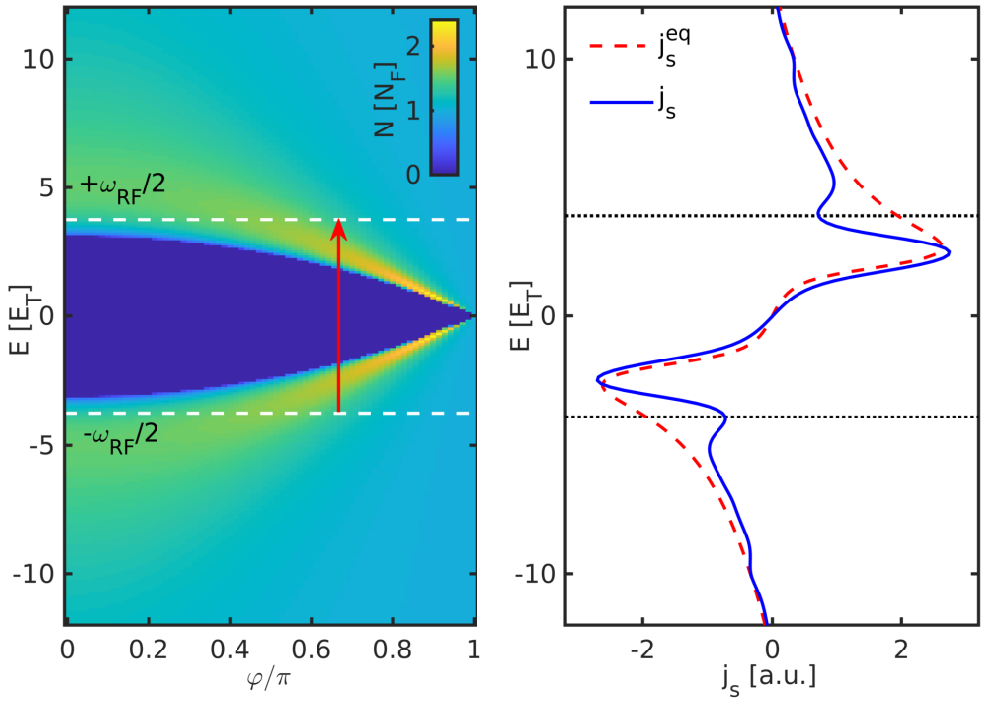

Figure B.5: Left: a schematic of the microwave induced interband transitions (red arrow), the white dashed lines indicate the microwave frequency. Right: The induced changes to the spectral supercurrent (solid blue line), and its value in equilibrium (dashed red line), at $\varphi = \frac{2\pi}{3}$. The dashed lines show that the frequency of the microwave drive.

The experiment presented here explores the high-frequency dynamics of SNS junctions, in particular the response of the system to a drive whose frequency exceeds the inverse diffusion time, in order to look for these dynamical nonequilibrium effects. The theoretical part of the work is based on [82], and was performed in collaboration with Pauli Virtanen and Tero Heikkilä. The results are published in [85].

The device under study is a mesoscopic SNS junction (S=Nb, N=Ag) of intermediate length. The experiment was set up in such a way to enable DC biasing and measurements, as well as the application of RF radiation in a wide range of frequencies (up to $f_{RF} = 40$GHz)

and the detection of emitted radiation through an band-pass filter centered at $f_D = 6$GHz, with a width of about $\delta f_F = 2$GHz. If the junction is biased in DC such that a finite voltage V_{DC} appears across it, according to the 2nd Josephson relation, the phase difference will be driven at a frequency $\omega_J = \frac{2eV_{DC}}{\hbar}$. Then, finite RF power will be emitted by the junction (Josephson emission) at $n\omega_J$ with $P_n \propto I_{c,n}^2$, where n enumerates the harmonics of the CPR. When $n\omega_J$ coincides with $\omega_D = 2\pi f_D$, the detection frequency, this radiation can be detected and acts as a noninvasive probe of the junction current-phase relation. The experiments were performed in in a range of temperatures from $T = 250$mK to $T = 4.2$K for sample characterization. The results shown here were obtained at $T = 1.6$K, where the junction CPR is almost sinusoidal (in equilibrium).

By measuring the the critical current of the junction as a function of temperature, $I_c(T)$, and fitting it to a theoretical model the Thouless energy is found to be $E_T = 19\mu$eV ($\Delta_S = 55E_T$). This corresponds to irradiating the junction with radiation at $f_{RF} \approx 28.5$GHz to induce interband transitions at $\varphi = 0$ ($2E_g(\varphi = 0) = hf_{RF}$).

Again the results can be broken down into two parts:

- **Enhanced quasiparticle cooling**: During the first part of the experiment the sample was characterized in detail. It was found, by measuring the temperature dependence of the critical and retrapping currents as well as the temperature and frequency dependence of the Shapiro step width (and fitting them using the usual T^5 phonon cooling law), that the effective cooling rate, $K \approx 2.8\frac{\text{nW}}{\text{K}^5}$, is about a hundred times larger than the expected value (inferred based on the geometry of the device and the e-ph interaction rate in Ag). The normal metal shadows adjacent to the junction, which are a consequence of the fabrication procedure, were found to behave as "quasiparticle traps" and are the source of this effect. Although this is a rather technical finding, this mechanism enabled the observation of a novel nonequilibrium state. This is technical result, but it is essential here as the higher relaxation rate allowed us to explore novel nonequilibrium effects, beyond the well understood thermal ones.

- **Nonadiabatic dynamics of strongly driven junctions**: To address the junction CPR through the Josephson emission spectrum we can first measure the emitted power (without any external RF irradiation), as seen through the detection window, as a function of the V_{DC} across the junction, as is given in figure B.6. Two peaks are distinguishable, labeled P_1 and P_2. The Josephson emission can be modeled as two Gaussian-smeared peaks centered at ω_J and $2\omega_J$, corresponding to the emission associated with the first two CPR harmonics. By using the peak heights and widths as fitting parameters, and convolving the emission spectrum with the profile of our filter the experimental trace is nicely reproduced, confirming our association of these peaks to the first two harmonics of the CPR.

  With this result we can now proceed to study the response of the system to high frequency irradiation. The top two panels of figure B.7 show the heights of peaks P_1 (left scale) and P_2 (right scale) as a function of the normalized RF power $s = \dfrac{2eI_{RF}R_N}{\hbar\omega_{RF}}$, for two frequencies $f = 20.72$GHz (left, which is the threshold for efficiently driving transitions across the gap) and $f = 35.18$GHz (right, which is sufficiently high to induce interband transitions). With only the equilibrium adiabatic phase dynamics, induced by the microwave drive, in mind the harmonics of the CPR should be given by $I_{c,n} = I_{c,n}^{eq} J_0(ns)$, where n enumerates the

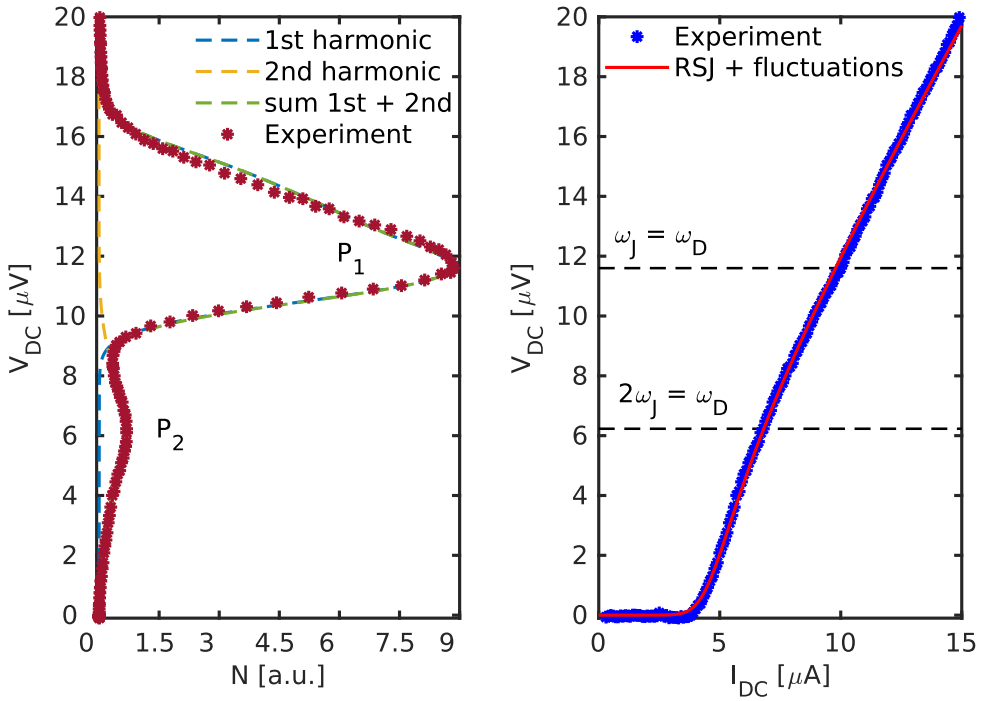

Figure B.6: Left: the detected power N as as a function of the voltage across the junction. Right: the $V(I)$ curve of the junction. The dashed horizontal lines indicate the voltages at which the two peaks are observed.

harmonics and J_0 is the Bessel function of first kind. This behavior is found at low powers ($s < 1$, see the full lines in B.7), while at higher powers, and especially for the higher frequency, there is a significant increase of the second harmonic amplitude, which is as expected from the interband transition picture.

To verify that this is a real effect we can reconstruct the CPR as $I^r(\varphi) \propto \sqrt{P_1}\sin(\varphi) + \sqrt{P_2}\sin(2\varphi)$ based on these measurements. Most notably, for the higher frequency there isn't a value of s at which the amplitudes of both $I_{c,1}$ (P_1) and $I_{c,2}$ (P_2) vanish. This suggests that, unlike in equilibrium, the critical current of the junction cannot be (fully) suppressed by microwave irradiation. By calculating the critical current based on the reconstructed CPR and comparing it to the directly measured value, and using an overall refactor as a fitting parameter, we achieved a good agreement between the two (see the full text of the thesis for the details). The implications of this result are twofold: firstly the Josephson spectroscopy gives a quantitatively good probe of the CPR, and more importantly shows that the system properties are unmodified compared to the $V_{DC} = 0$ case, allowing us to use the theory assuming a phase bias [82] to calculate the CPR.

By using the experimentally obtained parameters of the system and calculating response of the system we obtain the bottom two panels of B.7, which exhibit the same features as in experiment. More importantly, here we can distinguish between different contributions to the second harmonic. By neglecting the spectral changes and working only with a non-equilibrium distribution function (i.e. within the Eliashberg approximation), the amplitude of the second harmonic is greatly underestimated (the purple lines in B.7).

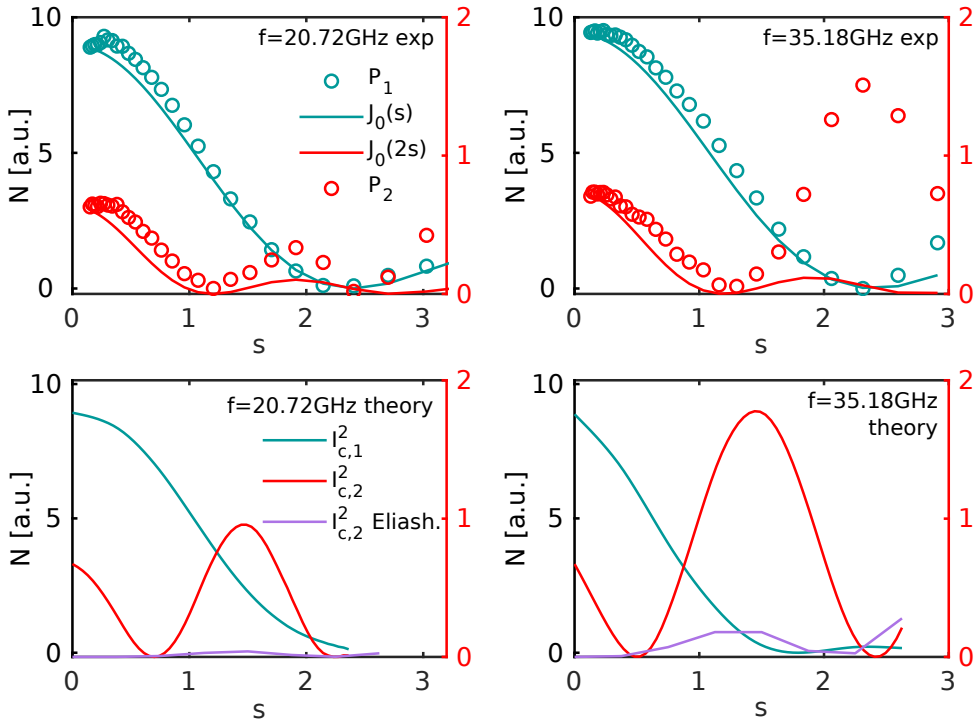

Figure B.7: Top left: the observed amplitudes of peaks P_1 (left scale) and P_2 (right scale) as a function of microwave power at $T = 1.6$K and $f = 20.72$GHz. In all four panels the 2nd harmonic is shown on the right scale. The calibration of s was done such that the low power behavior of peak P_1 follows $J_0(s)$. The second harmonic (peak P_2) roughly follows $J_0(2s)$. Top right: the same as top left but at $f = 35.18$GHz - at high powers the second harmonic (peak P_2) is significantly increased compared to $P_2(s = 0)J_0(2s)^2$. Bottom left (right): theoretical curves computed using $\Gamma/E_T = 0.4$, $k_BT/E_T = 7$, $\Delta/E_T = 55$ and $\hbar\omega_{RF}/E_T = 3$ ($\hbar\omega_{RF}/E_T = 7$), respectively. Within the Eliashberg approximation the second harmonic is negligible at all powers.

Therefore the spectral changes, as the ones shown in B.5, are essential for explaining the experimental data, revealing a novel dynamical out-of-equilibrium state as the origin of the effect.

The spectroscopic approach developed here could be used for several other types of weak links: it could be used to study the microwave induced CPR modifications in atomic contacts [106, 107]. In nanowire junctions with Majorana bound states, the microwave affected CPR might reveal signatures about the topologically forbidden transitions [108, 109, 110].

Appendix C

Long résumé en français

Cette annexe fournit un résumé de la thèse en français. Pour plus de détails, le lecteur est invité à consulter le texte principal ou les publications, qui sont reproduites intégralement en annexe D.

La caractéristique principale de la supraconductivité est un gap, Δ, dans le spectre d'excitations. Dans la théorie BCS de la supraconductivité, l'amplitude de ce gap est directement liée non seulement à la force du mécanisme d'appariement, mais aussi à la présence d'excitations (quasiparticules) et à leur distribution en énergie. Le rôle des excitations dans l'amplitude du gap est formellement décrit par une équation auto-cohérente. Alors qu'un appariement plus fort peut augmenter Δ, les excitations ne peuvent que le réduire. Néanmoins, il a été reconnu très tôt que l'ingénierie d'une fonction de distribution hors équilibre pour les quasiparticules peut conduire à des états fondamantaux instables originaux [1] ou même à augmenter la température critique [2].

Les quasiparticules peuvent être excitées thérmiquement, par absorption du rayonnement électromagnétique ou injection d'électrons non supraconducteurs. Lorsque la perturbation est sans charge, ce qui est le cas du rayonnement, seule l'énergie est transférée au supraconducteur. En raison de la symétrie électron-trou intrinsèque d'un supraconducteur BCS, il en résulte un nombre égal d'excitations de type électron et de type trou. Si au contraire une particule chargée est injectée dans le supraconducteur, l'équilibre entre les excitations de type électron et de type trou est rompu, tandis que la neutralité de la charge est préservée en retirant des paires de Cooper du condensat [3].

Ces deux types d'excitation correspondent à des modes d'excitation différents de la fonction de distribution, f, appelés mode d'énergie et mode de charge. Formellement, ils sont classés en fonction de la symétrie de la composante (hors équilibre) de la fonction de distribution par rapport au niveau de Fermi. Ces modes sont également appelés longitudinal (f_L) et transverse (f_T), car ils entrent avec un déphasage de $\pi/2$ dans l'équation auto-cohérente du gap [4].

La fonction de distribution hors-équilibre dans le supraconducteur dépend du taux d'excitation, de relaxation et de recombinaison des quasiparticules. Les différents mécanismes à l'œuvre établissent une hiérarchie des échelles de temps impliquées dans la relaxation des différentes composantes de f. Ainsi, le mode d'énergie étant, en générale, associé au temps de vie le plus long, il est responsable de la plupart des effets hors-équilibre observés dans les supraconducteurs.

L'élaboration d'un cadre théorique détaillé pour décrire le transport de l'énergie et des

charges n'est pas une tâche facile, car les équations cinétiques de la diffusion des quasiparticules comprennent des processus inélastiques (non locale en énergie), qui peuvent modifier localement le nombre de quasiparticules et leur distribution, ainsi que le paramètre d'ordre supraconducteur. Par exemple, un phonon de faible énergie, résultant de la recombinaison de deux quasiparticules, peut être réabsorbé ailleurs dans le supraconducteur, brisant ainsi une paire de Cooper [10].

La situation est plus simple lorsque la taille du dispositif devient plus petite que les longueurs de relaxation et de recombinaison des quasiparticules. En l'absence d'interactions, la fonction de distribution est essentiellement fixée par les conditions aux bords. Par exemple, pour un fil connecté à deux réservoirs, la fonction de distribution à chaque point du fil est une combinaison linéaire des fonctions de distribution des réservoirs. Ceci est bien décrit théoriquement dans le formalisme Keldysh-Usadel [11, 12, 13], en négligeant les termes de collision liés aux interactions inélastiques.

Le sujet de ce travail est le transport de quasiparticules dans cette limite de faible interaction. Les questions abordées respectivement dans les parties I et II de la thèse, sont :

- Est il possible d'enlever la dégénérescence de spin de la fonction de distribution ?
- La fonction de distribution hors équilibre peut-elle avoir un retour dynamique sur les propriétés spectrales d'un supraconducteur ?

Partie I : Physique du spin dans les supraconducteurs hors équilibre

Pendant longtemps, les travaux sur la supraconductivité hors équilibre se sont concentrés principalement sur les excitations sans spin [4]. La fonction de distribution des quasiparticules (QP) hors équilibre $f(E)$ peut être décomposée en une partie impaire par rapport au niveau de Fermi, c'est le mode d'énergie $f_L(E) = f(-E) - f(E)$ et en une partie paire, c'est le mode de charge $f_T(E) = 1 - f(E) - f(-E)$ [4, 14]. Si on considère que $f(E)$ est une fonction de Fermi alors les modes d'énergie et de charge peuvent être excités respectivement tout simplement par une température effective T^*_{QP} et un potentiel chimique $\mu_{QP} \neq 0$ (mesuré à partir de l'énergie de Fermi) comme représenté sur les deux panneaux supérieurs de la figure C.1. Le mode d'énergie contribue à une énergie finie (hors équilibre) stockée dans les excitations, tandis que le mode de charge conduit à un déséquilibre de charge [18], c'est-à-dire, un déséquilibre dans le nombre de QP de type trou et de type électon.

La possibilité de différentes fonctions de distribution pour les électrons de spin up et down a été soulevée pour les métaux normaux et les supraconducteurs. Dans les supraconducteurs [25, 26, 13, 11, 12, 27, 56], la décomposition de la fonction de distribution des quasiparticules $f(E)$ décrite précedement peut être généralisée au cas de QP polarisées en spin par l'addition des modes de spin $f_{T3}(E) = (f_{T\uparrow}(E) - f_{T\downarrow}(E))/2$ et d'énergie dépendant du spin $f_{L3}(E) = (f_{L\uparrow}(E) - f_{L\downarrow}(E))/2$ [11, 12, 13, 56]. Par construction, f_L et f_{L3} sont impairs en énergie, tandis que f_T et f_{T3} sont pairs. Ces nouveaux modes n'existent que si les QP de spin up et down ont des fonctions de distribution différentes, c'est-à-dire $f_\uparrow(E) \neq f_\downarrow(E)$. Pour bien comprendre la signification physique des modes dépendant du spin, il est plus facile de considérer le cas d'un supraconducteur en présence d'un splitting Zeeman de la densité d'états BCS (DOS), obtenu

en appliquant un champ magnétique externe H. Cela augmente (diminue) l'énergie des QP de spin up (down) de $E_Z = \frac{g}{2}\mu_B H = \mu_B H$ et divise le DOS de sorte que seules les excitations de spin down sont autorisées dans la plage d'énergie $\Delta - E_Z < |E| < \Delta + E_Z$. Toujours dans le cas simple d'une fonction de distribution de Fermi, le mode d'énergie dépendante du spin f_{L3} peut être compris en termes d'une température des QP dépendante du spin $T_\uparrow \neq T_\downarrow$, et le mode de spin f_{T3} en termes d'un potentiel chimique dépendant du spin $\mu_\uparrow \neq \mu_\downarrow$, voir les deux panneaux inférieurs de la figure C.1.

En raison de la symétrie du spectre d'excitation en présence d'un splitting Zeeman et des modes hors-équilibre, le mode de spin entraîne une accumulation de spin finie dans le supraconducteur, tout comme le mode d'énergie. De même, le mode de charge conduit à un déséquilibre de charge et il en va de même pour le mode d'énergie dépendant du spin. Ces affirmations sont formellement décrites par l'équation C.1 :

$$\begin{aligned} \mu_z &= \int_{-\infty}^{\infty} dE\big[f_L(E)N_- + f_{T3}N_+\big], \\ \mu &= \int_{-\infty}^{\infty} dE\big[f_T(E)N_+ + f_{L3}N_-\big] \end{aligned} \tag{C.1}$$

où $N_\pm = \frac{N_\uparrow \pm N_\downarrow}{2}$, $N_\uparrow$ et $N_\downarrow$ sont les DOS des QP avec spin up et down respectivement, μ est le déséquilibre de charge et μ_z le déséquilibre de spin.

Le mode énergie peut être excité par des perturbations neutres en charge telles que le rayonnement électromagnétique dont la fréquence est supérieure au gap supraconducteur [16]. Le mode de charge, en revanche, peut être excité en injectant des porteurs chargés (c'est-à-dire des électrons ou des trous) à travers une barrière tunnel. Dans le supraconducteur ils deviennent des quasiparticules [17]. Comme les quasiparticules ne sont pas instantanément converties en paires de Cooper, leur potentiel chimique est décalé vers le haut ou vers le bas par rapport à celui des paires de Cooper. Ceci a été mesuré comme une chute de tension *non locale* entre le supraconducteur et une électrode en métal normal couplé au supraconducteur par une barrière tunnel [18, 19]. Si des électrons ou des trous sont injectés à l'énergie $|E| > \Delta$, les deux modes de charge et d'énergie sont excités. Le temps de relaxation du mode énergie est le temps de diffusion inélastique (électron-phonon) [15] tandis que le mode de charge relaxe sur une longueur de relaxation de la charge [19, 20, 21, 22, 23].

Dans une expérience pionnière de type polariseur-analyseur, Johnson et al. [28] ont montré que l'injection de spins dans un métal normal à partir d'une électrode ferromagnétique est possible en appliquant une tension de polarisation à l'interface entre les deux. L'aimantation hors équilibre créée dans le métal normal est détectée électriquement, en mesurant la tension entre celui-ci et une seconde électrode ferromagnétique [29]. Ce signal *non local* est directement proportionnel au déplacement du potentiel chimique, μ_s, des électrons de spin up (down) dû à l'accumulation de spin [30, 31]. Les potentiels chimiques de spin up et down se déplacent de la même amplitude, mais avec des signes opposés. La longueur de relaxation du spin mesurée dans les métaux légers de haute pureté (qui ont un faible taux de collisions spin-orbite) peut atteindre 100μm, et le temps de relaxation du spin est d'environ 50ns [28].

Dans les films minces supraconducteurs, il est possible d'injecter du spin et d'exciter préférentiellement des QP d'un seul spin à partir d'une électrode normale (plutôt que ferromagnétique) : si le champ est appliqué parallélement au plan de l'échantillon, les courants d'ecrantage sont supprimés de façon quadratique en fonction de l'épaisseur de l'échantillon, ce qui permet d'appliquer un champ magnétique suffisamment important pour induire un split-

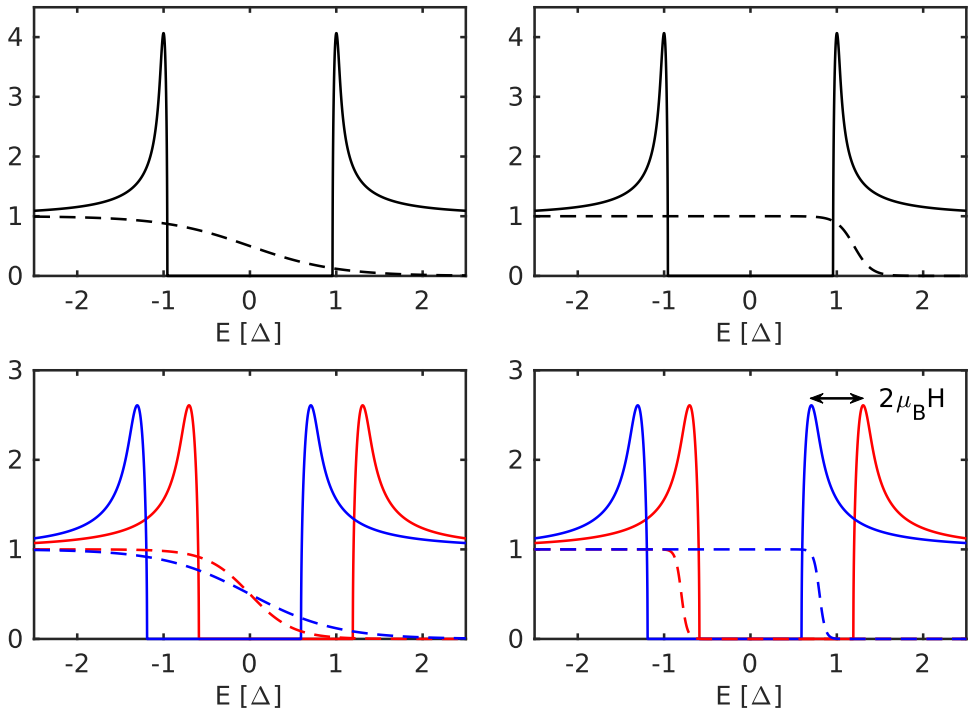

Figure C.1: Une représentation des différents modes de la fonction de distribution : en haut à gauche, une température effective T^*_{QP} $(H = 0)$, qui est une réalisation spécifique du mode d'énergie f_L, en haut à droite un potentiel chimique effectif μ_{QP} (avec une température finie, $H = 0$) qui est la fonction de distribution la plus simple qui excite le mode de charge f_T. Les panneaux inférieur gauche et inférieur droit montrent une température et un potentiel chimique dépendant du spin, correspondant aux réalisations les plus simples des modes d'énergie dépandant du spinf_{L3} et spin f_{T3} $(H > 0)$.

ting Zeeman dans la densité d'états. Ensuite, une aimantation peut être injectée en polarisant la jonction d'injection par une tension, V_{inj} de telle sorte que $\Delta - E_Z < |eV_{inj}| < \Delta + E_Z$. Dans cette plage d'énergie, selon la discussion précédente, seul la DOS de spin-down est non nulle, ce qui conduit à une accumulation finie de spins dans le supraconducteur.

Il a été démontré que l'injection de spin dans les supraconducteurs par cette méthode entraîne une accumulation de spin et de longue portée, provenant soit de f_L soit de f_{T3} [36, 37, 38]. Les mesures du temps de relaxation de spin, de l'aimantation hors-équilibre et de diffusion spin-orbite indiquent que l'accumulation finie de spin au-delà de la longueur de relaxation de spin λ_{sf} est presque entièrement due à f_L, car à la différence de f_{T3} ce mode relaxe sur une échelle bien plus grande λ_{rec} [39, 40]. À peu près au même moment, des températures efficaces différentes pour l'électron de spin up et down ont été observées dans des valves de spin [32]. En effet, une température efficace dépendante du spin est la manifestation la plus simple du mode d'énergie dépendant du spin, dans lequel les deux espèces de spin transportent des courants d'énergie différents.

Ce travail se concentre sur la recherche de l'état hors équilibre généré par l'injection d'un courant polarisé en spin à partir d'un métal normal, avec un accent particulier sur le mode d'énergie dépandant du spin f_{L3}.

En principe, il existe deux approches possibles pour y parvenir : soit sonder la décroissance

spatiale des accumulations de charge et de spin, car les quatre modes diffusent sur des échelles de longueur différentes, soit effectuer une spectroscopie sensible au spin de la population de QP. Dans cette expérience, nous avons adopté la deuxième approche.

À cette fin, plusieurs dispositifs ont été fabriqués sous la forme d'un fil diffusif de Al ultra-mince. Les quasiparticules sont injectées à partir d'une jonction tunnel avec un métal normal. Dans nos expériences, $E_Z > \alpha$, l'énergie de pair-breaking orbital, jusqu'à H_c, le champ critique du supraconducteur, nous permettant de résoudre les pics de cohérence de spin down et up dans le spectre d'excitation. Ainsi, lorsque nous injectons un courant électrique tunnel, la DOS agit comme un filtre de spin presque parfait pour $\Delta - E_Z < |eV_{inj}| < \Delta + E_Z$, même si la transmission de la barrière est indépendante du spin, ce qui nous permet d'injecter du spin et d'induire $f_\uparrow(E) \neq f_\downarrow(E)$ simultanément. Afin de sonder l'état hors-équilibre ainsi obtenu, plusieurs détecteurs supraconducteurs ont été placés à différentes distances de l'injecteur. Dans le but d'observer une distribution dépendant du spin, le detector le plus proche se trouve dans une longueur de relaxation de spin de l'injecteur, car la longueur de relaxation du mode d'énergie dépendant du spin est de l'ordre de λ_{SF}. Dans notre expérience, λ_{sf} est estimée à $\approx$ 240nm, alors que la distance minimale injecteur-détecteur est de 250nm. Les autres détecteurs ont été placés à quelques μm de distance, pour étudier la décroissance spatiale des quasiparticules injectées. Comme expliqué dans le texte de la thèse, le pic de cohérence de l'électrode du détecteur à Δ_D peut être utilisé comme une sonde spectroscopique de l'état hors-équilibre : en mesurant la conductance différentielle $G_{det}(V_{det})$ on sonde la densité QP à $E = \Delta_D + eV_{det}$, où Δ_D est le gap du détecteur. Les électrodes de détection ont été fabriquées en Al saupoudré d'une fine couche de Pt, qui induit une forte interaction spin-orbite dans le détecteur et mélange les spins. La densité d'états du détecteur n'est donc pas "splitté" Zeeman ce que de fait et d'une façon non intuitive donne un détecteur sensible au spin : les quasi-particules de spin down/up sont détectées à différents voltages/énergies $eV_{det}^{\downarrow/\uparrow} = \Delta \mp \mu_B H - \Delta_D$. Les mesures hors-équilibre ont été effectuées dans un réfrigérateur à dilution avec une température de base de $T = 90$mK. Tous les résultats théoriques ont été obtenus en utilisant la théorie développée dans [56]. Dans ce résumé, seules les données obtenues à l'aide du détecteur le plus proche sont présentées, car les autres montrent des résultats cohérents avec des expériences précédentes mais pas d'évidence de modes hors-équilibre dépendant du spin.[36, 37, 38].

Les principaux résultats de l'expérience peuvent être ventilés comme suit :

- **Observation d'une fonction de distribution hors-équilibre de type non-Fermi** : En appliquant une tension V_{inj} aux bords de la jonction tunnel d'injection, la fonction de distribution du métal normal est imprimée dans le supraconducteur. L'état hors équilibre qui en résulte est un état non thermique, caractérisé par un grand nombre de quasiparticules au bord du gap, en raison du pic de cohérence et de la mobilité décroissante des quasi-particules proches de $E = \Delta$, et une queue avec une marche à $E \approx eV_{inj}$. En effectuant une spectroscopie de quasiparticules dans la limite des courants d'injection faibles à champ magnétique nul à l'aide du détecteur le plus proche, on obtient précisément ce résultat, comme le montre la figure C.2. L'affirmation précédente n'est strictement vraie que si l'interaction entre quasiparticules est faible. En effet, à des courants d'injection plus élevés ou si la jonction de détection est plus éloignée de la jonction d'injection, on trouve une population de quasiparticules plus étalée en énergie et la coupure en forme de marche ne peut pas être observée. Cet argument sur la forme de la fonction de distribution peut être

justifié plus rigoureusement dans le cadre du formalisme de Keldysh-Usadel : Le temps de diffusion des qusiparticules de l'injecteur à l'extrémité du fil, ($\approx$ 20ns), est beaucoup plus court que le temps de recombinaison inélastique des quasiparticules ($\approx$ 400ns [5]), et par conséquent la relaxation de l'énergie a lieu dans les réservoirs. Cette affirmation a été vérifiée expérimentalement en sondant la décroissance spatiale du nombre de quasiparticules hors équilibre. Si nous nous concentrons sur la région de faible injection, les interactions entre quasiparticules peuvent être négligées, ce qui permet d'éliminer du modèle toutes les interactions inélastiques non locales, simplifiant ainsi grandement le problème. Les équations cinétiques peuvent être facilement résolues, ce qui permet d'obtenir une fonction de distribution avec une marche à $E \approx eV_{inj}$. Une simulation des spectres tunnel mesurés par la jonction de détection, obtenue à partir des fonctions de distribution calculées théoriquement est également présentée dans la figure C.2, elle montre un bon accord qualitatif avec les résultats expérimentaux. Cet effet a été observé à la fois pour toute valeur du champ magnétique (voir les régions bleu foncé proches de $I_{inj} = 0$ dans le panneau expérimental de la figure C.3) et indirectement par les mesures du gap en fonction de la densité des quasiparticules injectées $\Delta(N_{QP})$. Ces résultats montrent que pour des courtes échelles de longueur, l'injection de quasiparticules entraîne une fonction de distribution non thermique et que le supraconducteur ne peut pas être décrit par une température effective.

- **Observation d'une fonction de distribution dépendant du spin** : Comme discuté précédemment, en présence d'un splitting Zeeman, l'injection de quasiparticules avec une énergie comprise $\Delta - \mu_B H < |E| < \Delta + \mu_B H$ devrait, en principe, conduire à une fonction de distribution dépendante du spin. Dans notre expérience, l'accent a été mis sur le mode d'énergie dépendant du spin, qui peut être détecté car il produit un déséquilibre entre excitations de type trou et de type électron, appelé également déséquilibre de charge. On peut voir sur la figure C.1, ainsi que sur l'équation C.1, que la présence du mode d'énergie dépendant du spin crée un nombre inégal d'excitations "à faible énergie" de quasiparticules de type électron de spin down et de type trou de spin up (ces deux excitations portent la même aimantation car le trou de spin up enlève un électron de spin down). Ce déséquilibre de charge est situé au bord du gap, et n'est présent que si $N_\downarrow \neq N_\uparrow$ c'est-à-dire si la densité d'états un présente aucun splitting Zeeman. Ces propriétés du mode d'énergie dépendant du spin ont été utilisées pour en détecter sa présence expérimentalement. La sensibilité au spin de nos détecteurs SIS′ est obtenue en utilisant un supraconducteur sans splitting Zeeman comme électrode de détection. Comme auparavant, la conductance dynamique $G(V)$ sonde le nombre de quasiparticules à $E = eV_{det} + \Delta_D$, tandis que les quasiparticules proches des pics de cohérence de spin down/up sont sondés à $eV_{det}^{\downarrow/\uparrow} = \Delta \mp \mu_B H - \Delta_D$. La figure C.3 montre le spectre du détecteur le plus proche de l'injecteur, à $H = 1$T en fonction de la tension de détection et du courant d'injection, à la fois théoriquement (en haut) et expérimentalement (en bas). Tous deux présentent 4 pics distincts P_{1-4} correspondant respectivement aux trous de spin-down, aux trous de spin-up, aux électrons de spin-down et aux électrons de spin-up. Les pics expérimentaux P_1 et P_4 sont moins marqués car l'injection d'excitations à plus haute énergie correspond à un courant plus élevé, ce qui augmente la densité de QP et réduit le temps d'interaction entre quasiparticules, ce qui conduit à un lissage de la fonction de distribution. Cependant, les excitations à faible énergie, P_2 et P_3, sont les plus intéressantes. En traçant leurs hauteurs en fonction du courant d'injection (deux panneaux à droite sur la figure C.3), on trouve une composante asymétrique lorsque les quasiparticules sont injectées à $\Delta - \mu_B H < |eV_{inj}| < \Delta + \mu_B H$, ce

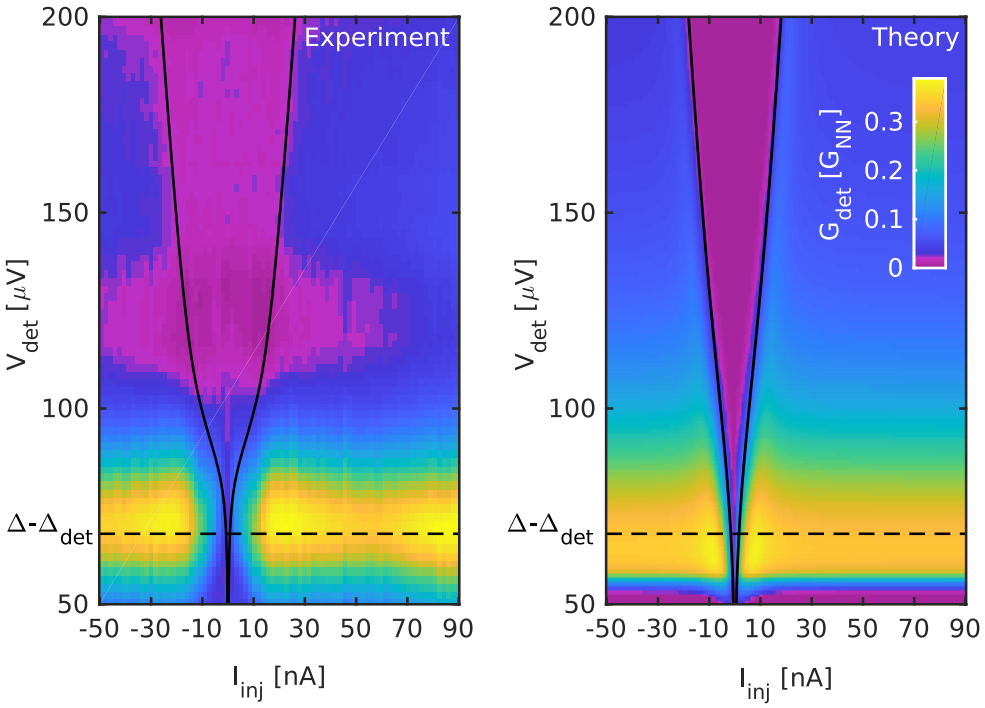

Figure C.2: A gauche : Le spectre $G(V_{det}) \propto N_{QP}(E = eV_{det} + \Delta_D)$ obtenu en utilisant le détecteur le plus proche à $H = 0$ en fonction du courant d'injection. Deux caractéristiques peuvent être identifiées : un signal important à $E = \Delta$ le long de la ligne horizontale en pointillés. Deuxièmement, aucune quasi-particule n'est détectée dans la région violette, qui est délimitée par les courbes expérimentales $I_{inj}(V_{inj})$ de l'injecteur (lignes noires continues), en dehors desquelles aucune densité QP finie n'est détectée. Cela implique que les QP ne sont détectés qu'à des énergies inférieures à $E = eV_{inj}(I_{inj})$. Les zones violettes non comptabilisées en dehors des limites de $I_{inj}(V_{inj})$ sont dues à la soustraction de fond non négligeable, comme détaillé dans le texte principal de la thèse. A droite : Une simulation du spectre du détecteur basée sur l'approche Keldysh-Usadel présentée de la même manière. La barre de couleur est commune aux deux panneaux.

qui implique un déséquilibre de charge dépendant du spin. Pour vérifier que ce déséquilibre de charge est localisé dans $\Delta - \mu_B H < |E| < \Delta + \mu_B H$, la composante impaire (par rapport à la tension de détection) de la trace expérimentale est indiquée sur la figure C.4. Le déséquilibre de charge n'est en effet observé que lorsqu'un courant polarisé de spin est injecté avec une énergie proche du gap.

Si ce déséquilibre de charge est lié au mode f_{L3}, il devrait disparaître à champ nul. Le panneau droit de la figure C.4 montre l'évolution de la composante impaire de la conductance au bord du gap en fonction du champ magnétique. Comme attendu elle disparaît à $H = 0$. Sur cette base, ainsi que grâce à des vérifications supplémentaires pour distinguer le déséquilibre de charge induit par les modes de charge et d'énergie dépendant du spin, nous affirmons que les effets observés sont attribués au mode f_{L3}. C'est la première observation d'une fonction de distribution dépendant du spin dans un supraconducteur.

Une suite directe de l'expérience pourrait consister à améliorer le schéma de détection et à effectuer une déconvolution pour sonder directement la fonction de distribution et donc les

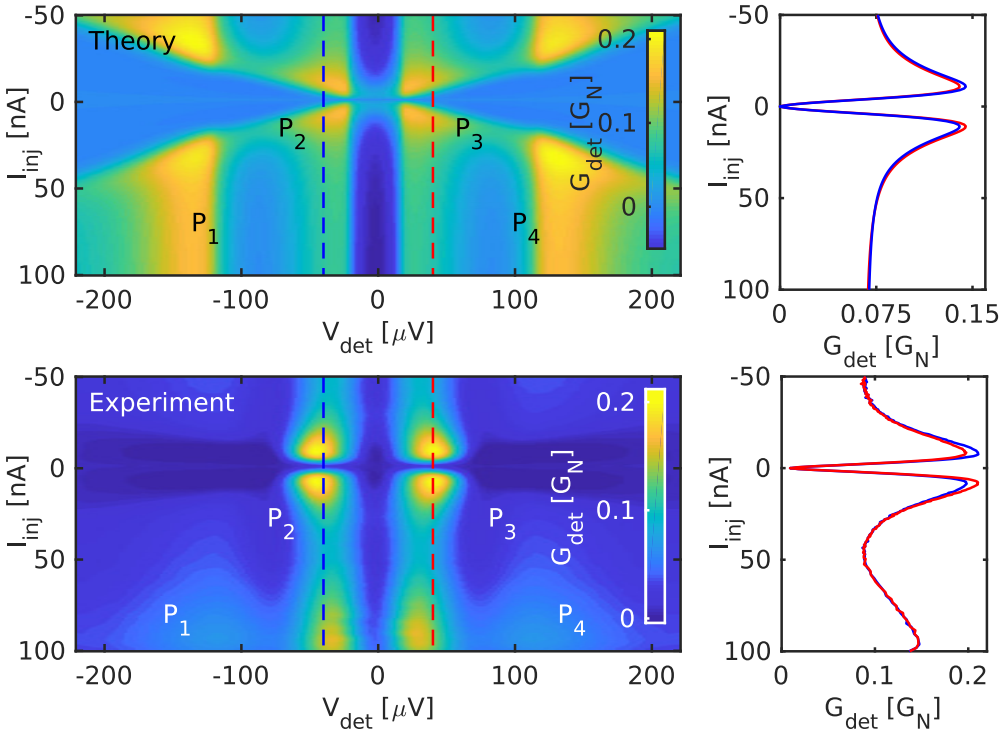

Figure C.3: A gauche : les courbes $G_{det}(V_{det})$ théorique (en haut) et expérimentale (en bas) du détecteur le plus proche en fonction du courant d'injection présentées sous forme de carte de couleurs à $H = 1$T. A droite : les coupes de lignes correspondantes à $eV = \Delta - \mu_B H - \Delta_D$ en fonction du courant d'injection, prises le long des lignes pointillées (les traces sont codées en couleur). L'élément impair de ces traces implique la présence d'un déséquilibre de charge dépendant du spin.

taux d'interaction entre quasiparticules. En outre, en utilisant des dispositifs de géométrie similaire, on pourrait étudier la conversion spin-charge [104] et supraconductivité induite par une tension finie à haut champ magnétique [105] comme prévu théoriquement.

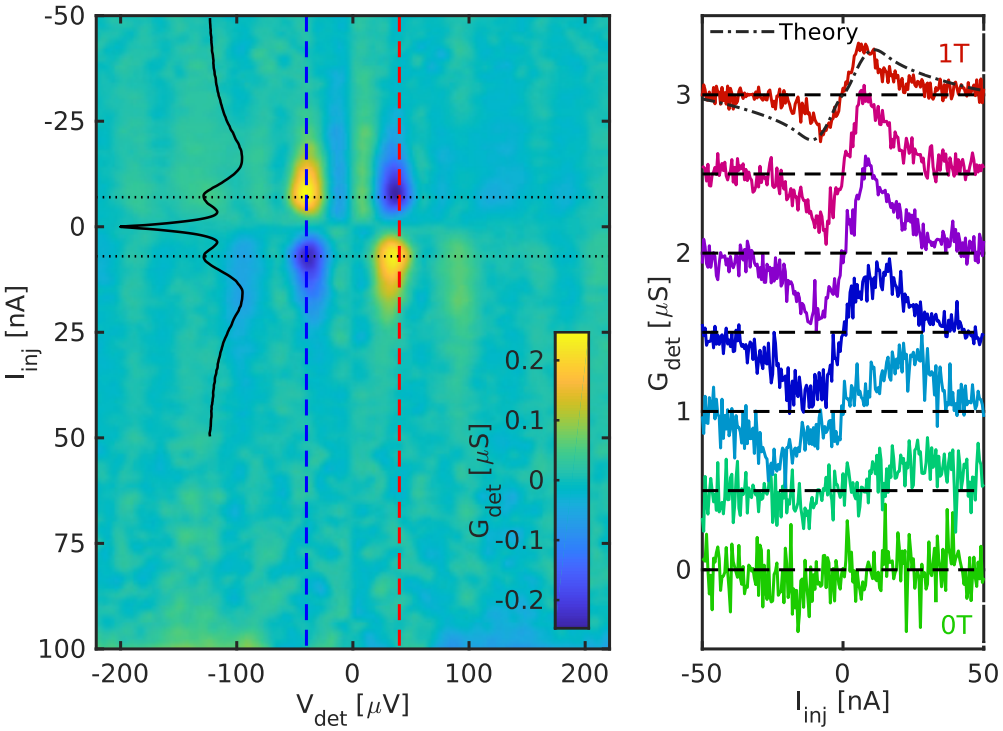

Figure C.4: A gauche : la composante impaire de la carte de couleurs expérimentale présentée dans la figure C.3. A droite : la composante impaire des courbes $G_{det}(V_{det})$ à $eV_{det} = \Delta - \mu_B H - \Delta_D$ en fonction du courant d'injection, pour plusieurs champs magnétiques équidistants de $H = 0$T à $H = 1$T. La ligne noire en pointillés est la composante impaire de la courbe théorique présentée sur la figure C.3. Les traces sont décalées verticalement pour plus de clarté.

Partie II : Dynamique des jonctions Josephson

Les jonctions Josephson sont largement utilisées en électronique quantique comme dispositifs non linéaires non dissipatifs. Lorsque deux supraconducteurs sont couplés à travers une fine couche isolante, la dynamique de la jonction est déterminée par la dynamique des réservoirs, car le temps tunnel est de l'ordre de quelques fs [75]. En outre, en raison du grand gap en d'énergie dans l'isolant (≈ 2eV), la barrière reste toujours à l'équilibre.

La situation est différente lorsque le point faible entre les deux supraconducteurs est formé par un fil métallique désordonné (diffusif). En raison de la densité finie des états au niveau de Fermi et du transport diffusif dans le fil, deux échelles de temps apparaissent [76] : le couplage entre les deux réservoirs supraconducteurs est fixé par le temps de diffusion dans le fil $\tau_D = \frac{L^2}{D}$, l'autre échelle de temps est le temps de relaxation de l'énergie τ_e qui correspond au temps nécessaire pour que le fil revienne à l'équilibre thermique. Par conséquent, la dynamique des jonctions Josephson de type supraconducteur-normal-supraconducteur ou SNS en abrégé n'est pas liée à la dynamique des réservoirs mais plutôt à la diffusion et à la relaxation des électrons dans le métal normal (N).

Comme le tunnel de paires de Cooper n'est pas le mécanisme de transport dans les jonctions SNS, un autre mécanisme donne lieu à un supercourant fini : un électron dans N, avec une énergie égale ou inférieure à Δ, ne peut pas traverser l'interface N/S car il n'y a pas d'états disponibles à cette énergie dans S. Il est donc réfléchi comme un trou et une paire de

Cooper est transférée dans le supraconducteur, ce processus est appelé réflexion d'Andreev. Le trou rétrodiffusé acquiert une phase supplémentaire égale à celle de la fonction d'onde macroscopique dans le supraconducteur. Le trou suit la trajectoire inversée de l'électron [77] jusqu'à ce qu'il atteigne la deuxième interface N/S, où il est reconverti en électron en absobant une paire de Cooper du supraconducteur. Des états liés apparaissent dans N car la phase acquise pendant ce processus doit être un multiple entier de 2π, ces états liés sont appelés états d'Andreev (ABS). En raison du transport diffusif dans les jonctions SNS, ces états forment un continuum d'énergie inférieure au gap du supraconducteur. Mais en raison de la longueur finie du fil métallique, ces états liés ont une énergie minimale, E_g, de l'ordre de l'énergie de Thouless $E_T = \frac{\hbar}{\tau_D} = \frac{\hbar D}{L^2}$. L'effet Josephson est alors compris en termes de supercourant transporté par le spectre continu de ABS. Lorsque la différence de phase φ entre les deux supraconducteurs n'est pas nulle, l'énergie d'excitation minimale est modifiée comme $\propto |\cos(\varphi/2)|$, ainsi le supracourant dépend de φ..

Cette image physique peut être formalisée théoriquement en utilisant l'approche quasi-classique de la fonction de Green, en particulier par le formalisme d'Usadel qui décrit les systèmes désordonnés [14, 55]. On constate que le spectre d'excitation à une particule dans le métal normal possède un gap, et dans la limite de la jonction longue ($E_T \ll \Delta$), il est égal à $E_g(\varphi = 0) \approx 3,1E_T$ et se ferme à $\varphi = \pi$. De même, à partir de l'équation d'Usadel, on peut calculer le courant spectral en fonction de l'énergie et de la différence de phase $j_s(E, \varphi)$, appelé aussi densité de courant spectrale. Pour obtenir le supercourant à travers la jonction, il faut multiplier j_s par la (composante impaire de la) fonction de distribution et intégrer en fonction de l'énergie [78] :

$$I_s = \int_{-\infty}^{\infty} \mathrm{Im}(j_s) f_L(E) dE \tag{C.2}$$

La dépendance en phase du supercourant (relation courant-phase ou CPR) apparait plus clairement en décomposant par la méthode de Fourier cette expression: $I_s = \sum_n I_{c,n} \sin(n\varphi)$, où $I_{c,n}$ est le courant dépendant de l'harmonique n-th et φ la différence de phase macroscopique entre les supraconducteurs. Il est donc possible de manipuler directement le courant à travers une jonction SNS par le biais d'une fonction de distribution hors équilibre. À titre d'exemple, Yip [79] a montré que l'inversion du signe de la densité du courant spectral à une énergie suffisamment élevée peut être utilisé pour créer une jonction "π" [80].

Comme l'a souligné Eliashberg [81] pour les supraconducteurs homogènes et récemment généralisé théoriquement aux jonctions SNS [82], le rayonnement micro-ondes peut également être utilisé pour créer une fonction de distribution hors-équilibre, de sorte que les excitations de faible énergie qui ont le plus de poids dans l'affaiblissement de la supraconductivité sont dépeuplés. Cela conduit donc à une augmentation du paramètre d'ordre (pour les supraconducteurs homogènes) et du courant critique pour les jonctions SNS. Ainsi le pompage par micro-ondes a été utilisé pour augmenter la température critique des supraconducteurs en modifiant la distribution en énergie des quasiparticules excitées thérmiquement [83].

Dans une jonction SNS, le mini-gap, E_g, produit un supercourant qui dépend de la phase non seulement par la densité de courant spectrale à l'équilibre mais aussi par les taux d'absorption et d'émission qui dépendent de la densité des états [82]. On peut identifier deux types différents de transitions induites par les micro-ondes : les transmissions intra-bandes qui redistribuent les quasi-particules dans la partie trou ou électron du spectre, et les transitions inter-bandes qui favorisent les transitions à travers le mini-gap, créant ainsi une paire d'excitations (électronique et trou). Ces transitions inter-bandes peuvent être comprises

comme un effet dynamique de "rupture de paire", qui modifie également les propriétés spectrales du système - un creux/crête apparaît dans le spectre (et la densité du courant spectral) à $E = \pm\hbar\omega_{RF}/2$, ce qui est montré dans la figure C.5. Cela modifiera intrinsèquement le courant qui circule dans la jonction et, par conséquent, la relation courant-phase, ou CPR, acquiert des harmoniques supérieures qui ne sont pas présentes à l'équilibre [82, 84].

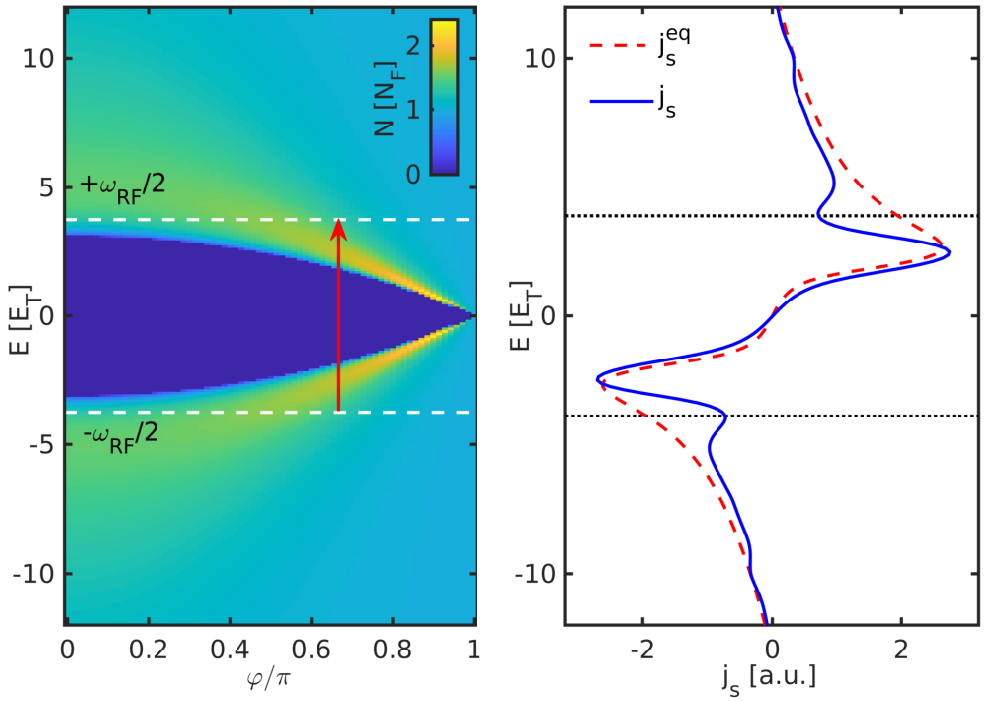

Figure C.5: A gauche : un schéma des transitions inter-bandes induites par la pompe (flèche rouge), les lignes blanches pointillées indiquent la fréquence de la pompe. A droite : Modification du courant spectral (ligne bleue continue), et sa valeur à l'équilibre (ligne rouge en pointillés), à $\varphi = \frac{2\pi}{3}$. Comme pour la figure de droite les lignes pointillées montrent la fréquence de l'excitation micro-ondes.

L'expérience présentée ici explore la dynamique haute fréquence des jonctions SNS, en particulier la réponse du système à une excitation dont la fréquence dépasse l'inverse du temps de diffusion, afin de rechercher ces effets dynamiques hors-équilibre. La partie théorique du travail est basée sur [82], et a été réalisée en collaboration avec Pauli Virtanen et Tero Heikkilä. Les résultats sont publiés dans [85].

Le dispositif à l'étude est une jonction SNS mésoscopique (S=Nb, N=Ag) de longueur intermédiaire. L'expérience a été mise en place de manière à permettre les mesures en courant continu, ainsi que l'application d'une excitation RadioFréquence (RF) dans une large gamme de fréquences (jusqu'à $f_{RF} = 40$GHz) appelée pompe et la détection de la radiation émise à travers un filtre passe-bande centré à $f_D = 6$GHz, avec une largeur d'environ $\delta f_F = 2$GHz. Si la jonction est polarisée en courant continu de telle sorte qu'une tension finie V_{DC} apparaît, selon la relation Josephson, la une puissance, P_n, émise par la jonction (émission Josephson) à $n\omega_J$ avec $\omega_J = \frac{2eV_{DC}}{\hbar}$ est égale à $P_n \propto I_{c,n}^2$. Lorsque $n\omega_J$ coïncide avec $\omega_D = 2\pi f_D$, la fréquence de détection, ce rayonnement peut être détecté. De cette façon on peut accéder aux différentes harmoniques de la relation courant-phase. Les expériences ont été réalisées

dans une gamme de températures allant de $T = 250\text{mK}$ à $T = 4,2\text{K}$ Ces expériences ont permis de caractériser l'échantillon en detail. Les résultats nouveaux présentés ici ont été obtenus à $T = 1,6\text{K}$, où la CPR est presque sinusoïdale (à l'équilibre).

En comparant la mesure du courant critique de la jonction en fonction de la température, $I_c(T)$, avec la théorie, on obtient l'énergie de Thouless ($E_T = 19\mu\text{eV}$,$\Delta_S = 55E_T$). Cela correspond à une fréquence $f_{RF} \approx 28,5\text{GHz}$ nécessaire pour induire des transitions inter-bande à $\varphi = 0$ ($2E_g(\varphi = 0) = hf_{RF}$).

Ici à nouveau, les résultats peuvent être décomposés en deux parties :

- **Refroidissement des quasiparticules** : Pendant la première partie de l'expérience il a été constaté, en mesurant la dépendance en température du courant critique, du courant de re-trapping et des pas de Shapiro que le taux de refroidissement effectif, $K \approx 2,8\frac{\text{nW}}{\text{K}^5}$, est environ cent fois plus grand que la valeur attendue (déduite sur la base de la géométrie du dispositif et du taux d'interaction electron-phonon dans l' Ag). Les contacts métalliques normales adjacentes à la jonction, qui sont une conséquence de la procédure de fabrication, se sont avérées être des "pièges à quasi-particules" et sont considérés à l'origine de cet effet. C'est un résultat technique, mais essentiel car ce taux de relaxation élevé nous a permis d'explorer des nouveaux effets hors-équilibre, au-delà des effets thermiques bien connus.

- **Dynamique non-adiabatique haute fréquence** : Pour étudier la CPR de la jonction à partir du spectre d'émission Josephson, nous pouvons d'abord mesurer la puissance émise (sans pompe) à travers le filtre passe-bande de détection, en fonction de la tension V_{DC} à travers la jonction, comme le montre la figure C.6. On distingue deux pics, marqués P_1 et P_2. L'émission Josephson peut être modélisée sous la forme de deux pics gaussiens centrés à ω_J et $2\omega_J$, correspondant à l'émission associée aux deux premières harmoniques de la CPR. En utilisant les hauteurs et largeurs de pics comme paramètres d'ajustement, et en convoluant le spectre d'émission avec le profil de notre filtre, la trace expérimentale est bien reproduite. Ce résultat confirme que ces deux pics sont associés aux deux premières harmoniques de la CPR.

  Nous pouvons maintenant procéder à l'étude de la réponse de la relation courant-phase à l'irradiation à haute fréquence. Les deux panneaux supérieurs de la figure C.7 montrent l'amplitude des pics P_1 (échelle de gauche) et P_2 (échelle de droite) en fonction de la puissance RF normalisée $s = \dfrac{2eI_{RF}R_N}{\hbar\omega_{RF}}$, pour deux fréquences $f = 20.72\text{GHz}$ (à gauche, qui est le seuil pour des transitions à travers le mini-gap) et $f = 35,18\text{GHz}$ (à droite, qui est suffisamment élevé pour induire des transitions inter-bandes). En tenant compte uniquement de la dynamique adiabatique de la phase les harmoniques de la CPR devraient être données par $I_{c,n} = I_{c,n}^{eq}J_0(ns)$, où n est l'indice des harmoniques et J_0 est la fonction de Bessel de première espèce. Ce comportement se retrouve aux faibles puissances ($s < 1$, voir les lignes complètes dans C.7), alors qu'aux puissances plus élevées, et surtout pour la fréquence la plus élevée, il y a une augmentation significative de l'amplitude de la deuxième harmonique, ce qui est attendu dans l'image des transitions inter-bandes.

  Pour vérifier qu'il s'agit bien d'un effet réel, nous pouvons reconstituer la CPR sous la forme $I^r(\varphi) \propto \sqrt{P_1}\sin(\varphi) + \sqrt{P_2}\sin(2\varphi)$ sur la base de ces mesures. En particulier, pour la fréquence la plus élevée, il n'existe pas de valeur de s à laquelle les amplitudes de $I_{c,1}$ (P_1) et de $I_{c,2}$ (P_2) disparaissent. Cela suggère que, contrairement à l'équilibre, le courant critique de la jonction ne peut pas être (entièrement) supprimé par l'irradiation

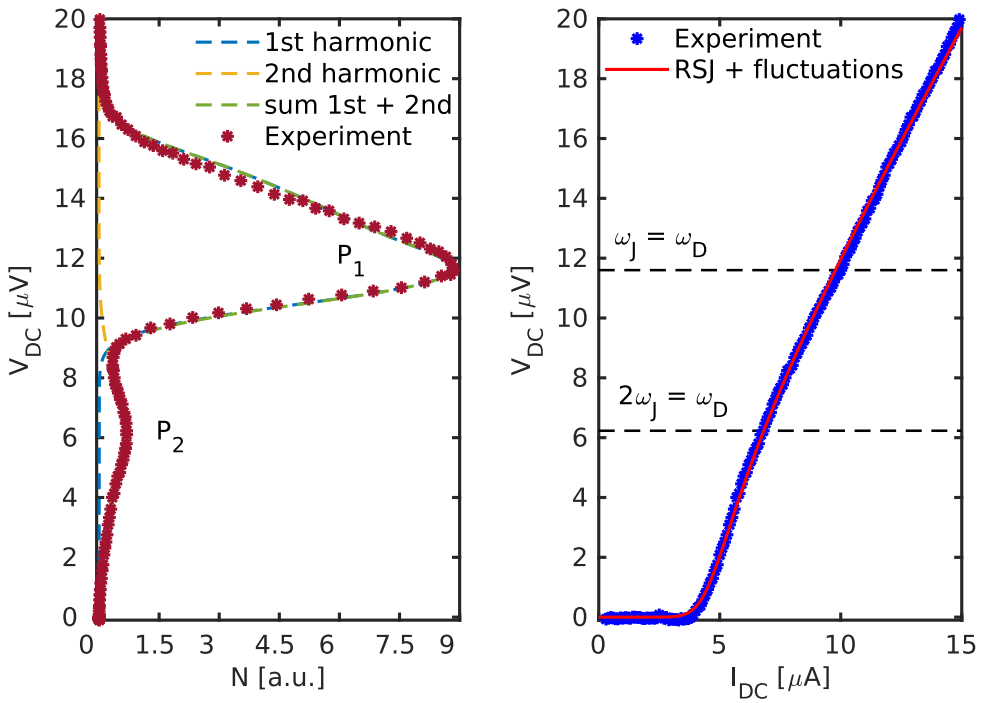

Figure C.6: Gauche : la puissance détectée N en fonction de la tension aux bornes de la jonction. A droite : la courbe $V(I)$ de la jonction et le fit théorique obtenu en utilisant le modéle Resistive-Shunted-Junctions (RSJ). Les lignes horizontales en pointillés indiquent les tensions auxquelles les deux pics sont observés.

micro-ondes. En calculant le courant critique sur la base de la CPR reconstruite et en le comparant aux valeurs mesurées nous avons obtenu un bon accord entre les deux (voir le texte complet de la thèse pour les détails). Les implications de ce résultat sont doubles : tout d'abord, la spectroscopie Josephson donne une bonne sonde quantitative de la CPR, et plus important encore, elle montre que les harmoniques mesurées à tension finie (mais faible par rapport à la fréquence d'irradiation) ne sont pas modifiées par rapport au cas $V_{DC} = 0$, ce qui nous permet d'utiliser la théorie développé à $V_{DC} = 0$ [82] pour calculer la CPR à tension finie.

En utilisant les paramètres du système obtenus expérimentalement et en calculant la réponse du système à partir de la théorie de [82], nous obtenons les deux derniers panneaux de la figure C.7, qui présentent les mêmes caractéristiques observées dans l'expérience. Nous pouvons en particulier distinguer les différentes contributions à la deuxième harmonique. En négligeant les changements induits par la pompe sur la densité de courant spectrale et en travaillant uniquement avec une fonction de distribution hors équilibre (c'est-à-dire dans le cadre de l'approximation d'Eliashberg), l'amplitude de la seconde harmonique est fortement sous-estimée (les lignes violettes dans la figure C.7). Par conséquent, les changements du spectre d'excitation, comme ceux qui sont indiqués dans C.5, sont essentiels pour expliquer les données expérimentales, révélant un nouvel état dynamique hors équilibre à l' origine de l'effet.

L'approche spectroscopique développée ici pourrait être utilisée pour étudier d'autres types de jonctions Josephson comme par exemple les contacts atomiques ou [106, 107] ou

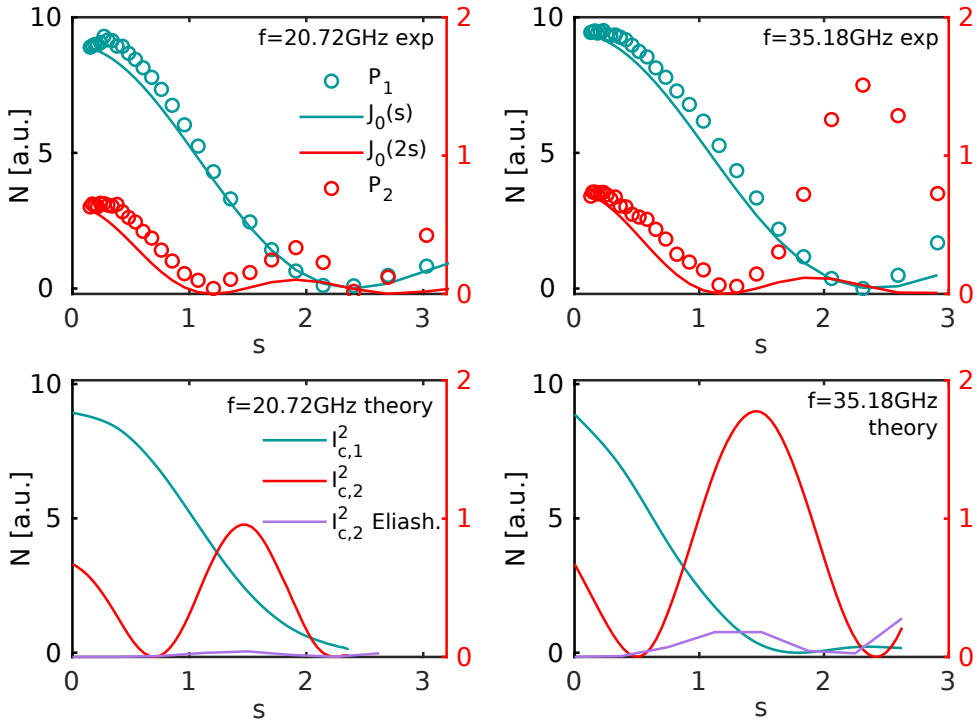

Figure C.7: En haut à gauche : les amplitudes observées des pics P_1 (échelle de gauche) et P_2 (échelle de droite) en fonction de la puissance de la pompe à $T = 1,6$K et $f = 20,72$GHz. Dans les quatre panneaux, la 2-éme harmonique est indiquée sur l'échelle de droite. L'étalonnage de s a été effectué de telle sorte que le comportement à faible puissance du pic P_1 suit $J_0(s)$. La deuxième harmonique (crête P_2) suit approximativement $J_0(2s)$. En haut à droite : même chose qu'en haut à gauche mais pour $f = 35.18$GHz - à des puissances élevées, la deuxième harmonique (crête P_2) est sensiblement augmentée par rapport à $P_2(s = 0)J_0(2s)^2$. En bas à gauche (droite) : courbes théoriques calculées respectivement à l'aide de $\Gamma/E_T = 0,4$, $k_BT/E_T = 7$, $\Delta/E_T = 55$ et $\hbar\omega_{RF}/E_T = 3$ ($\hbar\omega_{RF}/E_T = 7$). Dans l'approximation d'Eliashberg, la deuxième harmonique est négligeable à toutes les puissances.

les jonctions à base de nanofils semiconducteurs avec les états liés de Majorana. Dans ce dernier cas, les modifications de la CPR induites par l'irradiation micro-ondes pourraient être utilisées pour révéler des signatures sur les transitions topologiquement interdites [108, 109, 110].

Appendix D

Articles

Evidence for spin-dependent energy transport in a superconductor

M. Kuzmanović,[1] B. Y. Wu,[1,2] M. Weideneder,[3,4] C. H. L. Quay,[1] and M. Aprili[1]

[1] *Laboratoire de Physique des Solides (CNRS UMR 8502), Université Paris-Saclay 91405 Orsay, France*
[2] *Graduate Institute of Applied Physics, National Taiwan University, Taipei 10617, Taiwan*
[3] *Laboratoire de Physique des Solides (CNRS UMR 8502), Université Paris-Saclay, 91405 Orsay, France*
[4] *Institute for Experimental and Applied Physics, University of Regensburg 93053 Regensburg, Germany*

In the spin energy excitation mode of normal metals and superconductors, spin up and down electrons (or quasiparticles) carry different heat currents. This mode occurs only when spin up and down energy distribution functions are non-identical, most simply when the two spins have different effective temperatures, and can be excited by spin-polarised current injection into the system. While evidence for spin-dependent heat transport has been observed in a normal metal, these measurements averaged over the distribution function of the electrons. By performing spectroscopy of quasiparticle populations in a mescoscopic superconductor, we reveal distribution functions which are strongly out-of-equilibrium, i.e. non-Fermi-Dirac. In addition, unlike in normal metals, the spin energy mode in superconductors is associated with a charge imbalance (different numbers of hole- and electron-like quasiparticles) at the superconducting gap edge, in finite Zeeman magnetic fields. Our spectroscopic technique allows us to observe this charge imbalance and thus unambiguously identify the spin energy mode. Our results agree well with theory and contribute to laying the foundation for spin caloritronics with superconductors.

PACS numbers:

INTRODUCTION

The Seebeck effect, in which a temperature gradient leads to a charge current, was first observed about two centuries ago. Together with its Onsager reciprocal, the Peltier effect, it forms the basis of the field of thermoelectricity or coupled charge and heat transport [1]. Coupled charge and spin transport, or spintronics, emerged in the late 1980s [2]. Later, spin caloritronics or coupled heat, charge and spin transport [3, 4] became an experimental reality with the observation of the spin Seebeck effect [5] and spin-dependent Peltier effects [6] in normal metals, and very recently large spin-dependent thermoelectric effects in superconductor-based devices [7–10].

Early work in the field focused on temperature differences between (magnetic) materials associated with spin and/or charge currents. Within a given material, it was pointed out that spin up and down carriers (electrons or quasiparticles) can also have different temperatures [11–16]. When this happens, the spin energy mode of the system is excited and the two spin species carry different heat currents. Evidence for spin-dependent heat transport was recently observed in a normal metal [17] but not in superconductors. Moreover, due to the aggregate nature of the measurements in normal metals (giant magnetoresistance of a spin valve), detailed information on the distribution function could not be obtained.

Here, we study thin-film superconducting aluminium. As our measurements are spectroscopic, we are able to reveal quasiparticle (QP) populations which cannot be described by effective temperatures (i.e. they are strongly out-of-equilibrium). Instead, they carry an 'imprint' of the electron distribution function in the normal metal from which current is injected into the superconductor, to generate QPs. Further, unlike in normal metals, the spin energy mode in superconductors gives rise to a charge imbalance (i.e. different numbers of electron- and hole-like quasiparticles) with a specific energy and magnetic field dependence. Our spectroscopic measurements allow us to observe this imbalance and thus unambiguously identify the spin energy mode. The presence of the spin energy mode in turn necessarily implies that the distribution functions of spin up and down quasiparticles are different.

SPINFUL EXCITATION MODES OF OUT-OF-EQUILIBRIUM SUPERCONDUCTORS

The ground state of conventional (Bardeen-Cooper-Schrieffer) superconductors is composed of Cooper pairs of electrons in a spin singlet configuration. In equilibrium, this macroscopic quantum state can carry a dissipationless charge current (known as a supercurrent), but not spin or energy currents. In contrast, the single particle excitations, or quasiparticles, are spin-1/2 fermions, which can carry spin, energy and charge currents. The density of states of these QPs ($\rho(E)$) is zero in an energy range $\pm\Delta$ about the Fermi energy (E_F), and has coherence peaks just above this gap (Figure 1a).

Out-of-equilibrium quasiparticle populations in superconductors can be described by the particle energy distribution function $f(E)$. Neglecting the QP spin, $f(E)$ can be decomposed based on symmetry into energy $f_L(E) = f(-E) - f(E)$ and charge $f_T(E) = 1 - f(E) - f(-E)$ modes [18, 19]. The simplest $f(E)$ which excites these

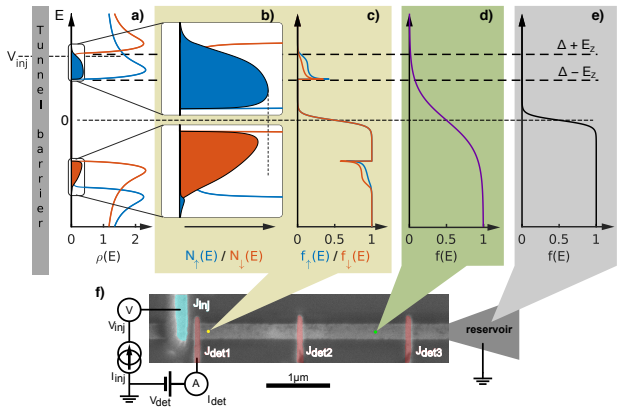

Figure 1 | Generation and detection of out-of-equilibrium quasiparticles (QP) in a superconductor. a, Spin up (blue) and down (red) QP density of states (DOS) in the superconductor in an in-plane magnetic field, which induces both a Zeeman splitting and orbital depairing. The blue and red shaded regions are proportional to, respectively, the number of spin up and spin down quasiparticles ($N_\uparrow$ and $N_\downarrow$) near the first detector. This was calculated with the density of states in **a**, the reservoir distribution function in **e** and the indicated injection voltage V_{inj}. For clarity, the imbalance between the number of electron-like QPs and the number of hole-like QPs (the charge imbalance), has been multiplied five times. This can be seen to occur in a specific energy range. **b**, Zoom in of **a**. **c**, Predicted spin up (blue) and down (red) QP distribution functions at the indicated distance from the injector. The distribution functions show peaks at the superconducting gap edge, as well as a step-like cutoff at eV_{inj}. **d**, Farther than an electron-electron interaction length ($\approx 1\mu$m) from the injector, we expect the quasiparticle distribution function to be spin-independent and close to an effective temperature. The trace shown here is an illustration, not a calculation. **e**, QPs are assumed to be at equilibrium at the reservoir. **f**, False colour scanning electron micrograph of the device, and a schematic drawing of the spectroscopy measurement setup. The horizontal superconducting wire is 6nm Al. The injector (100nm Cu, cyan) and the detectors (8 nm Al/0.1 nm Pt, red) form tunnel junctions with the wire, with the latter's native oxide as the barrier.

modes are, respectively, an effective temperature (different from the lattice temperature) and a charge imbalance. In the presence of a charge imbalance, the number of electron- and hole-like quasiparticles are non-identical, and the quasiparticle chemical potential is different from the Fermi energy.

In the spinful case, this decomposition can be generalised by the addition of spin and spin energy modes, $f_{T3}(E) = f_{T\uparrow}(E) - f_{T\downarrow}(E)$ and $f_{L3}(E) = f_{L\uparrow}(E) - f_{L\downarrow}(E)$ [14, 16]. f_{L3} is most simply excited by a spin-dependent temperature and f_{T3} by a spin-dependent chemical potential. The spin and spin energy modes only exist if spin up and down QPs have different distribution functions, i.e. if $f_\uparrow(E) \neq f_\downarrow(E)$. By construction, f_L and f_{L3} are odd in energy, while f_T and f_{T3} are even in energy. In the following, we focus mainly on f_{L3}, the spin energy mode.

To generate different spin up and down distribution functions, it is necessary to preferentially excite quasiparticles of one spin species. In thin superconducting films, this can be done by applying an in-plane magnetic field H, which lowers (raises) the energy of spin up (down) QPs by the Zeeman energy E_Z and splits the DOS so that only spin up excitations (spin up electron-like and spin down hole-like quasiparticles) are allowed in the energy range $\Delta - E_Z \leq |E| \leq \Delta + E_Z$ (Figure 1b). ($E_Z = \mu_B H$, with μ_B the Bohr magneton and H the magnetic field.) Current injection in this energy range thus creates spin-polarised quasiparticles regardless of the magnetic properties of the tunnel barrier or the injector electrode.

For our experiments, we use thin-film superconducting (S) aluminium wires, with a native insulating (I) oxide layer, across which lie normal metal (N) and superconducting (S') electrodes. The former is used as an injector and the latter as detectors (Figure 1f). S is terminated on both sides by reservoirs at a distance of about 5μm from the NIS junction. The magnetic field (H) is applied in the plane, parallel to S.

Our basic spectroscopy measurement consists of injecting a constant current I_{inj} at the injector J_{inj}, and measuring the current I_{det} and/or the differential conductance $G_{det} = dI_{det}/dV_{det}$ as a function of the applied voltage (V_{det}) at one of the detectors (J_{det1}, J_{det2} and J_{det3} in Figure 1f). Measurements were performed in a dilution refrigerator with a base temperature of 90mK. J_{det1} lies within both a electron-electron interaction length ($\lambda_{e-e} \approx 1\mu$m [20, 21]) and a spin-flip length ($\lambda_{sf} \approx 300$ nm [22]) of the injector.

We model our system using the Usadel-Keldysh equations, which describe out-of-equilibrium diffusive superconductors. (See Supp. Info. for details.) Following Ref.s [16, 23], we solve these numerically in one dimension, assuming negligible (inelastic) electron-electron and electron-phonon interactions, and include a Zeeman magnetic field. Experimental parameters are used in the model: the normal state diffusion constant $D \approx 10\frac{\text{cm}^2}{\text{s}}$, $L = 10\mu$m, $R(J_{inj}) = 13\text{k}\Omega$. The diffusion time from the injector to the reservoirs is $\tau_{diff} = l_{inj-res}^2/D \approx 20$ns where $l_{inj-res}$ is the injector-reservoir distance $\approx L/2$. As τ_{diff} is much small than the QP recombination time ($\tau_{rec} \gtrsim 1\mu s$[24]), QPs relax and recombine at the reservoirs. At the interface with the injector, the boundary conditions are given by spectral current continuity and the injector distribution function $f_{inj}(E - eV_{inj})$,

assumed to be Fermi-Dirac.

In our numerical results for the closest detector (Figure 1c), we see that the quasiparticle distribution function bears signatures of both the density of states in S (Figure 1b) as well as the distribution function in the injector: It has a peak at $E = \Delta$ and goes sharply to zero at $E = V_{inj}e$. The distribution function is also spin-dependent.

To interpret our experimental results, it is helpful to understand the link between the spin energy mode f_{L3} and charge imbalance by considering the particle number as a function of energy:

$$N(E) = N_\uparrow(E) + N_\downarrow(E) = f_\uparrow(E)\rho_\uparrow(E) + f_\downarrow(E)\rho_\downarrow(E) \quad (1)$$

$$= \rho_+(E)[1 - f_L(E) - f_T(E)] - \rho_-[f_{T3}(E) + f_{L3}(E)] \quad (2)$$

Here $\rho_\uparrow(E)$ and $\rho_\downarrow(E)$ are the DOS of spin up and spin down QPs respectively, $\rho_+(E) := \frac{1}{2}[\rho_\uparrow(E) + \rho_\downarrow(E)] = \rho(E)$ and $\rho_-(E) \equiv \frac{1}{2}[\rho_\uparrow(E) - \rho_\downarrow(E)]$.

Here we notice that the term $\rho_-(E)f_{L3}(E)$ is even in energy, which means that the spin energy mode f_{L3} *adds* particles at both positive and negative energies, and raises the overall quasiparticle chemical potential, thus creating a charge imbalance. (Figure 1b) In addition, the multiplication by $\rho_-(E)$ means that f_{L3} add particles in the energy range $\Delta - E_Z \leq |E| \leq \Delta + E_Z$, regardless of the injection voltage or other experimental parameters. (Figure 1b) f_T also creates a charge imbalance, which however appears at low magnetic fields and high energies. Our spectroscopic technique allows us distinguish between f_{L3} and f_T, based on their different energy dependences. We refer the reader to Ref. [16] and the Supp. Info. for further theoretical details.

SPECTROSCOPIC SPIN-SENSITIVE QUASIPARTICLE DETECTION

We first characterise both injector and detector junctions, and explain our spectroscopy technique. Figure 2a shows the differential conductance of the injector $G_{inj} = dI_{inj}/dV_{inj}$ as a function of the applied voltage (V_{inj}) at different H. At the temperatures of our experiment, G_{inj} is almost exactly proportional to the density of states in S [25]. We can see that H induces Zeeman splitting of the QP DOS. H also couples to the orbital degree of freedom, inducing screening supercurrents and hence a rounding of the QP coherence peak due to orbital depairing [25, 26]. The depairing parameter, found by fitting the data with an Abrikosov-Gor'kov depairing (see Supp. Info.), is $\alpha = R_{ORB}H^2$, with $R_{ORB} \approx 6.5\frac{\mu\text{eV}}{\text{T}^2}$, and the critical field $H_c \approx 2.7$T. In the results shown here, the Zeeman energy is always greater than the depairing parameter. (See Supp. Info. for details.)

If the detector temperature is much smaller than the superconducting energy gap in S' ($k_B T_{det} \ll \Delta_{det}$, with

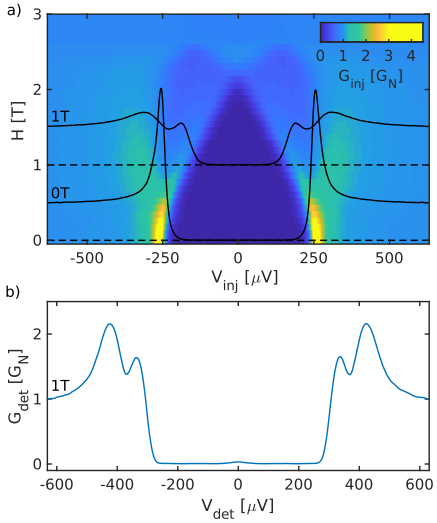

Figure 2 | Characterisation of injector and detector junctions. a, Differential conductance of the injector junction G_{inj} as a function of injector voltage V_{inj} and magnetic field H, and slices at $H = 0$T and $H = 1$T (black traces). **b**, Differential conductance of the detector junction G_{det} as a function of the detector voltage V_{det} at $H = 1$T without any injection current. We see the Zeeman splitting of the quasiparticle density of states in the superconducting wire as the detector is not Zeeman-split.

k_B Boltzmann's constant), the differential conductance of SIS' junctions as a function of the applied voltage in the subgap region $V < (\Delta + \Delta_{det})/e$ is given by

$$G_{det}(V_{det}) = \frac{1}{eR_N}\int \rho(E)f(E)\frac{\partial\rho_{det}(E + eV_{det})}{\partial V_{det}}dE \quad (3)$$

where $\rho_{det}(E)$ the density of states in S', e the electron charge and R_N the normal state resistance of the detector junction.

Most of the integral comes from the coherence peak in ρ_{det} at $E = \Delta_{det}$. This peak picks out the number of quasiparticles in S ($\rho(E)f(E)$), shifted by Δ_{det}. In other words, $G_{det}(V_{det} - \Delta_{det}/e)$ gives the number of QPs at energy $E = eV_{det}$, while $I_{det}(V_{det} - \Delta_{det}/e)$ gives the total number of QPs for $E \leq eV_{det}$. Our measurements thus give us spectroscopic information on the QPs. (See Supp. Info. for details.)

At finite magnetic fields, these spectroscopic measurements become spin-sensitive if Zeeman spin-splitting occurs in S but not in S'; the unsplit coherence peak in S' separately probes the number of QPs in S at the two gap edges for spins up and down, respectively at $V_{det}^{\uparrow(\downarrow)} = |\Delta \pm \mu_B H - \Delta_{det}|/e$.

We suppress the spin-splitting in S' through the strong spin-orbit coupling of sprinkled Pt, which acts as a spin-

mixer. (See Methods, Supp. Info. and as Ref.s [26–29]) Figure 2b shows $G_{det}(V_{det})$ at different H and $I_{inj} = 0$. At $H = 1$T, we see two peaks, as expected for a non-spin-split detector. (Were there a Zeeman splitting in S' equal to that in S, the situation would be equivalent to two SIS junctions in parallel, one for each spin, and there would be a single peak in $G_{det}(V_{det})$ instead of two [40].) We note also that the detector current is typically $0.1 - 1\text{nA} \ll I_{inj} \sim 10 - 100\text{nA}$ throughout the subgap region: the detector is close to equilibrium

NON-FERMI-DIRAC QUASIPARTICLE ENERGY DISTRIBUTIONS

Measurements at zero magnetic field already reveal non-Fermi Dirac distributions. Figure 3a shows the current-voltage characteristics of the closest detector junction at two injection currents: 0nA (black trace) and 120nA (red trace). We focus on the low-voltage range before the abrupt rise of I_{det} at $V_{det} = (\Delta + \Delta_{det})/e$, where the opposite-energy coherence peaks of S and S' align. We see that the red trace is higher than the black. This indicates the presence of additional QPs created by injection [41].

This creation of quasiparticles by current injection can also be seen in the differential conductance measurement, $G_{det}(V_{det})$ at three values of I_{inj}: 0nA, $\approx$ 13nA and 120nA (Figure 3b). Here, we see more clearly that most of the quasiparticles are at the gap edge ($eV_{det} = \Delta$). If we try to fit the trace at $I_{inj} \approx 13$nA with a thermal QP distribution, it is clear that this grossly over-estimates the number of QPs at high energies (Figure 3b, dotted line). The quasiparticles do not thermalise.

Instead, as shown in our calculations (Figure 1) and discussed earlier, the quasiparticle states in S are filled up to V_{inj}: the electron distribution function in N is 'imprinted' onto the quasiparticles in S. This can be seen by overlaying the $I_{inj}(V_{inj})$ measurement in Figure 3a, shifted by Δ_{det}/e, onto a plot of G_{det} as a function of (V_{det}) and I_{inj} (Figure 3c). Note that, at each current, the injector voltage falls exactly at the location of a step in G_{det} (seen here as a change in colour). The accumulation of quasiparticles at the gap edge in S can also be seen on this colour scale as a yellow horizontal feature.

Our calculations reproduce both the step-like feature corresponding to $I_{inj}(V_{inj} + \Delta_{det}/e)$, as well as the horizontal feature (Figure 3d). Thus, at a distance of about 300nm $\ll \lambda_{e-e}$ from the injector (i.e. at J_{det1}) and in the energy range of interest for the detection of the f_{L3} mode, the quasiparticles have not yet thermalised, and it is reasonable to neglect electron-electron interactions.

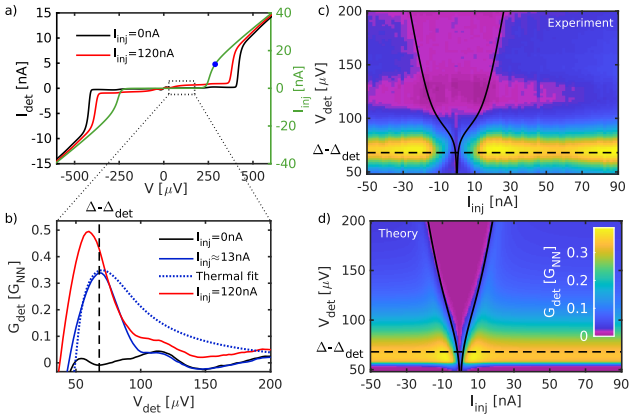

Figure 3 | Non-Fermi-Dirac quasiparticle distribution. **a**, Current I_{det} as a function of voltage V_{det} across the SIS' detector junction J_{det1} for injection currents $I_{inj} = 0$nA (black) and $I_{inj} = 120$nA (red). On the right vertical scale, I_{inj} as a function of voltage V_{inj} across the NIS injector junction J_{inj} (green). $H = 0$ throughout this figure. **b**, Differential conductance G_{det} as a function of V_{det} across J_{det1} for $I_{inj} = 0$nA (black), $I_{inj} \approx 13$nA (blue, blue dot in **a**), and $I_{inj} = 120$nA (red). The vertical dashed line indicates $eV_{det} = \Delta - \Delta_{det}$; G_{det} at this voltage is proportional to the number of quasiparticles in the superconducting wire at $E = \Delta$. An attempted fit with an effective temperature $T^* \approx 1.1$K in S reproduces the peak at $I_{inj} = 13$nA, but grossly overestimates the QP population at higher energies (dashed blue line). In this fint, we use the experimentally determined values $\Delta = 245\mu$eV and $\Delta_{det} = 180\mu$eV, $T_{det} = 90$mK and a phenomenological depairing $\alpha \approx 1\%\Delta$. **c**, G_{det} at J_{det1} as a function of V_{det} and I_{inj} with the slice at $I_{inj} = 0$ subtracted from all data. The black lines show the measurement of $\pm I_{inj}(V_{inj})$ from **a** shifted downwards by Δ_{det}/e. The black lines fall at the location of a step-like feature in the colour map, as expected: as shown in Figure 1b, QPs in S are created up $E \approx eV_{inj} + k_BT$, leading to a step-like cutoff in the distribution function. The dashed line again indicates $eV_{det} = \Delta - \Delta_{det}$, where the QP density is maximal due to the coherence peak in the DOS of S. **d**, Theoretical prediction of **c**, with the Δ, Δ_{det} and α as in **b**

SPIN ENERGY MODE

At finite magnetic fields, current injection at low energies becomes spin-polarised: we expect different distribution functions for spin up and down quasiparticles, and in particular to excite the spin energy mode. We show in Figure 4a calculations of G_{det} as a function of V_{det} (in the sub-gap region) and of I_{inj}, at 1T where the density of states in S is well spin-split (Figure 2a). Following

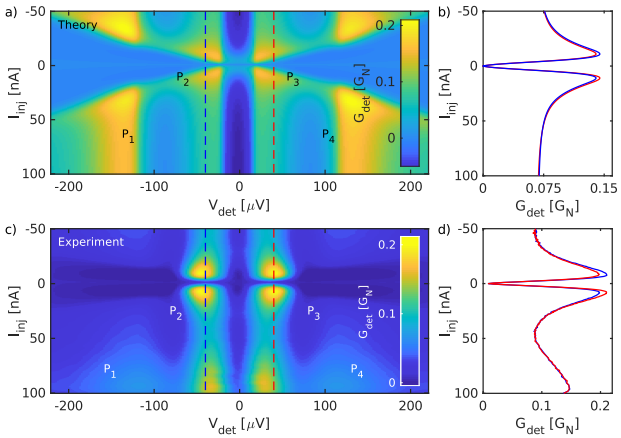

Figure 4 | Spin energy mode. a,c, Theoretical calculations for and measurements of the differential conductance as a function of voltage and injection current at J_{det1} for $H = 1$T. The peaks $P_1 - P_4$ observed experimentally and reproduced in our calculations are due to spin up (P_2, P_3) and spin down (P_1, P_4) excitations. **b,d**, Vertical slices of **a** and **b** at $eV_{det} = \pm|\Delta - \Delta_{det} - \mu_B H|$ (red for + and blue for -), indicated by the dashed blue and red lines. A charge imbalance can be seen, i.e. the red and blue traces are not identical.

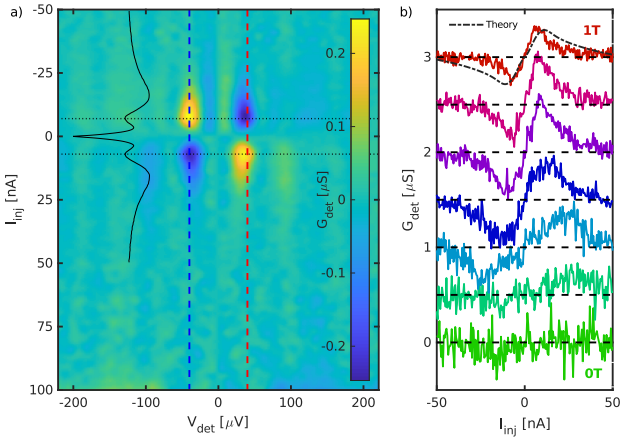

Figure 5 | Close-up of the spin energy mode. a, The odd-in-energy component of Figure 4c, corresponding to a charge imbalance. This only appears at the gap edge: the vertical dashed lines indicate $V_{det} = \pm|\Delta - \Delta_{det} - E_Z|/e$. The signal is maximal (horizontal dotted lines) when only spins of one species are injected: $G_{inj}(V_{inj})$ is shown (thin black line) on the left and top axes. **b**, A vertical slice of **a** at $V_{det} = (\Delta - \Delta_{det} - E_Z)/e$ and the same measurement at different magnetic fields linearly spaced down to $H = 0$T. The theoretical prediction for $H = 1$T is shown in black. The charge imbalance increases slightly then decreases as the magnetic field is lowered. At $H = 0$ it is undetectable.

features from low to high energies, we expect peaks in $G_{det}(V_{det})$ at $eV_{det} = (\pm|\Delta - \Delta_{det} - E_Z|)$ which we shall call P_2 and P_3, corresponding to the coherence peaks of spin up excitations (spin up electron-like or spin down hole-like quasiparticles). Peaks at $V_{det} = \pm|\Delta - \Delta_D + E_Z|$ (P_1 and P_4), corresponding to the coherence peaks of spin down excitations, appear when I_{inj} is increased and spin down QPs are also injected.

Comparing this to the data (Figure 4c), we see P_2 and P_3 clearly, but P_1 and P_4 are less prominent. This is due to the increased electron-electron interaction at high energies and QP number. (For clarity, the Josephson (i.e. supercurrent) contribution has been subtracted from G_{det}. See Supp. Info. for details.)

Next, we compare the number of electron- and hole-like quasiparticles by taking two slices of Figure 4c at $eV_{det} = +|\Delta - \Delta_D - \mu_B H|$ (Figure 4d). The traces are not identical. The difference between them, which is the charge imbalance, is maximal at $I_{inj} \approx 8$nA, corresponding to maximal spin polarisation of the injection current, i.e. when the injection voltage is just below the coherence peak of the second spin species. This charge imbalance is also reproduced in the calculation (Figure 4b).

The charge imbalance associated with f_{L3} has particular energy and magnetic signatures: it is expected to appear in the energy range $\Delta - E_Z \leq |E| \leq \Delta + E_Z$. In Figure 5a, we plot the component of the data in Figure 4a which is odd in V_{det}, which gives the charge imbalance. The odd component is indeed largest in the expected energy range. As the magnetic field is decreased, the charge imbalance is reduced, also as expected for the spin energy mode (Figure 5b): it is zero at zero magnetic field, and becomes visible when $E_Z > 3.5 k_B T$. At $H = 1$T. Our calculations reproduce the data well (Figure 5b, dash-dotted line).

The odd component of the data in Figures 4b and 4d, which comes from f_{L3}, is small compared to the even component, which comes from either f_L or f_{T3}. The quasiparticles from f_L or f_{T3} contribute to a finite magnetisation in the superconductor, previously detected by other methods [30–33]. At $H = 0$, we recover the previously observed charge imbalance signal [34–38], associated with the f_T mode, which occurs at high energies and low magnetic fields. (See Supp. Info.)

As expected, we do not observe f_{L3} at J_{det2} or J_{det3}, where the spin up and down QP distribution functions have become identical. (See Supp. Info.)

Compared to normal metals and semiconductors, the spin energy mode in superconductors has the advantage of being excitable by using the spin-split DOS. Its association with an energy-localised charge imbalance make

it easy to distinguish from other modes. Using superconductors as detectors allowed us to have spectroscopic information on the quasiparticles, by using the coherence peak in the detector density of states. This work paves the way for new spin-dependent heat transport experiments, as well as the generation of spin supercurrents by out-of-equilibrium distribution functions in conventional superconductors [16, 39].

[1] Tritt, T., Subramanian, M. et al. Harvesting energy through thermoelectrics: power generation and cooling. MRS Bull **31**, 113 (2006).

[2] Žutić, I., Fabian, J. & Das Sarma, S. Spintronics: Fundamentals and applications. Reviews of Modern Physics **76**, 323–410 (2004).

[3] Boona, S. R., C., M. R. & Heremans, J. P. Spin caloritronics. Energy & Environmental Science **7**, 885–910 (2014).

[4] Bauer, G. E. W., Saitoh, E. & van Wees, B. J. Spin caloritronics. Nature Materials **11**, 391–399 (2012).

[5] Uchida, K. et al. Observation of the spin Seebeck effect. Nature **455**, 778–781 (2008).

[6] Gravier, L., Serrano-Guisan, S., Reuse, F. & Ansermet, J.-P. Spin-dependent Peltier effect of perpendicular currents in multilayered nanowires. Physical Review B **73**, 052410 (2006).

[7] Machon, P., Eschrig, M. & Belzig, W. Giant thermoelectric effects in a proximity-coupled superconductor-ferromagnet device. New Journal of Physics **16**, 073002 (2014).

[8] Ozaeta, A., Virtanen, P., Bergeret, F. S. & Heikkilä, T. T. Predicted very large thermoelectric effect in ferromagnet-superconductor junctions in the presence of a spin-splitting magnetic field. Physical Review Letters **112**, 057001 (2014).

[9] Kolenda, S., Wolf, M. & Beckmann, D. Observation of Thermoelectric Currents in High-Field Superconductor-Ferromagnet Tunnel Junctions. Physical Review Letters **116**, 097001 (2016).

[10] Kolenda, S., Sürgers, C., Fischer, G. & Beckmann, D. Thermoelectric effects in superconductor-ferromagnet tunnel junctions on europium sulfide. Physical Review B **95**, 224505 (2017).

[11] Hatami, M., Bauer, G. E. W., Zhang, Q. & Kelly, P. J. Thermal Spin-Transfer Torque in Magnetoelectronic Devices. Physical Review Letters **99**, 066603 (2007).

[12] Heikkilä, T. T., Hatami, M. & Bauer, G. E. W. Spin heat accumulation and its relaxation in spin valves. Physical Review B **81**, 100408 (2010).

[13] Giazotto, F., Taddei, F., D'Amico, P., Fazio, R. & Beltram, F. Nonequilibrium spin-dependent phenomena in mesoscopic superconductor–normal metal tunnel structures. Physical Review B **76**, 184518 (2007).

[14] Morten, J. P., Brataas, A. & Belzig, W. Spin transport in diffusive superconductors. Physical Review B **70**, 212508 (2004).

[15] Bobkova, I. V. & Bobkov, A. M. Recovering of superconductivity in S/F bilayers under spin-dependent nonequilibrium quasiparticle distribution. JETP Letters **101**, 407–412 (2015).

[16] Heikkilä, T. T., Silaev, M., Virtanen, P. & Bergeret, F. S. Thermal, electric and spin transport in superconductor/ferromagnetic-insulator structures. Progress in Surface Science **94**, 100540 (2019).

[17] Dejene, F. K., Flipse, J., Bauer, G. E. W. & Wees, B. J. v. Spin heat accumulation and spin-dependent temperatures in nanopillar spin valves. Nature Physics **9**, 636–639 (2013).

[18] Schmid, A. & Schön, G. Linearized kinetic equations and relaxation processes of a superconductor near t_c. Journal of Low Temperature Physics **20**, 207–227 (1975).

[19] Quasiclassical Green's function approach to mesoscopic superconductivity. Superlattices and Microstructures **25**, 1251–1288 (1999).

[20] van Son, P. C., Romijn, J., Klapwijk, T. M. & Mooij, J. E. Inelastic scattering rate for electrons in thin aluminum films determined from the minimum frequency for microwave stimulation of superconductivity. Physical Review B **29**, 1503–1505 (1984).

[21] Santhanam, P. & Prober, D. E. Inelastic electron scattering mechanisms in clean aluminum films. Physical Review B **29**, 3733–3736 (1984).

[22] Quay, C. H. L., Weideneder, M., Chiffaudel, Y., Strunk, C. & Aprili, M. Quasiparticle spin resonance and coherence in superconducting aluminium. Nature Communications **6**, 1–6 (2015).

[23] Bergeret, F. S., Silaev, M., Virtanen, P. & Heikkilä, T. T. Colloquium: Nonequilibrium effects in superconductors with a spin-splitting field. Reviews of Modern Physics **90**, 041001 (2018).

[24] Martinis, J. M., Ansmann, M. & Aumentado, J. Energy Decay in Superconducting Josephson-Junction Qubits from Nonequilibrium Quasiparticle Excitations. Physical Review Letters **103**, 097002 (2009).

[25] Tinkham, M. Introduction to Superconductivity (Dover, Mineola, 1996), 2 edn.

[26] Fulde, P. High field superconductivity in thin films. Advances in Physics **22**, 667–719 (1973).

[27] Tedrow, P. M. & Meservey, R. Critical magnetic field of very thin superconducting aluminum films. Physical Review B **25**, 171–178 (1982).

[28] Meservey, R., Tedrow, P. M. & Bruno, R. C. Tunneling measurements on spin-paired superconductors with spin-orbit scattering. Physical Review B **11**, 4224–4235 (1975).

[29] Bruno, R. C. & Schwartz, B. B. Magnetic Field Splitting of the Density of States of Thin Superconductors. Physical Review B **8**, 3161–3178 (1973).

[30] Hübler, F., Wolf, M. J., Beckmann, D. & v. Löhneysen, H. Long-range spin-polarized quasiparticle transport in mesoscopic al superconductors with a zeeman splitting. Physical Review Letters **109**, 207001 (2012).

[31] Silaev, M., Virtanen, P., Bergeret, F. S. & Heikkilä, T. T. Long-Range Spin Accumulation from Heat Injection in Mesoscopic Superconductors with Zeeman Splitting. Physical Review Letters **114**, 167002 (2015).

[32] Bobkova, I. V. & Bobkov, A. M. Long-range spin imbalance in mesoscopic superconductors under Zeeman splitting. JETP Letters **101**, 118–124 (2015).

[33] Bobkova, I. V. & Bobkov, A. M. Injection of nonequilibrium quasiparticles into Zeeman-split superconductors: A way to create long-range spin imbalance.

Physical Review B **93**, 024513 (2016).
[34] Lemberger, T. R. One-to-one correspondence of charge-imbalance relaxing mechanisms with pair-breaking mechanisms in superconductors. Physical Review B **29**, 4946–4950 (1984).
[35] Hübler, F., Lemyre, J. C., Beckmann, D. & v. Löhneysen, H. Charge imbalance in superconductors in the low-temperature limit. Physical Review B **81**, 184524 (2010).
[36] Kleine, A. et al. Magnetic field and contact resistance dependence of non-local charge imbalance. Nanotechnology **21**, 274002 (2010).
[37] Cadden-Zimansky, P., Jiang, Z. & Chandrasekhar, V. Charge imbalance, crossed Andreev reflection and elastic co-tunnelling in ferromagnet/superconductor/normal-metal structures. New Journal of Physics **9**, 116–116 (2007).
[38] Takane, Y. & Nagato, Y. Magnetic Field Effect on Charge Imbalance Conversion in Superconducting Wires. Journal of the Physical Society of Japan **77**, 093713 (2008).
[39] Aikebaier, F., Silaev, M. A. & Heikkilä, T. Supercurrent-induced charge-spin conversion in spin-split superconductors. Physical Review B **98**, 024516 (2018).
[40] The asymmetrical signal in Figure 5 would remain in the data, but we would be unable to differentiate the contribution from the two spins and clearly identify f_{L3}.
[41] Such measurements of 'excess QPs' have been made in extended junctions, but because of the spatial averating, the spectroscopic information was lost.

ACKNOWLEDGEMENTS

We acknowledge valuable discussions with Tero Heikkilä, Mikhail Silaev and Wolfgang Belzig; and an ANR JCJC grant (SPINOES) from the French Agence Nationale de Recherche. BYW is grateful for a College of Science (CoS) Travel Grant and Scholarship from the National Taiwan University. We also thank Freek Massee, Hadar Steinberg and Suchitra Sebastian for helpful comments on the manuscript.

AUTHOR CONTRIBUTIONS

MK fabricated the devices and performed the numerical calculations. MK and MA made the measurements. MK, MA and CQHL analysed the data and wrote the manuscript. BYW and MW were involved in earlier stages of the work.

COMPETING FINANCIAL INTERESTS

The authors declare no competing financial interests.

METHODS

The superconducting wire is 6nm Al, while the injector is 100nm Cu and the detectors 8nm Al/0.1nm Pt. The devices were fabricated with standard electron-beam lithography and evaporation techniques. The NIS and SIS' junctions have conductances per unit area $\approx 1.9\frac{\mathrm{mS}}{\mu\mathrm{m}^2}$ and $\approx 3.3\frac{\mathrm{mS}}{\mu\mathrm{m}^2}$ respectively (corresponding to barrier transparencies of $\approx 2\times10^{-5}$). All measurements were performed using standard lock-in techniques in a dilution refrigerator with a base temperature of 90mK. The lock-in frequency is typically $17-37$Hz and the excitation voltage 5μV. The out-of-plane component of H was compensated to be $\leq 1\%$ of the total field.

PHYSICAL REVIEW RESEARCH **1**, 032009(R) (2019)

Rapid Communications

Nonadiabatic dynamics in strongly driven diffusive Josephson junctions

J. Basset,[1,*] M. Kuzmanović,[1] P. Virtanen,[2,3] T. T. Heikkilä,[3] J. Estève,[1] J. Gabelli,[1] C. Strunk,[1,4] and M. Aprili[1]

[1]*Laboratoire de Physique des Solides, CNRS, Univ. Paris-Sud, Université Paris Saclay, 91405 Orsay Cedex, France*

[2]*NEST, Istituto Nanoscienze-CNR and Scuola Normale Superiore, I-56127 Pisa, Italy*

[3]*University of Jyväskylä, Department of Physics and Nanoscience Center, P.O. Box 35 (YFL) University of Jyväskylä, Finland*

[4]*Institute of Experimental and Applied Physics, University of Regensburg, D-93040 Regensburg, Germany*

(Received 13 February 2019; revised manuscript received 1 October 2019; published 30 October 2019)

By measuring the Josephson emission of a diffusive superconductor–normal metal–superconductor (SNS) junction we access the harmonic content of the current-phase relation (CPR). We experimentally identify a nonadiabatic regime in which the CPR is modified by high frequency microwave irradiation. This observation is explained by the excitation of quasiparticles in the normal wire induced by the electromagnetic field. The distortion of the CPR originates from the phase-dependent out-of-equilibrium distribution function which is strongly affected by the ac response of the spectral supercurrent. For a phase difference approaching π, transitions across the minigap are dynamically favored, leading to a supercurrent reduction. This finding is supported by a comparison with the quasiclassical Green's function theory of superconductivity in diffusive SNS junctions under microwave irradiation.

DOI: 10.1103/PhysRevResearch.1.032009

At sufficiently low temperatures, superconductors cannot absorb microwave radiation of energy smaller than the superconducting energy gap Δ [1–3]. In Josephson weak links instead, where two superconductors (S) are weakly coupled through a long diffusive metallic wire (N), radiation can be absorbed in N because the induced gap in the density of states or minigap [4,5] is considerably smaller than Δ. In this Rapid Communication we show that the out-of-equilibrium state originating from such absorption and its feedback on the quasiparticle spectrum of the wire strongly modifies the current-phase relation (CPR) [6] of the junction. In particular we observe a large increase of its second harmonic which reflects the peculiar out-of-equilibrium distribution function obtained under high frequency microwave irradiation. This finding is in good agreement with the quasiclassical theory of superconductivity in which the effect of the microwave drive on the spectral current density is taken into account [7].

In proximity-coupled Josephson junctions, Andreev reflections lead to a coherent superposition of electron-hole excitations in the weak link, which carry the supercurrent [8,9]. These excitations form a quasicontinuum of Andreev bound states (ABS) [5,9]. The single particle density of states in N develops a minigap $E_g(\varphi)$ whose amplitude depends on the phase difference, φ, between the two superconductors [6,10,11] and is minimal for $\varphi = \pi$ [12,13]. In long wires the minigap is set by the diffusion time $\tau_D = L^2/D$ and is proportional to the Thouless energy, $E_{\rm Th} = \hbar/\tau_D$ as $E_g(0) \approx 3.1E_{\rm Th} \ll \Delta$ [14], where D and L stand for the diffusion coefficient and the length of the wire, respectively. The supercurrent is related to the Andreev spectrum via the spectral current density $j_s(E,\varphi)$ and the distribution function $f(E,\varphi)$ [8]:

$$I(\varphi) = \frac{1}{eR_N}\int [1-2f(E,\varphi)]j_s(E,\varphi)dE, \qquad (1)$$

where R_N is the normal state resistance of the wire. The periodic phase dependence in $j_s(E,\varphi)$ gives rise to a Fourier expansion of $I(\varphi)$ with coefficients $I_{c,n}$, such that the CPR reads [9]

$$I(\varphi) = \sum_{n=1}^{\infty} I_{c,n}\sin(n\varphi). \qquad (2)$$

At thermal equilibrium $f(E)$ is the Fermi distribution function and is independent of φ.

The purpose of this work is to induce and probe the out-of-equilibrium state obtained in the *strongly nonadiabatic* regime for which the frequency of the microwave drive $\omega_{\rm rf}$ exceeds both the energy relaxation rate Γ and the minigap: $\Gamma < 2E_g/\hbar \lesssim \omega_{\rm rf}$ [15]. In this situation both the spectral supercurrent $j_s(E,\varphi)$ and the distribution function are altered by the pair-breaking induced by the microwave absorption, i.e., by a direct excitation of quasiparticles across the minigap.

Experimentally we address $I_{c,n}$ by measuring the ac-Josephson effect [16] under microwave illumination. We demonstrate that the harmonic content of the Josephson emission is drastically modified due to the quasiparticle energy redistribution within the normal wire. The comparison with the microscopic theory [7] reveals that the time dependence of the ABS spectrum is essential, as the effect arises from the backaction of the time-dependent spectrum to the out-of-equilibrium distribution function. This observation, in the strongly nonadiabatic regime, goes beyond the usual

*julien.basset@u-psud.fr

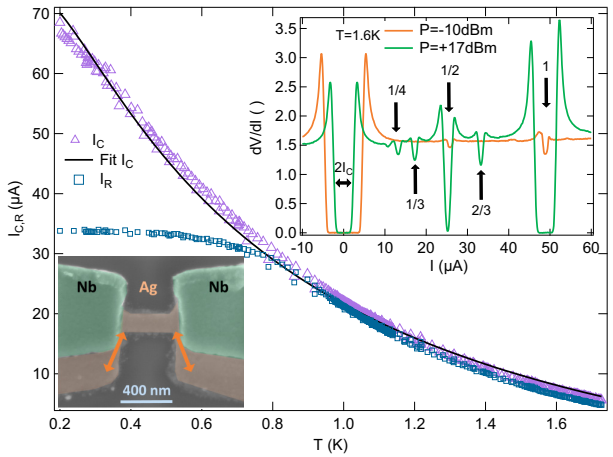

FIG. 1. Temperature dependence of the critical and retrapping currents of the junction. Top inset: differential resistance dV/dI vs dc current I at $T = 1.6$ K for two irradiation powers ($\omega_{rf}/2\pi = 35.18$ GHz). The high power curve exhibits subharmonic Shapiro steps (see arrows and corresponding fractions). Bottom inset: scanning electron micrograph of the junction. Green shading highlights the superconductor (Nb) and light orange the normal part (Ag). Arrows point at metallic reservoirs acting as heat sinks.

Eliashberg approximation [17] in which the ac-spectral supercurrent plays no role [18,19].

To investigate the ac-Josephson emission, we have fabricated a radio-frequency compatible SNS junction by e-beam lithography. The junction is obtained by angular e-gun evaporation of a 70 nm thick layer of Nb (S) and a 40 nm thick layer of silver (N) [see Fig. 1(b)]. The normal metal length is $L = 400$ nm and it has a normal state resistance $R_N = 1.6\Omega$. Normal metal reservoirs (see inset of Fig. 1) act as heat sinks reducing the energy relaxation times of quasiparticles. The measurement circuit is presented in the Supplemental Material (SM) [20]. The sample is connected through two bias tees which allow dc biasing, microwave excitation ($\omega_{rf}/2\pi \in [0 - 40]$ GHz), and detection.

The temperature dependence of the critical current $I_c(T)$ together with the retrapping current $I_r(T)$ are presented in the main panel of Fig. 1. The two curves separate below $T_h \approx 0.8$ K, where self-heating becomes relevant [21]. We fit the I_c data (black line in Fig. 1) to obtain an estimate of the Thouless energy $E_{Th} \approx 19 \pm 2$ μeV [22], which sets the minigap to $2E_g(0) \approx 118$ μeV $\equiv 28.5$ GHz. By comparing with two shorter samples we verified that the Thouless energy scales as $1/L^2$ provided that the effective wire length is roughly 250 nm longer than the geometrical gaps between the Nb leads as observed in previous experiments (see SM [20] and [22–24]). Finally, the diffusion coefficient is found to be $D \approx 90$ cm^2/s (see SM [20], which also include Refs. [25–29]), which is close to previous experiments using similar junctions [24]. The inset of Fig. 1 shows the differential resistance as a function of the dc-current bias under microwave excitation ($\omega_{rf}/2\pi = 35.18$ GHz) at $T \approx 1.6$ K $> T_h$. The zero resistance plateaus correspond to Shapiro steps at $V_{dc} = n/m\,\hbar\omega_{rf}/2e$ (n and m integers) [30]. The temperature dependence of the maximum amplitude I_S of the main Shapiro step ($n = 1, m = 1$) allows one to verify the quality of the heat sinks (see Ref. [31] and SM [20]) and deduce the quasiparticle energy relaxation rate $\Gamma/2\pi \approx 4.6$ GHz, which corresponds to the escape time of the hot quasiparticles out of the junction given by the diffusion time $\tau_D = 1/\Gamma \approx 35$ ps. To further characterize our junction we show in Fig. 2(a) the critical current [32] as a function of the normalized applied microwave field amplitude $s = eV_{ac}/\hbar\omega_{rf}$ for two excitation frequencies $\omega_{rf}/2\pi = 20.72$ GHz and $\omega_{rf}/2\pi = 35.18$ GHz. As one increases the microwave power the critical current follows roughly the zeroth order Bessel function $|J_0(2s)|$. Note that the absolute value of s is hard to calibrate accurately. We have here chosen to scale s such that the minimum of the experimental data (I_c) and the minimum of $|J_0(2s)|$ (adiabatic limit) match. Interestingly, the critical current I_c for $\omega_{rf}/2\pi = 35.18$ GHz does not vanish at $s \approx 1.2$ as expected in the adiabatic limit [33,34]. We address this new regime by analyzing the CPR.

The CPR of long SNS junctions under microwave radiation has been investigated in Ref. [24] in a phase-biased configuration using a Hall sensor and low microwave frequencies ($\omega_{rf} < 2E_g/\hbar$). The alternative approach we take in this experiment is to directly measure the ac-Josephson emission spectral density N_J (V^2/Hz) generated by the junction when dc current biased across a microwave circuit allowing a galvanic coupling to microwaves. We perform the experiment in the limit where the Josephson frequency is small compared to the excitation frequency ($\omega_J = 2eV_{dc}/\hbar < \omega_{rf}$) so that the two frequency scales are separated and we can consider a modified CPR with the fast oscillation averaged out (see SM [20] for details). The frequency of the emitted ac radiation from the nth harmonic of the CPR obeys the relation $\omega_{J,n}/2\pi = 2enV_{dc}/h$. Therefore, at a fixed dc voltage the harmonic content of the CPR appears as multiple peaks in the spectrum of the emitted Josephson radiation. As it is technically very demanding to perform such an experiment in a large bandwidth, we adopted a strategy in which the radiation is measured in a band of about 2.5 GHz centered around $\omega_0/2\pi = 6.5$ GHz. In this experimental situation, the contribution from the nth harmonic appears as a radiation peak when the voltage is equal to $V_{dc,n} = \hbar\omega_0/2en$.

We then measure the Josephson radiation spectral density N_J as a function of the applied dc current and microwave power for different ω_{rf} [35]. Such measurements, presented in Figs. 2(b) and 2(c), show two emission peaks at $V_{dc} \approx \hbar\omega_0/4e \approx 6$ μeV ($I_{dc} = 6.5$ μA at low power) and $V_{dc} \approx \hbar\omega_0/2e \approx 12$ μeV ($I_{dc} = 10$ μA at low power) corresponding respectively to the second and the first harmonic of the CPR [letters **B** and **A** in Fig. 2(b)]. The width of these two peaks is set by the combined effects of thermal noise and the finite measurement bandwidth of the setup [see SM [20] and dashed lines in Fig. 2(c)]. To avoid a reduction of $I_{c,1}$ by electron heating due to the dc power, the bath temperature has to be sufficiently large, allowing the electron-phonon coupling in the heat sinks (see inset of Fig. 1) to be effective. In our case we evaluate $\Delta T \approx +1.6$ mK at $T = 1.6$ K (see SM [20]). We follow the amplitude of peaks **A** and **B** as a function of the microwave power for two frequencies as shown in Figs. 2(d) and 2(e). As one increases the power,

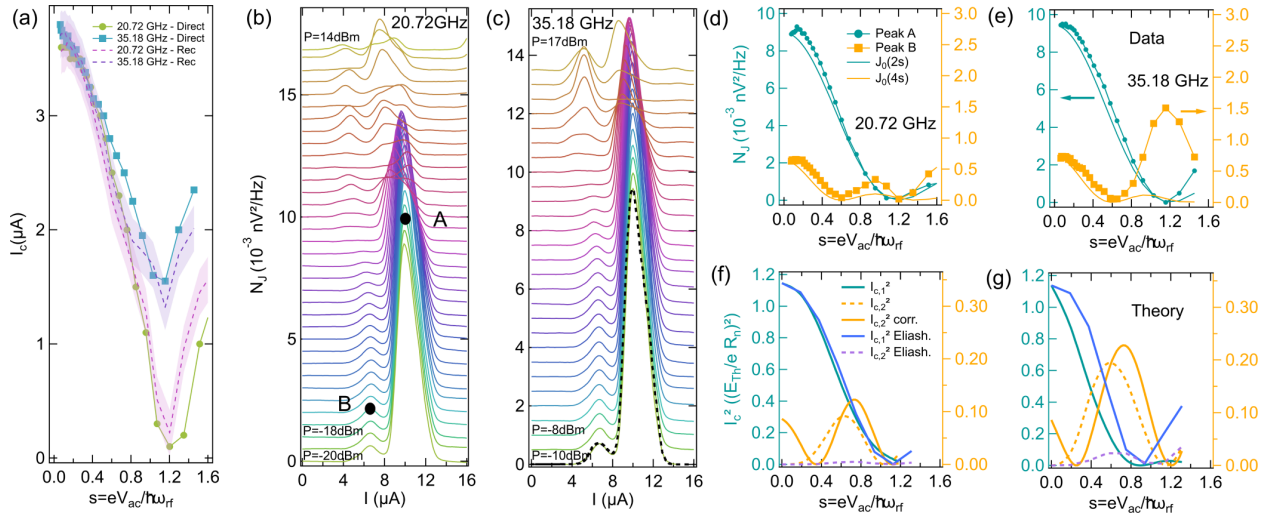

FIG. 2. (a) Power dependence of the critical current for two applied microwave frequencies together with reconstructed critical currents (see text). (b) ac-Josephson spectral density N_J vs dc current for increasing microwave power (the powers expressed in dBm are the ones at the output of the microwave generator; the power step size between curves is 1 dBm) at $\omega_{rf}/2\pi = 20.72$ GHz. (c) Idem (b) for 35.18 GHz. Dashed curve is the expected emission within the ω_0 band (see SM [20]). (d) Power dependence of emission peak amplitudes A and B in Fig. 2(b) for $\omega_{rf}/2\pi = 20.72$ GHz. Bessel functions J_0 correspond to the adiabatic limit (see text) and are scaled to match the lowest power data points. (e) Idem (d) for 35.18 GHz. (f) Calculated power dependence of the squared harmonics $I^2_{c,1}$ and $I^2_{c,2}$ (proportional to experimental N_J) for parameters $\hbar\omega_{rf}/E_{Th} = 3$, $\Gamma/E_{Th} = 0.4$, $k_BT/E_{Th} = 7$, and $\Delta/E_{Th} = 55$. (g) Idem (f) but for $\hbar\omega_{rf}/E_{Th} = 7$.

peak **A**, related to the first harmonic, decreases following roughly a zeroth order Bessel function [see blue lines in Figs. 2(d) and 2(e)]. Peak **B**, that corresponds to the second harmonic, has a more complicated behavior. It starts from a nonzero value [36], vanishes, and then displays a second maximum at higher rf powers and high frequencies in a way whose height is not consistent with the adiabatic phase dynamics [compare yellow squares and lines in Figs. 2(d) and 2(e)].

From the power dependence of the harmonics weight of the CPR obtained from peaks **A** and **B**, it is possible to reconstruct, up to a scaling factor, a power-dependent critical current that one may compare to the measured one. To do so, we reconstruct a CPR based on the first two measured harmonics and take its maximum value. The result is reported as dashed lines in Fig. 2(a) and demonstrates reasonable agreement with the measured I_c [37]. Such a verification indicates that measuring the ac-Josephson effect for small, but finite, dc voltage is a good probe of the CPR. This justifies the use of the existing theory of diffusive SNS junctions under microwave irradiation at zero dc voltage.

In the following we use the theory developed by Virtanen *et al.* [7] to account for our experimental data. In this theory both the spectral current density and the out-of-equilibrium distribution function can be obtained by solving the Usadel equation in the Keldysh-Nambu representation. When $\Gamma < 2E_g/\hbar$, the microwave bias affects the distribution function more efficiently than the spectral current density which acquires, however, a component at the frequency of the drive. The dynamics of the current couples back to the distribution function which strongly modifies the CPR. To understand qualitatively the backcoupling of the ac current to the distribution function we can analytically write the modifications of the distribution function $\delta f = f - f_0$ in the linear response limit. It reads

$$\begin{aligned}\Gamma\langle\rho\rangle\delta f = {} & \eta_-(E+\hbar\omega_{rf})f_0(E+\hbar\omega_{rf})[1-f_0(E)] \\ & -\eta_+(E)f_0(E)[1-f_0(E+\hbar\omega_{rf})] \\ & +\eta_+(E-\hbar\omega_{rf})f_0(E-\hbar\omega_{rf})[1-f_0(E)] \\ & -\eta_-(E)f_0(E)[1-f_0(E-\hbar\omega_{rf})]. \end{aligned} \quad (3)$$

Here, $\langle\rho\rangle$ is the spatially averaged density of states inside the junction. $f_0(E)$ is the equilibrium Fermi-Dirac distribution function and $\eta_+(E)$ and $\eta_-(E)$ are the energy-dependent photon absorption and emission rates, respectively. At low frequencies $\omega_{rf} < 2E_g/\hbar$, the transition rates are given to a good accuracy by unperturbed spectral functions, similarly as in the Eliashberg [17] and Mattis-Bardeen [2] theories of photoabsorption. At $\omega_{rf} > 2E_g/\hbar$, however, the ac current flowing in the weak link starts to break Cooper pairs (i.e., promote quasiparticles across the gap). An accurate description of the energy dependence of this process requires a more complete consideration of the dynamics of the spectral quantities.

We solve the Usadel equations numerically using the experimental parameters E_{Th}, ω_{rf} and the quasiparticle relaxation rate Γ close to the above inferred value. We compute the time-average spectral current under the high-frequency drive ω_{rf}, which yields the effective current-phase relation $I(\varphi, s)$ relevant for the lower-frequency phase dynamics (see SM [20] and [7]). The result is shown in Fig. 3(a) for the irradiation frequency $\omega_{rf}/2\pi = 35.18$ GHz. As the power is increased, the current-phase relation is distorted and shows a maximum shifted towards smaller phase values. This negative shift demonstrates that the second harmonic value is positive

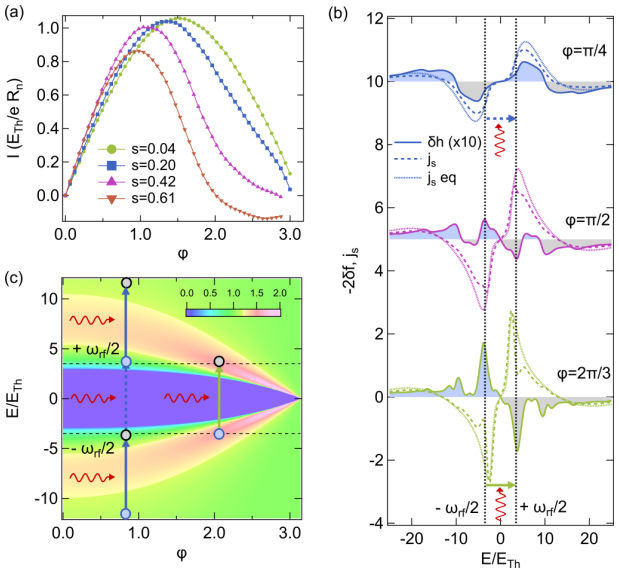

FIG. 3. (a) Calculated current-phase relation for different reduced power s. Calculation parameters are $\hbar\omega_{\rm rf}/E_{\rm Th} = 7$, $\Gamma/E_{\rm Th} = 0.4$, $k_{\rm B}T/E_{\rm Th} = 7$, and $\Delta/E_{\rm Th} = 55$. (b) Calculated equilibrium $j_{\rm s,eq}$ and nonequilibrium $j_{\rm s}$ spectral currents and modifications of the distribution function $-2\delta f$ for different phases. Calculation parameters are as in (a). Full (dashed) horizontal arrows represent the high (low) probability interband transitions. (c) Color-coded sketch of the normalized energy-phase dependent density of states of a long diffusive SNS junction. Full (dashed) vertical arrows represent the high (low) probability inelastic transitions. Gray (blue) circles represent electronlike (holelike) quasiparticles.

under illumination and not negative as expected from the equilibrium CPR at low temperatures [9]. We quantitatively extract the weights of the different harmonics by fitting the calculated CPR with the formula $I = \sum_{k=0}^{9} I_{\rm c,k}\sin(k\varphi)$, where $I_{\rm c,k}$ are the fitting parameters. We show in Figs. 2(f) and 2(g) the power dependence of the first two harmonics squared, $I_{\rm c,1}^2$ and $I_{\rm c,2}^2$ [Eq. (2)], which should be proportional to the experimental spectral density $N_{\rm J}$.

In order to obtain a comparison between the theory and the experiment, at low power, we have to include a negative phenomenological contribution $I_{\rm c,2\,pheno}$ to match the measured second harmonic at $s = 0$. Its precise origin remains to be determined [36]. In this way, the experimental data shown in Figs. 2(d) and 2(e) coincide with a corrected version of the calculations $I_{\rm c,2}^2\,{\rm corr} = (I_{\rm c,2} - |I_{\rm c,2\,pheno}|J_0(4s))^2$ (see SM [20] for details). This correction provides a good agreement between the theory and the experimental data in the full power range with little effect at high power where the strongly nonadiabatic regime appears [see dashed and solid yellow lines around $s \approx 0.7$ in Figs. 2(f) and 2(g)]. As demonstrated by the purple dashed lines in Figs. 2(f) and 2(g), the Eliashberg theory [17] fails to explain our experimental data because it neglects the coupling between the phase dynamics and the distribution function.

The distortion of the CPR can be understood by inspection of the microwave-induced changes of the spectral supercurrent $j_{\rm s}(E,\varphi)$ and distribution functions $-2\delta f(E,\varphi) = -2[f(E,\varphi) - f_0(E)]$ shown in Fig. 3(b). For small values of the phase φ [see top curves in Fig. 3(b)], the changes in the distribution function are dominated by intraband transitions leading to the function $-2\delta f$ and $j_{\rm s}$ having the same sign and shape. For larger phase values instead, transitions across the gap are favored and visible as peaks in the distribution function [see central and lower curves in Fig. 3(b)]. These peaks are located at energies $E = \pm\hbar\omega_{\rm rf}/2e$, i.e., at the middle of the energy ranges $|E| \in [E_{\rm g}, \hbar\omega_{\rm rf} - E_{\rm g}]$ participating in across-the-gap transitions. Note that the peak positions [vertical lines in Fig. 3(c)] are independent of $E_{\rm g}$. The peaks originate from the transition probability that is influenced by the ac response of the spectral supercurrent, which deviates from the equilibrium one as shown in Fig. 3(c). Importantly, these peaks have a sign that is opposite to the spectral current implying that the Cooper pair breaking results in a reduction of the total supercurrent.

In conclusion, we performed a microwave spectroscopy of the ac-Josephson effect in a diffusive weak link in the *strongly nonadiabatic* regime for which inelastic transitions across the minigap are possible. The microwaves are found to drastically enhance the second harmonic of the CPR as a result of the backcoupling of the ac-spectral supercurrent to the distribution function. Future experiments shall investigate the Josephson emission at high frequency in limits where the frequency of the emitted photons is comparable to the minigap in the normal wire [40,41]. Besides diffusive-metal SNS junctions, the spectroscopic approach could be used for several other types of weak links. In particular, microwaves also modify the CPR in atomic contacts [42,43]. In nanowire junctions with Majorana bound states, the microwave affected CPR might reveal signatures about the topologically forbidden transitions [44–46].

We acknowledge valuable discussions with B. Reulet, F. Massee, H. Bouchiat, M. Ferrier, R. Deblock, and S. Guéron. This work has partially been funded by the European Union's Horizon 2020 research and innovation programme under Grant Agreement No. 800923, and the Academy of Finland Grant No. 317118. C.S. thanks the CNRS and the Université Paris-Sud for hospitality and funding his stay at the Laboratoire de Physique des Solides.

[1] R. E. Glover and M. Tinkham, Phys. Rev. **104**, 844 (1956).
[2] D. C. Mattis and J. Bardeen, Phys. Rev. **111**, 412 (1958).
[3] M. Tinkham, *Introduction to Superconductivity*, 2nd ed. (McGraw-Hill, New York, 1996).
[4] W. Belzig, C. Bruder, and G. Schön, Phys. Rev. B **54**, 9443 (1996).
[5] M. Ferrier, B. Dassonneville, S. Guéron, and H. Bouchiat, Phys. Rev. B **88**, 174505 (2013).
[6] A. A. Golubov, M. Yu. Kupriyanov, and E. Illichev, Rev. Mod. Phys. **76**, 411 (2004).
[7] P. Virtanen, T. T. Heikkilä, F. S. Bergeret, and J. C. Cuevas, Phys. Rev. Lett. **104**, 247003 (2010).

[8] Y.-K. Yip, Phys. Rev. B **58**, 5803 (1998).

[9] T. T. Heikkilä, J. Särkkä, and F. K. Wilhelm, Phys. Rev. B **66**, 184513 (2002).

[10] I. O. Kulik, Sov. Phys. JETP **30**, 944 (1970).

[11] H. le Sueur, P. Joyez, H. Pothier, C. Urbina, and D. Estève, Phys. Rev. Lett. **100**, 197002 (2008).

[12] D. A. Ivanov, R. von Roten, and G. Blatter, Phys. Rev. B **66**, 052507 (2002).

[13] B. Dassonneville, A. Murani, M. Ferrier, S. Guéron, and H. Bouchiat, Phys. Rev. B **97**, 184505 (2018).

[14] F. Zhou, P. Charlat, B. Spivak, and B. Pannetier, J. Low Temp. Phys. **110**, 841 (1998).

[15] If the energy relaxation rate is the larger energy scale, the junction displays microwave-induced phase dynamics only, as in tunnel junctions.

[16] D. N. Langenberg, D. J. Scalapino, B. N. Taylor, and R. E. Eck, Phys. Rev. Lett. **15**, 294 (1965).

[17] G. M. Eliashberg and B. I. Ivlev, in *Nonequilibrium Superconductivity*, edited by D. N. Langenberg and A. I. Larkin (North-Holland, Amsterdam, 1986), p. 211.

[18] J. M. Warlaumont, J. C. Brown, T. Foxe, and R. A. Buhrman, Phys. Rev. Lett. **43**, 169 (1979).

[19] F. Chiodi, M. Aprili, and B. Reulet, Phys. Rev. Lett. **103**, 177002 (2009).

[20] See Supplemental Material at http://link.aps.org/supplemental/10.1103/PhysRevResearch.1.032009 for detailed information on samples and the measurement setup, estimate of the quantum corrections, analysis of the self-heating effect, and details on the comparison between experiment and theory.

[21] A. De Cecco, K. Le Calvez, B. Sacépé, C. B. Winkelmann, and H. Courtois, Phys. Rev. B **93**, 180505(R) (2016).

[22] P. Dubos, H. Courtois, B. Pannetier, F. K. Wilhelm, A. D. Zaikin, and G. Schön, Phys. Rev. B **63**, 064502 (2001).

[23] P. Dubos, H. Courtois, O. Buisson, and B. Pannetier, Phys. Rev. Lett. **87**, 206801 (2001).

[24] M. Fuechsle, J. Bentner, D. A. Ryndyk, M. Reinwald, W. Wegscheider, and C. Strunk, Phys. Rev. Lett. **102**, 127001 (2009).

[25] K. K. Likharev, Rev. Mod. Phys. **51**, 101 (1979).

[26] F. Pierre, A. B. Gougam, A. Anthore, H. Pothier, D. Esteve, and N. O. Birge, Phys. Rev. B **68**, 085413 (2003).

[27] A. H. Steinbach, J. M. Martinis, and M. H. Devoret, Phys. Rev. Lett. **76**, 3806 (1996).

[28] L. L. Isaacs, J. Chem. Phys. **43**, 307 (1965).

[29] G. L. Ingold and Y. V. Nazarov, in *Single Charge Tunneling*, edited by H. Grabert and M. H. Devoret, NATO Advanced Study Institute, Series B: Physics (Plenum Press, New York, 1992), Vol. 294, pp. 21–107.

[30] S. Shapiro, Phys. Rev. Lett. **11**, 80 (1963).

[31] J. Basset *et al.* (unpublished).

[32] The measured critical current is the current at which the differential resistance reaches the trigger value $dV/dI = 0.04\Omega$. This current might differ from the intrinsic critical current by a multiplication factor (see SM [20]) due to current fluctuations. The microwave power dependence which is of interest here is however qualitatively unaffected.

[33] K. K. Likharev, *Dynamics of Josephson Junctions and Circuits* (Gordon and Breach Science Publishers, New York, 1986).

[34] A. Barone and G. Paterno, *Physics and Applications of the Josephson Effect* (Wiley-Interscience, New York, 1982).

[35] The values of N_J take into account the whole microwave setup calibration. A systematic scaling uncertainty is then expected in the extracted values. See SM [20] for the noise spectral density calibration.

[36] Surprisingly, at low power we observe emission not only at $\hbar\omega_0/2e$ but also at $\hbar\omega_0/4e$, whereas it should not be present in this range of temperature. This large second harmonic has been reported previously in Refs. [23,39] and potentially explained theoretically by Lempitskii [38].

[37] In order to compare the *reconstructed* I_C from the measured signal N_J to the *directly* measured I_C [Fig. 2(a)], we use a scaling factor to match the zero-power value of the *directly* measured I_C. This scaling is mandatory because one cannot know perfectly the gain of the amplification chain (see SM [20]).

[38] S. V. Lempitskli, Sov. Phys. JETP **58**, 624 (1983).

[39] K. W. Lehnert, N. Argaman, H.-R. Blank, K. C. Wong, S. J. Allen, E. L. Hu, and H. Kroemer, Phys. Rev. Lett. **82**, 1265 (1999).

[40] E. Riedel, Z. Naturforsch. Teil A **19**, 1634 (1964).

[41] C. A. Hamilton and S. Shapiro, Phys. Rev. Lett. **26**, 426 (1971).

[42] F. S. Bergeret, P. Virtanen, T. T. Heikkilä, and J. C. Cuevas, Phys. Rev. Lett. **105**, 117001 (2010).

[43] L. Bretheau, Ç. Ö. Girit, H. Pothier, D. Esteve, and C. Urbina, Nature (London) **499**, 312 (2013).

[44] R. S. Deacon, J. Wiedenmann, E. Bocquillon, F. Domínguez, T. M. Klapwijk, P. Leubner, C. Brüne, E. M. Hankiewicz, S. Tarucha, K. Ishibashi, H. Buhmann, and L. W. Molenkamp, Phys. Rev. X **7**, 021011 (2017).

[45] H. Ren *et al.*, Nature (London) **569**, 93 (2019).

[46] A. Fornieri *et al.*, Nature (London) **569**, 89 (2019).

Bibliography

[1] Jhy-Jiun Chang and DJ Scalapino. "New instability in superconductors under external dynamic pair breaking". In: *Physical Review B* 10.9 (1974), p. 4047. DOI: 10.1103/PhysRevB.10.4047.

[2] J.E. Mooij. *Nonequilibrium superconductivity, phonons, and Kapitza boundaries*. Ed. by Kenneth E Gray. Vol. 65. Springer Science & Business Media, 2012. Chap. 7, pp. 191–229. DOI: 10.1007/978-1-4684-3935-9.

[3] John Clarke. *Nonequilibrium superconductivity, phonons, and Kapitza boundaries*. Ed. by Kenneth E Gray. Vol. 65. Springer Science & Business Media, 2012. Chap. 13, pp. 353–422. DOI: 10.1007/978-1-4684-3935-9.

[4] Albert Schmid and Gerd Schön. "Linearized kinetic equations and relaxation processes of a superconductor near Tc". In: *Journal of Low Temperature Physics* 20.1 (1975), pp. 207–227. ISSN: 1573-7357. DOI: 10.1007/BF00115264.

[5] SB Kaplan et al. "Quasiparticle and phonon lifetimes in superconductors". In: *Physical Review B* 14.11 (1976), p. 4854. DOI: 10.1103/PhysRevB.14.4854.

[6] PJ De Visser et al. "Evidence of a nonequilibrium distribution of quasiparticles in the microwave response of a superconducting aluminum resonator". In: *Physical review letters* 112.4 (2014), p. 047004. DOI: 10.1103/PhysRevLett.112.047004.

[7] Chandra M Natarajan, Michael G Tanner, and Robert H Hadfield. "Superconducting nanowire single-photon detectors: physics and applications". In: *Superconductor science and technology* 25.6 (2012), p. 063001. DOI: 10.1088/0953-2048/25/6/063001.

[8] K Serniak et al. "Hot nonequilibrium quasiparticles in transmon qubits". In: *Physical review letters* 121.15 (2018), p. 157701. DOI: 10.1103/PhysRevLett.121.157701.

[9] R-P Riwar et al. "Normal-metal quasiparticle traps for superconducting qubits". In: *Physical Review B* 94.10 (2016), p. 104516. DOI: 10.1103/PhysRevB.94.104516.

[10] W. Eisenmenger. *Nonequilibrium superconductivity, phonons, and Kapitza boundaries*. Ed. by Kenneth E Gray. Vol. 65. Springer Science & Business Media, 2012. Chap. 3, pp. 73–109. DOI: 10.1007/978-1-4684-3935-9.

[11] F Sebastian Bergeret et al. "Colloquium: Nonequilibrium effects in superconductors with a spin-splitting field". In: *Reviews of Modern Physics* 90.4 (2018), p. 041001. DOI: 10.1103/RevModPhys.90.041001.

[12] "Thermal, electric and spin transport in superconductor/ferromagnetic-insulator structures". In: *Progress in Surface Science* 94.3 (2019), p. 100540. ISSN: 0079-6816. DOI: https://doi.org/10.1016/j.progsurf.2019.100540.

[13] Jan Petter Morten, Arne Brataas, and Wolfgang Belzig. "Spin transport in diffusive superconductors". In: *Phys. Rev. B* 70 (21 2004), p. 212508. DOI: 10.1103/PhysRevB.70.212508.

[14] "Quasiclassical Green's function approach to mesoscopic superconductivity". In: *Superlattices and Microstructures* 25.5 (1999), pp. 1251 –1288. ISSN: 0749-6036. DOI: https://doi.org/10.1006/spmi.1999.0710.

[15] Francesco Giazotto et al. "Opportunities for mesoscopics in thermometry and refrigeration: Physics and applications". In: *Rev. Mod. Phys.* 78 (1 2006), pp. 217–274. DOI: 10.1103/RevModPhys.78.217.

[16] PJ De Visser et al. "Number fluctuations of sparse quasiparticles in a superconductor". In: *Physical review letters* 106.16 (2011), p. 167004. DOI: 10.1103/PhysRevLett.106.167004.

[17] Michael Tinkham. "Tunneling generation, relaxation, and tunneling detection of hole-electron imbalance in superconductors". In: *Physical Review B* 6.5 (1972), p. 1747. DOI: 10.1103/PhysRevB.6.1747.

[18] John Clarke. "Experimental observation of pair-quasiparticle potential difference in nonequilibrium superconductors". In: *Physical Review Letters* 28.21 (1972), p. 1363. DOI: 10.1103/PhysRevLett.28.1363.

[19] F Hübler et al. "Charge imbalance in superconductors in the low-temperature limit". In: *Physical Review B* 81.18 (2010), p. 184524. DOI: 10.1103/PhysRevB.81.184524.

[20] Thomas R. Lemberger. "One-to-one correspondence of charge-imbalance relaxing mechanisms with pair-breaking mechanisms in superconductors". In: *Phys. Rev. B* 29 (9 1984), pp. 4946–4950. DOI: 10.1103/PhysRevB.29.4946.

[21] Yositake Takane and Yasushi Nagato. "Magnetic Field Effect on Charge Imbalance Conversion in Superconducting Wires". In: *Journal of the Physical Society of Japan* 77.9 (2008), p. 093713. DOI: 10.1143/JPSJ.77.093713.

[22] A Kleine et al. "Magnetic field and contact resistance dependence of non-local charge imbalance". In: *Nanotechnology* 21.27 (2010), p. 274002. DOI: 10.1088/0957-4484/21/27/274002.

[23] P Cadden-Zimansky, Z Jiang, and Venkat Chandrasekhar. "Charge imbalance, crossed Andreev reflection and elastic co-tunnelling in ferromagnet/superconductor/normal-metal structures". In: *New Journal of Physics* 9.5 (2007), p. 116. DOI: 10.1088/1367-2630/9/5/116.

[24] AG Aronov. "Spin injection and polarization of excitations and nuclei in superconductors". In: *Zh. Eksp. Teor. Fiz* 71 (1976), pp. 370–376. URL: http://www.jetp.ac.ru/cgi-bin/e/index/e/44/1/p193?a=list.

[25] Francesco Giazotto et al. "Nonequilibrium spin-dependent phenomena in mesoscopic superconductor–normal metal tunnel structures". In: *Physical Review B* 76.18 (2007), p. 184518. DOI: 10.1103/PhysRevB.76.184518.

[26] Irina Vyacheslavovna Bobkova and AM Bobkov. "Recovering of superconductivity in S/F bilayers under spin-dependent nonequilibrium quasiparticle distribution". In: *JETP Letters* 101.6 (2015), pp. 407–412. DOI: 10.1134/S0021364015060041.

[27] TT Heikkilä, Moosa Hatami, and Gerrit EW Bauer. "Spin heat accumulation and its relaxation in spin valves". In: *Physical Review B* 81.10 (2010), p. 100408. DOI: 10.1103/PhysRevB.81.100408.

[28] Mark Johnson and Robert H Silsbee. "Interfacial charge-spin coupling: Injection and detection of spin magnetization in metals". In: *Physical Review Letters* 55.17 (1985), p. 1790. DOI: 10.1103/PhysRevLett.55.1790.

[29] Mark Johnson and RH Silsbee. "Spin-injection experiment". In: *Physical Review B* 37.10 (1988), p. 5326. DOI: 10.1103/PhysRevB.37.5326.

[30] PC Van Son, H Van Kempen, and P Wyder. "Boundary resistance of the ferromagnetic-nonferromagnetic metal interface". In: *Physical Review Letters* 58.21 (1987), p. 2271.

[31] T Valet and A Fert. "Theory of the perpendicular magnetoresistance in magnetic multilayers". In: *Physical Review B* 48.10 (1993), p. 7099. DOI: 10.1103/PhysRevLett.58.2271.

[32] FK Dejene et al. "Spin heat accumulation and spin-dependent temperatures in nanopillar spin valves". In: *Nature Physics* 9.10 (2013), p. 636. DOI: 10.1038/nphys2743.

[33] Michael Tinkham. *Introduction to superconductivity*. Courier Corporation, 2004.

[34] Peter Fulde. "High field superconductivity in thin films". In: *Advances in Physics* 22.6 (1973), pp. 667–719. DOI: 10.1080/00018737300101369.

[35] RVA Srivastava and W Teizer. "Analytical density of states in the Abrikosov–Gor'kov theory". In: *Solid State Communications* 145.9-10 (2008), pp. 512–513. DOI: 10.1016/j.ssc.2007.11.030.

[36] C. H. L. Quay et al. "Spin imbalance and spin-charge separation in a mesoscopic superconductor". In: *Nature Physics* 9.2 (2013), pp. 84–88. ISSN: 1745-2481. DOI: 10.1038/nphys2518.

[37] Michael J Wolf et al. "Spin injection from a normal metal into a mesoscopic superconductor". In: *Physical Review B* 87.2 (2013), p. 024517. DOI: 10.1103/PhysRevB.87.024517.

[38] F Hübler et al. "Long-range spin-polarized quasiparticle transport in mesoscopic Al superconductors with a Zeeman splitting". In: *Physical review letters* 109.20 (2012), p. 207001. DOI: 10.1103/PhysRevLett.109.207001.

[39] CHL Quay et al. "Quasiparticle spin resonance and coherence in superconducting aluminium". In: *Nature communications* 6 (2015), p. 8660. DOI: 10.1038/ncomms9660.

[40] CHL Quay et al. "Frequency-domain measurement of the spin-imbalance lifetime in superconductors". In: *Physical Review B* 93.22 (2016), p. 220501. DOI: 10.1103/PhysRevB.93.220501.

[41] Yaroslav Tserkovnyak, Arne Brataas, and Gerrit EW Bauer. "Enhanced Gilbert damping in thin ferromagnetic films". In: *Physical review letters* 88.11 (2002), p. 117601. DOI: 10.1103/PhysRevLett.88.117601.

[42] Mircea Trif and Yaroslav Tserkovnyak. "Dynamic magnetoelectric effect in ferromagnet/superconductor tunnel junctions". In: *Physical review letters* 111.8 (2013), p. 087602. DOI: 10.1103/PhysRevLett.111.087602.

[43] Caroline Richard, Manuel Houzet, and Julia S Meyer. "Andreev current induced by ferromagnetic resonance". In: *Physical review letters* 109.5 (2012), p. 057002. DOI: 10.1103/PhysRevLett.109.057002.

[44] Takahiro Moriyama et al. "Tunnel barrier enhanced voltage signal generated by magnetization precession of a single ferromagnetic layer". In: *Physical review letters* 100.6 (2008), p. 067602. DOI: 10.1103/PhysRevLett.100.067602.

[45] Jiang Xiao, Gerrit EW Bauer, and Arne Brataas. "Charge pumping in magnetic tunnel junctions: Scattering theory". In: *Physical Review B* 77.18 (2008), p. 180407. DOI: 10.1103/PhysRevB.77.180407.

[46] Yaroslav Tserkovnyak, T Moriyama, and John Q Xiao. "Tunnel-barrier-enhanced dc voltage signals induced by magnetization dynamics in magnetic tunnel junctions". In: *Physical Review B* 78.2 (2008), p. 020401. DOI: 10.1103/PhysRevB.78.020401.

[47] Yaroslav Tserkovnyak et al. "Nonlocal magnetization dynamics in ferromagnetic heterostructures". In: *Reviews of Modern Physics* 77.4 (2005), p. 1375. DOI: 10.1103/RevModPhys.77.1375.

[48] Y Kajiwara et al. "Transmission of electrical signals by spin-wave interconversion in a magnetic insulator". In: *Nature* 464.7286 (2010), p. 262. DOI: 10.1038/nature08876.

[49] Nikolai Kopnin. *Theory of nonequilibrium superconductivity*. Vol. 110. Oxford University Press, 2001. DOI: 10.1093/acprof:oso/9780198507888.001.0001.

[50] EM Lifshitz and LP Pitaevskii. "Statistical Physics (Part 2), Vol. 9 of Landau and Lifshitz". In: *Course of Theoretical Physics, 2nd ed.(Pergamon, Oxford, 1980)* (1980).

[51] Aleksei Alekseevich Abrikosov, Lev Petrovich Gor'kov, and Igor' Ekhiel'evich Dzyaloshinskii. *Quantum field theoretical methods in statistical physics*. Vol. 4. Pergamon, 1965.

[52] Richard D Mattuck. *A guide to Feynman diagrams in the many-body problem*. Courier Corporation, 1992.

[53] Piers Coleman. *Introduction to many-body physics*. Cambridge University Press, 2015.

[54] Gert Eilenberger. "Transformation of Gor'kov's equation for type II superconductors into transport-like equations". In: *Zeitschrift für Physik A Hadrons and nuclei* 214.2 (1968), pp. 195–213. DOI: 10.1007/BF01379803.

[55] Klaus D Usadel. "Generalized diffusion equation for superconducting alloys". In: *Physical Review Letters* 25.8 (1970), p. 507. DOI: 10.1103/PhysRevLett.25.507.

[56] Mihail Silaev et al. "Long-range spin accumulation from heat injection in mesoscopic superconductors with zeeman splitting". In: *Physical review letters* 114.16 (2015), p. 167002. DOI: 10.1103/PhysRevLett.114.167002.

[57] M. J.D. Powell. "A Fortran subroutine for solving systems of nonlinear algebraic equations". In: (Nov. 1968). URL: https://www.osti.gov/biblio/4772677-fortran-subroutine-solving-systems-nonlinear-algebraic-equations.

[58] D. Esteve F. Pierre H. Pothier and M.H. Devoret. "Energy Redistribution Between Quasiparticles in Mesoscopic Silver Wires". In: *Journal of Low Temperature Physics* 118.5 (2000), pp. 437–445. ISSN: 1573-7357. DOI: 10.1023/A:1004606420464.

[59] Kei Yosida. "Paramagnetic susceptibility in superconductors". In: *Physical Review* 110.3 (1958), p. 769. DOI: 10.1103/PhysRev.110.769.

[60] Jabir Ali Ouassou, Tom Doekle Vethaak, and Jacob Linder. "Voltage-induced thin-film superconductivity in high magnetic fields". In: *Phys. Rev. B* 98 (14 2018), p. 144509. DOI: 10.1103/PhysRevB.98.144509.

[61] DR Heslinga and TM Klapwijk. "Enhancement of superconductivity far above the critical temperature in double-barrier tunnel junctions". In: *Physical Review B* 47.9 (1993), p. 5157. DOI: 10.1103/PhysRevB.47.5157.

[62] CS Owen and DJ Scalapino. "Superconducting state under the influence of external dynamic pair breaking". In: *Physical Review Letters* 28.24 (1972), p. 1559. DOI: 10.1103/PhysRevLett.28.1559.

[63] M Lenander et al. "Measurement of energy decay in superconducting qubits from nonequilibrium quasiparticles". In: *Physical Review B* 84.2 (2011), p. 024501. DOI: 10.1103/PhysRevB.84.024501.

[64] Satadeep Bhattacharjee and Manas Sardar. "Spin polarized carrier injection into high-T c superconductors: a test for the superconductivity mechanism". In: *Physical Review B* 62.10 (2000), R6139. DOI: 10.1103/PhysRevB.62.R6139.

[65] R Meservey and PM Tedrow. "Properties of very thin aluminum films". In: *Journal of Applied Physics* 42.1 (1971), pp. 51–53. DOI: 10.1063/1.1659648.

[66] Ro A Klemm, A Luther, and MR Beasley. "Theory of the upper critical field in layered superconductors". In: *Physical Review B* 12.3 (1975), p. 877. DOI: 10.1103/PhysRevB.12.877.

[67] R Meservey, PM Tedrow, and Peter Fulde. "Magnetic field splitting of the quasiparticle states in superconducting aluminum films". In: *Physical Review Letters* 25.18 (1970), p. 1270. DOI: 10.1103/PhysRevLett.25.1270.

[68] R. Meservey, P. M. Tedrow, and Ronald C. Bruno. "Tunneling measurements on spin-paired superconductors with spin-orbit scattering". In: *Phys. Rev. B* 11 (11 1975), pp. 4224–4235. DOI: 10.1103/PhysRevB.11.4224.

[69] ""Small" Junctions in a Magnetic Field". In: *Physics and Applications of the Josephson Effect*. John Wiley and Sons, Ltd. Chap. 4, pp. 69–95. ISBN: 9783527602780. DOI: 10.1002/352760278X.ch4.

[70] P. M. Tedrow and R. Meservey. "Critical magnetic field of very thin superconducting aluminum films". In: *Phys. Rev. B* 25 (1 1982), pp. 171–178. DOI: 10.1103/PhysRevB.25.171.

[71] PC Van Son et al. "Inelastic scattering rate for electrons in thin aluminum films determined from the minimum frequency for microwave stimulation of superconductivity". In: *Physical Review B* 29.3 (1984), p. 1503. DOI: 10.1103/PhysRevB.29.1503.

[72] P Santhanam and DE Prober. "Inelastic electron scattering mechanisms in clean aluminum films". In: *Physical Review B* 29.6 (1984), p. 3733. DOI: 10.1103/PhysRevB.29.3733.

[73] RC Dynes et al. "Tunneling study of superconductivity near the metal-insulator transition". In: *Physical Review Letters* 53.25 (1984), p. 2437. DOI: 10.1103/PhysRevLett.53.2437.

[74] DA Browne, K Levin, and KA Muttalib. "Coulomb-induced anomalies in highly disordered superconductors: Application to tunneling". In: *Physical review letters* 58.2 (1987), p. 156. DOI: 10.1103/PhysRevLett.58.156.

[75] Pierre Février and Julien Gabelli. "Tunneling time probed by quantum shot noise". In: *Nature Communications* 9.1 (2018), p. 4940. ISSN: 2041-1723. DOI: 10.1038/s41467-018-07369-6.

[76] F. Chiodi, M. Aprili, and B. Reulet. "Evidence for Two Time Scales in Long SNS Junctions". In: *Phys. Rev. Lett.* 103 (17 2009), p. 177002. DOI: 10.1103/PhysRevLett.103.177002.

[77] T. M. Klapwijk. "Proximity Effect From an Andreev Perspective". In: *Journal of Superconductivity* 17.5 (2004), pp. 593–611. ISSN: 1572-9605. DOI: 10.1007/s10948-004-0773-0.

[78] Tero T. Heikkilä, Jani Särkkä, and Frank K. Wilhelm. "Supercurrent-carrying density of states in diffusive mesoscopic Josephson weak links". In: *Phys. Rev. B* 66 (18 2002), p. 184513. DOI: 10.1103/PhysRevB.66.184513.

[79] S.-K. Yip. "Energy-resolved supercurrent between two superconductors". In: *Phys. Rev. B* 58 (9 1998), pp. 5803–5807. DOI: 10.1103/PhysRevB.58.5803.

[80] J. J. A. Baselmans et al. "Direct Observation of the Transition from the Conventional Superconducting State to the π State in a Controllable Josephson Junction". In: *Phys. Rev. Lett.* 89 (20 2002), p. 207002. DOI: 10.1103/PhysRevLett.89.207002.

[81] GM Eliashberg. "Film superconductivity stimulated by a high- frequency field". In: *JETP LETT.* 11.3 (1970), pp. 114–116. URL: http://www.jetpletters.ac.ru/ps/1716/article_26086.shtml.

[82] Pauli Virtanen et al. "Theory of Microwave-Assisted Supercurrent in Diffusive SNS Junctions". In: *Phys. Rev. Lett.* 104 (24 2010), p. 247003. DOI: 10.1103/PhysRevLett.104.247003.

[83] TM Klapwijk and JE Mooij. "Microwave-enhanced superconductivity in aluminium films". In: *Physica B+ C* 81.1 (1976), pp. 132–136. DOI: 10.1016/0378-4363(76)90249-7.

[84] M. Fuechsle et al. "Effect of Microwaves on the Current-Phase Relation of Superconductor–Normal-Metal–Superconductor Josephson Junctions". In: *Phys. Rev. Lett.* 102 (12 2009), p. 127001. DOI: 10.1103/PhysRevLett.102.127001.

[85] J. Basset et al. "Nonadiabatic dynamics in strongly driven diffusive Josephson junctions". In: *Phys. Rev. Research* 1 (3 2019), p. 032009. DOI: 10.1103/PhysRevResearch.1.032009.

[86] "Voltage Current Characteristics". In: *Physics and Applications of the Josephson Effect*. John Wiley and Sons, Ltd. Chap. 6, pp. 121–160. ISBN: 9783527602780. DOI: 10.1002/352760278X.ch6.

[87] BD Josephson. "Coupled superconductors". In: *Reviews of Modern Physics* 36.1 (1964), p. 216. DOI: 10.1103/RevModPhys.36.216.

[88] Konstantin Konstantinovich Likharev. *Dynamics of Josephson junctions and circuits*. Gordon and Breach science publishers, 1986.

[89] Sidney Shapiro. "Josephson currents in superconducting tunneling: The effect of microwaves and other observations". In: *Physical Review Letters* 11.2 (1963), p. 80. DOI: doi.org/10.1103/PhysRevLett.11.80.

[90] CC Grimes and Sidney Shapiro. "Millimeter-wave mixing with Josephson junctions". In: *Physical Review* 169.2 (1968), p. 397. DOI: 10.1103/PhysRev.169.397.

[91] Peter Russer. "Influence of microwave radiation on current-voltage characteristic of superconducting weak links". In: *Journal of Applied Physics* 43.4 (1972), pp. 2008–2010. DOI: 10.1063/1.1661440.

[92] IK Yanson, VM Svistunov, and IM Dmitrenko. "Experimental observation of the tunnel effect for Cooper pairs with the emission of photons". In: *Sov. Phys. JETP* 21 (1965), p. 650. URL: http://www.jetp.ac.ru/cgi-bin/e/index/e/21/3/p650?a=list.

[93] Max Hofheinz et al. "Bright side of the Coulomb blockade". In: *Physical review letters* 106.21 (2011), p. 217005. DOI: 10.1103/PhysRevLett.106.217005.

[94] Toshiaki Matsui and Hiroshi Ohta. "Mesoscopic SNS mixers using negative resistance at low voltage". In: *Superconductor Science and Technology* 12.11 (1999), p. 859. DOI: 10.1088/0953-2048/12/11/350.

[95] Yuli V Nazarov. "Novel circuit theory of Andreev reflection". In: *Superlattices and microstructures* 25.5-6 (1999), pp. 1221–1231. DOI: 10.1006/spmi.1999.0738.

[96] S Guéron et al. "Superconducting proximity effect probed on a mesoscopic length scale". In: *Physical review letters* 77.14 (1996), p. 3025. DOI: 10.1103/PhysRevLett.77.3025.

[97] Hélène Le Sueur et al. "Phase controlled superconducting proximity effect probed by tunneling spectroscopy". In: *Physical review letters* 100.19 (2008), p. 197002. DOI: 10.1103/PhysRevLett.100.197002.

[98] DC Mattis and John Bardeen. "Theory of the anomalous skin effect in normal and superconducting metals". In: *Physical Review* 111.2 (1958), p. 412. DOI: 10.1103/PhysRev.111.412.

[99] P. Dubos et al. "Josephson critical current in a long mesoscopic S-N-S junction". In: *Phys. Rev. B* 63 (6 2001), p. 064502. DOI: 10.1103/PhysRevB.63.064502.

[100] B. T. Matthias, T. H. Geballe, and V. B. Compton. "Superconductivity". In: *Rev. Mod. Phys.* 35 (1 1963), pp. 1–22. DOI: 10.1103/RevModPhys.35.1.

[101] FC Wellstood, C Urbina, and John Clarke. "Hot-electron effects in metals". In: *Physical Review B* 49.9 (1994), p. 5942. DOI: 10.1103/PhysRevB.49.5942.

[102] KW Lehnert et al. "Nonequilibrium ac Josephson effect in mesoscopic Nb-InAs-Nb junctions". In: *Physical review letters* 82.6 (1999), p. 1265. DOI: 10.1103/PhysRevLett.82.1265.

[103] F. Pierre et al. "Dephasing of electrons in mesoscopic metal wires". In: *Phys. Rev. B* 68 (8 2003), p. 085413. DOI: 10.1103/PhysRevB.68.085413.

[104] Faluke Aikebaier, Mihail A Silaev, and TT Heikkilä. "Supercurrent-induced charge-spin conversion in spin-split superconductors". In: *Physical Review B* 98.2 (2018), p. 024516. DOI: 10.1103/PhysRevB.98.024516.

[105] Jabir Ali Ouassou, Tom Doekle Vethaak, and Jacob Linder. "Voltage-induced thin-film superconductivity in high magnetic fields". In: *Physical Review B* 98.14 (2018), p. 144509. DOI: 10.1103/PhysRevB.98.144509.

[106] FS Bergeret et al. "Theory of microwave-assisted supercurrent in quantum point contacts". In: *Physical review letters* 105.11 (2010), p. 117001. DOI: 10.1103/PhysRevLett.105.117001.

[107] L Bretheau et al. "Exciting Andreev pairs in a superconducting atomic contact". In: *Nature* 499.7458 (2013), p. 312. DOI: 10.1038/nature12315.

[108] Russell S Deacon et al. "Josephson radiation from gapless Andreev bound states in HgTe-based topological junctions". In: *Physical Review X* 7.2 (2017), p. 021011. DOI: 10.1103/PhysRevX.7.021011.

[109] Hechen Ren et al. "Topological superconductivity in a phase-controlled Josephson junction". In: *Nature* 569.7754 (2019), p. 93. DOI: 10.1038/s41586-019-1148-9.

[110] Antonio Fornieri et al. "Evidence of topological superconductivity in planar Josephson junctions". In: *Nature* 569.7754 (2019), p. 89. DOI: 10.1038/s41586-019-1068-8.

[111] M. Kuzmanović et al. *Evidence for spin-dependent energy transport in a superconductor*. 2020. eprint: arXiv:2001.04422.

université PARIS-SACLAY
ÉCOLE DOCTORALE
Physique en Île-de-France (EDPIF)

Titre: Transport hors-équilibre et de spins dans les supraconducteurs mésoscopiques

Mots clés: Supraconductivité hors-équilibre, Physique mésoscopique, Spintronique

Résumé: A l'etat fondamental les supraconducteurs peuvent transporter un courant sans dissipation appelé supercourant mais pas de courant d'énergie ou de spin. En revanche, les excitations élémentaires des fermions de spin 1/2, connues sous le nom de quasi-particules (QP), peuvent transporter aussi bien de l'aimantation, de la charge et de la chaleur.

Dans ce travail, des quasiparticules ont été injectées dans un fil supraconducteur ultra-mince ($<$ 10nm) en aluminium par effet tunnel. Un champ magnétique appliqué parallèlement au fil se couple au spin des quasiparticules par effet Zeeman et les excitations hors équilibre crées dans le fil sont polarisées en spin. Une spectroscopie sensible au spin sur cet état hors équilibre, montre que la fonction de distribution devient dépendante du spin et en particulier que la dégérenescence de spin du mode d'énergie est supprimée (illustré par $T_\downarrow \neq T_\uparrow$). De plus, en sondant la fonction de distribution à des échelles de longueur plus courtes que la longueur de l'interaction électron-électron, un état de non-équilibre non-thermique est observé (c'est-à-dire non Fermi-Dirac).

Dans une deuxième expérience, les effets hors-équilibre dus à l'absorption de radiation micro-ondes sur le transport coherent de jonctions Josephson SNS (supraconducteur-normal-supraconducteur) ont été étudiés. A cause du temps de diffusion fini dans le métal normal, ces structures hybrides ont une dynamique électronique propre. Le couplage Josephson a été étudié en mesurant soit le courant critique, soit le rayonnement micro-onde émis par effet Josephson AC à tension V_{DC} finie. L'effet Josephson AC est une sonde à fréquence finie non-invasive de la relation courant-phase de la jonction. Il a été observé que si la fréquence de la pompe micro-onde dépasse $\hbar\omega_{RF} \gg 2E_g$, où E_g est le minigap de la jonction, les transitions interbandes induites par l'absorption des photons de la pompe dans le métal-normal augmentent fortement l'anharmonicité de la relation courant-phase. Pour expliquer cet effet, il faut prendre en compte la fonction de distribution hors-équilibre et les propriétés spectrales de la jonction. Cela révèle un nouvel état dynamique hors-équilibre.

Title: Spin and out-of-equilibrium transport in mesoscopic superconductors

Keywords: Out-of-equilibrium superconductivity, mesoscopic physics, spintronics

Abstract: The ground state of conventional superconductors can carry a dissipationless current (a supercurrent) but not energy or spin currents. In contrast, single-particle excitations, known as quasiparticles (QP), can carry spin, charge and heat currents. In this work quasiparticles were injected into a superconducting Al wire by tunneling from a normal metal. If a Zeeman field is applied the created excitations can be spin polarized. By performing spin-sensitive spectroscopy on this out-of-equilibrium state it was found that the distribution function becomes spin-dependent, in particular the spin-energy mode (most easily exemplified by $T_\downarrow \neq T_\uparrow$) is excited. Additionally, by probing the distribution function at lengthscales shorter than the electron-electron interaction length a truly nonequilibrium state is found (i.e. not Fermi-Dirac).

In a second experiment, the effects of high-frequency microwave irradiation on the properties of SNS (Superconductor-Normal-Superconductor) Josephson junctions were studied. Junction properties were probed by measuring either the critical current or the emitted Josephson radiation at finite V_{DC} which is a noninvasive probe of the junction current-phase relation. It was observed that if the irradiation frequency exceeds $\hbar\omega_{RF} \gg 2E_g$, where E_g is the junction minigap, the induced interband transitions greatly increase the anharmonicity of the current-phase relation. To explain this effect, the nonequilibrium character of both the distribution function and the spectral properties of the junction need to be taken into account, revealing a novel nonequilibrium state.

Université Paris-Saclay
Espace Technologique / Immeuble Discovery
Route de l'Orme aux Merisiers RD 128 / 91190 Saint-Aubin, France